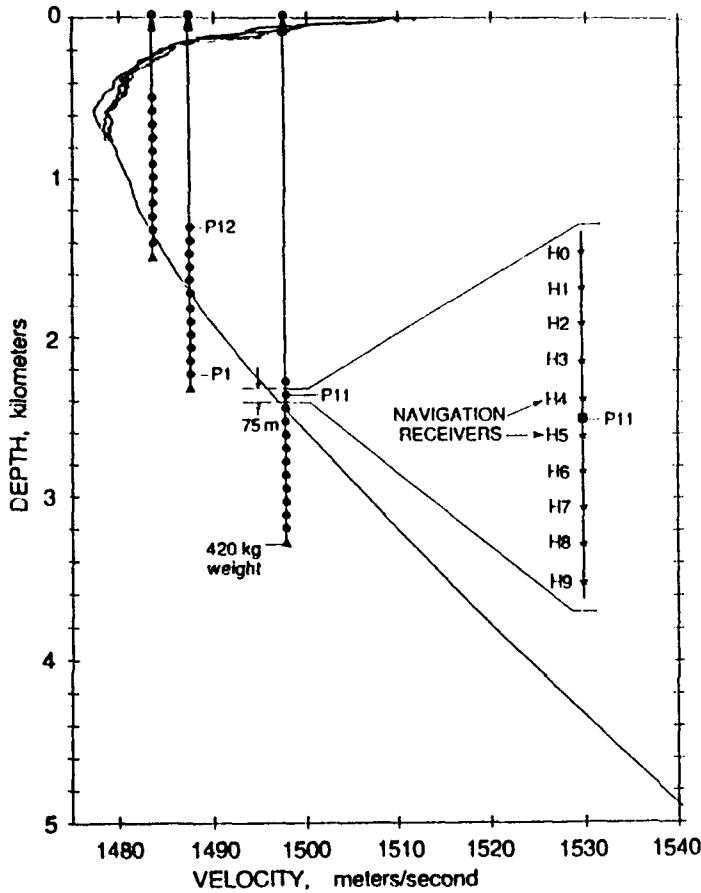


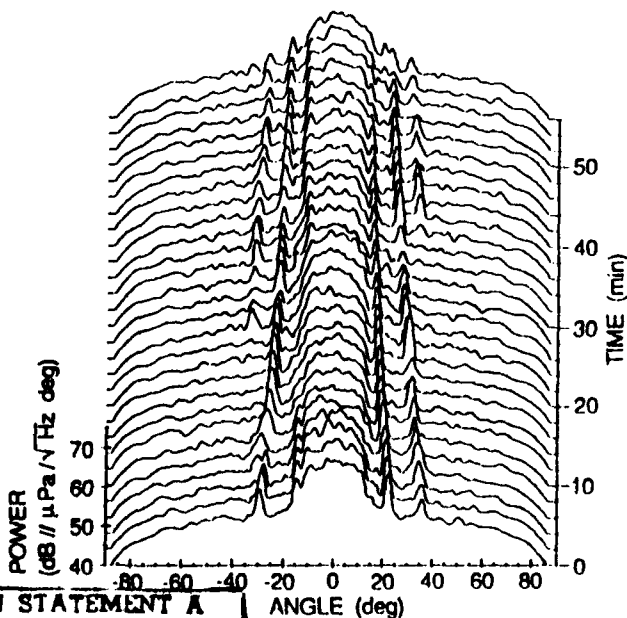
AD-A215 541

Large Aperture Acoustic Array

Barbara J. Sotirin



SIO Reference 89-10



SDTIC
 ELECTE
 NOV 24 1989
 B D

Marine Physical Laboratory
 Scripps Institution of Oceanography
 University of California, San Diego
 San Diego, California 92152

DISTRIBUTION STATEMENT A

Approved for public release;
 Distribution Unlimited

MPL-U-47/89
 July 1989

89 11 21 048

REPORT DOCUMENTATION PAGE

1a REPORT SECURITY CLASSIFICATION UNCLASSIFIED			1b RESTRICTIVE MARKINGS			
2a SECURITY CLASSIFICATION AUTHORITY			3 DISTRIBUTION/AVAILABILITY OF REPORT Approved for public release; distribution unlimited.			
2b DECLASSIFICATION/DOWNGRADING SCHEDULE						
4 PERFORMING ORGANIZATION REPORT NUMBER(S) SIO REFERENCE 89-10 [MPL-U-47/89]			5 MONITORING ORGANIZATION REPORT NUMBER(S)			
6a NAME OF PERFORMING ORGANIZATION Marine Physical Laboratory		6b OFFICE SYMBOL (If applicable) MPL	7a NAME OF MONITORING ORGANIZATION Office of Naval Research Department of the Navy			
6c ADDRESS (City, State, and ZIP Code) University of California, San Diego Scripps Institution of Oceanography San Diego, CA 92152			7b ADDRESS (City, State, and ZIP Code) 800 North Quincy Street Arlington, VA 22217-5000			
8a NAME OF FUNDING/SPONSORING ORGANIZATION Office of Naval Research		8b OFFICE SYMBOL (If applicable) ONR	9. PROCUREMENT INSTRUMENT IDENTIFICATION NUMBER N00014-79-C-0472, N00014-87-C-0127			
8c ADDRESS (City, State, and ZIP Code) Department of the Navy 800 North Quincy Street Arlington, VA 22217-5000			10. SOURCE OF FUNDING NUMBERS			
			PROGRAM ELEMENT NO.	PROJECT NO.	TASK NO.	WORK UNIT ACCESSION NO.
11 TITLE (Include Security Classification) LARGE APERTURE ACOUSTIC ARRAY						
12 PERSONAL AUTHOR(S) Barbara J. Sotirin						
13a TYPE OF REPORT sio reference		13b TIME COVERED FROM _____ TO _____		14 DATE OF REPORT (Year, Month, Day) July 1989		15 PAGE COUNT 167
16 SUPPLEMENTARY NOTATION						
17 COSATI CODES			18 SUBJECT TERMS (Continue on reverse if necessary and identify by block number)			
FIELD	GROUP	SUB-GROUP	large aperture acoustic array, ambient noise, spatial distribution,			
19 ABSTRACT (Continue on reverse if necessary and identify by block number) A large aperture acoustic array for investigating the spatial distribution of low frequency ambient noise has been designed, built and deployed from Research Platform <i>FLIP</i> in the NE Pacific. Design constraints of such an array include a large dynamic range to accommodate the absolute levels encountered within this band and a large aperture with many elements to achieve good spatial resolution at low frequencies. Deployed vertically, the large aperture subjects the array to an inhomogeneous current field which necessitates the implementation of a navigation subsystem for estimating the array shape prior to beamforming. Navigation results show that the array is nearly vertical, responding to wind, tides, internal waves and surface motion. Knowledge of the individual element response is also required for accurate beamforming, thus a system calibration must be executed. An intimate understanding of the array as a measurement system is required for accurate analysis of the data it collects. Due to the constraints imposed by the physical size and number of elements, an <i>in situ</i> method was utilized to evaluate array system performance and characterize the response of individual elements. Acoustic measurements recorded during the passage of a local storm, provide a unique opportunity to investigate the impact of the wind driven source mechanism on the structure of the low frequency noise field. Beamformed data illustrate the detailed spatial structure of low frequency noise. Upward looking beams reflect local surface effects while horizontal looking beams are dominated by energy from distant sources which cannot be absolutely identified. The surface directed beams display a threshold type behavior suggesting the abrupt onset of a source mechanism such as breaking waves.						
20 DISTRIBUTION/AVAILABILITY OF ABSTRACT <input type="checkbox"/> UNCLASSIFIED/UNLIMITED <input checked="" type="checkbox"/> SAME AS RPT <input type="checkbox"/> DTIC USERS			21. ABSTRACT SECURITY CLASSIFICATION UNCLASSIFIED			
22a NAME OF RESPONSIBLE INDIVIDUAL Barbara J. Sotirin			22b TELEPHONE (Include Area Code) (619) 534-1787		22c OFFICE SYMBOL MPL	

Large Aperture Acoustic Array

Barbara J. Sotirin

SIO Reference 89-10



University of California, San Diego
Marine Physical Laboratory
Scripps Institution of Oceanography
San Diego, California 92152

MPL-U-47/89
July 1989

Table of Contents

Table of Contents i

List of Figures iii

List of Tables v

Acknowledgements vi

Abstract vii

Introduction 1

1. Large Aperture Digital Acoustic Array

1.1 Abstract 3

1.2 Introduction 3

1.3 Array Description 4

1.3.1 Uplink Data Stream 6

1.3.2 Topside Electronics 10

1.3.3 Downlink Command Stream 10

1.3.4 Navigation 12

1.4 Experimental Results 14

1.5 Summary 20

2. Acoustic Navigation of a Large Aperture Array

2.1 Abstract 23

2.2 Introduction 23

2.3 Travel Time Measurements 24

2.4 Position Estimation 28

2.4.1 Least Squares Formulation 28

2.4.2 Implementation 31

Transponder Localization 31

FLIP and Array Element Localization 35

2.4.3 Simulations 35

2.5 Data Analysis 39

2.6 Conclusions 48

3. On Array Performance: A Methodology of System Calibration and Noise Identification

3.1 Abstract 51

3.2 Introduction 51

3.3 System Description 52

3.4 Laboratory Calibration 54

3.4.1 Nominal Element Calibration 54

3.4.2 Electrical Self Noise Level 56

3.5 Performance Indicators 62

3.5.1 Time Series 62

Distribution/	
Availability Codes	
Dist	Avail and/or Special
A-1	



3.5.2	Time Series Distribution	63
3.5.3	Bit Distribution	64
3.5.4	Power Spectral Density	66
3.5.5	Channel to Channel Coherence	66
3.5.6	Narrowband Spectral Estimate Across Array	68
3.5.7	Spectral Estimate Distribution	68
3.5.8	Beampatterns	71
3.5.9	Beam Levels	71
3.5.10	Beam Correlation Levels	74
3.5.11	Line Frequency Analysis	76
3.6	Array Calibration	76
3.6.1	Method Description and Data Collection	79
	Narrowband	79
	Broadband	80
	Phase	82
3.6.2	Results	82
	Magnitude	82
	Phase	85
3.7	Conclusions	85
4. Fine-Scale Measurements of the Vertical Ambient Noise Field		
4.1	Abstract	87
4.2	Introduction	87
4.3	Temporal Variability	89
	4.3.1 Statistical Tests	90
	4.3.2 Spectral Estimate Variability	94
4.4	Interpreting Beamformed Data	96
	4.4.1 Spectrum Restoration	97
	4.4.2 Simulations	101
4.5	Vertical Directionality as a Function of Wind Speed	106
	4.5.1 Data Processing	107
	4.5.2 Array Strum	109
	4.5.3 Ambient Noise as a Function of Wind Speed	110
4.6	Conclusion	122
Appendix A. Element and Processor Identification		129
Appendix B. Array Beampattern		133
Appendix C. Navigation Software for the MPL Vertical Line Array		
A.1	Abstract	135
A.2	Introduction	135
A.3	Transponder Localization	136
	A.3.1 Data Collection	136
	A.3.2 Software Implementation	138
	A.3.3 Simulations	141
A.4	Array Travel Time Acquisition	142
A.5	Array Spatial Localization	144
A.6	Acknowledgements	145
A.7	References	146

List of Figures

Chapter I

1.1	Vertical deployment configuration	5
1.2	Array section block diagram	7
1.3	Array system diagram	9
1.4	Navigation overview	13
1.5	Preliminary navigation results	15
1.6	Array deployment depths for the September 1987 seatest	16
1.7	Ambient noise variation with respect to wind and depth	17
1.8	Time series display of acoustic channels	19
1.9	Seismic profiler contamination	21

Chapter II

2.1	Navigation overview	25
2.2	Travel time acquisition	28
2.3	Array navigation receivers and sound speed profiles	32
2.4	Spatial configuration for navigation during the September 1987 sea test	36
2.5	Error simulation results	38
2.6	Comparison of GPS satellite and acoustic navigation	41
2.7	Error distributions	42
2.8	<i>FLIP</i> position time series	43
2.9	Tidal current ellipse	44
2.10	Array position time series	45
2.11	Spectrum of array motion	47
2.12	Array shape	49

Chapter III

3.1	Array section schematic	53
3.2	Power supply spectra	55
3.3	Common mode switching noise	58
3.4	Channel gain difference	59
3.5	System noise coherence	60
3.6	System noise directionality	60
3.7	System noise spectral levels	61
3.8	Time series	62
3.9	Time series and bit distribution	63
3.10	Bit distribution	64
3.11	Power spectral density	65
3.12	Channel to channel coherence	67
3.13	Narrowband spectral estimate	69
3.14	Spectral estimate distribution	70
3.15	Beampatterns	72
3.16	Beam levels	73
3.17	Beam correlations levels	75
3.18	Line frequency spatial distribution	77

3.19	Narrowband transmission range	78
3.20	Calibration modeling	78
3.21	Narrowband magnitude results	84
3.22	Ambient noise variability	81
3.23	Narrowband phase results	82
3.24	Broadband magnitude results	84

Chapter IV

4.1	Cumulative distribution two-sample test	91
4.2	Data stationarity	92
4.3	Cumulative distribution one-sample test	93
4.4	Variability of ambient noise spectral levels across the array	94
4.5	Variance as a function of time	96
4.6	Angular resolution of the array	97
4.7	Spectrum restoration simulation	99
4.8	Ambient noise spectrum restoration	100
4.9	Virtual beam simulation	104
4.10	Measured virtual beam levels	105
4.11	Array strum arrivals	108
4.12	Continuous directional time series	112
4.13	Pedestal rays	113
4.14	Spatial distribution of ambient noise as a function of depth	115
4.15	Spatial distribution of ambient noise as a function of frequency	116
4.16	Spatial distribution of ambient noise as a function of wind speed	117
4.17	Spectral levels vs. time	118
4.18	Spectral levels as a function of linear wind speed	120
4.19	Directional time series	121

Appendix C

C.1	<i>FLIP</i> navigation system detection of transponder replies	147
C.2	Transponder localization program flow	148
C.3	Navigation overview	149
C.4	Spatial configuration for navigation during the September 1987 sea test	150
C.5	3D error surface	151
C.6	Monte Carlo simulation of initial transponder positions	152
C.7	Array navigation receivers	153
C.8	Navigation timing diagram	154
C.9	Data tape format	155
C.10	Receiver error distribution	156
C.11	Correlated output from a single receiver	157
C.12	Raw navigation data	158
C.13	Transponder reply detection	159
C.14	Slant range data	160

List of Tables

Chapter I

1.1	Comparison of Vertical Arrays	5
1.2	Available Array Commands	11
1.3	Ambient noise spectral variation with wind speed	18

Chapter II

2.1	Sound speed impact on travel time predictions	33
2.2	Navigation error simulations	40

Chapter III

3.1	Narrowband transmission parameters	79
3.2	Results of narrowband calibration	83

Chapter IV

4.1	Equivalent beamwidth	101
4.2	Mainbeam to sidelobe ratio (dB) at 55 Hz	102
4.3	Mainbeam to sidelobe ratio (dB) with -35 dB array sidelobes	103
4.4	Temporal vs. spatial transform parameters	109
4.5	Vertical directionality data: wind speed vs. depth	114

Appendix A

A.1	Element identification for channels 1-60	130
A.2	Element identification for channels 61-120	132
A.3	Processor identification - September 1987	133

ACKNOWLEDGEMENTS

I wish to thank the members of my committee for their time spent reviewing the work presented in this dissertation, and for their constructive criticisms. I am particularly indebted to Bill Hodgkiss and John Hildebrand for accepting to supervise my work for the past four years, and for sustaining the interest of the Office of Naval Research in funding this project (Contract No. N00014-79-C-0472).

The development of the array system is primarily the work of Vince Pavlicek, who deserves a special mention for his generosity, patience and astounding feats of engineering. Although the idea and funding originated with Vic Anderson and Fred Spiess, Vince provided the only continuity for the project over its seven year life, assisting this work not only with engineering expertise but intuitive insight regarding the data analysis as well.

The work presented here relies on data collected at sea, and it would not have been possible without the cooperation of the officers, crew and scientific parties of the Research Platforms *FLIP* and *ORB* and the tow ships *USS Narragansett* and *Navajo* during the test cruises. This includes the engineers from the array group: Tony Aja, Dick Harriss, Howard Humphrey, Vince Pavlicek, Pam Scott, and Norm Waters.

I am grateful to Bill Hodgkiss, John McInerny and Eric Wolin for developing and maintaining the outstanding data processing and analysis facility at MPL. I also wish to express my sincere gratitude to Jo Griffith for expertly drafting all the figures and for putting up with the last minute crises.

Among my friends and colleagues who have helped me on countless occasions I want to give special credit to Chris de Moustier whose encouragement, companionship and personal example helped me through some critical times. He spent many hours reviewing this manuscript, provided many valuable suggestions, the opportunity for discussion and a determination worth emulating. Sue Cohea and Gayle Watring listened to countless hours of shop talk and insisted that I take a break once in a while; and Gerald D'Spain, Phil Hammer, Lee Culver, Rick Brienza, and Jean-Marie Tran assisted me with many helpful references and suggestions, and created a strong interactive work environment.

For their support and encouragement of my initial decision to return full time to the university environment (and student wages), providing stimulating discussions, expert advice and countless lunches, I wish to acknowledge four of my favorite people: Homer Bucker, George Pickens, Tom Stixrud and Howie Wilcox. I will be proud to remain their friend for years to come.

Finally, I would like to thank my family; my sisters, Patty, Chre and Pauli, and my brother Bob who didn't raise an eyebrow at my sudden transition from classical music to engineering and supported me throughout the endeavor, my mother Muriel for intentionally neglecting to tell me that there might be some things I couldn't do, and my father Paul who listened patiently every week to what went wrong, insisting time and time again that he believed, and still believes.

ABSTRACT OF THE DISSERTATION**Large Aperture Acoustic Array**

by

Barbara J. Sotirin

Doctor of Philosophy in Electrical Engineering (Applied Ocean Science)
University of California, San Diego, 1989
Professor John A. Hildebrand, Co-Chairperson
Professor William S. Hodgkiss, Jr., Co-Chairperson

A large aperture acoustic array for investigating the spatial distribution of low frequency ambient noise has been designed, built and deployed from Research Platform *FLIP* in the NE Pacific. Design constraints of such an array include a large dynamic range to accommodate the absolute levels encountered within this band and a large aperture with many elements to achieve good spatial resolution at low frequencies.

Deployed vertically, the large aperture subjects the array to an inhomogeneous current field which necessitates the implementation of a navigation subsystem for estimating the array shape prior to beamforming. Navigation results show that the array is nearly vertical, responding to wind, tides, internal waves and surface motion.

Knowledge of the individual element response is also required for accurate beamforming, thus a system calibration must be executed. An intimate understanding of the array as a measurement system is required for accurate analysis of the data it collects. Due to the constraints imposed by the physical size and number of elements, an *in-situ* method was utilized to evaluate array system performance and characterize the response of individual elements.

Acoustic measurements recorded during the passage of a local storm, provide a unique opportunity to investigate the impact of the wind driven source mechanism on the structure of the low frequency noise field. Beamformed data illustrate the detailed spatial structure of low frequency noise. Upward looking beams reflect local surface effects while horizontal looking beams are dominated by energy from distant sources which cannot be absolutely identified. The surface directed beams display a threshold type behavior suggesting the abrupt onset of a source mechanism such as breaking waves.

INTRODUCTION

Spectral levels of low frequency sound (20-200 Hz) in the ocean are affected by environmental conditions in the local area, however investigations of this dependency are usually contaminated by noise arriving at near horizontal angles from distant sources due to the relatively low attenuation of sound in this frequency band. One method of discriminating against the horizontally arriving sound is to utilize the directional measurement capabilities of a vertical acoustic array in the beamforming process.

The low frequency spatial noise field is difficult to measure accurately. It requires a large dynamic range, a large aperture and many elements. A large array aperture imposes other constraints. It subjects a vertically deployed array system to differential water currents which are capable of moving it physically. This imparts a phase difference between individual element responses and for coherent processing, the time-varying array element positions must be defined. The physical size and large number of elements also lead to the investigation of *in-situ* calibration methods and array performance evaluations.

This dissertation discusses the attributes of a large aperture acoustic array in measuring the fine-scale variability of the oceanic ambient noise field at low frequencies. It is divided into four chapters and an appendix. Each chapter is self-contained and was written for publication in a refereed scientific journal. As a result, some redundancy exists between chapters, particularly in system description.

The first chapter introduces the electronic and mechanical characteristics of the array system, as well as deployment scenarios from the Research Platform *FLIP*. An intimate understanding of the array as a measurement system is required for accurate analysis of the data it collects.

In the second chapter, high frequency acoustic transponder signals are used to estimate array element positions. The navigation method is discussed and results are compared to independently acquired satellite positions of *FLIP*. The positional time series data are analyzed in terms of the expected source functions: wind, tides, internal waves and surface effects.

In the third chapter, data collected during an experiment are used to implement *in-situ* array calibration and performance evaluation techniques. Two independent methods provided individual element amplitude estimates and verified system noise constraints.

The fourth chapter presents the fine-scale structure of the vertical ambient noise field. Emphasis was placed on data collected during the passage of a local storm which provides a unique picture of wind-induced noise at low frequencies.

Due to the continuation of the array program at the Marine Physical Laboratory, the software techniques introduced in the second chapter along with system errors and simulations were carefully documented and appear in the appendix.

Further investigation into low frequency spatial distribution would benefit by simultaneous characterization of the surface wave field, horizontal as well as vertical spatial resolution and accurate estimates of distant sources (ships and storms).

Chapter 1

LARGE APERTURE DIGITAL ACOUSTIC ARRAY

1.1 ABSTRACT

A digital array of 120 acoustic channels and 900 m in length has been constructed to study low frequency (20-200 Hz) ambient noise in the ocean. The array may be deployed vertically or horizontally from the research platform *FLIP* and the array elements are localized within a high frequency acoustic transponder network. This paper describes the instrumentation, telemetry and navigation systems of the array during a vertical deployment in the northeast Pacific. Preliminary ambient noise spectra are presented for various array depths and local wind speeds. Ambient noise in the frequency band above 100 Hz or below 25 Hz increases with local wind speed. However, in the frequency band 25-100 Hz ambient noise is independent of wind speed and may be dominated by shipping sources.

1.2. INTRODUCTION

A digital array of 120 acoustic channels and 900 m length has been constructed for study of low frequency (20-200 Hz) ambient noise. A large aperture array is required for high resolution directional information at low frequencies. A well filled array is required to provide low side-lobe levels for study of ambient noise. This paper describes the characteristics of a large aperture linear array of hydrophones which may be deployed vertically or horizontally from the research platform *FLIP*. Preliminary observations of low frequency ambient noise are described from a vertical deployment of this array in the northeast Pacific during September 1987.

Oceanic ambient noise is the prevailing sustained background of sound in the ocean. These noise levels place constraints on the operation of acoustic sensors in the ocean. For this reason it is valuable to understand the sources generating the sound, the absolute levels and the spectral shapes of ambient noise. Low frequency noise is particularly important because of its low attenuation and therefore its ability to propagate over long distances. Only recently has it been practical to investigate the directionality of ambient noise sources at low frequency (less than 100 Hz) due to power, size and cost constraints.

The following have been identified as sources of low frequency noise in the ocean [Urick, 1983]: shipping, wind and waves, seismic disturbances, and nonlinear ocean wave interactions. In the frequency band between 20 Hz and 100 Hz, shipping is thought to be the dominant noise source where shipping sources are present [Bannister *et al.*, 1979; Burgess and Kewley, 1983]. This component may include reverberative paths, perhaps related to prominent bottom topographic features, as well as forward scattering and channeling of the shipping sources. The variation of shipping noise may depend on whether the sources are of single-ship or multiple-ship origin and whether they are local or distant.

At frequencies between 100 and 200 Hz, sea surface noise generated by wind and waves may be dominant. The reported contribution by local wind sources in this band is quite variable, ranging from a difference in spectral level of approximately +18 to -4 dB// μ Pa/ \sqrt Hz [Urlick, 1983; Wilson, 1983]. The sources responsible for this variation may be identified by examining the vertical and horizontal directionality. Distant storms and noise generated at the edges of the ocean due to waves breaking on cliffs, rocks, or beaches as well as the nonlinear generation due to interference of incoming and reflected coastal swell may produce an azimuthally non-uniform contribution; local wind should induce a vertically variable contribution.

The unique capabilities of the array described in this paper allow its deployment as a high performance vertical or horizontal array. Arrays previously used to measure low frequency vertical directionality are listed in Table 1.1 to facilitate comparison. The number of elements (120) and large aperture (900 m) of our array is substantially greater than previously reported vertical arrays. This large aperture will allow higher resolution vertical directionality than was previously available. Horizontal directionality is usually measured using large aperture towed arrays. Our array can be moored horizontally because of its neutrally buoyant design. When operated in the horizontal configuration, the flow noise affecting our array is significantly less than for towed arrays, leading to improved array performance.

Number of Elements	Aperture meters	Hydrophone Spacing	Frequency Range Hz	Deployment Depth (actual) meters	Deployment Platform	Reference
120	900	uniform	20-200	400-3100	FLIP*	this paper 1988
11	34	nested subarrays	62.5-1K	200	free floating	[14] Buckingham and Jones 1987
48	115	uniform	0-450	sound channel	FLIP	[15] Hodgkiss and Fisher 1986
27	93	uniform	0-600	sound channel	FLIP	[15] Hodgkiss and Fisher 1986
31	180	nested subarrays	20-800	300	free floating	[3] Burgess and Kewley 1983
31	310	uniform	45-100	1500	surface ship	[16] Wales and Diachok 1982
12	237	logarithmic	<200	300-3100	free floating	[17] Browning, <i>et al</i> 1982
20	<560 (variable)	uniform	5-400	700-4800	FLIP	[18] Tyce 1982 and [19] Anderson 1979
40	97	geometric	112-1414	4400	anchored to bottom	[20] Axelrod, <i>et al</i> 1965

* FLIP (Floating Instrument Platform) is a manned 100 meter spar buoy stable platform operated by the University of California, San Diego, Marine Physical Laboratory.

Table 1.1. Comparison of Vertical Arrays.

1.3. ARRAY DESCRIPTION

This section describes the array electrical and mechanical design. The array has a modular design, which facilitates assembly and transportation, and allows for

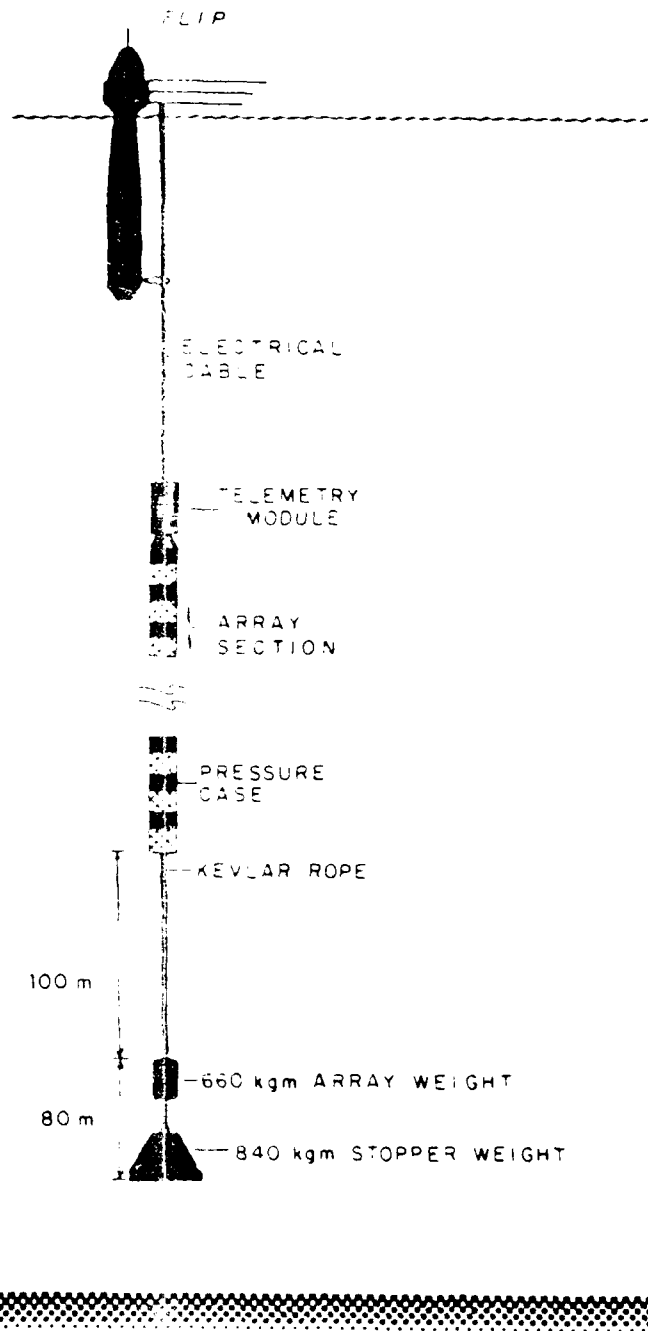
VERTICAL ARRAY
CONFIGURATION

Figure 1.1 Vertical deployment configuration of the low frequency digital acoustic array from the research platform *FLIP*.

a variable aperture. It is separable into identical hose sections of 10 elements each, joined together by in-line interchangeable pressure cases. Each of the 10 elements consists of two hydrophones, a preamp, a filter and a line driver submerged in insulating noroma oil. The oil filled hoses are neutrally buoyant in seawater, necessary for horizontal deployments. The interelement spacing is 7.5 m and the elements are secured within the 2.54 cm diameter urethane hose by a kevlar line which is terminated near each end of the hose subsection. In-line pressure cases are located between each hose section of 10 hydrophones. The pressure cases are 45 cm long with a 7.6 cm outside diameter providing a low profile cross-section. These pressure cases house non-pressure tolerant electronics for processing and telemetering the hydrophone signals. Hydrophone data are transmitted asynchronously along the array to a telemetry module near the *FLIP* end of the array. This module buffers the data and synchronously transmits it through a double-lay armored electrical cable to the surface where it is recorded by the data acquisition computer (LSI-11). The tension carried by the electrical support cable is transferred at the telemetry module to a 1.5 cm diameter kevlar line. During vertical deployment, the hoses and pressure cases are attached to the kevlar line which has 310 kg at its bottom to maintain verticality. The array is deployed from the research platform *FLIP* which maintains station by a multipoint moor. The array is suspended from a hydrographic winch which allows it to be lowered to a specified depth below *FLIP*. Figure 1.1 shows a schematic of the array configuration during vertical deployment.

The coaxial armored uplink electrical cable carries frequency multiplexed data in three bands: uplink data, downlink commands and dc power. The spectrum allocated for the uplink data is from 100 kHz up to approximately 1.5 MHz. The uplink data rate is 1 Mbit per second encoded using a Miller code to reduce the bandwidth required to approximately 500 kHz. The downlink spectrum is from 100 kHz down to 1.5 kHz. The downlink data is encoded on a 20 kHz carrier which is used to synchronize the data sampling clocks, and a command synchronization bit sequence is transmitted every 2 msec. The cable simultaneously carries the DC power for the array. Each section of the array has DC-to-DC converters that produce 5 volts at 600 mA and ± 15 volts at 150 mA to power the electronics and hydrophone elements. The sections are in series so that they use the same current; the voltage necessary for the complete array is 5.1 volts times the number of sections. The power loss in the armored uplink cable is proportional to the current and does not change as the number of array sections changes.

1.3.1. Uplink Data Stream

This section describes the uplink of acoustic data from the array hydrophones to the topside electronics. The data stream originates at the hydrophones. It is amplified, filtered, converted to a digital signal, reformatted and finally transmitted to the surface as shown schematically in Figure 1.2. The hydrophones are an Aquadyne AQ-1 with a sensitivity of -204 dB re 1 V/ μ Pa and a capacitance of 12 nf. AQ-1 hydrophones have been calibrated with respect to pressure, temperature and frequency and exhibit a well-behaved response over the range of operating conditions [Lastinger, 1982]. There is a 2 to 3 dB re 1 V/ μ Pa sensitivity increase from low pressure (near surface) to high pressure (6000 m), a 0.2 to 0.3 dB re 1 V/ μ Pa sensitivity increase from 0° C to 22° C and a ± 0.2 dB re 1 V/ μ Pa sensitivity variation across a frequency band of 10 to 1000 Hz. There are two hydrophones per array element wired in series for an element sensitivity of -198 dB re 1 V/ μ Pa.

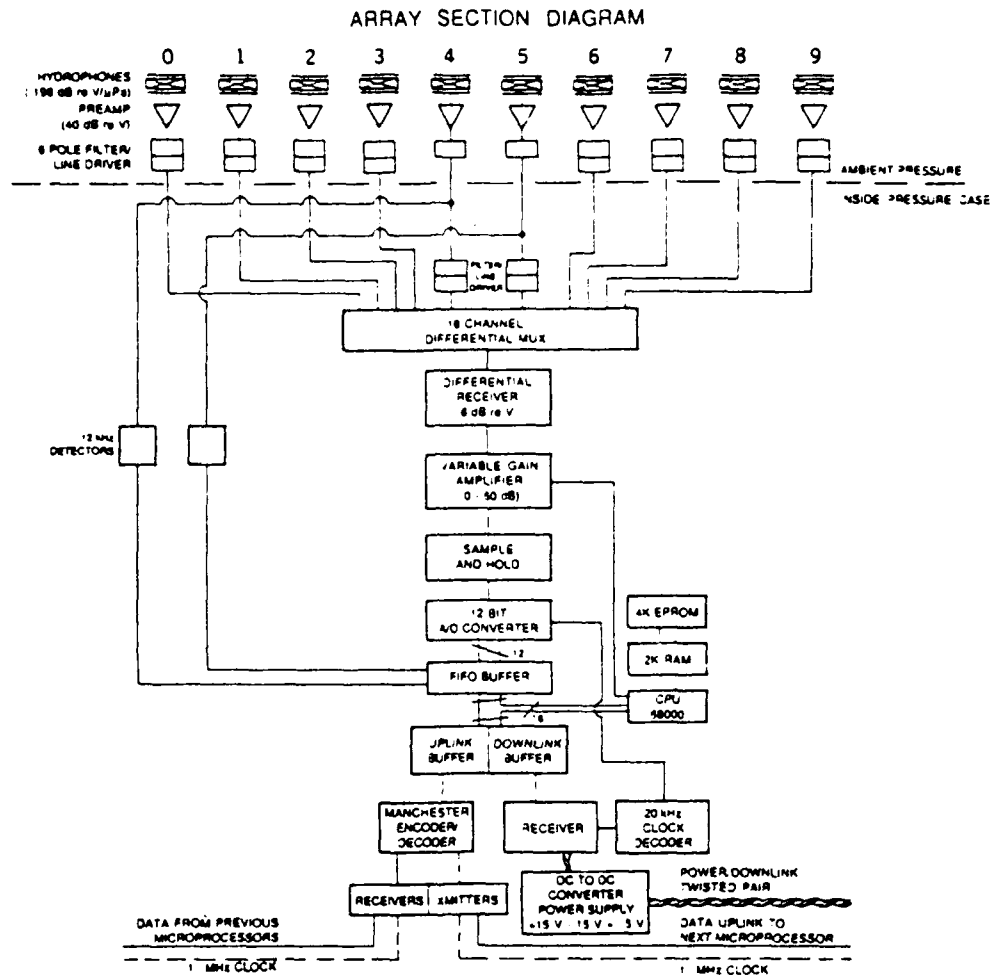


Figure 1.2 Array Section Block Diagram. The hydrophone signals are amplified and filtered at the element except for hydrophones 4 and 5 which are filtered within the processor pressure case to allow detection of 12 kHz navigation signals. The low frequency acoustic signals are multiplexed, amplified, captured by the sample and hold and converted to digital format before being transmitted to the surface.

Tested at a constant depth (1830 m), the relative phase of the hydrophones is within 0.2° ; changing the depth from just below the surface to full operating depth (3000 m) induced a relative phase change between hydrophones which was less than 0.6° . The hydrophone output is applied to a very low noise FET preamplifier with 40 dB of gain. The minimum expected acoustic noise level is approximately 45 dB re 1 μ Pa at 100 Hz [Wenz, 1962] and the electrical noise in the preamp is approximately 15 dB below this level. The output is filtered by a six pole low pass phase-matched filter with a corner frequency at 220 Hz and whose in band gain is 1. The preamp has a low frequency cutoff below 10 Hz. A differential line driver is used to transmit the signal a distance of up to 33.75 m to a processor pressure case. There are 10 elements per 75 m section with each processor receiving 5 inputs from the hose on either side. The two elements immediately adjacent to a processor pressure case are filtered within the pressure case rather than at the element to provide 12 kHz acoustic information required for navigating the array.

In the processor pressure case the hydrophone inputs are selected sequentially by a differential multiplexer, converted from differential to single-ended signals, amplified by a programmable variable gain amplifier, captured by a sample-and-hold circuit and converted to 12 bit digital form. The programmable analog to digital converter (A/D) clock is synchronous with the 20 KHz downlink carrier and the A/D outputs are stored in a 16 word first-in first-out (FIFO) register before the processor is interrupted to take the 10 data words. Of the 16 bits per word stored in the FIFO, twelve bits are data, two bits are from the navigation detectors, and two bits are hardware status flags. Prior to low pass filtering, the signals from the hydrophones adjacent to the pressure case are routed to a 12 kHz detection circuit. This circuit compares the signal level in a narrow band receiver at 12 kHz to the level of a broad band receiver to determine the presence or absence of a 12 kHz acoustic transponder signal. The 1-bit detection from each circuit is multiplexed in with every 12-bit hydrophone word as it is stored in the FIFO. The CPU is a Motorola 68000 operating at 4 MHz with 4K ROM and 2K RAM available. The 4 MHz clock is derived from a 16 MHz crystal which is phase locked to a 1 MHz clock signal from the telemetry module. The software is interrupt driven with the highest priority interrupt responding to the A/D. The second highest priority interrupt transmits the processed data and the lowest priority services the downlink synchronization sequence. The signal data are loaded from the FIFO into a large RAM buffer and the CPU then processes the data before presenting it to a Manchester code repeater/encoder for transmission.

The array processors are synchronized by a downlink pattern at a 500 Hz rate. At synchronization the farthest processor from FLIP transmits a synchronization word and the processed data. Each sequential processor repeats the data bit stream from the processor before and inserts its data followed by a unique ID within a specified time window. At the FLIP end of the array is a telemetry module which contains a Manchester decoder, a FIFO, and a synchronous data transmitter. The telemetry module converts the asynchronous data along the array to a continuous data stream up the cable to FLIP. It adds frame sync words and null data when the FIFO is empty or busy. The data are driven up the cable at a 1 MHz rate by a high power amplifier (10 watts) to overcome the cable attenuation of approximately 45 dB re 1 V. A bit stream containing data from all the array sections is available every 2 msec at FLIP.

ARRAY SYSTEM DIAGRAM

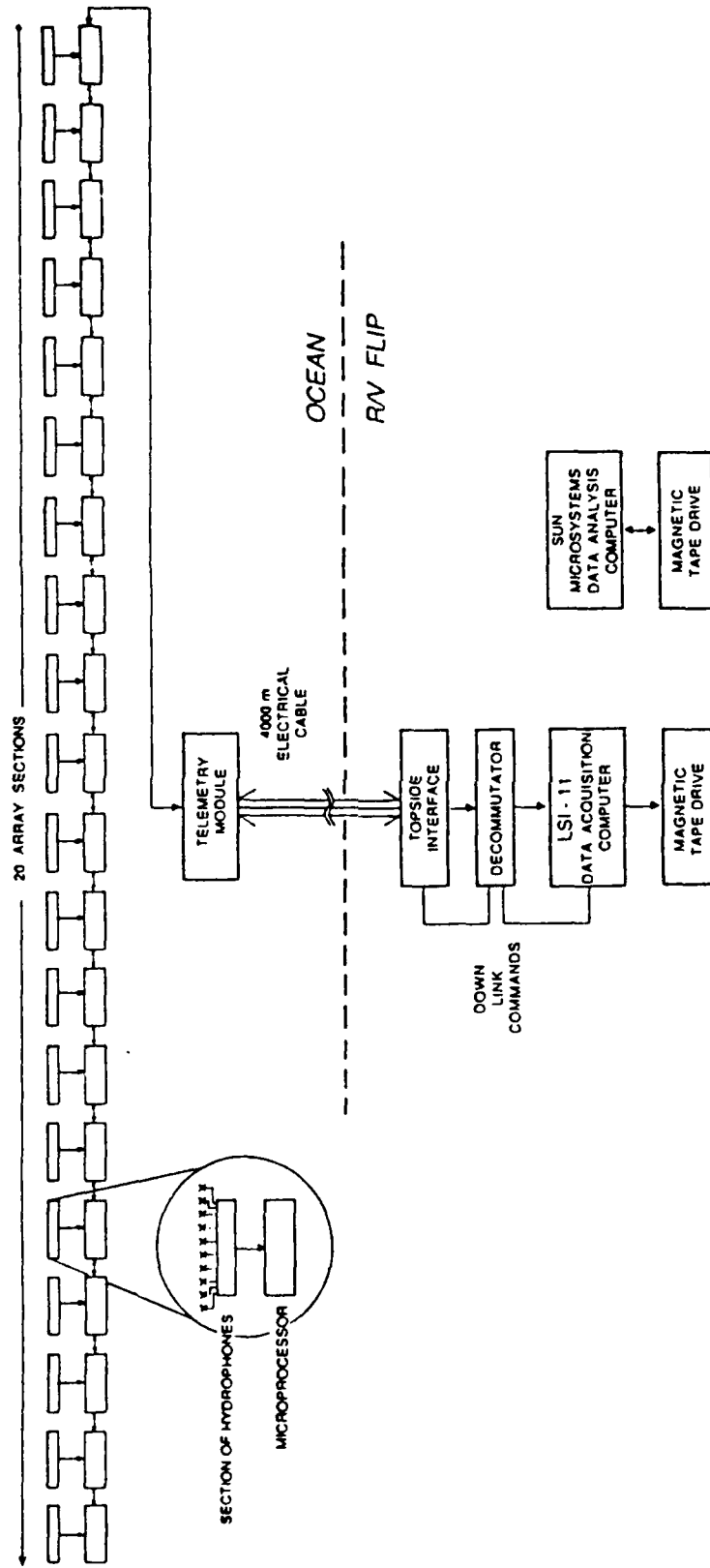


Figure 1.3 Array System Diagram. The data path from the hydrophones through the telemetry module to the magnetic tape drive is shown. Further analysis of the data is accomplished by a Sun Microsystems computer.

1.3.2. Topside Electronics

This section describes the topside data acquisition system (Figure 1.3). The uplink data are presented to an array interface module where they are amplified and filtered to remove cable phase distortion. A Decom Systems bit synchronizer/decommutator locks to the frame sync word in the data bit stream, and decodes the data to present it to the data acquisition computer (LSI-11). The decommutator hardware transfers data by direct memory access (DMA) to a ring buffer initialized by the LSI-11 data handler software. An eight word header containing a buffer ID and the timing and sequence information is prepended to the ring buffer prior to the transfer to magnetic tape. The tape transfer is a DMA directly from the ring buffer thus avoiding the overhead in an intermediate user buffer transfer. A buffer counter tracks the number of transfers and when the tape is full, the handler automatically begins accessing a second tape drive without loss of data. Confirmation of the buffer ID, buffer counter, frame sync word and processor ID during data processing verifies the integrity of the telemetry system.

1.3.3. Downlink Command Stream

This section describes the downlink of commands from the topside data acquisition computer to the array processors. The commands are entered at the operator terminal or from a set of switches on the array interface box and may be sent at any time while the array is operating. The maximum downlink command data rate is limited to 550 baud to ensure accuracy of transmission. Downlink commands may be specific to selected processors or broadcast to all processors. There are three categories of commands as shown in Table 1.2: diagnostic, control/initialization, and data format. The left-most hex number of Table 1.2 is the command byte sent by the data acquisition computer to the array. The last column indicates the type of command, Diagnostic, Initialization or data Format. The diagnostic commands assist in localizing errors in individual processors. Allowable functions are to test memory, read specific memory locations, enter and execute additional machine code, alter the processor position in the uplink bit stream, turn off the transmitter of the addressed processor so the bit stream is passed around it, and full or partial resets. The control/initialization commands modify array operational parameters. The *select* command determines the order in which hydrophones or other sensors are digitized, allowing selection of other sensors such as depth gauges. The *scan off* command causes only one hydrophone to be digitized per section. The *A/D rate* commands selects the rate at which the A/D will digitize the incoming data. The *variable gain* commands selects specific gain outputs of a two stage amplifier. Gains between 5 and 1000 are obtained by selecting a gain of 1, 5, 10 or 20 from the first stage and 5, 8, 12, or 20 from the second stage. The *data format* commands determine the data format to be transmitted. The formats available transmit some combination of test data, hydrophone data, navigation data and a processor ID. The *navigation receiver* commands select which navigation receiver signal is digitized when the choice of data format restricts the number of navigation bits transmitted.

41	DIAG 2 ON		memory test then full init	D
42	SHOW HWID		hwid pos swid eeee	D
43	DIAG 1 ON		analog data test	D
44	DIAG 1 OFF			D
45	SCAN ON		scans through phones	I
46	SCAN OFF		selects only one phone	I
47	SOFT INITIALIZE			D
48		OFF		I
49		5K		I
4A	AD RATE	10K		I
4B		20K		I
4C	NAV RCVR 0			I
4D	NAV RCVR 1			I
4E	ENABLE RAM PROGRAM			D
50-5F	SEL HYD N		N=0 through F	I
60		1	stage 1	I
61		5		I
62		10		I
63		20		I
64	VAR GAIN	5	stage 2	I
65		8		I
66		12		I
67		50		I
68		1000		I
69		6	send 5's (nav0) or A's (nav1)	F
6A		5	10 phones + nav	F
6B		4	2 nav words + 8 phones	F
6C	DATA FORMAT	3	10 phones	F
6D		2	test tape	F
6E		1	listen	F
6F		OFF		F
70-7F	NEW POSITION = N		N=0 through F	DI
80		OFF	get data from memory location:	D
81		2000	(adad aaaa cccc) address, contents	D
82		2200		D
83		2400		D
84		2820		D
85		28D4		D
86		2900		D
87	DIAG 3	2940		D
88		2980		D
89		29C0		D
8A			D
8B			D
8C		2F00		D
8D		2FC0		D
8E			D
8F	INCREMENT ADDR IN DIAG 3 ABOVE			D
90	UPLINK OFF			D
91	UPLINK ON			D
92	STORED SINUSOID ON			D
93	STORED SINUSOID OFF			D
99	FULL RESET			D

Table 1.2. Available Array Commands

1.3.4. Navigation

Array acoustic navigation is accomplished by detecting the return signals of near bottom acoustic transponders [McGehee and Boegeman, 1966]. A minimum set of three transponders are interrogated from *FLIP* at unique frequencies and their replies are detected by the array. The time of arrival of each reply corresponds to the range between the transponder and the array element. A set of ranges are determined for each array navigation element and input to a program which calculates element position [Lowenstein, 1966].

The transponders employed were developed for navigation of the MPL deep tow fish [Spiess *et al*, 1966]. For navigation of the array these transponders are deployed in roughly a one nautical mile equilateral triangle about *FLIP*. They are anchored above the sea floor by a 100 m length of line. To increase the reliability of detection in a noisy environment, the receive circuitry in the transponders (as well as in the array) compares the energy in a narrow band (200 Hz effective bandwidth) about the interrogation frequency to the total energy received in a passband of approximately 1.5 kHz. By adjusting the bandwidth and Q of the recognition circuitry, a short recognition time (>1 msec) and high noise rejection are achieved. The interrogation signal for each transponder is unique and upon detection the transponder replies with a 3 msec 12 kHz pulse which is received and recorded by *FLIP* and the array.

The transponder locations must be surveyed to determine their relative positions before using them to navigate the array. The transponder locations are adjusted relative to an arbitrary origin by an iterative approach which alternately determines ship positions from known transponder positions and transponder positions from known ship positions using a least squares approach. The initial transponder positions are derived from the GPS satellite navigation positions of the surface ship as each transponder is deployed. A data set containing slant ranges, depths, and initial positions is input to the navigation program. The difference between the calculated and measured positions defines the error.

The horizontal projection (Figure 1.4) of the slant range between a given transponder and a given surface ship position (or *FLIP* or an array element) is:

$$H_{proj}(ntr, npos) = \sqrt{S^2 - D^2}$$

where *ntr* indicates a particular transponder, *npos* indicates a particular fix or position of the surface ship, *S* is the slant range from the source to that transponder and *D* is the transponder depth minus the source depth. The mean squared error is:

$$E_{mse} = 1/N \sum (rngxy - H_{proj})^2 \quad \text{where } rngxy = \sqrt{(x_{ss} - x_{T1})^2 + (y_{ss} - y_{T1})^2}.$$

The horizontal range *rngxy* is determined by the initial X-Y positions where x_{ss} and y_{ss} represent the position of the surface ship and *N* is the number of transponders. If the RMS errors are large the position is adjusted and the process iterates. The adjustment is calculated using the method of steepest descent to follow the mean squared error gradient to a minimum. For known transponder positions, the perturbed ship position in the x direction is:

$$x_{ss} = x_{ss} + h E_{mse}(x_{ss}, y_{ss})$$

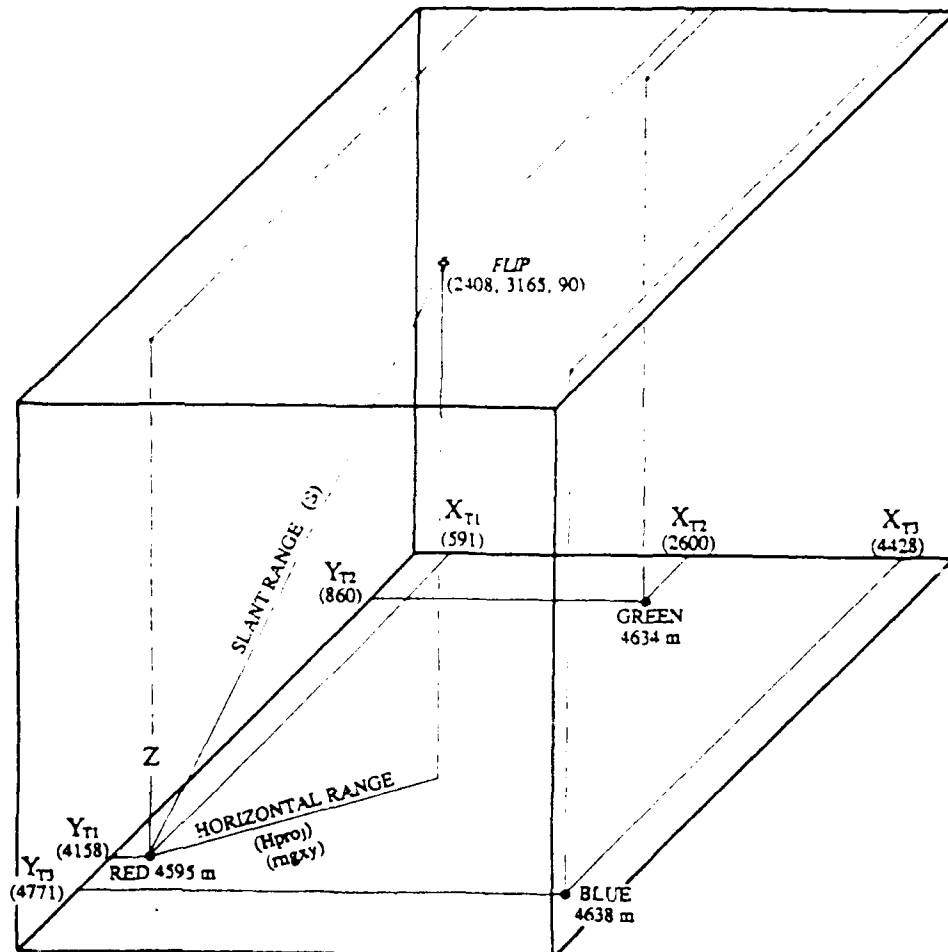


Figure 1.4 Navigation Overview. The horizontal projection is estimated first by using the slant range and depths (*Hproj*) and then with the initial X-Y positions (*rngxy*).

$$x_{ss} = x_{ss} + h * (x_{ss} - x_{T1}) * (rngxy - Hproj) / (rngxy * N).$$

where x_{ss} is the surface ship position, h is the step size, and E_{mse} is the derivative of the error function with respect to x . The y -direction adjustment is calculated similarly. When the RMS error becomes small the current position is saved.

Assuming the ship positions are known parameters, the transponder positions are adjusted using the same technique. Upon completion of the adjustment loops, the RMS error for all the transponders is evaluated. If this error is not acceptable, then the RMS errors associated with each ship position are examined, any position with an error greater than a specified value is deleted and the process begins again. This method gives the best transponder locations in a least squares sense which are consistent with the available data.

The array and *FLIP* are navigated similarly. A hydrophone located at the bottom of *FLIP* transmits a series of transponder interrogation sequences (TIS). A TIS consists of four interrogation pulses at ten second intervals followed by a silent interval. The first three pulses are at the interrogate frequencies of the bottom transponders (10, 10.5 and 11 kHz). Upon receiving an interrogation pulse a bottom transponder replies with a 3 msec pulse at 12 kHz. The fourth TIS pulse is at 12 kHz and is received by the array navigation elements to indicate array depth. The array therefore receives four consecutive 12 kHz pulses, whose timing indicates the transponder ranges and depth beneath *FLIP*. The array samples the 12 kHz pulses at an operator selected rate (typically 0.4 msec). The CPU decimates the data if necessary to provide a continuous time series consistent with the number of bits allowed for navigation. The interrogation sequence is synchronized with the data sampling timebase in the array and the initiation time of the sequence is recorded. The navigation time series establishes the range from each navigation element to each transponder after removal of the *FLIP* to transponder ranges [Sotirin *et al*, 1988]. The ranges are corrected for a varying sound speed profile by integrating over the ray path.

Calculation of the hydrophone position begins by determining the two intersections of the horizontal projection arcs. The third transponder range determines which intersection is used as an initial position. The data are iterated as described above to reduce the RMS errors. Array element relative location accuracies of a few meters may be achieved by this method. Examples of array element positions from the September 1987 experiment are displayed in Figure 1.5, demonstrating the relative motion. The symbols represent the array at four hour increments spanning a 24 hour period. There is less than 1° tilt from vertical across the 900 m array aperture. The motion of *FLIP* (Figure 1.5a) appears to be driven by the increasing northerly wind over the time analyzed (see Figure 1.7h). The north-south motion of the array (Figure 1.5b) is affected by the motion of *FLIP* as well as tidal motion. The east-west array motion (Figure 1.5c) is primarily tidally driven, with a semi-diurnal period.

1.4. EXPERIMENTAL RESULTS

Ambient noise data are presented from an experiment conducted in the northeast Pacific during the month of September 1987. Data were collected for 20 days, approximately 400 km southwest of Monterey in 4700 m of water. The programmable data sampling rate was selected at 500 Hz. The array was deployed at

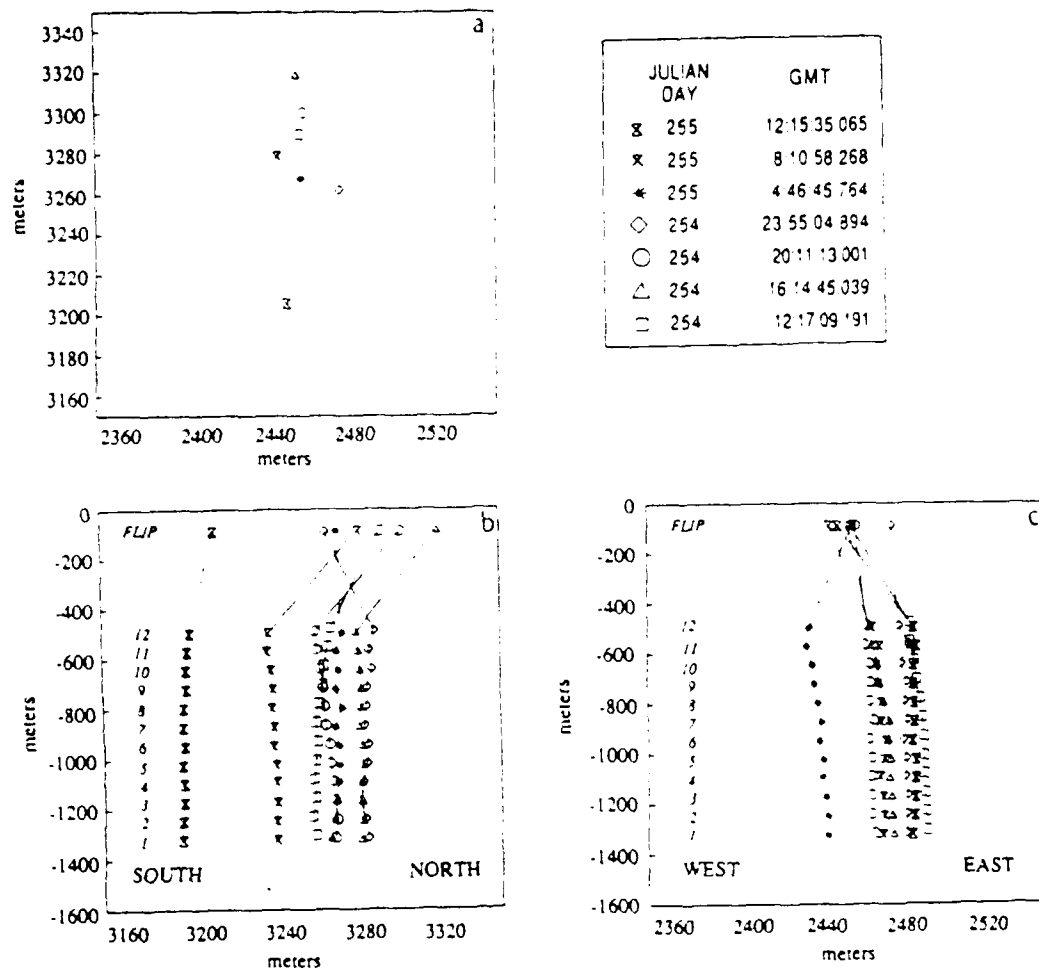


Figure 1.5 Navigation Results. A time series of the array position sampled approximately every four hours. The three plots represent (a) a plan view in X (increasing toward the east) and Y (increasing toward the north), (b) X versus depth and (c) Y versus depth. The scale in (b) and (c) is enhanced in the vertical direction by 8:1.

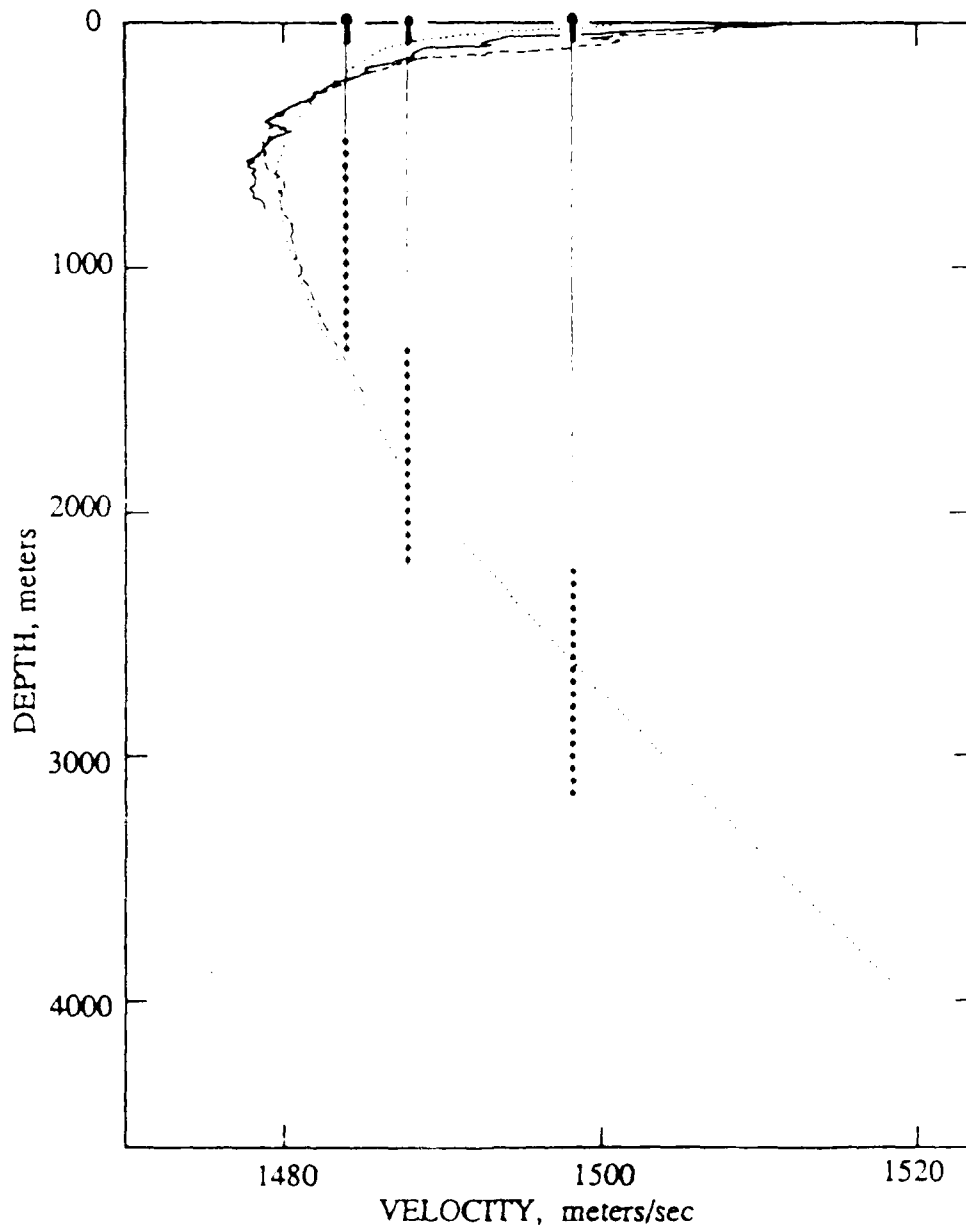


Figure 1.6 Array deployment depths for the September 1987 seatest. The three curves represent: (a) the historical sound speed profile (dotted) obtained from the National Oceanographic Data Center [12] for the experimental area and time of year (designated area 25C), (b) the sound speed (dashed) obtained from a Conductivity, Temperature and Depth (CTD) cast deployed from a surface ship approximately 40 km northwest of the array and (c) the sound speed (solid) calculated with the Clay and Medwin [13] equation using the historical salinity data and an expendable bathymetric thermistor (XBT) deployed from *FLIP*.

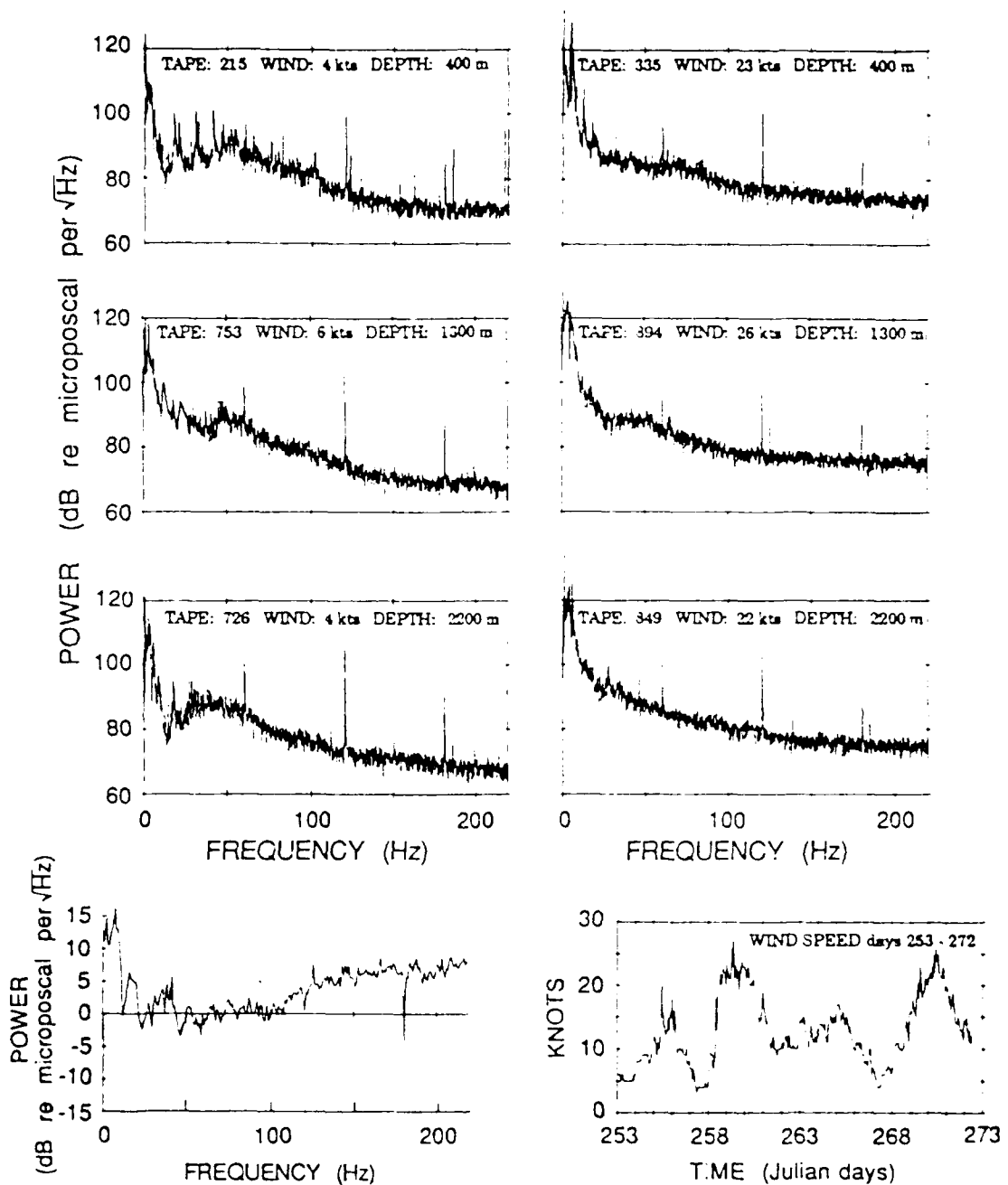


Figure 1.7 Ambient Noise variation with respect to wind and depth. Depths indicated are nominal for the top of the array, the hydrophone shown is 675 m deeper. Data were extracted on different days to obtain similar environmental conditions. The narrow band signals are interference from equipment aboard *FLIP*. (a) Wind: 4 kts, Depth: 400 m, Jday: 257; (b) Wind: 28 kts, Depth: 400 m, Jday: 259; (c) Wind: 6 kts, Depth: 1300 m, Jday: 267; (d) Wind: 26 kts, Depth: 1300 m, Jday: 270; (e) Wind: 4 kts, Depth: 2300 m, Jday: 267; (f) Wind: 22 kts, Depth: 2300 m, Jday: 269; (g) Representative spectral difference with wind; (h) Wind speed (kts) vs. Julian Day (Jday).

various water depths spanning the water column from 400 m to 3100 m. Figure 1.6 shows the array depth superimposed on the sound speed profile.

Representative hydrophone spectra illustrate the ambient noise variation with depth and wind speed (Figure 1.7). The local wind speed varied from 4 to 28 knots during the experiment as shown in Figure 1.7h. The spectra were obtained by incoherently averaging eleven 8192-point FFT's with 50 percent overlap of a Kaiser-Bessel ($\alpha=2.5$) windowed time series. The nearly uniform spectral level with depth is consistent with previous investigations [Morris, 1978; Urick, 1983]. There is a distinct difference in spectral level as wind speed increases (Figure 1.7g). The spectra at a nominal depth of 1300 m at low wind speed (Figure 1.7c) and high wind speed (Figure 1.7d) were bin averaged and subtracted to provide a measure of wind speed dependent variations. Significant variation in ambient noise was observed for frequencies above 100 Hz and below 25 Hz. Above 100 Hz at all depths, an increasing amplitude and distinct whitening of the spectra are observed at high wind speeds. The observed spectral difference is consistent with previous observations which are diverse in this frequency band (see Table 1.3).

Change in Spectral Level	Change in Wind	Frequency	Reference
$\text{dB}/\mu\text{Pa}/\sqrt{\text{Hz}}$	kts	Hz	
+18	4-6 to 28-33	200	Urick 1983
+9	10-40	200	Burgess and Kewley 1983
+7	4-6 to 22-28	200	this paper 1988
+7	10-30	150	Morris 1978
+5	18-28	177	Shooter and Gentry 1981
+4	5-28	177	Perrone 1969
0	6-22	200	Hodgkiss and Fisher 1986
-4	low-high	165	Wilson 1983

Table 1.3. Ambient Noise Spectral Variation with Wind Speed.

Another effect of the wind is the level of mechanical vibration or strum which increases with wind speed. This source is important to the spectral shape below 25 Hz at all wind speeds but may contribute energy between 25 and 50 Hz at higher wind speeds. The bandwidth of the strum contaminated noise increases with wind speed and decreases with depth. Preliminary analysis indicates that frequency-wavenumber filtering is effective in removing this noise source as the vibrational modes travel at velocities other than that of acoustic energy. In the band between 20 and 100 Hz the spectral amplitude was independent of wind speed. Shipping may be the dominant noise source for this band as the experiment was in an area of high shipping density. The characteristic spectral "hump" due to shipping noise was observed throughout the experiment. Narrow band 60 Hz harmonics are seen in the spectra and are generated either mechanically or electrically by *FLIP*. There was no evidence of 60 Hz lines during laboratory studies of the array self noise. The 60 Hz harmonics are narrow band and do not degrade the broadband signal analysis.

A graphic display of the output of 120 acoustic channels recording an air gun source at a range of 500 km is shown in Figure 1.8. In this plot, a compressive

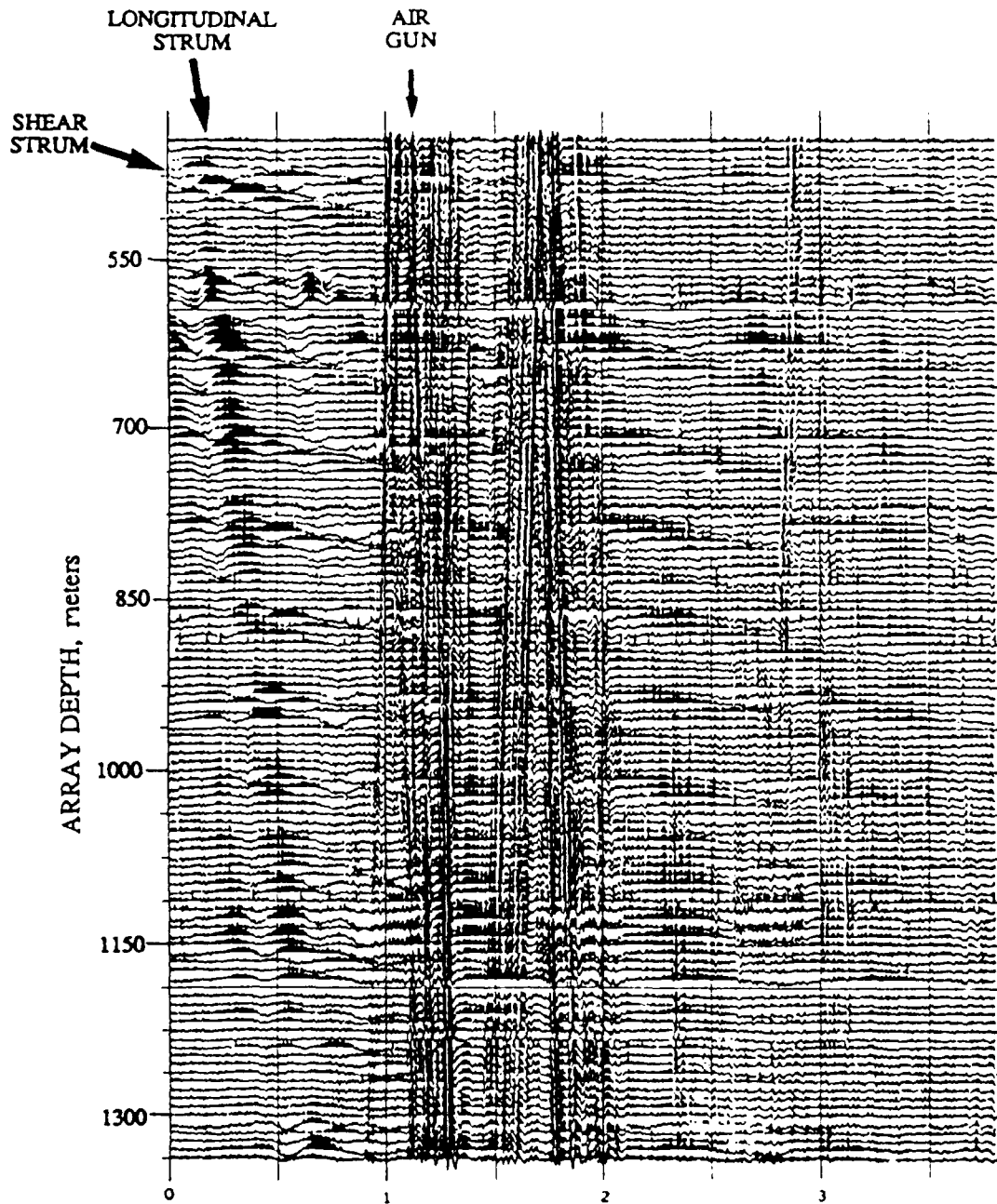


Figure 1.8 Time Series Display of Acoustic Channels. A graphic display of the acoustic channels shows an air gun source at a range of 300 miles as well as longitudinal and transverse (shear) strum modes. The time record displayed is 3.5 seconds. The array hydrophone depths span 400 m to 1300 m.

pressure field, or positive voltage excursion, is represented as a filled line, a rarefactive pressure field or negative voltage is represented as an unfilled line. The air gun is seen as a series of impulsive arrivals that appear as both downward-propagating and upward-propagating wavefronts across the array. In addition, two modes of mechanical vibration (strum) are identified in Figure 1.8. The first mode is a longitudinal vibration of the kevlar support cable, probably due to vertical motions of *FLIP* pulling on the support cable. This mode propagates with a phase velocity of 1800 m/sec and appears as a downward-propagating transient in Figure 1.8. The second mode is a transverse vibration of the kevlar support cable, probably excited by water currents. This mode propagates with a phase velocity of 40 m/sec and appears as a series of shallow-dipping lines with an interference pattern every 75 m, corresponding to the spacing of the inline pressure cases.

The air gun array is seen as a contaminant in the spectra of the ambient noise data in Figure 1.9a. Since the operating area of the air gun array was shallow, the ocean bottom altered the arrival, part of which is coupled into the deep sound channel by down-slope conversion and arrives at the array in a multipath structure at a variety of angles. The effect of the profiler is significant in the 125 to 250 Hz band where it dominates the spectra, clearly distorting the 10 dB/octave rolloff of the ambient noise. The profiler was extracted (Figure 1.9b) by removing the visible signal from the array time series, padding the remaining data to 8192 points and producing the spectrum as described above with no overlapping. The profiler spectra in Figure 1.9c was calculated from 800 data points and a rectangular window, and shows the ambient noise spectra uncontaminated by the profiler.

1.5. SUMMARY

This paper describes the low frequency digital acoustic array designed and built at the Marine Physical Laboratory. A sea test has been conducted to verify the vertical deployment, telemetry, acoustic navigation and ambient noise measurement capabilities of the array. Navigation of the array was conducted within an acoustic transponder net. Ambient noise spectra from single array elements were consistent with previous observations of shipping noise in the frequency band between 20 Hz and 100 Hz. At frequencies above 100 Hz sea surface noise generated by local wind and waves was observed. Current efforts are underway to investigate the vertical directional spectra of low frequency noise measured by the array.

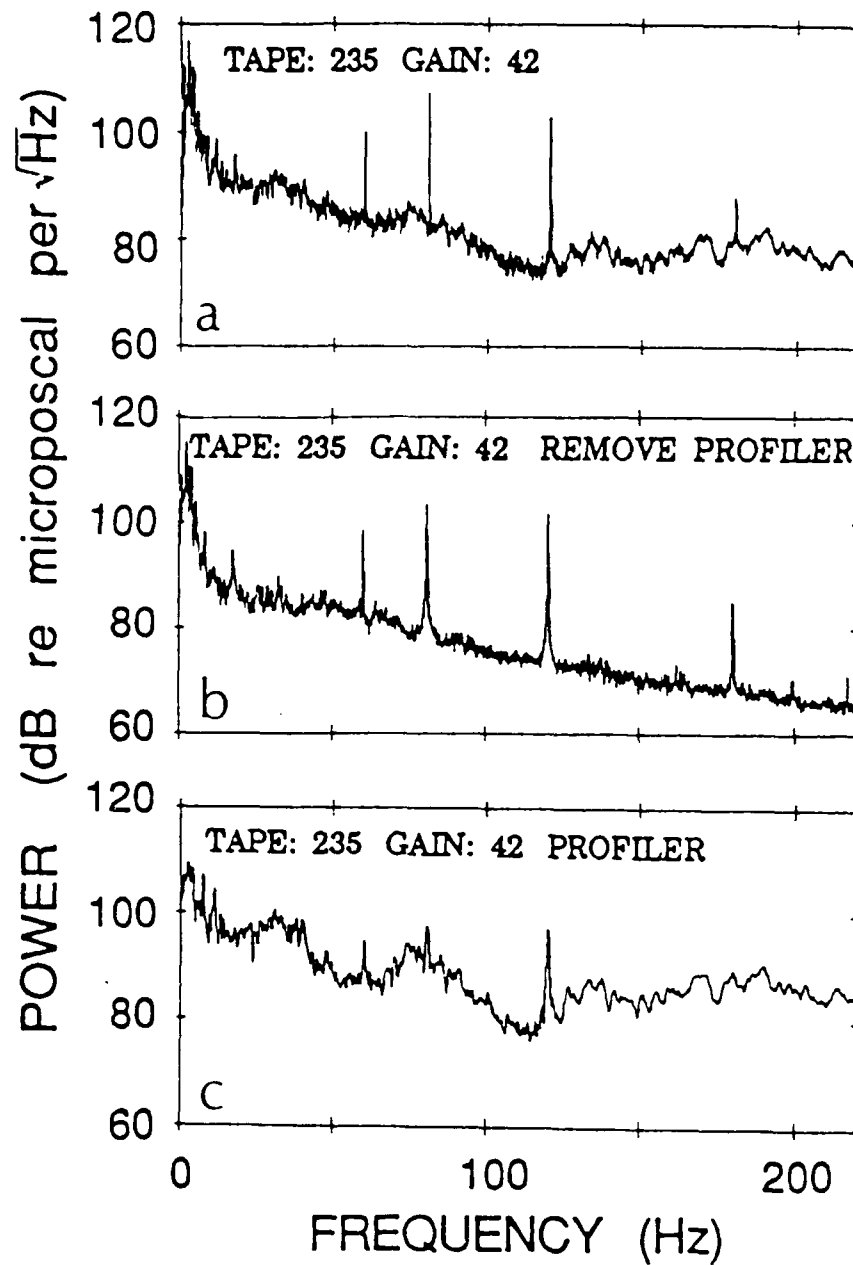


Figure 1.9 Seismic Profiler Contamination. The effect of the air gun signal is seen to be clearly contaminating the ambient noise spectra. (a) Original data acquired at array channel 24. (b) Same data as (a) with profiler signal removed. (c) Profiler signature as seen at the array.

Chapter 2

ACOUSTIC NAVIGATION OF A LARGE APERTURE ARRAY

2.1. ABSTRACT

Acoustic travel time measurements were used to navigate the elements of a large aperture (900 m) acoustic array. Array navigation system performance was evaluated during a vertical deployment in the northeast Pacific from the research platform *FLIP*. A network of bottom-moored acoustic transponders were interrogated from *FLIP* and their 12 KHz replies were detected by receivers at 75 m intervals within the array. A nonlinear least squares algorithm was used to estimate *FLIP* and array element positions from the travel time measurements. The *FLIP* positions derived from this procedure agreed with positions obtained from Global Positioning System (GPS) satellite navigation within a 10 m RMS error. Navigated positions for *FLIP* were internally consistent with a 0.5 m mean RMS error and standard deviation of 1.1 m and for an array element were consistent with a 2.8 m mean RMS error and standard deviation of 0.8 m. The resulting time series of array and *FLIP* motions were analyzed with respect to wind, tidal and internal wave forcing functions. Wind and tidal forcing had the greatest influence on *FLIP* motion whereas tidal and internal wave forcing had the greatest influence on array motion.

2.2. INTRODUCTION

Large aperture arrays produce high resolution directional information by coherently combining signals from individual array elements. Estimates of array shape and element position are required because of the dependence of signal phase on element location. Navigation of such an array in the ocean requires a known reference system in a spatially and temporally varying environment.

A 900 m, 120 element low frequency acoustic array has been developed by the Marine Physical Laboratory [Sotirin and Hildebrand, 1988]. The array is capable of being deployed either horizontally or vertically up to an ocean depth of 6000 m. Navigation of the array is an important part of its operational requirements and the subsystem implemented to perform the navigation must meet design specifications. The position accuracy required is on the order of a few meters, the duration of deployment is on the order of a few months, an operating range of up to 10 km must be viable, the size and cost of the system must be manageable, and the sampling rate must be sufficient to resolve array dynamics due to water currents, tides, wind and internal waves.

Techniques commonly used in ocean positioning systems are based on mechanical, electromagnetic or acoustical signals [Spiess, 1983]. Mechanical positioning devices capable of the accuracy required include inertial systems, pressure sensors, tilt meters, measuring rods and sound-velocity meters. The cost and size requirements of instrumenting a 900 m array with such sensors is prohibitive, although pressure sensors would be valuable for depth positioning in combination with an alternative method for lateral positioning. Electromagnetic

systems are either surface systems whose signals are highly attenuated in water but are useful in determining the position of a surface vessel (e.g. Global Positioning System, GPS), or pulsed laser systems which are currently under development and may eventually be effective within a 1 km range. The technique most easily adapted to a large aperture array deployed in the water column is acoustic navigation. Such systems measure the travel time of acoustic energy between two points in the ocean, are capable of resolving a few meters over a 10 km range and are cost effective and physically manageable. Based on these considerations, an acoustic navigation subsystem was implemented as an integral part of the array.

This paper describes the array acoustic navigation system and its operation during a vertical deployment from Research Platform *FLIP* in the northeast Pacific during September 1987. We describe the hardware system and acquisition of travel time measurements and associated errors, the nonlinear least squares estimation of array spatial positions, and the analysis of *FLIP* and array time-varying positions during the deployment.

2.3. TRAVEL TIME MEASUREMENTS

Acoustic travel time measurements provide range information between the array and a set of fixed transponders. Ranges to three or more transponders are required to calculate *FLIP* position and array position and shape. The navigation hardware consisted of three bottom moored acoustic transponders, two transmit/receive timing units mounted on *FLIP* (one used for *FLIP* navigation and the other used for array navigation), an interrogator/receiver located at the bottom of *FLIP* and 12 KHz acoustic detectors distributed along the array. At a known time, an interrogation signal is transmitted from *FLIP*. This signal triggers a transponder reply which is then detected by the array or the *FLIP* receiver systems. The travel times between the transponders, *FLIP*, and the array detectors determine array position and shape.

During the September 1987 experiment, three navigation transponders were moored in 4700 m of water distributed as a 1.4 km equilateral triangle. *FLIP*'s position was maintained in the middle of the transponder network by a 3-point moor (Figure 2.1). The transponders were deployed by a surface support ship operating a GPS satellite navigation receiver for absolute positional information. The transponders were equipped with anchors (175 kg) to secure them to the ocean floor and to constrain the horizontal movement during descent (sink rate of approximately 1 m/s). Once anchored, they were buoyed up above the anchor on 100 m lines with 130 kg of hard floats to limit horizontal movement and to insure a well separated bottom bounce. They operate by detecting a unique interrogation frequency and answer with a 3 ms reply at 12 KHz with a source level of 190 dB re 1 μ Pa at 1 m. The recognition delay time is 0.5 to 3 ms depending upon the signal to noise ratio of the interrogation pulse [Boegeman, 1988]. Due to the proximity of *FLIP*, the absence of other local high frequency ambient noise sources and the manual control of the signal level on the interrogator, a constant delay time of less than 1 ms was assumed.

The interrogation pulse was sent from a transceiver mounted on the bottom of *FLIP* (90 m in depth). The pulse level was adjusted manually above the ambient noise for consistent transponder replies. The pulse was triggered by either a chart recorder to navigate *FLIP* or by an interrogation circuit to navigate the array. The chart recorder trace, set on a one second sweep rate, displayed the 12 KHz

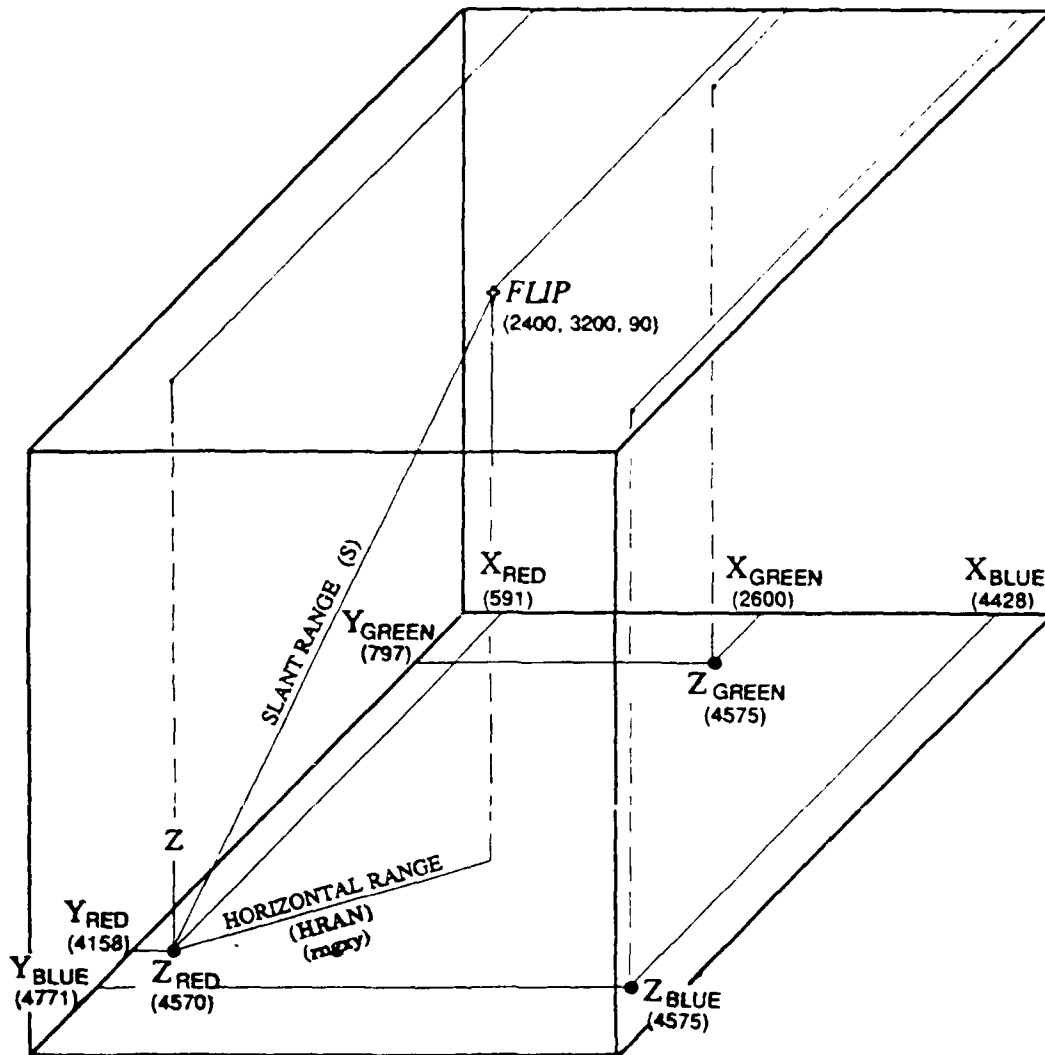


Figure 2.1 Navigation overview. The navigation system consists of three bottom moored transponders in an equilateral triangle about *FLIP* and the vertical array. The transponders are designated by color: red, green and blue. The initial xyz coordinates of the transponders and of the *FLIP* interrogator are indicated.

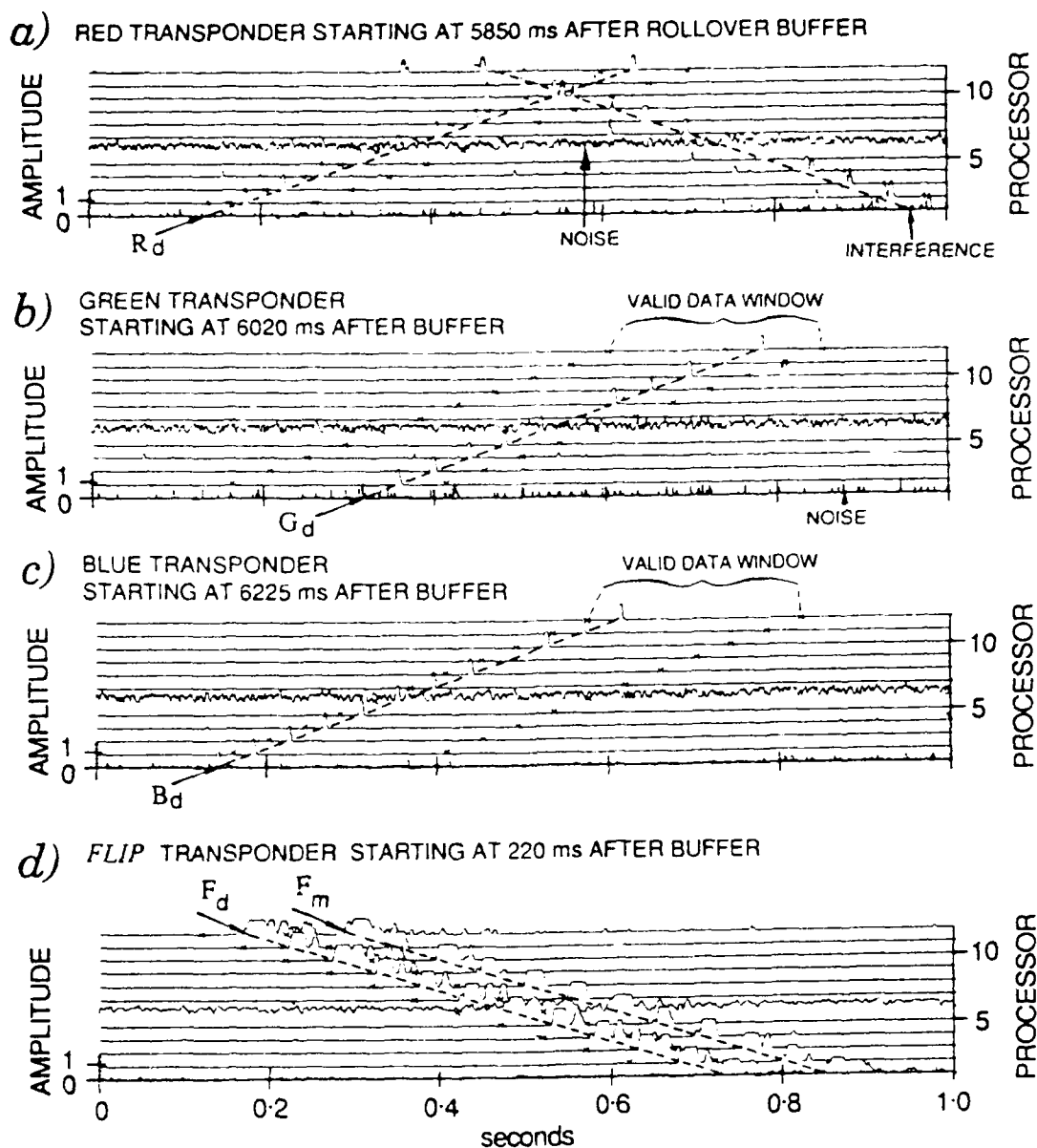


Figure 2.2 Travel time acquisition. The 12 array navigation receivers each detect four pulses during a 65.536 s navigation cycle. The normalized correlated receiver outputs are shown during a one second interval bracketing each detection. The top trace represents the output of the top receiver, followed in sequence by the deeper receivers. The first three panels (a), (b), and (c) represent the detected replies of the three transponders, arriving at the deepest receiver first and traveling up through the water column to the shallower receivers. The last panel (d) is the detection of the 12 KHz pulse transmitted from *FLIP* traveling down the array, with a surface reflection arriving about 120 ms after the direct pulse. The small x's represent the valid data window. The start time is indicated at the top of each panel.

transponder reply amplitudes in a 500 Hz band with a transmit/receive delay time of 0.1 ms. Each transponder was interrogated individually to facilitate identification and transmitted a reply pulse once per second for 45 seconds. Since the *FLIP* transducer was also used as an interrogator for the array navigation system, only one system was operable at a time; consequently the *FLIP* navigation data were recorded only once an hour during the sea test. Round trip travel times for navigating *FLIP* were measured by hand from the chart recorder output with an estimated RMS error of 2-3 ms.

The 900 m array was deployed vertically from *FLIP* with a 420 kg weight attached to maintain a nearly vertical orientation. The array navigation subsystem was composed of 12 hydrophones with 75 m spacing monitored by 12 individually programmable processors. Each of the 12 processors contained tuned navigation receivers designed to detect the 12 KHz transponder reply in a 200 Hz band with a -6 dB minimum signal to noise ratio. Once per minute the transceiver on *FLIP* sent out 4 pulses: three unique transponder interrogation pulses followed by a 12 KHz pulse for depth ranging. The 12 KHz transponder replies (3 ms) and the 12 KHz depth ranging pulse from *FLIP* (10 ms) were recorded in series as a one bit output every 0.4 ms by each of the array navigation receivers. The interrogation sequence clock was synchronized with the array timebase and recorded every 128 ms.

To calculate the travel time, the time of the transponder return must be determined relative to the time of the interrogation. The signal which initiated the interrogation sequence was found by linear interpolation of the interrogation sequence clock. The leading edge of the return pulse was found by recreating each of the navigation receiver time series, and correlating these binary time series with a pulse replica which depended upon array receiver noise and level of detection. A one second time interval of the normalized correlation output from each array section is shown for each transponder in Figure 2.2. The correlated arrival across the array of each transponder reply is evident; interference and noise are also evident. To reduce the chances of detecting a noise spike or multipath return rather than the direct transponder reply, a window was invoked for each expected return during which time the data were considered valid, as shown by the small x's in Figure 2.2. The window was allowed to track the replies as the arrival time shifted with array movement. The travel time from the transponder to the array is the difference between the departure time of the interrogation pulse and the arrival time of the transponder reply at the leading edge of the correlated signal minus the travel time from *FLIP* to the transponder and the constant system delay times.

The accuracy of the travel time measurements from the bottom transponders to the array was dependent upon factors which affected all receivers similarly as well as factors which varied with each array receiver. The factors with similar effect were the ambient ocean noise in the 12 KHz band which has a typical level of 30-40 dB// μ Pa/ $\sqrt{\text{Hz}}$ and the transponder performance which introduced timing errors [Sotirin and Hodgkiss, 1989]. The factors which varied with receiver were the drift in the array clock phase lock loop circuitry which introduces small sampling time errors, the *FLIP* to transponder travel time measurement error (the resultant error in array to transponder range increases as depth decreases) of order 1.5 ms, and the noise and detection threshold of the array receivers. The variation in receiver error [Sotirin and Hodgkiss, 1989] is confined for the most part to a mismatch in detection threshold due to the temperature sensitivity of the capacitors and high failure rate of the inductors in the tuned navigation filters. This variation was estimated at 2 ms during laboratory tests of the frequency sensitivity of the tuned filters and by examining the length of the transponder

replies. Estimated accuracy for the array travel time measurements depends upon the receiver and the depth of the array but is typically 2-3 ms. The accuracy of the depth measurements is affected by the ambient ocean noise, the transmitter and detector noise, the detection threshold and the strength of the transmission. Measurement error in the travel times corresponding to array depths is estimated by calculating the mean standard deviation in 10 sample segments to be <1 ms.

2.4. POSITION ESTIMATION

In this section we determine where the three bottom transponders, the *FLIP* transceiver and the array elements are in 3-dimensional space using the travel times described in the previous section. The general problem of fitting model functions and parameters (spatial positions) to data (travel times) appears in many areas of applied science: as parameter estimation, regression analysis, inverse problems, filtering, process identification, and as an optimization problem in numerical analysis. Noise in the travel time measurements demand that sufficient data be collected to overdetermine the solution, requiring some kind of approximation method.

To approximate the solution, an optimization problem is defined to minimize differences between model predictions and actual measurements. The function relating predictions and measurements is determined by the problem structure and the error distribution. One approach is to minimize the differences with respect to a matrix norm. Analytically, the most viable choice is the l_2 norm resulting in the familiar least squares solution. If the errors are independent and distributed normally with a constant standard deviation then the l_2 norm coincides with the maximum likelihood solution. The least squares solution magnifies the effect of large errors and if the error distribution contains many outliers, the l_1 norm solution as described by Gill, Murray and Wright [1981] and implemented by Duckworth [1987] is an attractive alternative. Although the l_1 solution is more robust in terms of outliers, these errors continue to affect the solution, and an alternative approach is to remove the source of the large errors.

The navigation problem discussed here has been implemented in terms of the least squares method. The transponder net was localized separately to allow accurate real-time array navigation. The *FLIP* travel time measurements used for the transponder localization are very consistent and possess no large errors having been selected and verified by hand. Apriori knowledge of array measurement errors did not justify deviation from the assumed normal distribution. In the remainder of this section, a general description of the least squares formulation is followed by the specific details of implementation for the array navigation problem. The effect of specific types of errors are simulated and results are presented.

2.4.1. Least Squares Formulation

The *FLIP*, array and transponder positions were estimated by a nonlinear least squares method. The problem is to find the set of model parameters (spatial positions), given a set of measurements (travel times) plus noise. The least squares estimator identifies a realistic set of parameters by minimizing the sum of the squared errors, with an error defined by the difference between the model estimate and the measurement. For the set of measured data x_k (travel times), and the set of

parameters

a_j (spatial positions) which determine the model estimate $\hat{x}_k(a_j; j=1, N)$ (referred to as $\hat{\mathbf{x}}$ or \hat{x}_k), the least squares formulation is written as

$$\underset{\mathbf{a} \in R^N}{\text{minimize}} \left\{ F(\hat{\mathbf{x}}; \mathbf{a}) = \sum_{k=1}^M \frac{[x_k - \hat{x}_k]^2}{\sigma^2} = [\mathbf{x} - \hat{\mathbf{x}}]^T \mathbf{R}^{-1} [\mathbf{x} - \hat{\mathbf{x}}] \right\} \quad (2.1)$$

where the measurement errors are uncorrelated with identical variances σ^2 and \mathbf{R} is $\sigma^2 \mathbf{I}$. The error function $F(\hat{\mathbf{x}}; \mathbf{a})$ (designated as F), is minimized when the gradient \mathbf{g} of F with respect to the model parameters is zero,

$$\mathbf{g} = \frac{\partial F}{\partial \mathbf{a}} = -2[\mathbf{x} - \hat{\mathbf{x}}]^T \mathbf{R}^{-1} \frac{\partial \hat{\mathbf{x}}}{\partial \mathbf{a}} = 0. \quad (2.2)$$

In general, a closed formed (one step) least squares solution exists provided the set of equations is linear. For the array navigation problem however, the nonlinear mapping from measurement space to parameter space necessitates an iterative implementation. One such implementation is to approximate the smooth nonlinear functions described by F with a linear form of the Taylor's series expansion about an initial position \mathbf{a}_1 . In the immediate neighborhood of \mathbf{a}_1 ,

$$F(\hat{\mathbf{x}}; \mathbf{a} + h\mathbf{p}) = F(\hat{\mathbf{x}}; \mathbf{a}_1) + \sum_{j=1}^N h p_j \frac{\partial F}{\partial a_j} \Big|_{\mathbf{a}_1}$$

where h is a scalar, and \mathbf{p}_n is a direction vector guiding the search for a minimum. In terms of the iteration step the notation may be written:

$$F_{n+1} = F_n + h_n \mathbf{g}_n^T \mathbf{p}_n \quad (2.3)$$

where \mathbf{g}_n is the gradient of F at $\hat{\mathbf{x}}_n$. An acceptable minimum for F is obtained by calculating the estimate $\hat{\mathbf{x}}$ from an initial "best guess" for the parameters \mathbf{a}_1 , then developing a prescription which improves this initial guess, updating the parameters until specified convergence criteria are satisfied. A typical prescription to search for this minimum is to calculate $\hat{\mathbf{x}}$ from \mathbf{a}_1 , F_n from $\hat{\mathbf{x}}_n$ and \mathbf{x}_n and complete the following steps:

- (1) Compute a vector, \mathbf{p}_n , which is the search direction.
- (2) Compute a scalar step length, h_n .
- (3) Update the estimate of the parameters. Set $\mathbf{a}_{n+1} \leftarrow \mathbf{a}_n + h_n \mathbf{p}_n$, $n \leftarrow n + 1$.
- (4) Test for convergence. Calculate the forward problem, which determines current estimates $\hat{\mathbf{x}}_n$ of the measurements \mathbf{x} from current estimates of the parameters \mathbf{a}_n . Evaluate F_n and F_{n-1} with respect to the convergence criteria. If the conditions for convergence are satisfied, the current value of \mathbf{a}_n is considered the solution; if not, iterate by returning to step 1.

To implement this prescription, the choice of convergence criteria, search direction and step length must be considered; particular choices relating to array navigation will be specified in the following section. In an optimization problem,

the value at the minimum is generally not known and convergence criteria must be developed to bound the number of iterations while insuring that the resulting solution is sufficiently close to the real minimum. Specific criteria are defined by evaluating the magnitude of the gradient, the magnitude of the squared error, and the relative decrease in squared error with respect to acceptable tolerances δ_i as follows:

$$\begin{aligned} \|\mathbf{g}_n\| &< \delta_1 \\ F &< \delta_2 \\ 0 \leq F_{n-1} - F_n &< \delta_3 \\ \text{number of iterations} &> \frac{1}{\delta_4} \end{aligned}$$

Combinations of the above criteria determine convergence. The rate of convergence depends on the specific minimization algorithm, the initial estimates, and the error surface. The resulting minimum point could be either global or local. In general there are no sure methods for finding global minima, so the accuracy of the initial guess is important.

Consider the iterative step in the direction of search \mathbf{p} . In the univariate case, the only possible directions are positive or negative. As the number of dimensions increases, even to two, the number of possible directions is infinite. Search direction procedures are typically direct search methods or gradient search methods with the constraint that \mathbf{p} be a descent direction. Iterative search procedures having the general form of Eq. (2.3) lend themselves easily to gradient search methods. To define the gradient search, if \mathbf{g}_n is non-zero, there must exist a vector \mathbf{p}_n such that $\mathbf{g}_n^T \mathbf{p}_n < 0$. If \mathbf{p}_n is defined as $-\mathbf{g}_n$ and the gradient is nonzero, this direction is clearly a descent direction; the algorithm is recognized as the steepest descent method. It follows from Eq. (2.3) that for any small positive step size h , $F_{n+1} < F_n$. Since \mathbf{p}_n is in the direction of decreasing F , convergence is guaranteed provided h_n is chosen so that F is "sufficiently decreased" at each iteration. To be appropriate, h_n must be small enough to locate the minimum precisely and satisfy the immediate neighborhood constraint of Eq. (2.3), and at the same time large enough to search efficiently. The existence of guaranteed convergence of the algorithm does not imply that convergence will be achieved in an acceptable number of iterations. A common method used to define h is to follow the steepest descent gradient for the current iteration to a minimum. This dictates that the next search direction be nearly orthogonal to the current direction $\mathbf{g}_n^T \mathbf{p}_{n+1} \rightarrow 0$. It has been shown that the directions generated by this method asymptotically converge to only two directions for many problems [Sorenson, 1980], increasing the number of iterations immensely. This situation may be avoided by constraining the step size to be less than that required to reach the minimum in the current search direction. Although the rate of convergence of the steepest descent algorithm is known to be less than other methods [Gill *et al.*, 1981], the method is numerically stable and produces efficient results for the navigation problem considered here.

2.4.2. Implementation

We discuss implementation of the general nonlinear least squares method described above for the transponder and array navigation. The ingredients required for a least squares problem are: (1) the measurements \mathbf{x} , travel time detected at the array and at *FLIP*, (2) the initial estimates of the model parameters \mathbf{a} represented by *FLIP*, array and transponder xyz positions, (3) the mapping function from measurement space to parameter space which calculates the estimates $\hat{\mathbf{x}}$ from the parameters, and (4) the measurement errors σ . Although the general prescription is the same for the transponder localization and for the *FLIP*/array localization, there are differences in the implementation. In the following, the explicit inputs and implementation of the transponder localization are specified and the differences relating to *FLIP* and the array are discussed separately.

Transponder Localization: The two-way travel times between *FLIP* and the transponders were used for transponder xy position estimation. Normally data from an extensive surface ship survey would be available for localizing the transponders [Spiess, 1985; Smith *et al.*, 1975]. Although such a survey was conducted during the experiment, the data were not complete due to extreme noise levels of the surface ship; instead the data recorded by the *FLIP* navigation system was used. The *FLIP* data set defines a survey configuration which is not optimal, however, the extended time series and low errors of the *FLIP* measurements increase their reliability over the other available data sets. The unconventional geometry of these measurements imparts a rotational symmetry to the problem, as *FLIP* was moored in the center of a roughly equilateral triangle defined by the transponder positions. This physical constraint limits the amount of independent xy information which is contained in the measurements and tends to destabilize the problem. Our results were achieved by choosing well-constrained initial estimates of the xyz positions described below, by fixing the z component during the xy iteration, and by perturbing the *FLIP* positions independently of the transponder positions. In terms of Eq. (2.1) and (2.2), the model parameters a_j , $j = 1, N$, are the x and y positions of the *FLIP* transceiver and the three bottom transponders; these x and y positions define the horizontal projection of the slant range from a specified transponder to *FLIP* which is designated as $\hat{\mathbf{x}}_k$, $k = 1, M$. The measured travel times are converted to horizontal projections designated \mathbf{x}_k , $k = 1, M$, using the sound speed profile and the fixed z components as shown below. The number of horizontal projections, M , is 3 for the *FLIP* perturbations and 424 for the transponder perturbations.

The conversion from the time domain to the space domain is dependent on the sound speed profile between the specified depths. Assuming a constant sound speed and therefore a straight line path, and expanding the x_k 's for illustrative purposes, the measured travel time is related to the xyz position as:

$$\begin{aligned} \text{measured travel time} &= \frac{1}{c} [\text{slant range}] \\ \text{slant range} &= [(x_t - x_r)^2 + (y_t - y_r)^2 + (z_t - z_r)^2]^{1/2} \\ \text{horizontal projections} &= [(\text{slant range})^2 - (\delta z)^2]^{1/2} = [(x_t - x_r)^2 + (y_t - y_r)^2]^{1/2} \\ &\mathbf{x}_k = \hat{\mathbf{x}}_k \end{aligned}$$

where c is the sound speed, x_t, y_t, z_t represent the transmitter position and x_r, y_r, z_r

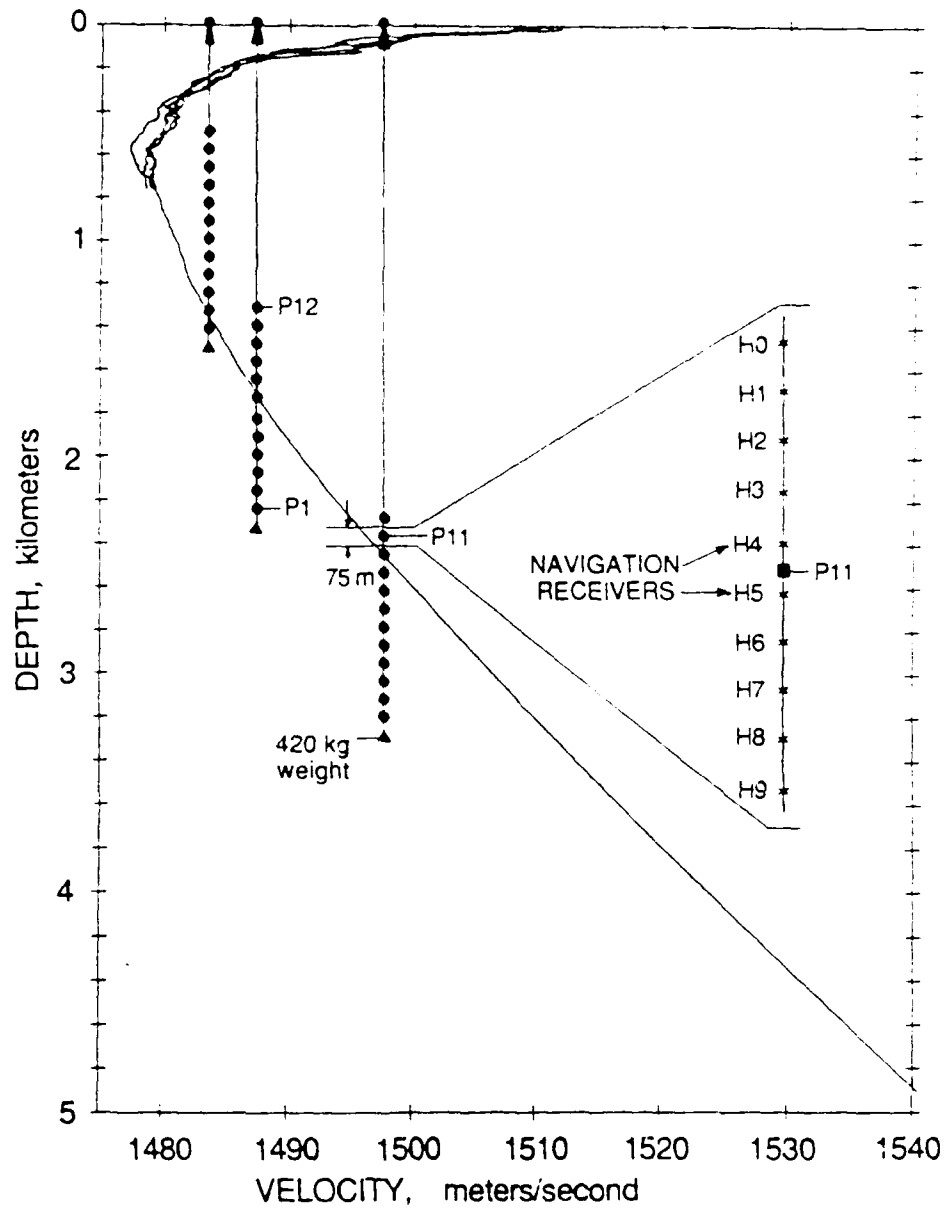


Figure 2.3 Array navigation receivers and sound speed profiles. The array was deployed at three nominal depths during the September 1987 experiment. The sound speed profile is used in the conversion from travel times to spatial position. This profile was calculated from CTD data (0 - 4900 m depth), and is shown with three profiles calculated from XBT data (0 - 700 m depth) chosen to illustrate the variation in sound speed in the upper ocean layer. The 12 array sections are each 75 m in length, with 10 receiving hydrophones spaced at equal increments. The navigation hydrophones are located adjacent to array section pressure cases. The data from one receiver per array section (H5) was recorded during the experiment.

represent the receiver position. Sound speed is not constant in the ocean environment and a varying sound speed profile refracts acoustic energy, however under certain conditions the harmonic mean, defined below, may be used with minimal error. To estimate the travel time differences due to refraction effects, the configuration parameters of the September experiment were specified and employed as inputs to the Generic Sonar Model (GSM) [Weinberg, 1985]. The GSM used generalized ray theory to calculate the ray path and travel time between a transmitter-receiver pair by assuming a sound speed profile with layers of constant gradient. The simulation results are presented in Table 2.1 which shows the travel time between an estimated transponder position and the array for a 12 KHz signal as a function of range, depth and sound speed profile. The first column represents the results generated by assuming a constant sound speed of 1500 m/s throughout the water column. The second column used the harmonic mean, calculated by numerical integration of the layered sound speed profile over depth to estimate travel time which is then converted to speed,

$$c = \frac{(z_T - z_0)}{\int_{z_T}^{z_0} \frac{dz}{C(z)}}$$

The $C(z)$ profile used in the equation above is shown in Figure 2.3 and was calculated using the Unesco equations [Fofonoff and Millard, 1983] relating conductivity to practical salinity, sound speed to salinity, temperature and pressure, and pressure to depth. The conductivity, temperature and pressure measurements were obtained from a surface ship on Julian day 267 at 2243 GMT within one nautical mile of the *FLIP* location. Sound speed profiles in the ocean are typically very stable below the thermocline over the time period of the sea test. The diversity in temperature at the surface however imparts temporal variations in the sound speed profile.

Travel time vs. sound speed, depth and range: Source depth = 4573m, Frequency = 12KHz					
Horizontal Range	Receiver Depth	GSM Travel Time predictions using:			
		Constant profile (1500m/s)	historic profile	harmonic mean	deep ctd
meters	meters	seconds			
2000	90	3.2724	3.2740	3.2733	3.2733
2600		3.4546	3.4563	3.4556	3.4555
2000	400	3.0848	3.0839	3.0834	3.0833
2600		3.2774	3.2765	3.2759	3.2758
3000		-	-	3.4243	3.4241
5000		-	-	4.3387	4.3382
10000		-	-	7.2181	7.2152
2600	1600	2.6325	2.6184	2.6175	2.6174
2600	2800	1.0972	1.0726	1.0717	1.0716

Table 2.1. Sound speed impact on travel time predictions.

Temperature measurements were acquired from expendable bathythermograph (XBT) casts deployed from *FLIP* twice a day throughout the experiment.

Temperature data were converted to sound speed and decimated to maintain consistency with program inputs. This conversion utilized historical salinity data [Churgin and Halminski, 1974] and was implemented by means of the following equation [Clay and Medwin, 1977]:

$$c = 1449.2 + 4.6T - 0.055T^2 + 0.00029T^3 + (1.34 - 0.10T)(S - 35) - 0.016z$$

where c = sound speed (m/s), T = temperature (°C), S = salinity (ppt), z = depth (m). The maximum difference in the harmonic mean due to time variation in surface temperatures was about 1.5 m/s (0.1% of the mean speed). This affects the predicted travel time from a transponder to a receiver at 90 m by about 3 ms (5 m). An error in the sound speed correction of the measurements, translates into a larger array element RMS error but does not substantially affect the estimated position due to the nearly equilateral triangle system configuration. Due to possible inaccuracies in the absolute XBT measurements, and the robust nature of the system configuration to errors in sound speed, the profile was considered constant over time and equal to the CTD calculations. The third column in Table 2.1 incorporates refraction effects due to changes in the sound speed profile $C(z)$ described above. The predictions generated by the GSM indicate that for the geometrical configuration of the September experiment shown in Figure 2.4, the error in travel time by assuming a straight line path with a constant average sound speed is 0.1 ms, therefore using the harmonic mean of the sound speed profile produces minimal error for the parameters of this experiment.

GPS satellite positions at *FLIP* and the surface ship during transponder deployment provided the initial estimates of the transponder xy positions to within 10's of meters. The clement weather which prevailed during the deployment and the negative buoyancy of the transponders (sink rate of ≈ 1 m/s) constrain the final transponder positions. Initial transponder depths were estimated by subtracting the transponder anchor line length from the echo-sounding depth measured at *FLIP*. The assumption that the sea floor is flat in the immediate area of *FLIP* was corroborated by bottom mounted Swallow floats deployed approximately two nautical miles from *FLIP*. Preliminary Swallow float depth estimates were within 15 m of the depth measured at *FLIP* [Hodgkiss and D'Spain, 1988].

Once the ingredients for the least squares method have been accumulated, the xy positions are adjusted until the root mean squared (RMS) error satisfies the convergence criteria. This is accomplished in several steps by first maintaining constant transponder positions and perturbing the *FLIP* positions to minimize errors, then holding the current *FLIP* positions constant while perturbing the transponder positions to minimize errors, then examining the mean squared error of each *FLIP* position to determine (via a user parameter) whether it should be preserved as a viable contributor, and finally repeating the entire procedure until the convergence criteria are satisfied. The perturbation adjustment is calculated with \mathbf{p} as the negative gradient. The step size is a constant (1.5) unless the RMS error is less than 1 m at which time the step size begins to decrease; as the minimum is approached, the step size is calculated as a function of the percent change in iterated RMS error. The convergence criteria are defined as follows: an absolute RMS error less than 0.15 m, a 0.15 percent change in the iterated RMS error, or a maximum of 30 iterations. A typical number of loop iterations for convergence of the September data set was 3 for each inner loop and 5 for the entire procedure, the repetition factor depending on the user parameters. A

detailed description of the software implementation and its usage is documented [Sotirin and Hodgkiss, 1989].

The transponder depths were iterated manually by minimizing the magnitude and dispersion of RMS error across the array. Increasing RMS errors across the array was shown by the simulations in the following section to be an indication of potential transponder depth error. The *FLIP* data base used to navigate the transponders was sampled during tidal peaks to discern whether there was any transponder movement due to tidal forces. No appreciable difference was observed and transponder movement is assumed to be negligible.

FLIP and Array Element Localization: The localization procedure for *FLIP* and the array is essentially the same as just described for the transponders. With the transponder positions known, the *FLIP* and array element navigation may be calculated in real time.

The initial xy positions for *FLIP* and the array elements were estimated from GPS positions after *FLIP* was moored (Julian day 255). Because *FLIP*'s position was maintained by a 3-point moor, the same initial xy position was used for each *FLIP* position throughout the test. If the initial xy position must be estimated without GPS or if the receiver is not moored, a geometric estimate may be obtained from the transponder slant ranges. The depths of the array elements were measured to within 1.5 m by the high frequency transmitter mounted on the bottom of *FLIP*. The 12 KHz signal was received by each navigation receiver without exception, however, there were indications of slight interference in the variability of the arrival time of the resulting correlated output. The array was deployed under 420 kg of tension to maintain verticality and constrain the depth parameter. A 1.5 m error in array depth, because this input is a fixed parameter in an equilateral configuration, translates into less than 0.5 m of error in the xy positions of the array but changes the RMS error by as much as 2.5 m.

The noise in the travel times measured at the array is greater than the noise in the hand-picked data measured at *FLIP*. To improve the data quality, various averaging, thresholding and interpolation schemes were incorporated in the processing software. Should a receiver not detect a return, or if the detected return is not within specified thresholds for range and depth variability, various interpolation/extrapolation software options may be specified. Prior to the least squares iterations, the data may be smoothed with a running average filter. The travel time measured at the array represents the time from *FLIP* to the transponder to the array. Therefore, the travel time measured at *FLIP* is interpolated and subtracted from the array travel time to provide the transponder to array travel time required by the least squares procedure.

2.4.3. Simulations

Simulations were conducted to examine the array position sensitivity to errors in the transponder and *FLIP* positions. The spatial configuration shown in Figure 2.4 simulates the September sea test; *FLIP* is centrally located in the transponder network (identified by colors) and the array is directly under *FLIP*. The transponders, *FLIP*, and the array are initially assigned to known positions with slant ranges as shown. Individual transponder positions were perturbed and the resulting array shape and relative errors were examined. These tests were conducted first with the array in a vertical orientation, that is the array element xy

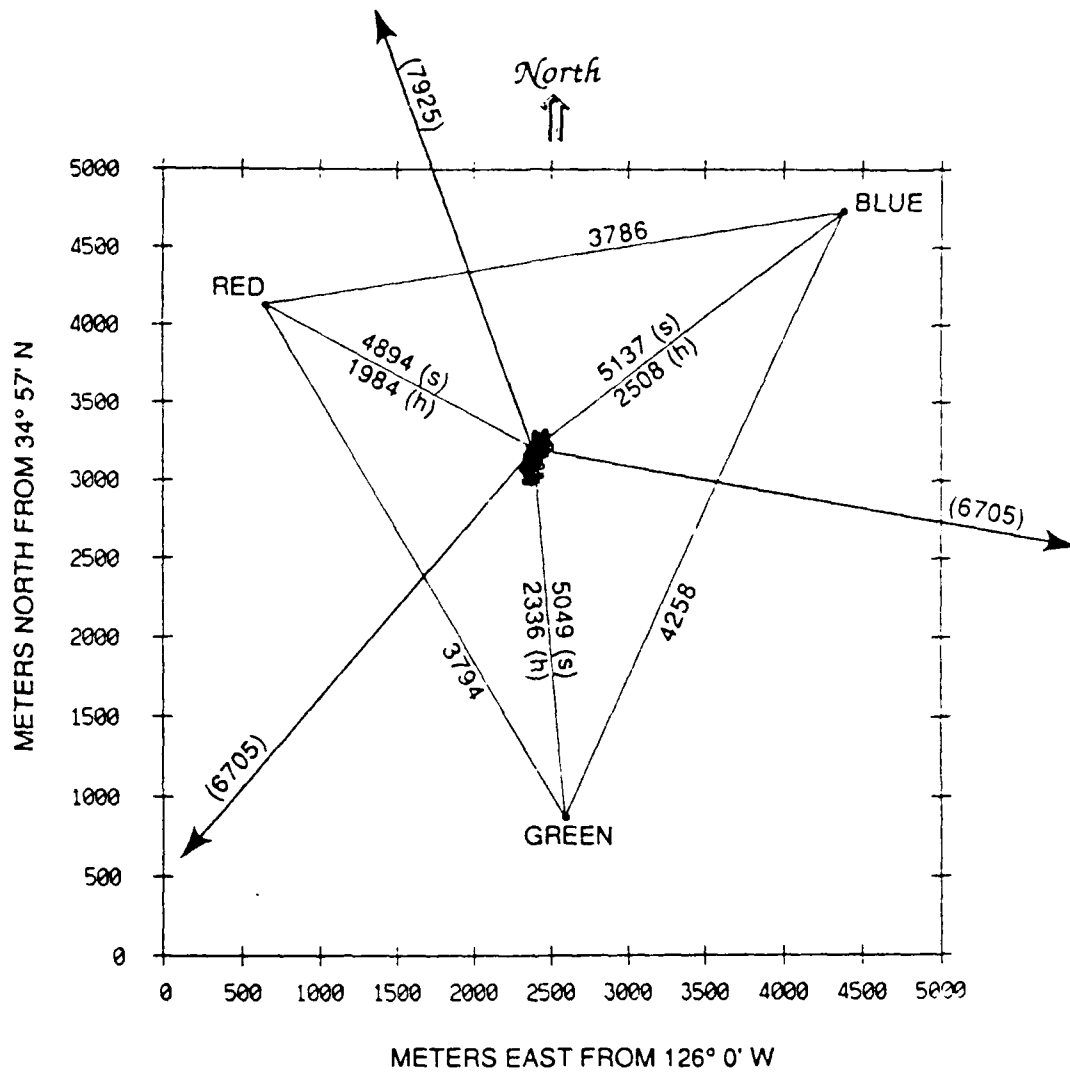


Figure 2.4 Spatial configuration for navigation during the September 1987 sea test. The estimated positions of *FLIP* and the 3 bottom transponders (red, green, blue) measured hourly over 18 days are shown in plan view. The *FLIP* mooring lines are represented by arrows, and the slant range (s) and horizontal projection of the slant range (h) are indicated in meters from an arbitrary *FLIP* xy position (2400,3200). Transponder baseline distances are indicated in meters.

positions were identical to those of *FLIP*, and then with the array straight but tilted 2° vertically at 225° azimuth. Zero mean gaussian random errors ($\sigma^2 = 3$) were added to the array travel times with no appreciable changes. The final simulation configuration perturbed the *FLIP* position. Because the array measures travel times of rays which originate at *FLIP*, errors in the *FLIP* parameters map into array positional errors.

The simulations provide an understanding not only of the error magnitudes but also of their dispersion across the array. With a +25 m perturbation in the x or y transponder positions, the effect on the initially vertical array is a horizontal translation in the direction of the transponder with no relative array positional errors. If an error is introduced in the z transponder position, the array is translated and tilted. Figure 2.5a shows the effect on the array as the blue transponder is perturbed by 100 m errors individually in x, y and z and finally simultaneous 100 m errors in x, y and z. Figure 2.5b shows the effect of transponder depth errors. Each transponder depth was increased and decreased individually by 10 m and 25 m. The dot in the center of the figure is the navigated array position with no input errors; with a decrease in transponder depth, the input slant range appears to be too long and the array is translated in a direction away from the transponder (notated by o's on the plot) and tilted slightly. An increase in transponder depth operates similarly except in a direction toward the transponder (notated by x's on the plot). The results of the simulations for the positive perturbations with an initially straight vertical array are compiled in Table 2.2. The columns indicate which parameter has been perturbed and the amount of the perturbation, the translation and percent change in horizontal range calculated for the *FLIP* position, system tilt and position RMS error (\sqrt{F} in Eq. 2.1). The RMS error is shown as a single number if the difference in error across the array was less than 0.1 m; when two numbers are shown, they indicate the error at *FLIP* and the bottom element of the array. By examining the *FLIP* translation and RMS error for the x and y perturbations in Table 2.2, it is clear that the x position is controlled by the red and blue transponders and the y position is controlled by the green and blue transponders (Figure 2.4). The difference in RMS error between the 3 transponders reflects the percent deviation from original slant range. The dispersion in RMS error was used to iterate the transponder depth. This can be seen, for example, in the results of the red depth perturbation which yields an RMS error at *FLIP* of 18.13 m, monotonically decreasing to 13.48 m at the bottom of the array. The array and *FLIP* positions are more sensitive to errors in transponder depth (60 to 70% of perturbation) than to errors in transponder horizontal (xy) position (<35% of perturbation). To demonstrate this sensitivity dichotomy, with *FLIP* at a known position x,y from a transponder, the *FLIP* translation T_z due to an error δ_z in transponder depth and the translation T_{xy} due to errors δ_x and δ_y in transponder xy position are:

$$T_z = h - s \sin(\cos^{-1}((d+\delta_z)/s))$$

$$T_{xy} = h - [(x - \delta_x)^2 + (y - \delta_y)^2]^{\frac{1}{2}}$$

where h and s are the horizontal and slant ranges respectively (Figure 2.4), d is the difference in depth between the base of *FLIP* and the transponder, x is the component of h in the \hat{x} direction and y is the component of h in the \hat{y} direction. *FLIP* is constrained by the experimental configuration to move approximately along the line defined by the horizontal projection of the slant range between the

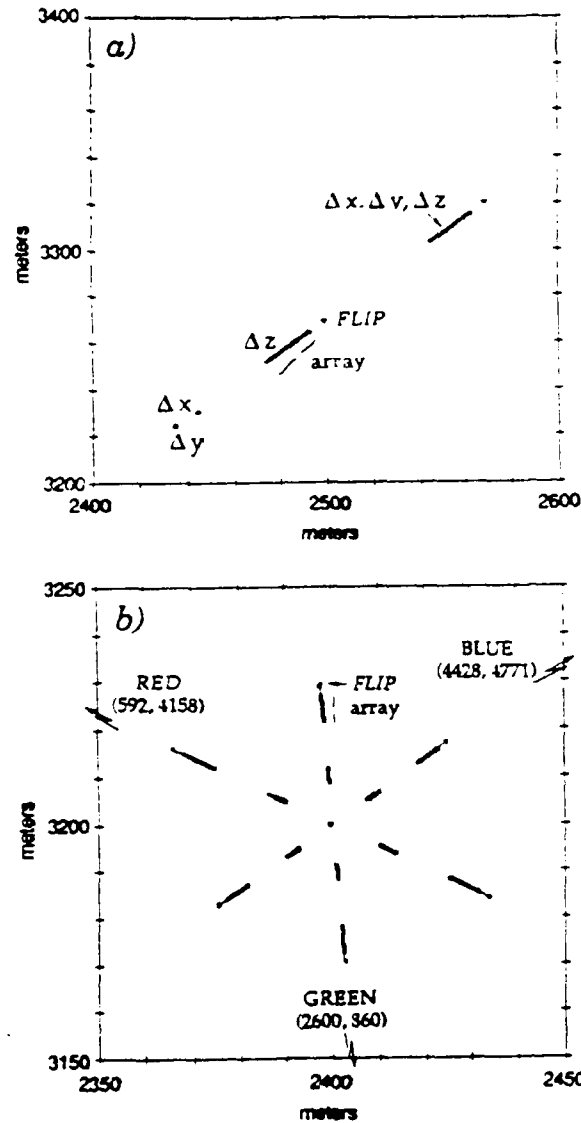


Figure 2.5 Error simulation results. The effect of errors in the transponder positions on the shape and position of *FLIP* and the array are shown in plan view. (a) Effect on the array as the blue transponder is perturbed by 100 m errors individually in x, y and z and simultaneous 100 m errors in x, y and z. The errors in transponder x and y positions translate the array, errors in transponder depth translate and tilt the array. (b) Detailed demonstration of the effect of transponder depth errors. Each transponder depth was increased and decreased individually by 10 m and 25 m. The dot in the center of the figure is the navigated array position with no input errors; with a decrease in transponder depth, the array is translated in a direction away from the transponder (notated by o's on the plot) and tilted slightly. An increase in transponder depth moves the array in the opposite direction (x's on the plot).

perturbed transponder position and *FLIP* (Figure 2.5). To quantify these translational errors, a δ_z of +25 m in the red transponder depth resulted in a 58 m *FLIP* xy position translation, and a δ_x of +25 m in the red transponder x position resulted in a *FLIP* xy position translation of only 22 m, illustrating that *FLIP* position is more sensitive to errors in transponder depth than to errors in transponder xy position.

An error in transponder position, when the array is tilted, will distort the vertical and azimuthal array orientation as well as impart a horizontal translation. A tilted array will show a horizontal translation comparable to the initially straight array but with azimuthal and vertical rotations. The vertical angular change is similar to that of the straight array for depth perturbations and small but noticeable for horizontal perturbations. The azimuthal angular change is larger, for both horizontal perturbations (0.3° tilt) and depth perturbations (14° tilt).

An error in a *FLIP* slant range also translates into an array positional error. An error which increases the slant range moves *FLIP* away from the transponder and the array closer. It also induces a tilt in the array making the bottom closer to the no-error position than the top, with a corresponding decrease in RMS error from the top to bottom of the array. Table 2.2 shows the results of the simulation for +25 m errors in the three transponder slant ranges to *FLIP*. A transponder slant range error δ_s before iteration creates a translation error:

$$T_s = h - \sqrt{h^2 - 2\delta_s s - \delta_s^2}$$

where h and s are defined above. An error δ_s of +25 m in the red transponder slant range yields a translation error T_s of 62.3 m prior to iteration.

These simulations quantify the mapping from slant ranges to xy positions. The adjustment direction is dictated by the measurement direction (horizontal range direction) not the model parameters (xy directions) nor the error direction. The positions of *FLIP* and the array are more sensitive to errors in transponder depth and *FLIP* slant range than to errors in transponder horizontal position. This sensitivity is attributed to the constraint of fixed array depth (negligible measurement errors) necessitating an assignment of the error to the horizontal projection. These errors are magnified and dispersed across the array. It was this dispersion which was used as a criteria for convergence during the transponder depth iteration.

2.5. DATA ANALYSIS

The motions of *FLIP* and the array are analyzed to determine the navigation accuracy, the extent of movement and possible forcing functions driving the system. The data consisted of the GPS satellite positions acquired at *FLIP*, estimated *FLIP* positions spanning a period of 18 days with one hour samples, and estimated array element positions at a nominal depth of 850 m spanning a 24 hour period. The GPS positions acquired aboard *FLIP* provide an independent verification of the estimated *FLIP* positions derived using the least squares method (Figure 2.6). The GPS positions in latitude and longitude were converted to meters from the least squares origin by calculating the local radius of the earth as follows [Stacey, 1976]:

Perturbation	% change in horizontal range projection	array tilt	Translation from initial position	RMS error	% of original perturbation
meters		degrees	meters	meters	
<i>FLIP and Array Position with Errors in Transponder Positions:</i>					
Red X+25	0.7780	0.000	15.802	7.11	28.4
Grn	-0.3095				
Blu	-0.2940				
Red X+25	0.0640	0.000	1.498	0.78	3.1
Grn X+25	-0.0550				
Blu	0.0049				
Red X+25	0.3333	0.000	14.161	6.45	25.8
Grn	0.2832				
Blu X+25	-0.5463				
Red Y+25	-0.3663	0.000	7.540	3.83	15.3
Grn	0.1708				
Blu	0.1198				
Red Y+25	-0.3880	0.000	15.849	8.73	34.9
Grn Y+25	0.6636				
Blu	-0.3567				
Red Y+25	0.2627	0.000	11.149	5.01	20.0
Grn	0.2223				
Blu Y+25	-0.4304				
Red Z+25	-1.8163	0.483	37.199	18.13, 13.48	72.5, 53.9
Grn	0.7907				
Blu	0.6567				
Red Z+25	0.8112	0.375	29.320	16.63, 12.39	66.5, 49.6
Grn Z+25	-1.2156				
Blu	0.6022				
Red Z+25	0.7076	0.382	30.631	14.46, 10.76	57.8, 43.0
Grn	0.6311				
Blu Z+25	-1.1915				
<i>FLIP and Array Positions with Errors in FLIP Slant Ranges:</i>					
Red +25	2.0453	0.424	41.936	19.04, 15.73	76.2, 62.9
Grn	-0.8346				
Blu	-0.7543				
Red +25	-0.8450	0.315	33.396	18.28, 15.20	73.1, 60.8
Grn +25	1.3848				
Blu	-0.7236				
Red +25	-0.7432	0.315	34.034	16.08, 13.51	64.3, 54.0
Red +25	-0.7432	0.315	34.034	16.08, 13.51	64.3, 54.0
Grn +25	-0.7054				
Blu +25	1.3250				

Table 2.2 Navigation error simulations.

$$x = r_p \delta(lat), \quad y = r_p \cos(lat) \delta(long)$$

$$r_p = a (1 - f \sin^2(lat)), \quad f = \frac{a - c}{a}$$

where x is the E-W distance, y is the N-S distance, r_p is the earth's radius at the position latitude, $\delta(lat)$ is the difference in latitude between the position and the origin, $\delta(long)$ is the difference in longitude, lat is the latitude of the position, a is the earth's equatorial radius and c is the earth's polar radius. The observed 10 m RMS deviation between the GPS and navigated *FLIP* positions is reassuring. *FLIP*

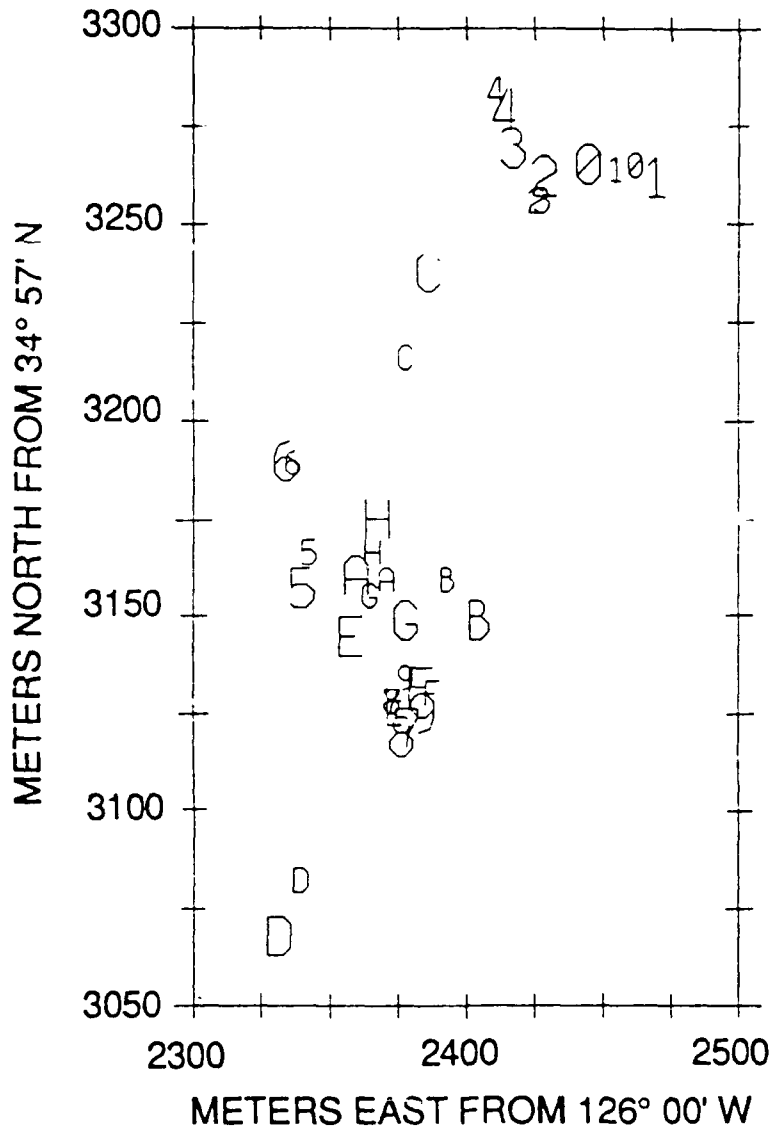


Figure 2.6 Comparison of GPS satellite and acoustic navigation. *FLIP* GPS positions are compared to those estimated by the least squares navigation. The large symbols represent the GPS positions while the corresponding small symbols represent the estimated *FLIP* positions. A bias correction, attributed to drift of the transponders during deployment, of 24.5 m was added to the NS estimated positions and 1.2 m to the EW estimated positions. The RMS difference between GPS and acoustic navigation positions is approximately 10 m.

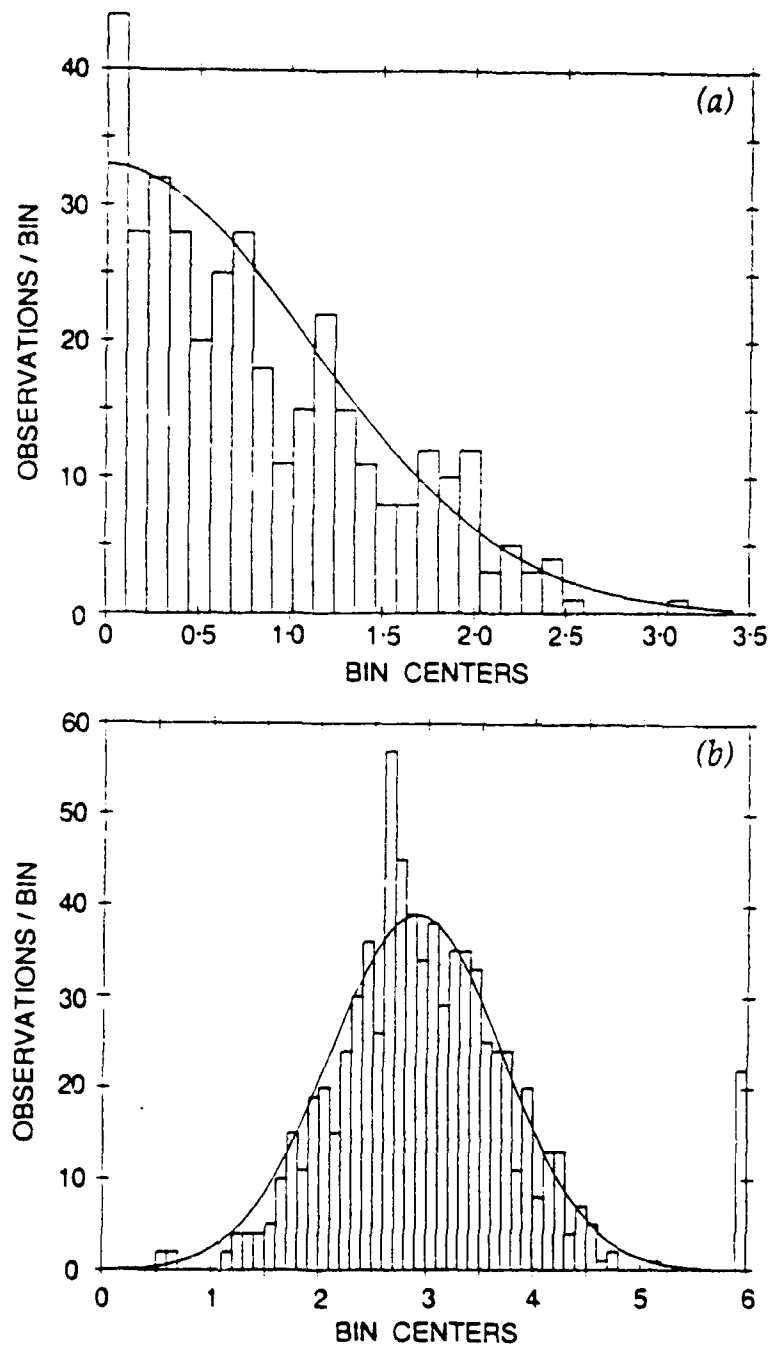


Figure 2.7 Error distributions. The error distributions shown for (a) *FLIP* and (b) array navigation receiver #8 are independent as illustrated by a runs test and gaussian at a 0.05 level of significance. The high transponder errors shown in the 6 m bin of (b) are due to transponder detection of multipath propagation.

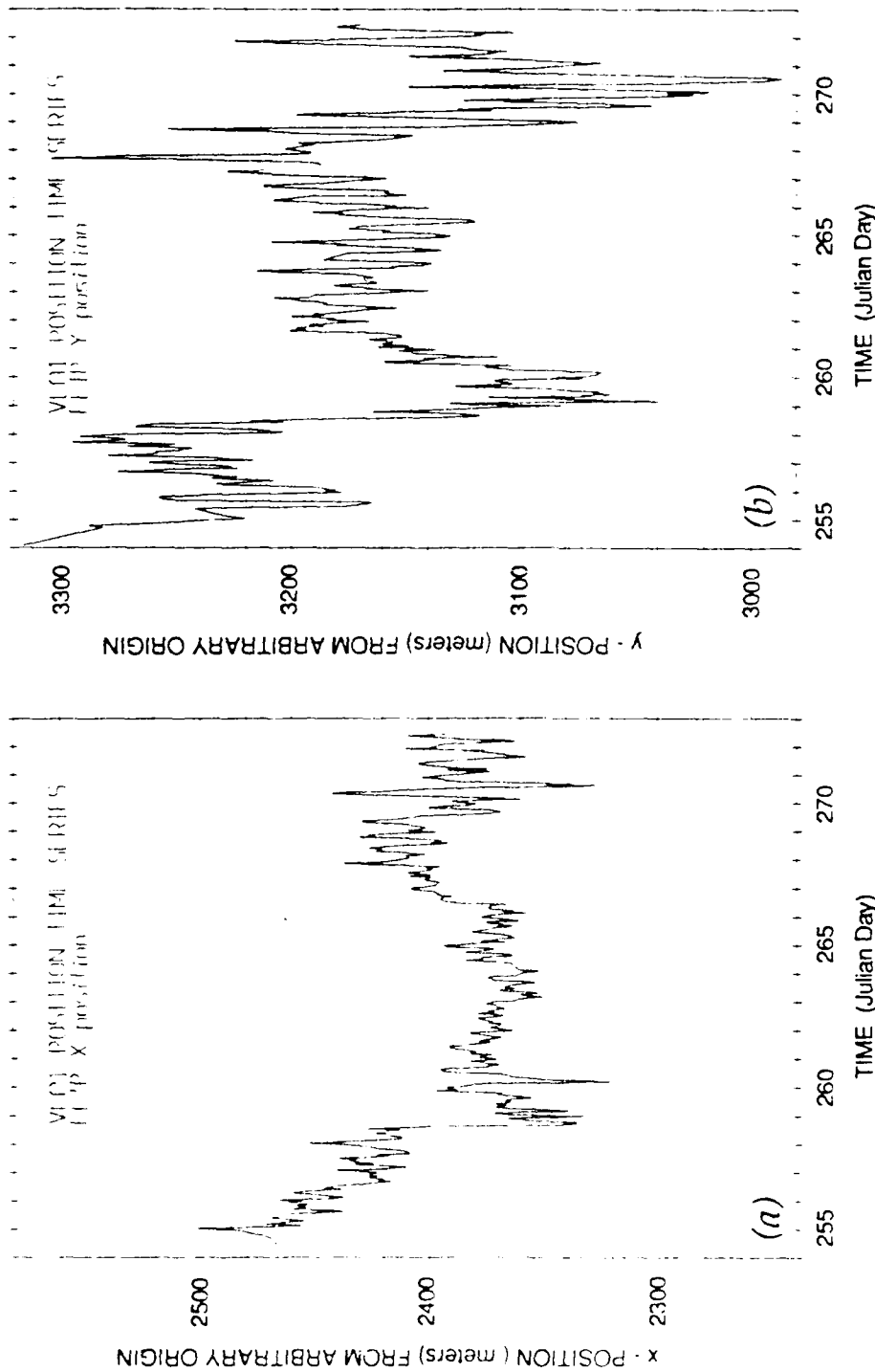


Figure 2.8 FLP position time series. The FLP positions are estimated approximately every hour and plotted over the 18 day experiment. The low frequency oscillations are wind induced motion while the half day cycles are caused by the tides.

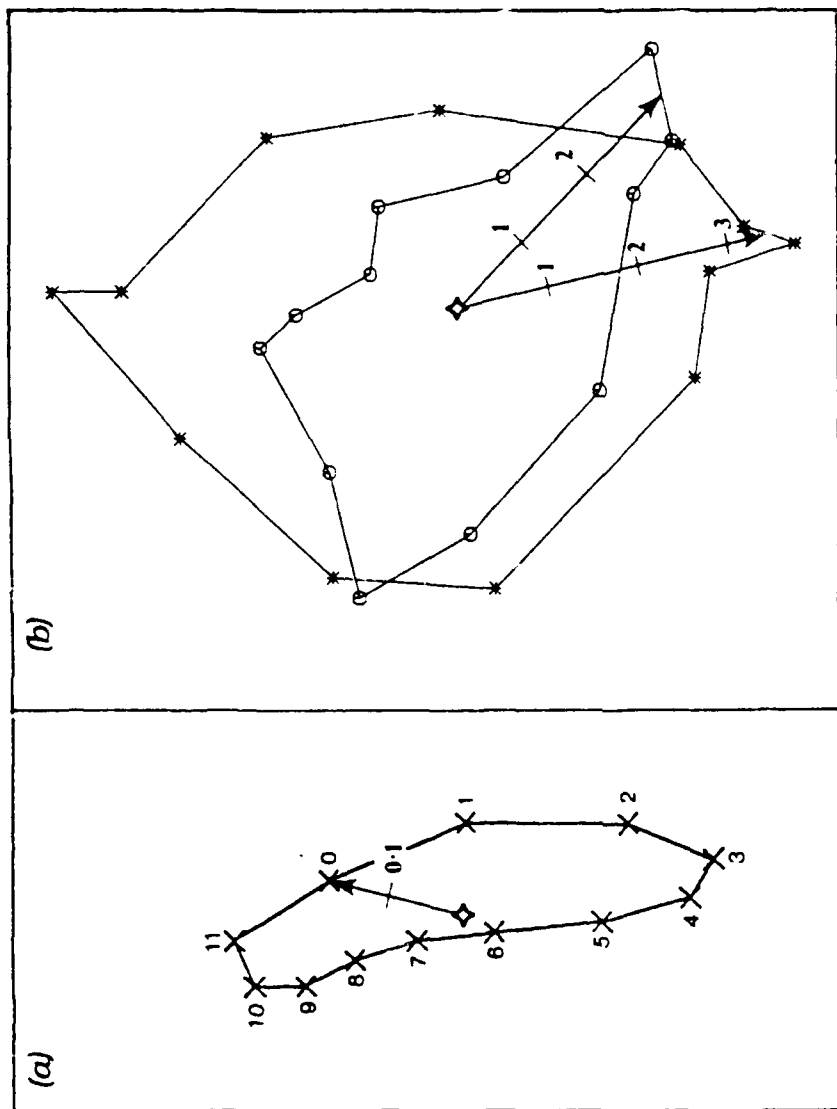


Figure 2.9 Tidal current ellipse. a) The current ellipse estimated from *FLIP* positions was calculated by finite differencing the 18 day time series, low pass filtering the resulting hourly estimates and then averaging 12 hour segments. The tips of the current vectors were plotted from a common origin every hour. The 0 GMT vector is marked in cm/s. b) Current meter data collected from *FLIP* represents 12 hour segment averages (o) over 13 days at 43 m and (*) over 20 days at 90 m. Mean velocities of 7.5 cm/s E, 0.64 cm/s N at the 43 m site and 7.2 cm/s E, -0.91 cm/s N at the 90 m site were removed.

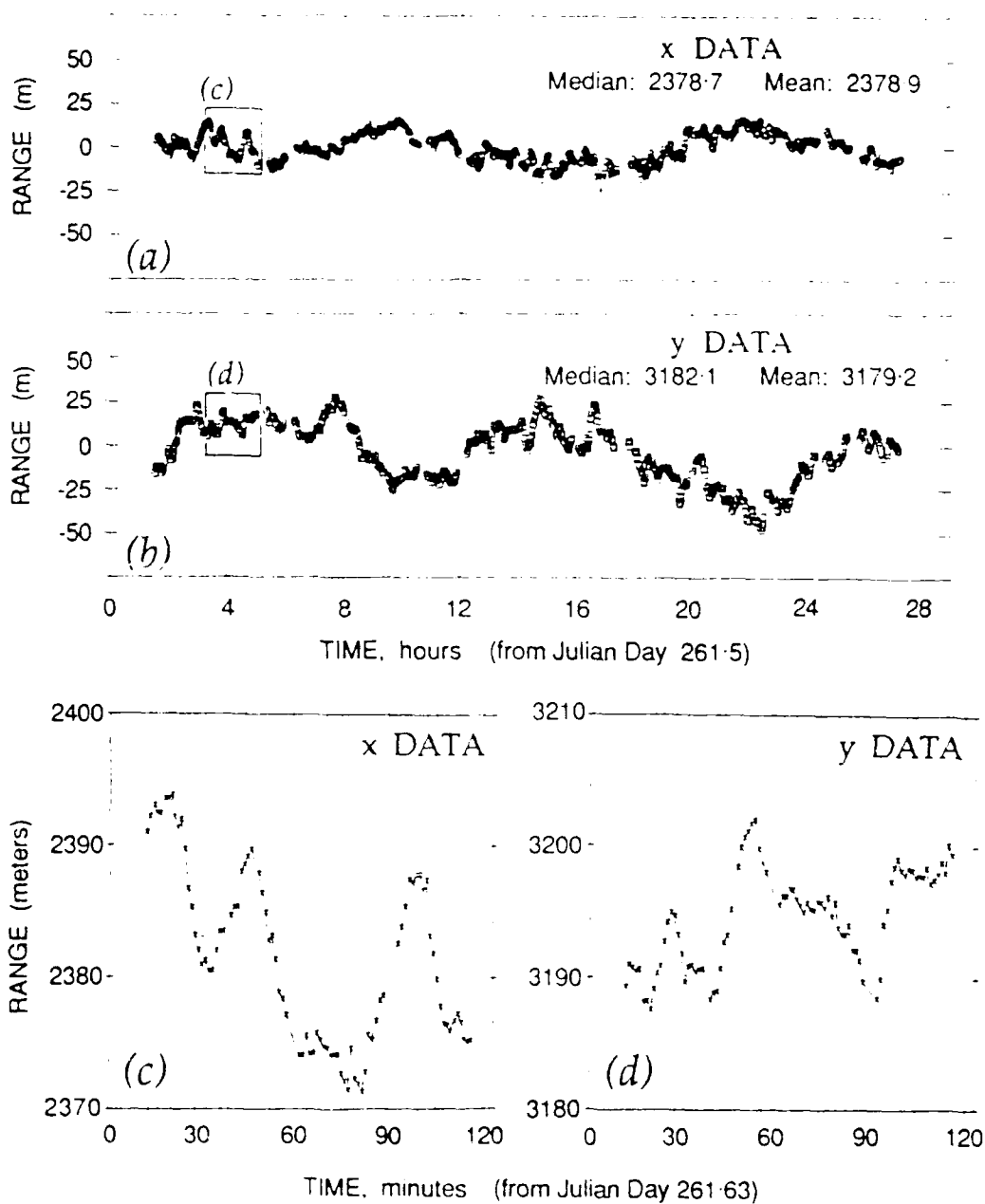


Figure 2.10 Array position time series. The estimated positions for the array section 8 navigation receiver are plotted relative their the median value. In (a) data increases toward the E, and in (b) toward the N. The low frequency oscillations are caused by tidal forces, and the higher frequency oscillations are caused by the internal waves or surface motion. The area identified by a box in (a) and (b) is expanded in (c) and (d) to illustrate this high frequency motion.

positional errors are independent and distributed normally at a χ^2 0.05 level of significance with zero mean and a standard deviation of 1.1 m. Array positional errors may deviate from a normal distribution depending on the nature of the transponder and receiver errors, however considering a receiver with low errors, a gaussian distribution of 2.9 m mean and 0.81 m standard deviation may be compared at a 0.05 level of significance. Receiver detection threshold mismatch, tuned filter drift, sound speed errors and errors in the *FLIP* position, as described earlier contribute to the mean. *FLIP* and array error distributions are shown in Figure 2.7.

The motion of *FLIP* (Figure 2.8) is primarily controlled by the local wind field, the tides and the tension on the mooring lines. The low frequency movement of *FLIP* is driven by the local wind, primarily from the north during the entire experiment. The wind speed has a high negative correlation with *FLIP* N-S positions and to a lesser correlation with *FLIP* E-W positions. At 35° N latitude the tidal cycle is semi-diurnal and appears as a prominent component in the *FLIP* time series. The tidal component in the E-W displacement lags 2 hours behind the N-S component producing a clockwise rotation. This rotation is also seen in the calculated tidal velocity ellipse (Figure 2.9) which lags the displacement by 90°. The tidal velocity ellipse, which includes contributions from both the barotropic and baroclinic modes, is comparable to simultaneous estimates of the current field recorded by current meters deployed at 50 m and 100 m below the water surface from *FLIP*. Although the current meter measurements are relative to *FLIP*, the tidal component is four times as strong as the constrained *FLIP* component and leads in phase due to *FLIP*'s massive structure and the mooring line constraints.

The motion of the array (Figure 2.10) is controlled by the tides, the motion of *FLIP*, and possibly by internal waves or higher frequency surface motion that is unresolved in the *FLIP* data set. The longest period movement of the array was on the order of days and was driven by *FLIP*'s response to the wind. This is inferred by the fact that the top array position was normally within a 30 m horizontal slant range of *FLIP* which traveled over 300 m during the 18 days (within 20 m in Figure 2.12). The tidal cycle is evident as a 12 hour oscillation in the 24 hour time series and as the 0.083 cycles/hour peak in the spectrum (Figure 2.11).

Higher frequency array oscillations appear in the expanded time series in Figure 2.10 c) and d), but are not stationary over the 24 hours and all but disappear from the spectrum during the averaging process. Although the sample to sample motion of the array is on the same order as the errors, the errors are independent and gaussian, therefore, we believe the fluctuations which occur with periods from 15 or 20 minutes to 2 hours are due to array motion. Modeling the array as a simple pendulum where the center of mass is derived from four component parts (uplink wire, array, kevlar and weights), the natural period of oscillation is just over one minute. The damped natural period for a velocity of 5 cm/s is seven minutes with a damping coefficient of slightly less than critical. Therefore, the high frequency motions must be due to environmental forcing functions. We believe it to be a combination of two processes: the coupling of the array to the surface and the array response to low order modes of the internal wave field. The motions whose periods are from tens of minutes to many hours (Väsälä frequency in the N. Pacific is about 20 minutes near the surface) and whose horizontal velocities of 1-2 cm/s are reasonable for a constrained internal wave response [Garrett and Munk, 1979] where typically horizontal currents are about 5 cm/s and horizontal current spectra is dominated by the lower order modes [Pinkel, 1989]. The motion spectrum does not show a peak at the local inertial frequency [Munk, 1981] nor an ω^{-2} energy

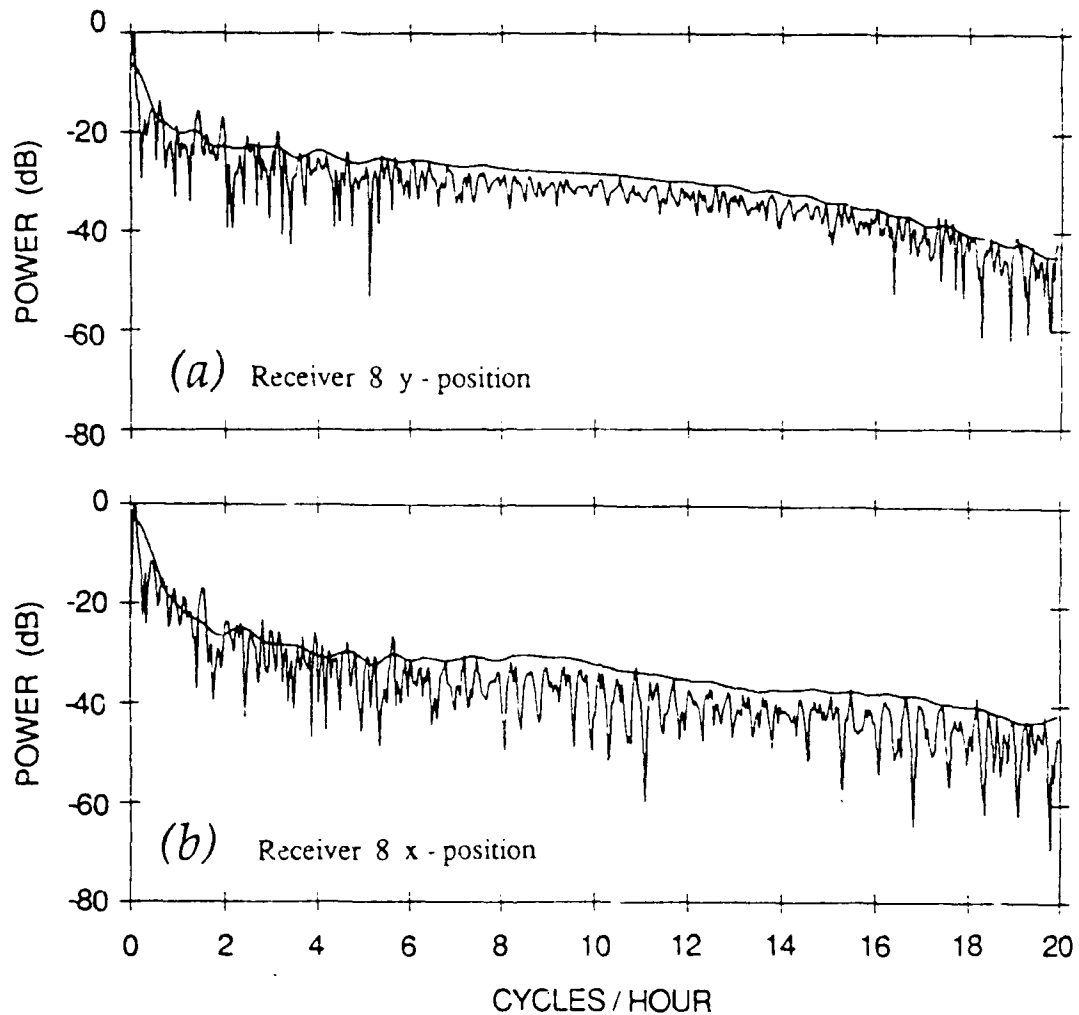


Figure 2.11 Spectrum of array motion. For receiver (a) x -position and (b) y -position, the smooth curve is an averaged 1024-pt spectrum of 15, 50% overlapped, Kaiser-Bessel windowed ($\alpha=2.5$) 128 point time series plotted on a relative scale. A single spectrum was computed similarly over the entire time series and plotted on the same relative scale with 0.039 cycles/hour resolution for more accurate identification of the narrowband spectral components.

dependency [Hu and Niiler, 1987] between the inertial frequency (0.048 cycles/hours) and the Väisälä frequency common in internal wave energy spectra. This characteristic shape is apparently filled in by the coupled response to surface generated motions.

The array shape during the first hour plotted in Figure 2.10 c) and d) is illustrated in Figure 2.12. The array is nearly straight much of the time with a maximum deviation of less than 5 m across the 900 m aperture. The horizontal deformation in the figure has been exaggerated for clarity, extending 50 m in the horizontal compared to 1600 m in the vertical. It is apparent that the array exhibits a more active response (presumably due to internal waves) than *FLIP* by examining the extent of *FLIP* motion compared to that of the array during the same time period. The array moves over four times the EW distance covered by *FLIP* during the hour plotted in Figure 2.12.

2.6. CONCLUSIONS

The least squares method was implemented to convert measured travel time data to spatial positions for *FLIP* and a 900 m vertical array by assuming a harmonic sound speed and normally distributed errors. Navigated *FLIP* positions (mean = 0.5 m, $\sigma = 1.1$ m) agree with positions obtained from GPS satellite navigation to within an RMS error of 10 m. A mean error as small as 2 m with a standard deviation of 0.8 m was obtained for array element position, however each receiver displayed a unique error distribution presumably due to variations in the array detectors. Array positions were found to be particularly sensitive to errors in *FLIP* position and transponder depth. This was demonstrated by simulation to be a result of the optimization constraints. Iteration of array depths and incorporation of a more accurate sound speed correction has shown promising preliminary results by reducing the mean RMS array element error to less than one meter, while leaving the estimated positions within 0.2 meters of the positions presented here. The navigated positions are tied to an absolute frame of reference using transponder GPS locations and the absolute positions are substantiated by the GPS positions at *FLIP* and the high negative correlation between *FLIP*'s N-S component and the wind speed. *FLIP*'s position was driven by the winds and tides but was constrained to approximately a 300 m range by a 3-point mooring. The array position was driven by tidal motions at a semi-diurnal period and apparently by internal waves and coupled surface wave motion at higher frequencies. Array high frequency motions were up to a factor of four larger than *FLIP* motions although the array normally maintained a vertical orientation to within a tilt angle of 2 degrees and remained within a 30 m range of *FLIP*.

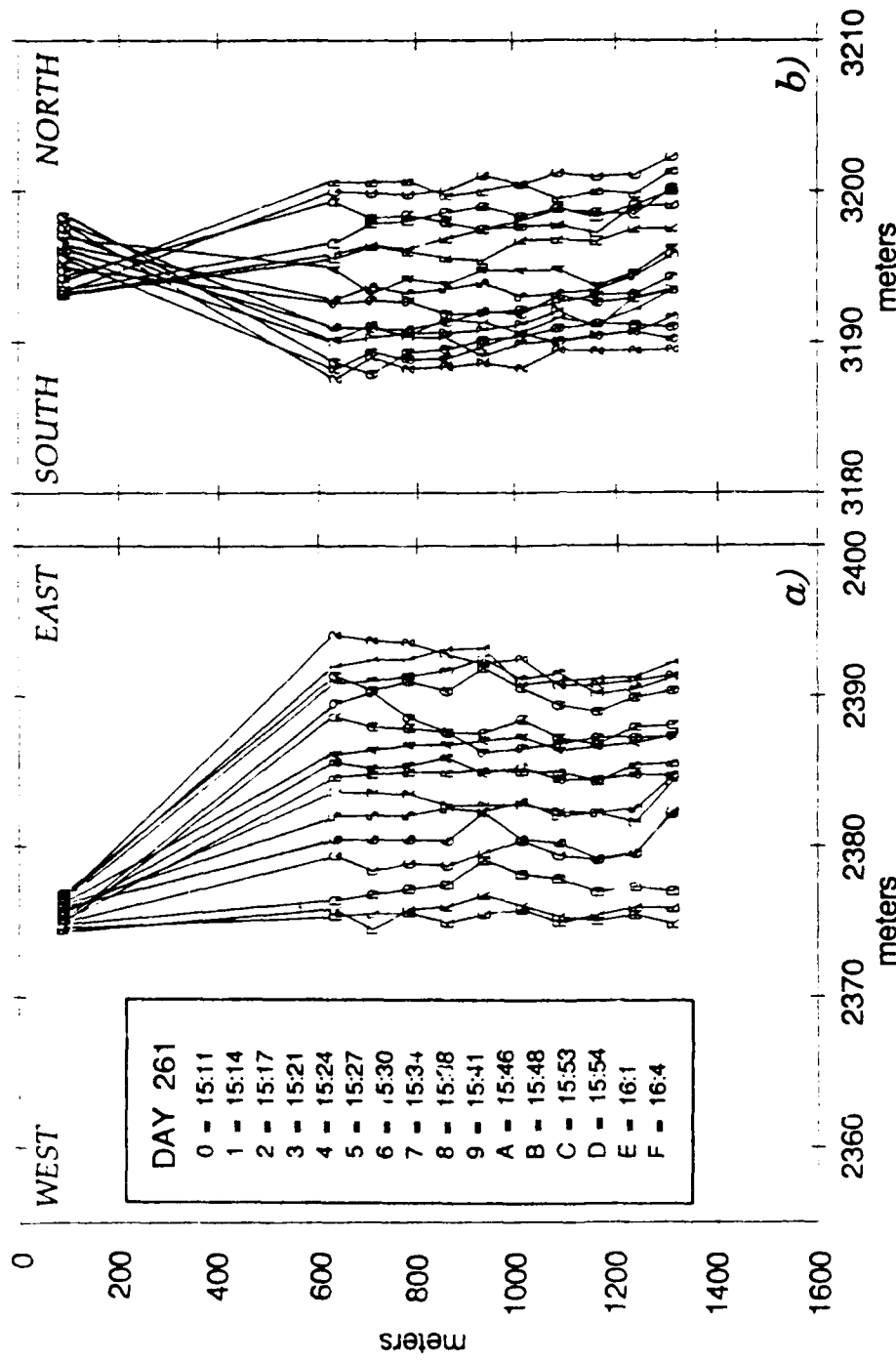


Figure 2.12 Array shape. The positions of the 10 deepest navigation receivers are shown over a one hour interval. The top two receiver positions were deleted due to their large errors. The two views are (a) East-West vs. depth, and (b) North-South vs. depth. The array maintains a vertical attitude over most of the time series. This is a subset of the data shown in Figure 2.10c and d and reveals that the array motion is greater than the *FLIP* motion during the same time period.

Chapter 3

ON ARRAY PERFORMANCE: A METHODOLOGY OF SYSTEM CALIBRATION AND NOISE IDENTIFICATION

3.1. ABSTRACT

The assumption that acoustic array measurements are a true reflection of the oceanic noise field can lead to misinterpretation of the data collected. Characterization of the array self noise levels and knowledge of individual element amplitude and phase responses are required to assess the results with confidence. In recent years emphasis on low frequencies and high resolution has led to the development of large aperture arrays with many elements. Establishing individual element calibrations and system noise levels of these arrays is not easily achieved in the laboratory environment due to facility and time constraints. Therefore, a series of tests are suggested to assist in the identification of system noise sources in such an array using a combination of oceanic ambient noise measurements and limited laboratory measurements. An *in-situ* element calibration is also discussed which compares magnitude estimates from two independent methods and generates a phase error curve. These methods are somewhat limited by incomplete knowledge of the environmental parameters and the statistical nature of ambient noise. Results are demonstrated using data collected by a large aperture vertical array deployed from the research platform *FLIP* in the NE Pacific.

3.2. INTRODUCTION

Acoustic arrays are commonly used to study many aspects of the ocean environment such as propagation effects, background noise, deep scattering layers, internal wave fields, and bottom characteristics to name a few. Interpretation of the data collected by such arrays must be viewed in terms of the array characteristics. All too often however, for data processing expediency, the characteristics of the array are assumed to be inconsequential and the effects of the instrumentation are not considered. This unrealistic attitude may lead to unsubstantiated conclusions.

The theoretical effect of element failure and random amplitude and phase errors on array sidelobe level has been examined by other investigators [Ramsdale and Howerton, 1980; Quazi and Nuttall, 1979; Quazi, 1982; Nuttall, 1979] and should there be element failures, algorithms for optimal reshading exist [Sherrill and Streit, 1987]. However, techniques for estimating these errors are not typically discussed.

Error sources must be realistically identified in order to separate the desired signal from the measurement. The measurement encompasses the hydrophone input modified by the channel response plus system noise. Our experience has been that catastrophic element failure occurs seldomly in real applications and post processing of array data must include criteria to identify elements with low performance, and evaluate their effect with respect to the application. The amplitude measurement of the incoming signal may be corrupted by a variety of factors including variable hydrophone sensitivities, inaccurate gain

amplifiers, quantizing errors, saltwater leakage, cable response, crosstalk, ground loops and digital switching noise. The phase measurement of the incoming signal may be modified by the element location, the phase response of electrical components and cables, crosstalk, switching noise and timing errors.

The purpose of this paper is to present a methodology for characterizing large aperture array system noise and estimating channel amplitude and phase responses using *in-situ* data. The methods recommended are applied to data collected by a 900 m, 120 channel acoustic array which was deployed vertically from the research platform *FLIP* in the Northeast Pacific during September 1987. Laboratory tests were minimized because of the large number of channels, the size of the array and time and facility constraints. Array system noise is characterized using ambient noise data collected during the experiment and when possible verified by subsystem laboratory tests. To estimate channel amplitude and phase errors, ambient noise and a series of narrowband signals transmitted from a known location with known source level were used.

3.3. SYSTEM DESCRIPTION

Array description with regard to system performance must address the physical and electrical attributes of the signal path. Utilizing *in-situ* data places the individual array elements in an almost constant temperature and pressure environment however the response of exposed components to the lower temperature and higher pressure must be considered. Physical layout of the signal path must also be considered for potential cross-talk, grounding and noise contamination. Design amplitude and phase characteristics for individual filters, amplifiers, cables, converters, etc. should be recorded. For coherent processing, the timebase in the array must be accurately calibrated and system delays accounted for.

The array addressed in this paper was composed of 120 elements separated physically into 12 hose sections each containing 10 elements spaced 7.5 meters apart with the first and last elements being 3.75 meters from either end of a hose. The sections were terminated at processor pressure cases which contain the electronics to process the data from the 10 physically closest elements. Therefore, electrically the elements in a single hose section were associated with two processors. The data stream originated at the hydrophones. It was amplified, filtered, converted to a digital signal, reformatted and finally transmitted to the surface where it was recorded on magnetic tape in real time. A detailed description of the entire array system is found in [Sotirin and Hildebrand, 1988].

One section of the low frequency signal path in the array is shown schematically in Figure 3.1. The power for the analog components is supplied by 12 individual section switching power supplies whose 5 VDC, 250 ma input is supplied by the 350 VDC, 4 A high power line running the length of the array. Array elements consisted of the transducer, preamplifier, anti-aliasing filter and differential line driver. The transducers were composed of two Aquadyne AQ-1 hydrophones wired in series to increase the sensitivity to a nominal -197 dB re 1 V/ μ Pa each with a 12 nF capacitance at mid ocean depths. The hydrophone output is amplified by a very low noise FET with 40 dB of fixed gain and a low frequency cutoff below 10 Hz. The preamplifier output is filtered by a phase matched, six pole, low pass filter with a corner frequency of 220 Hz and an in-band gain of 1. A differential line driver is used to transmit the bandpassed amplified signal to the

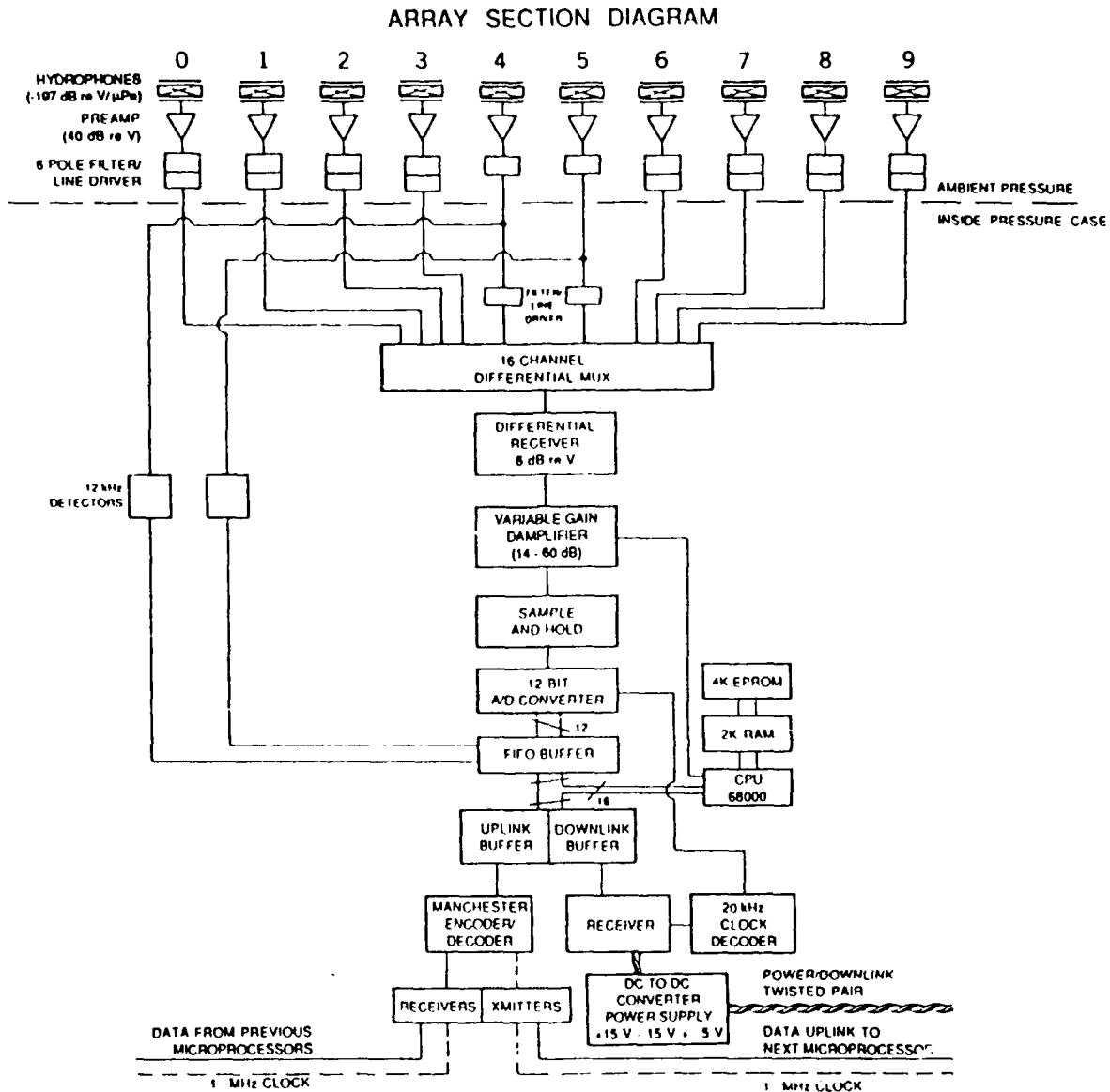


Figure 3.1 Array section schematic. The hydrophone signals are amplified and filtered at ambient temperature and pressure except for hydrophones 4 and 5 which are filtered within the processor pressure case to allow detection of 12 kHz navigation signals. The low frequency acoustic signals are multiplexed, amplified, captured by the sample and hold, and converted to digital format before being transmitted to the surface.

processor, a distance of up to 37.5 meters. Each processor receives signals from 10 elements, 5 from the hose section above and 5 from the hose section below. The two elements immediately adjacent to a processor are filtered within the processor pressure case rather than at the element to provide access to the 12 kHz acoustic information required for navigating the array [Sotirin and Hildebrand, 1989]. All array element components are subjected to ambient oceanic pressure.

Within the processor pressure case, the element inputs follow a common path. Each input is selected sequentially by a differential multiplexer, converted from differential to single-ended, amplified by a programmable variable gain amplifier (14 to 60 dB), then captured by a sample-and-hold circuit and converted to 12 bit digital form. In digital form the data is less susceptible to degradation by component response, noise, cross-talk and ground loops. The digital data integrity is monitored by several counters and synchronization words which are verified prior to processing. The timing for each processor is controlled by individual oscillators which are phase locked to a 1 MHz clock signal running the length of the array. Digital component delays (typically on the order of ns) are negligible at the 500 Hz (2 ms) data sampling rate. The sequential operation of the multiplexer imparts a deterministic phase shift of $\omega n \tau$ where ω is the frequency, n is the channel position (defined in Appendix A) and τ is the 0.2 ms sample frequency.

3.4. LABORATORY CALIBRATION

Laboratory tests were minimized due to lack of facilities in which an environmentally controlled system test could be executed and time constraints. Tests were performed under one atmosphere pressure and room temperature with no special electrical shielding. Nominal element calibration was conducted during array construction and the self noise tests were conducted for a 10 element array subsection. Typically, these tests are completed prior to the experiment to verify minimum operating conditions. However, during the September 1987 experiment, strict time constraints delayed completion of the tests until after the experiment.

3.4.1. Nominal Element Calibration

Each element was tested individually as it was constructed and the array hose section assembled. Within a hose section are the hydrophones, preamplifiers, filters and line drivers for 10 elements. As these electronics are subjected to ambient ocean pressures during deployment, the individual components used were pressure soaked and cycled to 8000 psi prior to fabrication. Typical hydrophone amplitude, phase and impedance responses were measured with respect to temperature and pressure [Lastinger, 1982]. Before the array is pulled into the urethane hose section, several tests were conducted to measure the pass band level, and -3 dB cutoff frequencies of the filters. Data for this test is presented in Appendix A. The pass band level was measured at 100 Hz by injecting a sinusoid electronically at the hydrophone input and monitoring the results at the differential line driver output. The signal is amplified by 40 dB in the preamplifier and received differentially, adding an additional 6 dB. The noise in this preamplifier has been measured to be approximately 30 dB re 1 μ Pa at 100 Hz in a shielded controlled environment. The level recorded is in dB referenced to the signal injected amplified by 46 dB, that is, the setup is designed to output a measurement

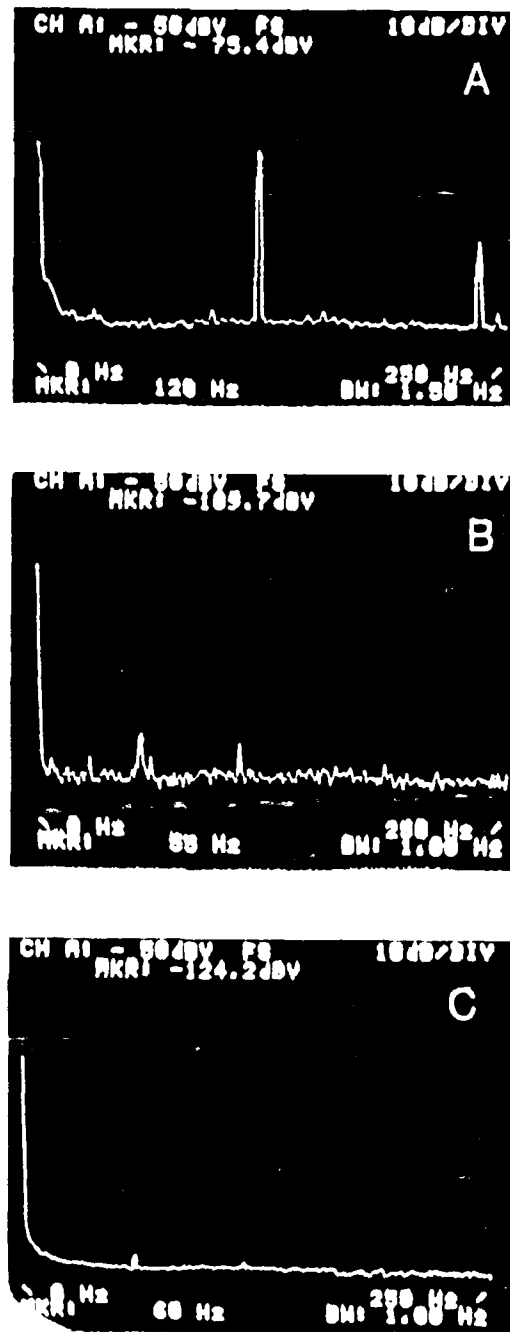


Figure 3.2 Power supply spectra. The photo of a spectrum analyzer window displays the spectra of (a) the DC-to-DC converter 5 VDC input, (b) the 5 VDC DC-to-DC output, and (c) the ± 15 VDC DC-to-DC output. Narrowband signals other than line frequency harmonics were intermittent.

of 0.0 dB for this test. All elements exhibit a pass band level at 100 Hz within ± 1 dB of the design level except the top element and the bottom element which are within 1.2 dB.

The high frequency cutoff was designed to accommodate a 500 Hz sampling frequency. The -3 dB cutoff frequency was measured by increasing the frequency of the signal injected as described above and monitoring the same output. Two elements in each section are low pass filtered after the signal is received by the processor to allow detection of the 12 kHz navigation pulses. These elements have an expected -3 dB cutoff frequency at 15 kHz. The remaining elements roll off at about 220 Hz. The low frequency cut off is about 5 Hz for all elements.

The operating environment at each individual element during a sea test is stable in temperature (at 3° C) and pressure. The element components should be invariant when subjected to this environment. The components most likely to change would be the capacitors. Preliminary pressure and temperature tests were conducted during which the capacitors were found to be virtually invariant over a pressure range of 0 to 6000 psi but capacitance values decreased with temperature. A decrease in capacitance increases the high frequency cutoff, and increases the potential for aliasing problems.

3.4.2. Electrical Self Noise Level

Laboratory tests conducted to determine the level of the electronic noise floor in the array were delayed until after the experiment. These tests consisted of decoupling the inputs to various stages of the signal path from the array and changing specific control options to ascertain the origin and amplitude of the array self noise. No special precautions were taken to insure the noise integrity of the array in the lab environment, therefore the data was subjected to a variety of additional noise sources which would not be encountered in an ocean environment. The narrow band signals apparent in the spectral plots are not stationary and are normally identified with an outside source such as machinery magnetostriction components and ship radar [Anderson, 1989].

The tests were conducted using 10 representative array elements. One array hose section was removed from the urethane tube and the hydrophone inputs to the preamplifiers were replaced by equivalent capacitors (channels 6-15). These 10 channels are addressed by two processors; processor 1 (P1) monitors channels 1-10, processor 2 (P2) monitors channels 11-20. The ± 15 volt power leads were removed from the elements whose phones were still connected (channels 1-5 and 16-20). The tests were conducted by recording data utilizing the same system setup as was used at sea [Sotirin and Brand, 1988]. The plots shown in Figures 3.3 and 3.4 are generated by incoherently averaging 46 FFT's (Kaiser-Bessel window, $\alpha = 2.5$) with 50% overlap which estimates the spectra within a confidence interval of +1.4 dB to -1.2 dB [Bendat and Piersol, 1971]. Increasing the number of averages to generate a confidence interval between +0.5 and -0.4 did not appreciably alter any of the spectra levels or character. The magnitude is normalized to a 1 Hz band and does not account for the array gain amplification but treats the array signal as a black box input at the analog-to-digital converter (ADC) to facilitate comparison between the gain settings. The actual noise levels initiated at the element are amplified by the fixed gain stage of 46 dB and by the variable gain stage which is notated on the individual plots. These levels are on the order of a microvolt making it extremely difficult to insure absolute repeatability in the tests within the

lab environment available.

The noise levels at various stages in the analog power circuit and data stream were measured. The power for the analog circuits must be regulated and free of harmonic content. In this array, the main array power supply was located aboard *FLIP* and each processor case contained two switching DC-to-DC converters, one at a +5 VDC output and the other at ± 15 VDC output. Frequency response for the input and two outputs are shown in Figure 3.2. The input to the converters has a significant 120 Hz level (-75.4 dBv/ $\sqrt{\text{Hz}}$) which is filtered and appears in the 5 VDC output at a low level (about -112 dBv/ $\sqrt{\text{Hz}}$); there are other intermittent narrow band peaks at 55 Hz and 6 Hz. There is also a 60 Hz signal at about -116 dBv/ $\sqrt{\text{Hz}}$. The noise level in the ± 15 volt power supply is quite flat with a 2 dB increase at 60 Hz to a -124.2 dBv level (Figure 3.2c). These narrow band levels are quite low and appear only intermittently in the low frequency self noise data. Contributors to the array self noise were identified by shorting the inputs to or bypassing stages. The spectra of the array system noise with the input to the variable gain stage shorted (see Figure 3.3f) was flat with an 8 or 9 mv variation at the ± 10 volt ADC indicating that no unexpected noise sources were active in this stage. The 12 bit ADC had a resolution of 4.8828 mv which when normalized over the system bandwidth of 250 Hz (23.98 dB) corresponds to a -70.2 dB level. There were two multiplexer modes, the scan on mode which samples each of 10 channels with a user selectable (5 kHz default) sampling frequency, and the scan off mode which samples only one channel. The noise contributed by the multiplexer and sample-and-hold amplifier (SHA) was measured by comparing the levels obtained with the input to the multiplexer for channel 8 (P1H2) hardwired to the differential receiver effectively bypassing the multiplexer, to those obtained using the same channel with the multiplexer operating in the scan off mode and during normal operation (scan on). Each exhibited the same spectral levels and characteristics indicating that no additional noise was injected at the multiplexer or SHA.

Although the data signals were driven differentially, there is the possibility of coupling common mode noise into the relatively low level analog data. The digital switching noise from the 1 MHz clock signal running the length of the array was of high enough level that it was not completely removed by the differential receivers (common mode rejection ratio of 80 dB). Clock noise is suspected in Figure 3.3 as spectrum levels tend to increase with wire length in the array (physical phone position from the processor) by as much as 15 dB. This noise was substantially decreased by the addition of a small 0.0153 μf capacitor at each of the multiplexer inputs which effectively shorts the inputs of the differential receiver at frequencies above about 10 kHz, indicating that it is high frequency noise generated in the array hose. As the variable gain is increased two distinct effects are noticeable. First, for a specific variable gain increase, the spectral levels are not amplified by the same amount channel to channel. Second, the relative spectral level increase in any particular channel does not coincide with the change in variable gain. Both of these effects could be attributed to high frequency noise being slew rate limited in the variable gain amplifier. Limiting the slew rate would effectively filter out the high frequency content and amplify only the low frequency portion, creating a gain discrepancy channel to channel and because slew rate increases as gain increases, more of the high frequency noise would be blocked, rectifying the discrepancies between channels as the gain is increased. These effects are shown in Figure 3.4 which displays the difference between channels 11 and 15 (farthest and closest respectively) and the channel 11 output for different variable gains. Ideally, as the variable gain is increased from 34 dB (top) to 54 dB

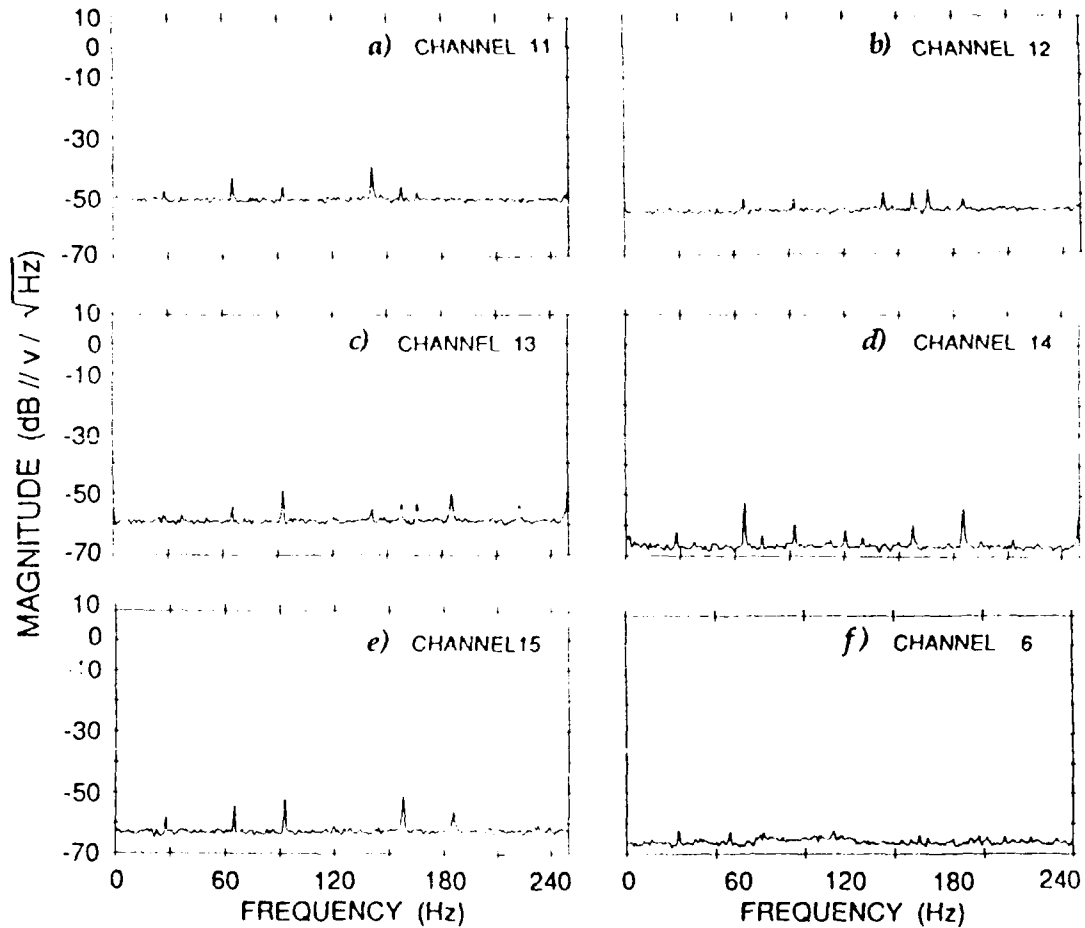


Figure 3.3 Common mode switching noise. The 1 MHz clock signal running the length of the array couples into the low level analog signals. This noise is suspected as the noise levels increase with increasing distance. In the figure, (a) Channel 11 transmits 33.75 m, (b) Channel 12 transmits 26.25 m, (c) Channel 13 transmits 18.75 m, (d) Channel 14 transmits 11.25 m, and (e) Channel 15 transmits 3.75 m. The final panel (f) shows the array output with the variable gain stage shorted.

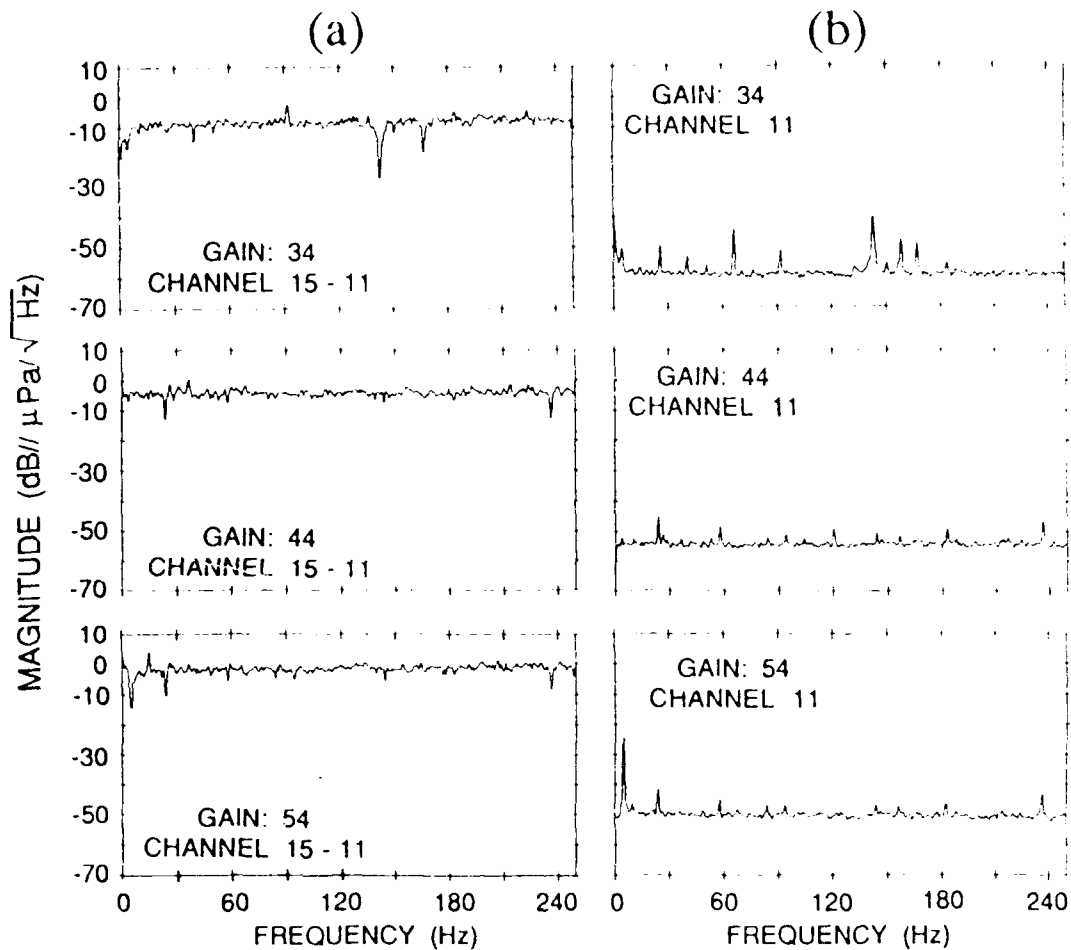


Figure 3.4 Channel gain difference. Slew rate limitation is suspected as a channel gain discrepancy correlates with transmit distance. The channel transmitting furthest (11) is compared to the closest channel (15). The difference between these channels (a) should ideally be zero at any gain setting. The variable gain stage was changed from 34 dB to 54 dB in 10 dB increments. The expected change in channel spectra level (b) is 10 dB for each increment however the actual measured change for channel 11 is about 5 dB.

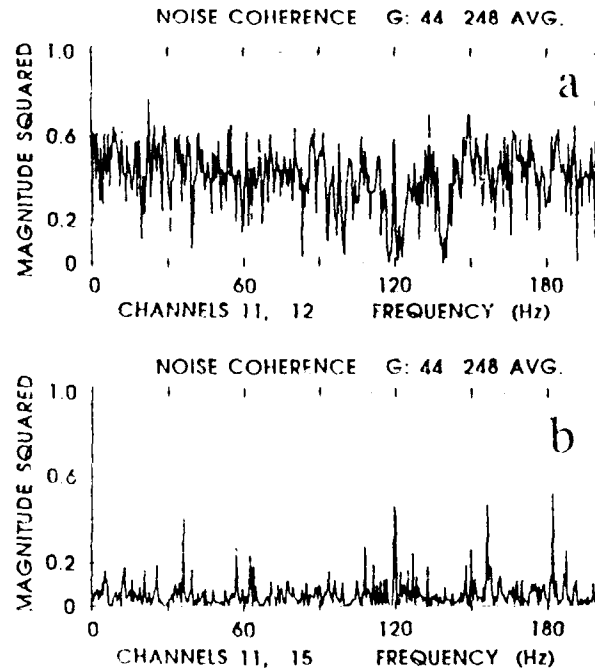


Figure 3.5 System noise coherence. The coupled noise shows a coherent structure across the array bandwidth. The top panel (a) displays the coherence between the channels at 33.75 m and at 26.25 m. The bottom panel (b) display the coherence between the channels at 33.75 m and at 3.75 m. Pair-wise coherence plots corroborate this result.

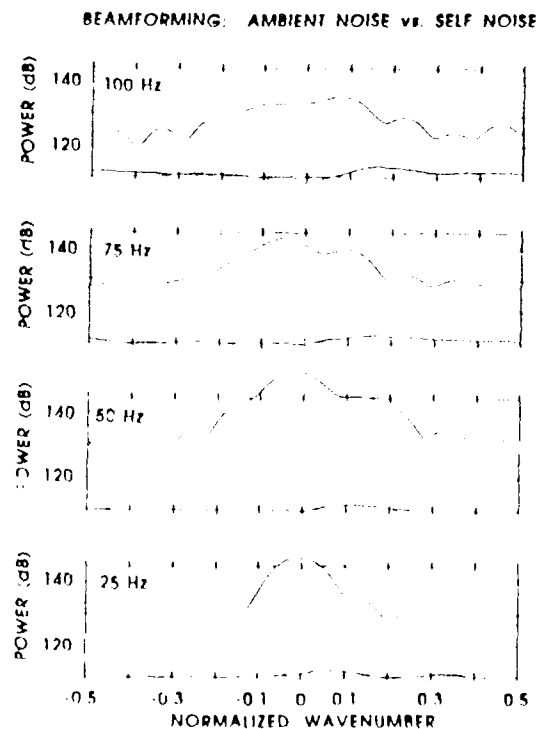


Figure 3.6 System noise directionality. The coherent noise is significant at only one or two channels per section in the array and does not affect the directionality noise levels which remain below that of the ambient noise.

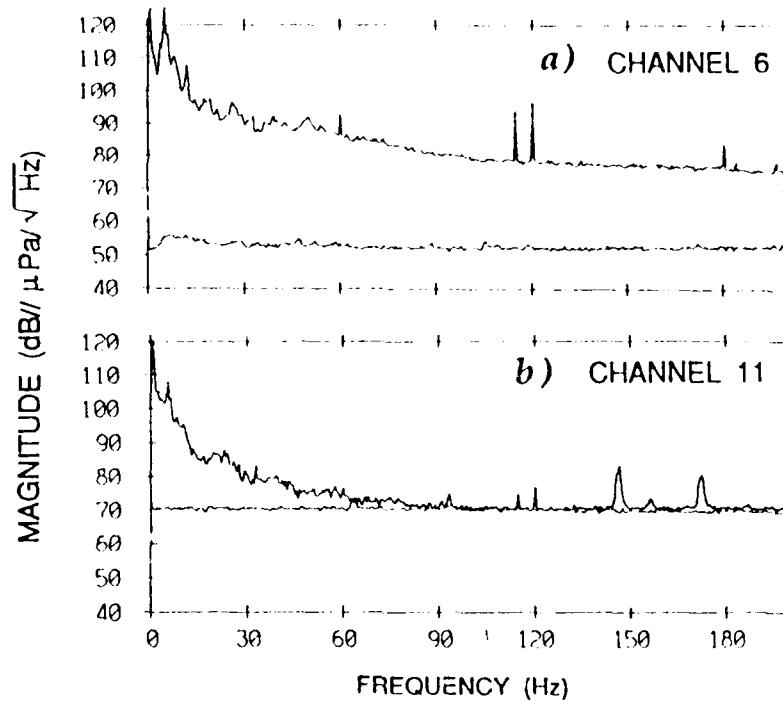


Figure 3.7 System noise spectral levels. The coherent noise spectral level is of concern as it approaches and possibly exceeds the ambient noise level. This level is dependent on the array gain setting, increasing as the gain decreases. The gain shown here is 34 dB; gain settings during the experiment averaged around 40 dB, with 34 dB used only during high wind conditions.

(bottom), the magnitudes in Figure 3.4a should always be 0 or at least constant, indicating that both channels are amplifying the signal by the same amount. This is the case only at a gain setting of 54 dB, where the slew rate filter effect would be strongest, eliminating more of the high frequency noise. The difference between channels increases as the gain and the slew rate limitations decrease. The second effect is observed by examining the change in magnitude for channel 11 (Figure 3.4b) as the gain increases. Changing the variable gain from 34 to 44 dB should produce a 10 dB increase in magnitude rather than the 4-5 dB increase shown for channel 1; although the effect is substantially less, there is an 15-20% reduction in effective gain in the closest channels as well.

This noise exhibits a coherent structure shown in Figure 3.5 which is effectively removed by the line filter capacitors. The high coherence effect is limited to only a few channels in the section and does not appear in the directionality plot of Figure 3.6. The beam levels are very consistent with no substantial increase in the broadside beam which is indicative of pervasive common mode noise. The array self noise levels at a relatively low array gain are compared (Figure 3.7) to corresponding measured ambient noise at the same gain settings. The quality of the high frequency data depends on the level of the incoming signal, the array variable gain setting and the channel position. The amount of degradation is elucidated in the following section.

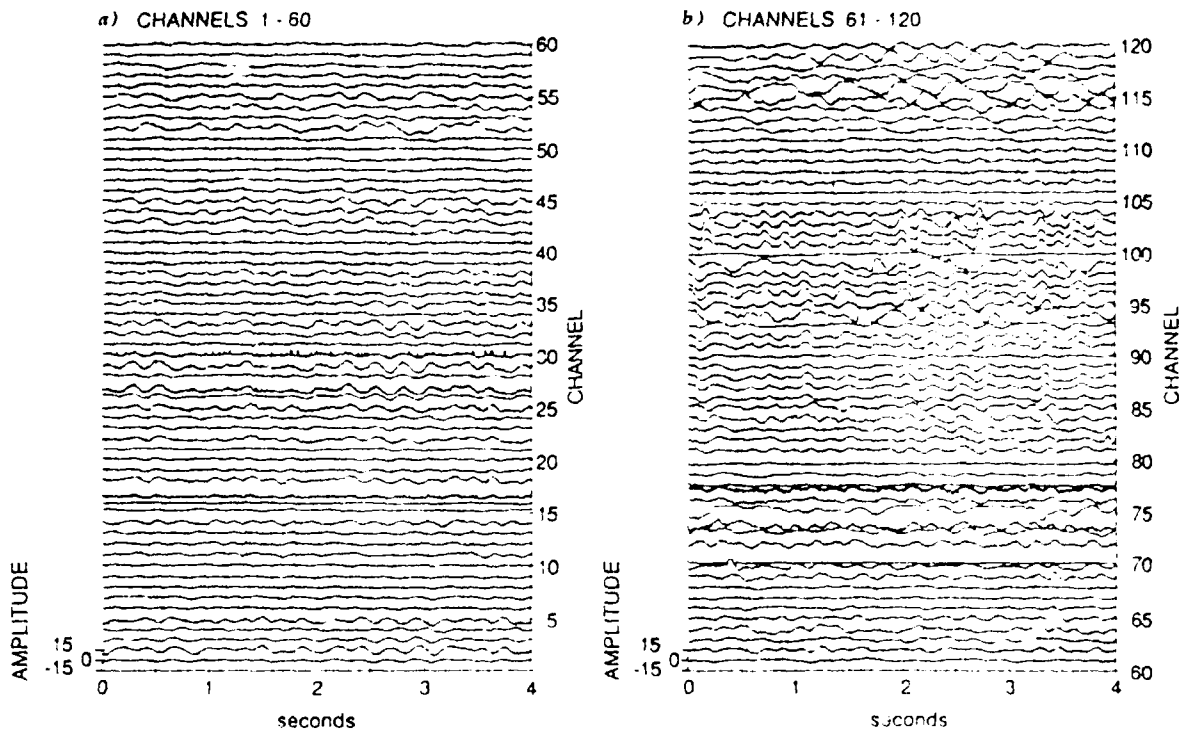


Figure 3.8 Time series. Two seconds of data is shown for 120 channels. Channel 1 is the deepest channel at about 1300 m. The amplitude is referenced to ± 10 VDC at the ADC.

3.5. PERFORMANCE INDICATORS

In-situ performance tests require a knowledge of the acoustic noise field used as a signal to enable identification of array system problems. Each test shows a different facet of array data characteristics and requires some interpretation.

3.5.1. Time Series

A 4 s time series of either the voltage (Figure 3.8) or power response of each channel provides insight into the signals received by the array, identifying biological disturbances, noise levels, and signal levels. It also insures that all sections of the array are telemetering, and clearly identifies certain types of occurrences such as dead channels (e.g. 71), insensitive channels (e.g. 21,100), high frequency glitches (e.g. 30, 77), saturation due to strum (e.g. 94, 99, 116), and saturation due to DC offsets (e.g. 75). Examination of an impulsive return during the experiment revealed a polarity reversal in some of the channels (indicated in Tables A.1 and A.2) which was subsequently corrected and is not shown in the figures presented here.

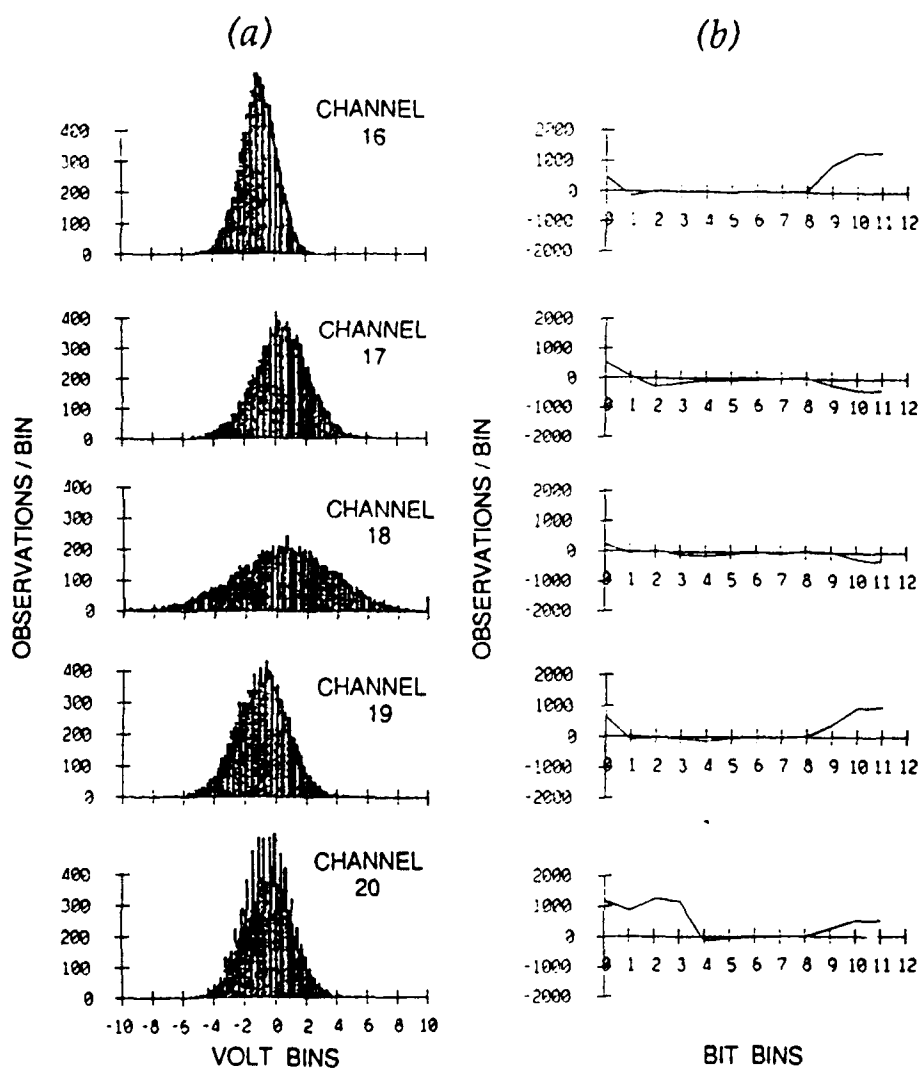


Figure 3.9 Time series and bit distribution. (a) The distribution for 16 s of the array element time series is calculated as a histogram with a bin width of 0.1 V. (b) The output of the ADC is an offset binary representation of the voltage. The array processors convert this to 2's complement samples. The 2's complement samples are used in the same process as the bit distribution simulations to generate the results shown here for the same 4096 samples used in the time series distribution.

3.5.2. Time Series Distribution

A histogram of the time series monitored by each channel indicates the voltage distribution of the signal being recorded. The distribution was calculated with 0.1 v bins over 16 s, and shows a Gaussian random process (left half of Figure 3.9). The variance of the distribution increases with gain and low frequency vibrations as in channel 18. The mean of the distribution corresponds to the DC offset of the channel (channel 16). The spiky character of channel 20 is an artifact of the software error discussed below.

3.5.3. Bit Distribution

The correct operation of the analog to digital converter (ADC) and some aspects of bit formatting and reformatting are verified by examining the distribution of each of the channel bits. If the ADC is correctly converting zero mean Gaussian random signals, the distribution of each bit representing the 2's complement digital signal should be high half of the time and low half of the time as the signal varies between positive and negative numbers, shown in Figure 3.10 by simulation. The simulations were implemented by generating a Gaussian random signal in volts with a different seed for each panel in Figure 3.10, clipping at ± 10 v (as the ADC does) and converting it to bit integer format before accumulating the high bits. The output format of the ADC's in the array was offset binary and the data was converted to 2's complement prior to the telemetry link. The conversion only requires that the most significant bit be complemented so the 2's complement representation is adequate for this investigation. The zero mean simulated signals have the expected distribution even in the event of clipping. A DC offset in the signal appears as a bias of the higher order bits in the distribution; the bias migrates to less significant bits with a decrease in the variance of the random signal, and the amplitude of the bias increases with the DC offset. The bit histogram of 4096 words telemetered by the array is shown in the right half of Figure 3.9 for 5 channels. The effect of a low amplitude signal (low variance) and negative DC offset in channel 16 (-0.81 V) is manifested as an increase in the occurrence of the high order bits. The distribution in Figure 3.10c simulates channel 16. The higher variance in channel 18 decreases the impact of the DC offset relative to channel 17. These results are corroborated by the time series and time series distribution data. The least significant 4 bits of the 10th channel (H0) in each section were contaminated by noise due to an error in the array software such that the data for H0 was logically OR'ed with the least significant four bits of the previous H8 data. The effect of this noise is shown in the distribution for channel 20. The least significant bits of all array channels also display a peculiar distribution. This is an indication of the switching noise level within the processor as it couples into the ADC and affects the more sensitive lower order bits (4.88 mv resolution). The lowest order bit is consistently affected decreasing the effective resolution of the system.

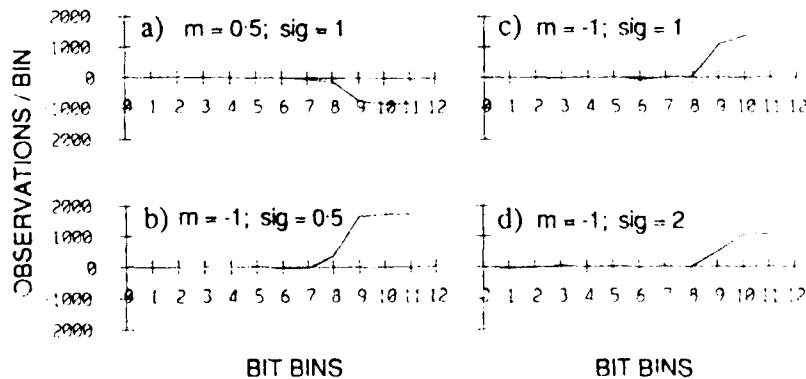


Figure 3.10 Bit distribution. The 2's complement samples are used in a process which records the number of times each bit is high in a 4096 sample series minus 2048. For a zero mean gaussian random process, this results in a near zero distribution for each bit. A non-zero mean process affects the most significant bits depending on the mean and standard deviation as seen by the simulations (a) mean = 0.5, standard deviation (σ) = 1, (b) mean = -1, σ = 0.5, (c) mean = -1, σ = 1, (d) mean = -1, σ = 2.

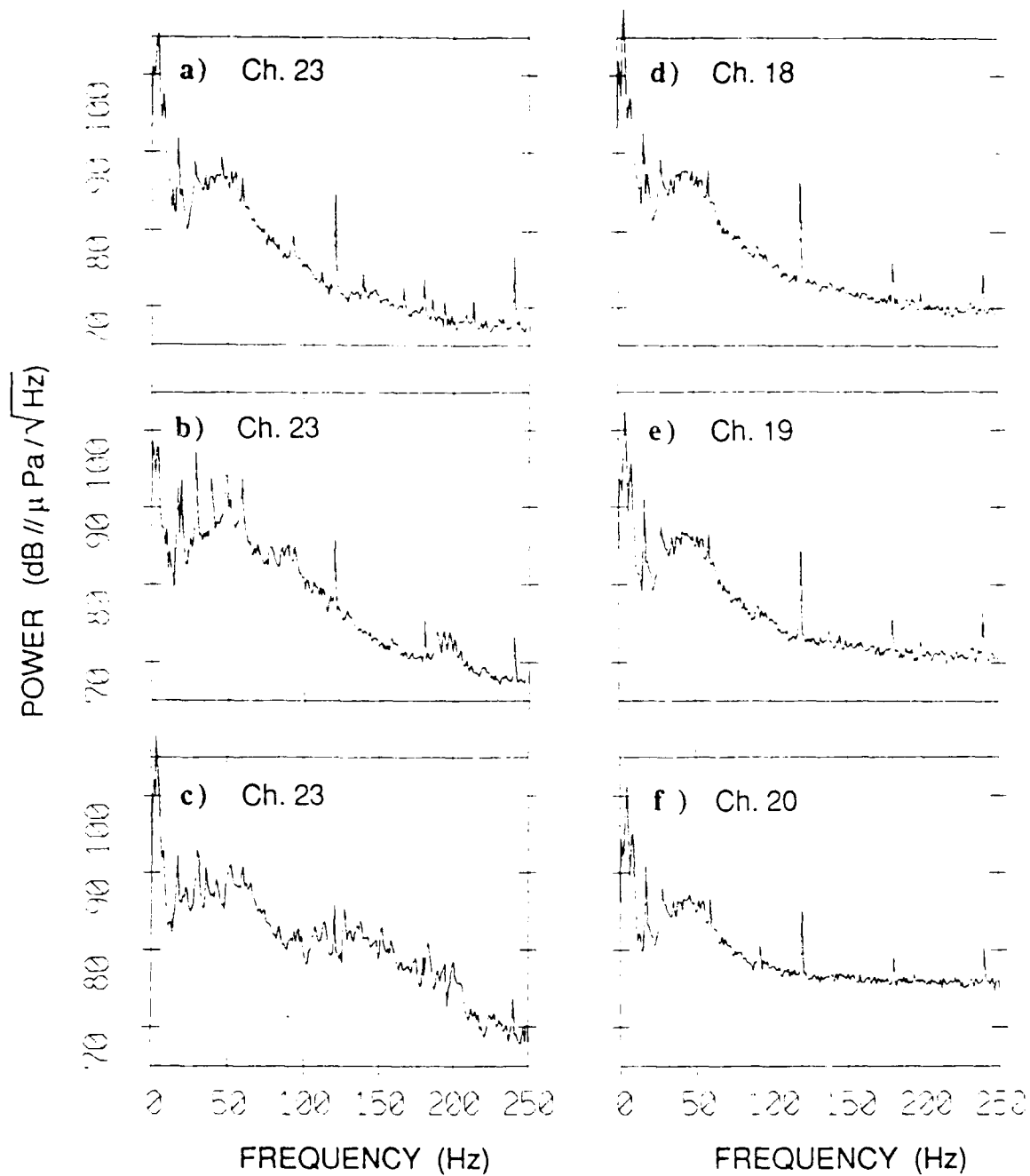


Figure 3.11 Power spectral density. The spectra were generated by incoherently averaging 15 8192-pt FFT of 50% overlapped, Kaiser-Bessel windowed ($\alpha=2.5$) time series. The data sequence was 2 minutes in length and the results were plotted as a 16 bin average yielding a 90% confidence interval of $+0.5/-0.4$ dB. The spectra show different facets of the ambient noise including (a) a typical array response, (b) local ship noise (low frequency) and a pseudo-random code transmission (200 Hz), (c) seismic profiler noise, (d, e and f) the effect of system noise on the high frequency response for channels furthest away (33.75 m) from the processor.

3.5.4. Power Spectral Density

The spectra illustrates a variety of characteristics of the array coupled with the acoustic noise field. To interpret array system noise, the acoustic noise field components must first be identified. The array is capable of resolving the frequency band between 10 and 220 Hz as discussed in Section II. The spectra shown in Figure 3.11 represent data taken at 4 different times to illustrate the variety of sources which contribute to the low frequency domain; within this band there are two major acoustic ambient noise contributors, ship generated noise and wind generated noise. A typical acoustic spectrum (Figure 3.11a) shows a broad hump due to shipping between 25 and 125 Hz at approximately 75 to 90 dB// $\mu\text{Pa}/\sqrt{\text{Hz}}$ which rolls off to about 70 dB// $\mu\text{Pa}/\sqrt{\text{Hz}}$ at the wind dominated high end of the spectrum. Noise due to array mechanical motion (strum) and biological sources is sometimes seen below 25 Hz. The close passage of a ship imparts tonal components to the low frequency end of the spectrum (b); a pseudo random coded signal is noticeable at 200 Hz. A seismic profiler operating off the coast of California appears periodically throughout the data set, degrading the ambient noise measurements above 100 Hz (c). Ambient noise source identification assists in selecting data which is not dominated by these processes such that system problems may be recognized. The 1 MHz clock switching noise discussed in the previous section is seen in panels d, e and f, where the panel f shows the signal from the hydrophone furthest away from the processor, and the higher frequency levels of this channel increase by 5 dB relative to the other channels, indicating that the system noise is interfering with the ambient noise measurements at the higher frequencies. The system noise is virtually white across the array frequency band (Figure 3.7) and the noise levels shown in Figure 3.11f do not affect the measurements above the 250 Hz level; e.g. channel 20 is capable of measuring acoustic levels above 76 dB// $\mu\text{Pa}/\sqrt{\text{Hz}}$. High levels are also seen for the closest hydrophones which are due to switching noise within the processor pressure case where the filtering for this signal resides; this noise is reduced with proper shielding. The line frequency harmonics exist at significant but variable levels and are discussed at the end of this section.

3.5.5. Channel to Channel Coherence

Coherence is a measure of the similarity of two signals. The data shown in Figure 3.12a-c is similar to other estimates of the coherence function of ambient noise [Hodgkiss and Fisher, 1987; Urick, 1983]; however in the interest of characterizing array noise, only significant aspects of the coherence data which pertain to array system noise are discussed. These are 1) the high coherence of the line frequency harmonics demonstrating that in spite of the variability in levels, the signals originate from the same source; 2) the notch near 10 Hz as the array filters rolloff and the relative self noise increases; 3) the low frequency peaks which are associated with the array strum and affect the width of the 10 Hz notch which increases with wind speed; and 4) the degradation of the characteristic shape of the elements filtered within the pressure case indicating that substantial incoherent noise is picked up by these channels particularly between 60 and 100 Hz. These particular channels (5 and 6) were chosen for illustration and have substantially higher noise levels than the other channels filtered within the processor case. Spatial correlation of isotropic ambient noise is a sinc function [Cron, Hassell and Keltonic, 1965] where the first zero occurs at $d/\lambda=0.5$ which corresponds to 100 Hz.

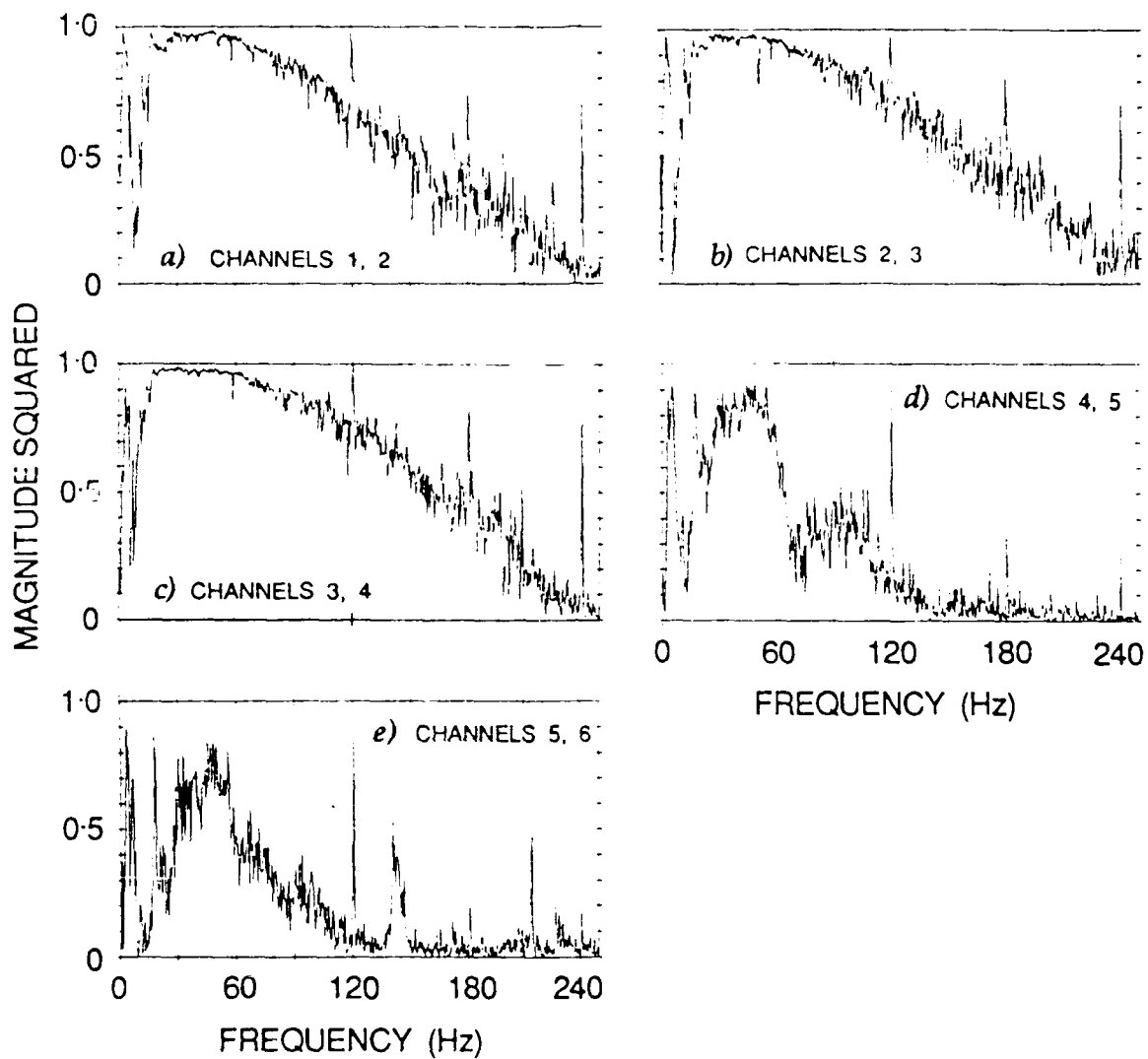


Figure 3.12 Channel to channel coherence. The coherence is calculated as the magnitude squared cross spectra of the specified channels normalized by the single channel spectra. The results shown in (a), (b) and (c) are typical of vertical ambient noise coherence. The results shown in (d) and (e) indicate the presence of incoherent noise in the channels filtered within the processor case (channels 5 and 6).

on the array coherence plot. Although the true distribution of ambient noise deviates from the isotropic assumption, the low coherence values at higher frequencies is expected. Therefore the high frequency clock noise discussed above does not affect the ambient noise coherence because at the frequencies of significant coherence, this noise level is below than of ambient noise.

3.5.6. Narrowband Spectral Estimate Across Array

The average spectral estimate of a particular frequency across the array may be used effectively in identifying channels with high noise levels and/or low sensitivity, providing a coarse relative calibration of the channel amplitudes and information concerning the extent of degradation in the ambient noise measurements due to system noise. Figure 3.13 are spectral averages for data received by each channel at 6 specified frequencies. The magnitudes of spectral estimates for one bin of width 0.98 Hz were averaged ($n=2583$) over a Kaiser-Bessel ($\alpha=2.5$) windowed time series 21.9 minutes long for each array channel. These linear estimates were averaged, calibrated and plotted in dB re $\mu\text{Pa}/\sqrt{\text{Hz}}$ reflecting the estimate for each array channel at a specific frequency. The 95% confidence level for the averages is ± 0.16 dB. The data were selected carefully avoiding any known nonstationary effects (e.g. seismic profiler, large strum amplitudes, nearby ships). The variation across the array is illustrated in Figure 3.13 for two frequencies within the shipping dominated part of the ambient noise spectrum (35 and 75 Hz), two line frequency harmonics (60 and 120 Hz), and two wind dominated frequencies (135 and 150 Hz). Although the general character of the data within each frequency pair is similar, there is a striking difference between the pairs. The level variation of the line harmonics (3.6d) is clearly shown; the pattern does not reflect any array section commonality. The effect of the coupled switching noise (seen in Figure 3.11f) is evident at the higher frequencies where the acoustic ambient noise levels are lower. Figure 3.13 e and f shows the variability in the 135 and 150 Hz spectral levels across the array as some channels are more susceptible to system noise components than others. A spatial transform across the array shows a broad peak at 0.02667 samples/m which corresponds to a 5 hydrophone spacing. Examination of the high frequency spectral components of each section shows that the two farthest and two closest channels to the processor exhibit a propensity for noise contamination however the levels are affected by the proximity of the wiring to the noise source within the wire bundle and are not predictable.

3.5.7. Spectral Estimate Distribution

The distribution of the power in the individual estimates discussed above provides a basis of confidence in the average level. The distribution (Figure 3.14) was calculated for each of the calibrated estimates with bin widths of $350 \mu\text{Pa}/\sqrt{\text{Hz}}$. The figure shows a Rayleigh distribution as expected for the square root of the sum of the squares of two normally distributed components (real and imaginary spectral components). This distribution is used to determine the sensitivity of the average value to outlier estimates. Differences in mean value reflect array calibration variations (channel 32); differences in variance reflect the noise level of the channel. Notice that although the channels filtered within the processor in array

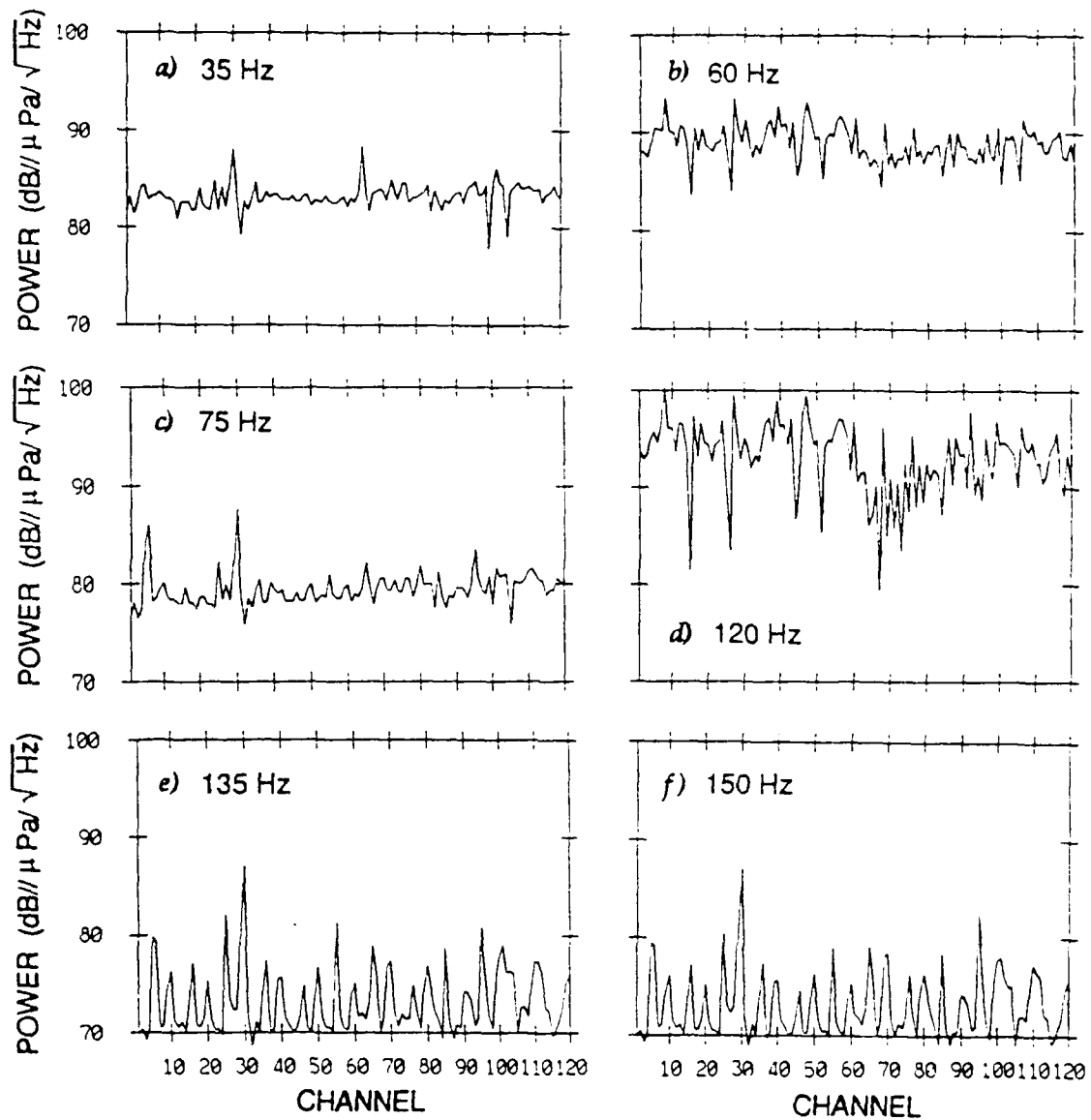


Figure 3.13 Narrowband spectral estimate. The spectral estimates for a specified bin (0.98 Hz bin width) were incoherently averaged ($N = 2583$) and plotted against array channel number. The time series were 21.9 minutes long and windowed with a Kaiser-Bessel ($\alpha=2.5$) function. The frequencies shown represent ambient noise, line frequency and system noise interference distributions.

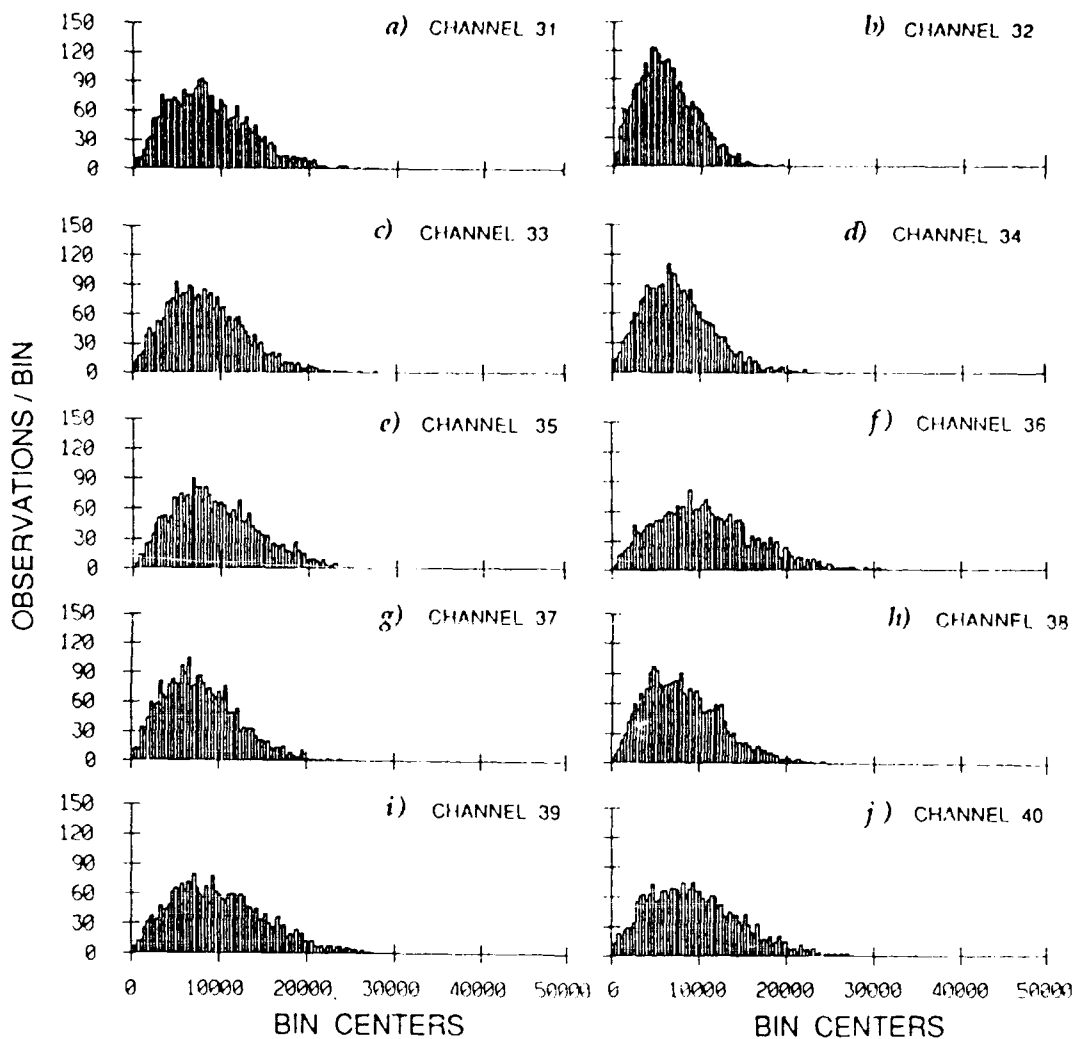


Figure 3.14 Spectral estimate distribution. The distribution was calculated as a histogram of calibrated (linear) spectral estimates with bin widths of $350 \mu\text{Pa}/\sqrt{\text{Hz}}$. Deviation from the expected Rayleigh distribution would require investigation.

section 1 (channels 5 and 6) indicated excessive noise levels on the coherence estimate (Figure 3.12) at 75 Hz and on the single frequency estimate across the array (Figure 3.13c), the same channels in section 3 (channels 35 and 36) shown here do not.

3.5.8. Beampatterns

One way to evaluate the array performance is to investigate the degradation in beampattern as errors are introduced to the amplitude and phase element responses. The amplitude and phase element errors reported in the next section were incorporated into the array beampattern calculation (derived in Appendix B):

$$AF = \sum_{n=0}^{N-1} (A + \delta A_n) e^{j(k(n - \frac{N-1}{2})d(\cos\theta - \cos\theta_0) + \delta\phi_n + 0.0002(ne)2\pi f)}$$

where A_n is the Kaiser-Bessel ($\alpha=1.5$) amplitude shading function, δA_n are the amplitude errors, $\cos\theta_0$ is the beam scanning angle, $\delta\phi_n$ represent the random phase errors due to element positional errors as well as electrical phase mismatch, and the last term is the phase sampling error discussed previously with ne = element number and f = frequency in Hz. Since a time shift in the time domain translates into a phase shift in the frequency domain, at a single frequency ω , the correction for this time offset $\tau=0.2$ ms is simulated in terms of a linearly increasing phase delay $e^{+jn\omega\tau}$ for each hydrophone n in a section. The results at 56 Hz are shown in Figure 3.15 for errors in amplitude obtained from the broadband averages, errors in phase from the narrowband calibration and the effect of phase sampling errors which is deterministic and can be removed from the acoustic signal. The beampattern incorporating both amplitude and phase errors (Figure 3.15e) shows a deterioration in side lobe level from the theoretical pattern (Figure 3.15a) and a slight distortion of the main beam. The resulting pattern has virtually constant side lobe levels at about 35 dB below the main beam.

3.5.9. Beam Levels

Directionality plots represent the spatial distribution of the data and potentially identify relative side lobe levels. The directional beams are calculated by taking a Fourier Transform of the spectral estimates at a single frequency after compensating for the sampling offset discussed above. The plots in Figure 3.16 are the result of computing a linear average, dB average and the standard deviation of the dB estimates [Wagstaff *et al.*, 1982] with $n = 63$ in the presence of a narrowband far field signal. The abscissa is normalized phase ($\frac{\phi}{2\pi} = \frac{d}{\lambda} \cos\theta$), with positive phase looking up, and the visible region marked by dotted lines (see Appendix B). A 5 or 6 dB variance is typical of a single transform estimate for a random process [Bendat and Piersol, 1971] and the 2 or 3 dB difference in the averages is caused by the nonlinear logarithm transformation of the Rayleigh distributed spectral time series. Should the beam estimates have significant outliers, the difference between the averages will increase as the linear average weights the outliers more heavily. A strong coherent arrival is indicated by a drop in variance and the coincidence of the two averages as seen in Figure 3.16. The directionality response is a function not only of the array side lobe levels and main beam width but of the noise field with

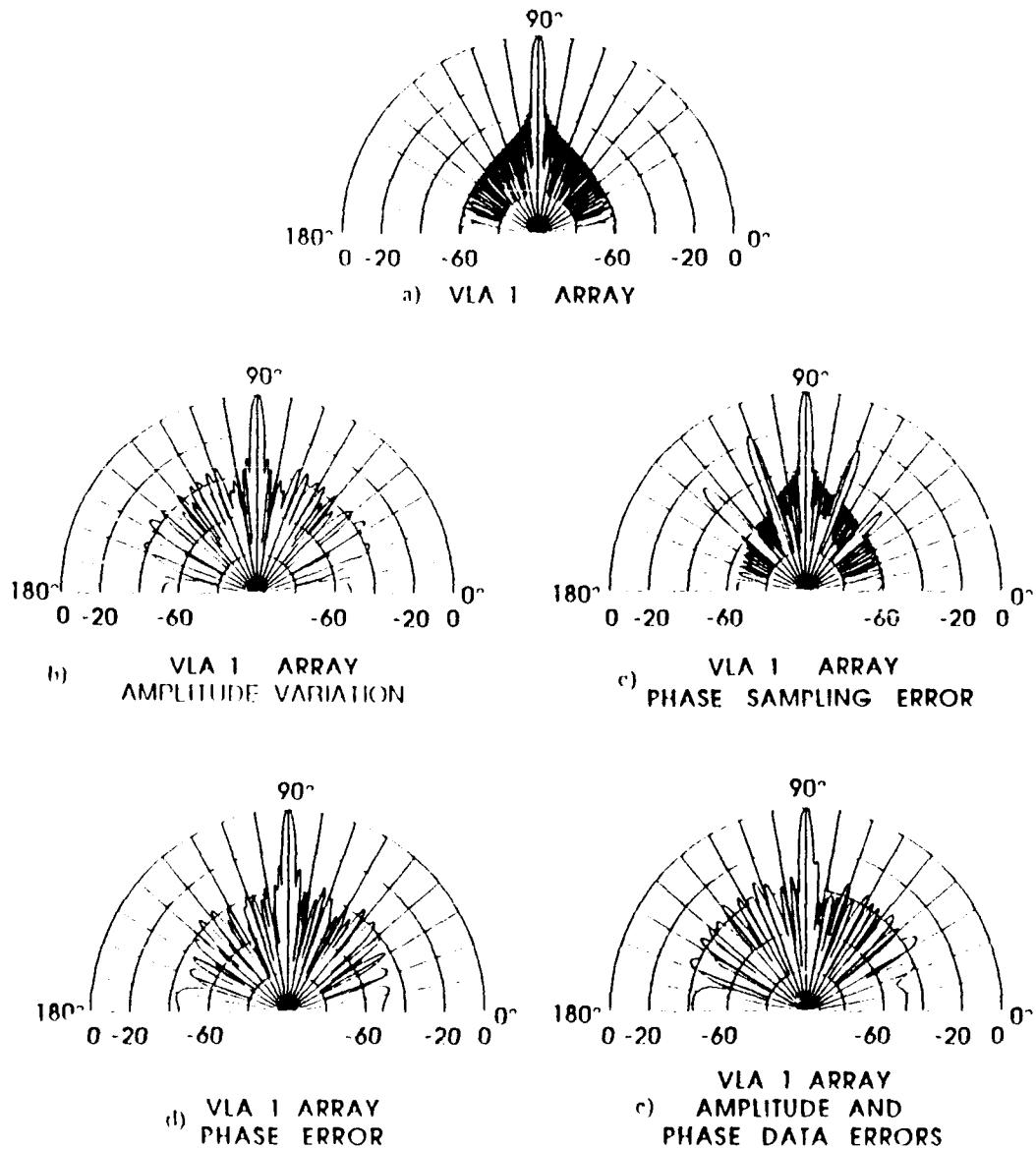


Figure 3.15 Beam patterns. The array beam patterns were calculated for the 120 element equally-spaced line array at 56 Hz with Kaiser-Bessel shading ($\alpha=1.5$). Errors were introduced in amplitude (b) and phase (c and d) and compared to the theoretical pattern shown in (a). The estimate of the true beam pattern incorporating the amplitude and phase calibration errors (e) indicates an almost constant side lobe level at -35 dB.

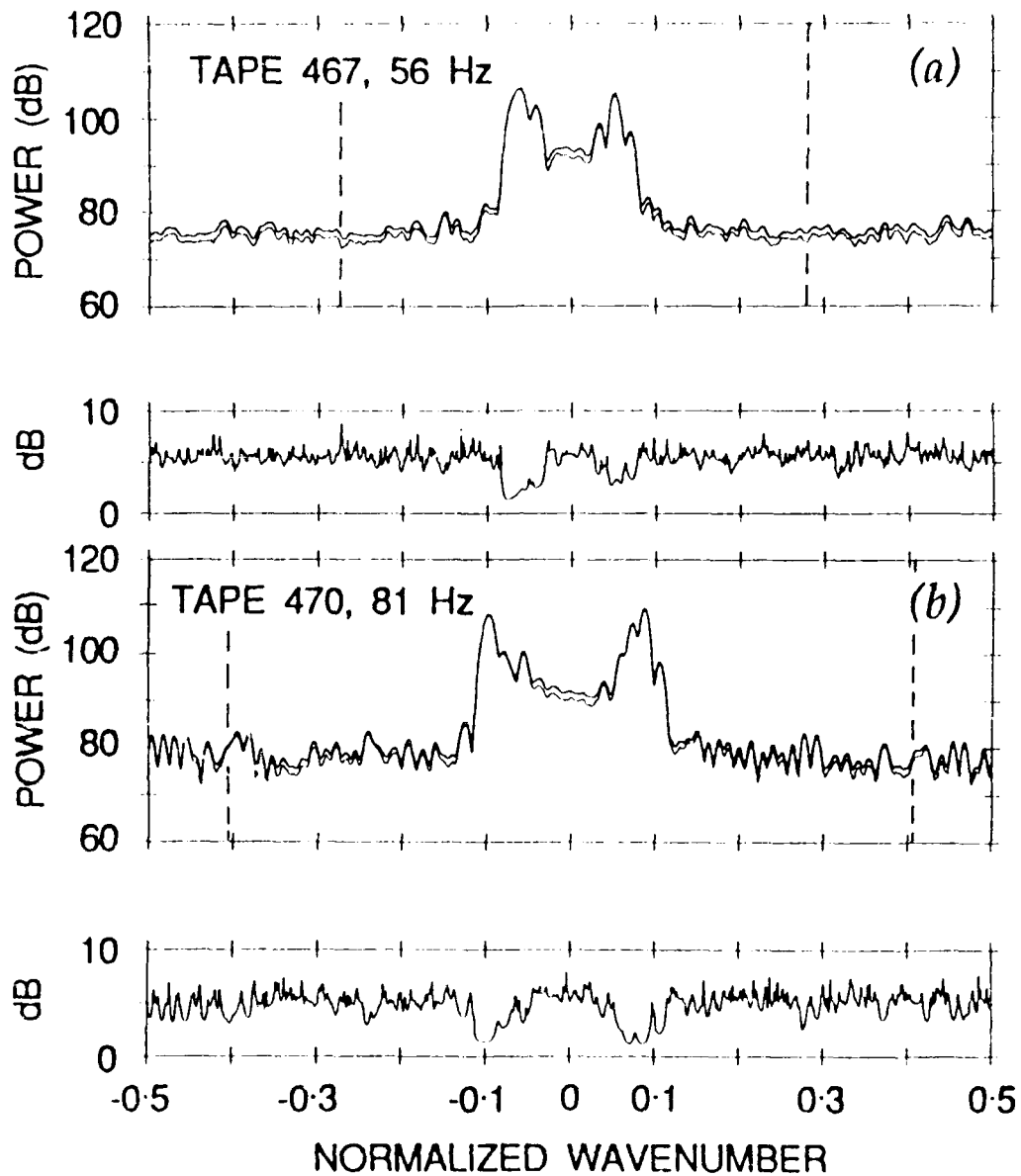


Figure 3.16 Beam levels. The beam levels are calculated by taking the Fourier Transform of a single frequency bin across the 120 array channels. The result is displayed as a linear average (top curve), a dB average (bottom curve) and the standard deviation of the dB estimates (separate plot). The ordinate is referenced to a watt/Hz/m and the abscissa is normalized phase ($\phi/2\pi$) with positive numbers looking up. The dotted lines mark the visible region.

which the array beam pattern is convolved. Simulations which assist in the interpretation of the directionality data as measured by this particular array are presented in [Sotirin and Hodgkiss, 1989]. The constant response at $|\phi| > 0.12^\circ$ indicates that both the ambient noise and the array side lobe level are essentially flat. The absence of a decrease in level as the main beam enters invisible space indicates that this level is dominated by the array side lobe response to the signal but does not indicate the relative side lobe level.

3.5.10. Beam Correlation Level:

The correlation beam to beam is an indication of coherent signal arrivals. Because the linear correlation function is normally interpreted in terms of a binormal joint beam distribution, an alternative nonparametric test is performed known as Spearman's rank correlation and has been used successfully by others [Wagstaff *et al.*, 1982]. Estimations of the power arriving at 64 specific directions are calculated as described above. If the value of these beam estimations are ordered for any one direction, and the position of the estimation within the ordered set is substituted for the actual value then the distribution of the positions or ranks is uniform provided each estimate is unique. If the estimates are not unique then they are assigned a midposition rank such that the sum of the ranks for any one beam is equal to $\sum_{i=1}^N i$ where N is the number of estimates. Once ranked, the correlation coefficient ρ_{jk} for beams j and k is calculated as the linear correlation of the ranks:

$$\rho_{jk} = \frac{\sum_{i=1}^N [(r_{ij} - \bar{r}_j)(r_{ik} - \bar{r}_k)]}{\left[\sum_{i=1}^N (r_{ij} - \bar{r}_j)^2 \sum_{i=1}^N (r_{ik} - \bar{r}_k)^2 \right]^{1/2}}$$

where r_{ij} and r_{ik} are the assigned ranks for the i th estimation of beam j or k . To verify that a nonzero value of ρ reflects the existence of a statistically significant correlation, the null hypothesis ($\rho_{jk} = 0$) is tested, where a significant correlation is indicated if the hypothesis is rejected. With the function w defined as:

$$w = \frac{1}{2} \ln \left[\frac{1 + \rho_{jk}}{1 - \rho_{jk}} \right]$$

where w is distributed normally with zero mean and a variance of $\sigma_w^2 = 1/(N-3)$ [Bendat and Piercol, 1971], the null hypothesis of zero correlation is accepted at the α level of significance if

$$-z_p \leq \sqrt{N-3} w < z_p \quad (3.1)$$

where $p = \alpha/2$ and z_p is the p quantile of a standard normal random variable. For display purposes, the correlation matrix M_{jk} consists of 100% on and above the main diagonal and 10% ρ_{jk} below the main diagonal if Equation 3.1 is not satisfied (0 if it is). In general, the results of tests which require a significant amount of data processing are more difficult to interpret in terms of the system noise and are not recommended as independent tests. However, used in conjunction with the other tests these results may support hypotheses. The beam correlation matrix for 4.25 Hz is displayed in Figure 3.17 at a 95% confidence level. Although this matrix

shows significant correlation between the beams, indicated by the grey level below the main diagonal, it is demonstrated below that this is an artifact of the amplitude variability in the signal. Although not an indication of high array side lobe levels which would be the interpretation inferred by others in the absence of a strong multipath acoustic signal, the results do indicate that there is a problem. A typical ambient noise matrix displays few nonzero levels below the main diagonal.

3.5.11. Line Frequency Analysis

The levels of the signals appearing at line frequency harmonics in the *in-situ* are surprisingly strong as the high power input to the array is filtered and the data is digitized in the array itself. The results of self noise tests performed in the laboratory show a conspicuous lack of any consistent 60 Hz harmonics in the spectrum. Although there are spurious peaks throughout the test data set, there were no perpetual signals which would suggest a system (electronic) generated noise source. This implies that the 60 Hz signals and associated harmonics observed in the *in-situ* data set were either acoustic in origin or an artifact of the setup aboard *FLIP*, and were not an inherent component of the array self noise. The acoustic data from the sea test indicated that the 120 Hz line is dominant, appearing mostly broadside (Figure 3.18a) and at high power levels (Figure 3.14d). Acoustic noise propagating from *FLIP* would appear endfire, with a monotonically decreasing level. Spectral levels of vibrational noise within the processor case would decrease as it propagated away from the processor. The 120 Hz signal appears in all array channel spectra at randomly varying levels and although the broadside component is 20 dB above the higher angle arrivals, there appear to be components that arrive at other angles (low variance and significant correlation). The appearance of these arrivals can be explained by examining the Fourier Transform of the channel magnitudes which behaves as an amplitude shading function in the beamformer. The result (Figure 3.18b) illustrates that the 'arrivals' are due to the variability in amplitudes. Not finding a suitable acoustic path for the line frequency harmonics to travel in, this noise must be coupled in through a grounding path in the array when it is deployed from *FLIP* or coupled in from the DC-to-DC converter inputs.

3.6. ARRAY CALIBRATION

The array calibration enables one to convert the ADC output recorded on tape to the pressure field seen by the hydrophones. A nominal calibration of a system is obtained from the design specifications of the component parts. For this particular array, the signal path conversion consists of the hydrophone sensitivity at the ambient environmental conditions (-197 dB re V/uPa), the preamplifier gain (40 dB re V), the differential receiver (6 dB re V), the variable gain stage (12 to 60 dB re V), and the ADC (46.23 di re counts/V). The calibrations addressed here refer to the deviation of the array elements from the nominal calibration. The *in-situ* amplitude calibration was determined from two independent methods. The narrowband calibration consists of comparing monochromatic transmissions, of known frequency and source levels from a navigated source position, to a predicted response. The broadband method assumes that the average ambient noise levels across the array do not vary significantly from the mean, so defective channels may

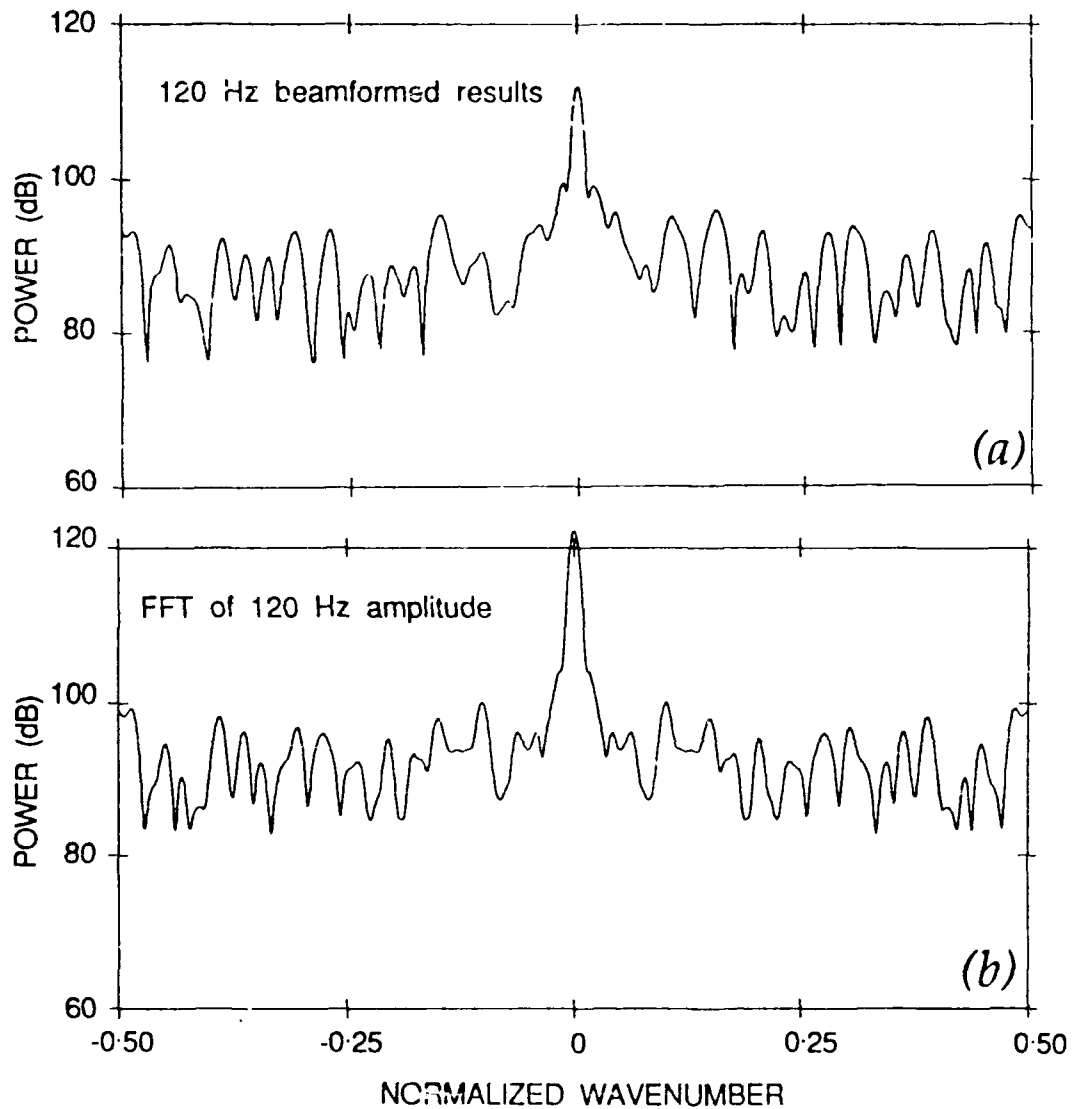


Figure 3.18 Line frequency spatial distribution. The correlation levels indicated at 120 Hz are shown to be an artifact of the amplitude variations across the array. The beamformed results (a) show a spatial distribution which is very similar to that obtained from the Fourier Transform of the magnitude estimates at 120 Hz (b). The similarity indicates that the arrivals from directions other than broadside are not due to coherent combinations.

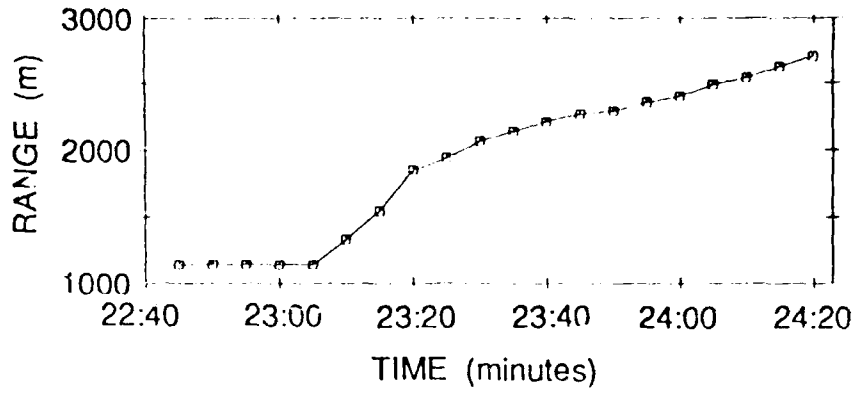


Figure 3.19 Narrowband transmission range. The range of the narrowband source from the array deployed from *FLIP* were recorded from ship's radar every 5 minutes during the transmissions.

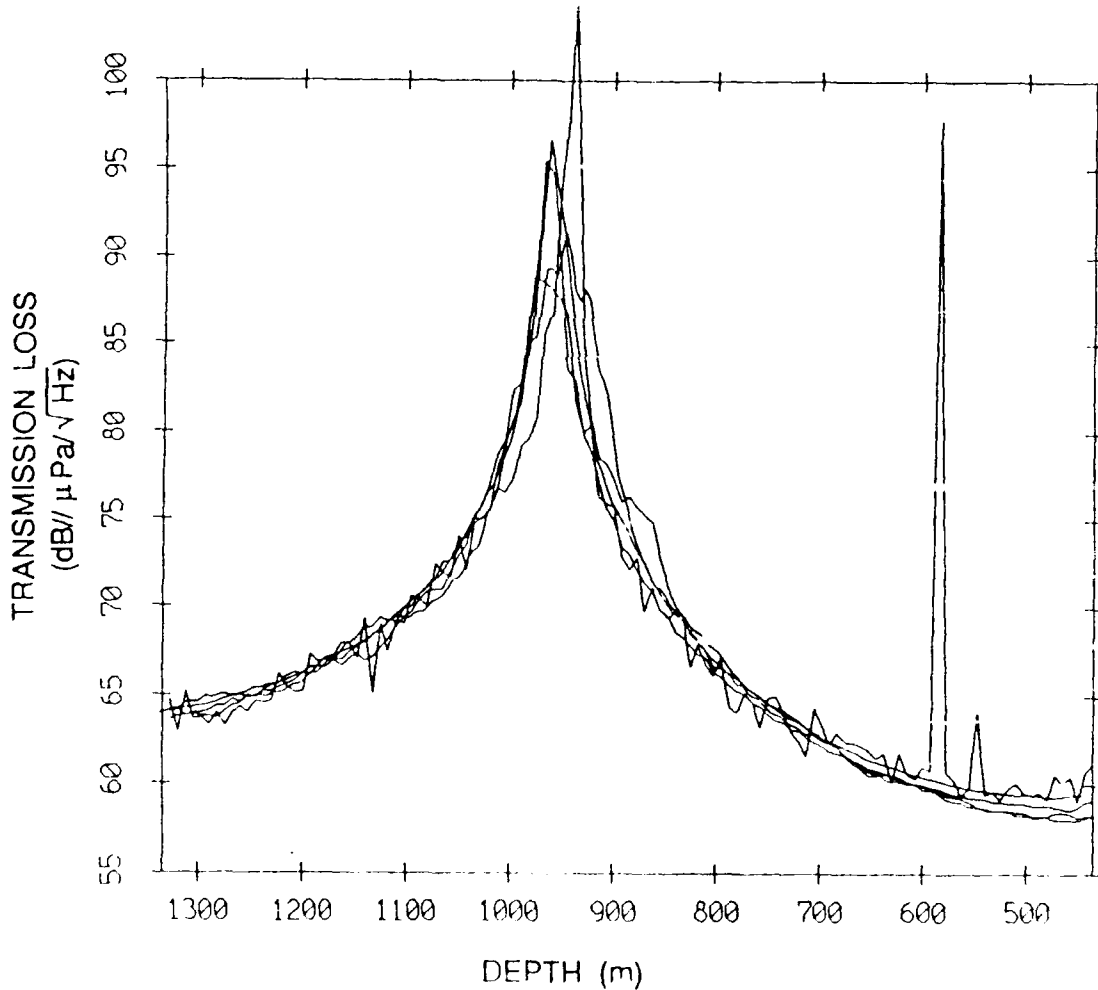


Figure 3.20 Calibration modeling. The transmission loss estimates of several different propagation models are shown for empirical comparison of the variability at array element depths. Array measurements are also plotted.

be identified by examining the variance and a relative calibration is obtained by examining the mean. To minimize the effect of variability in the environment over 1000 ambient noise spectra are normalized and averaged for the broad band estimate, and for the narrow band estimate, the strength of the signal was substantial compared to the noise (SNR of 45 dB// $\mu\text{Pa}/\sqrt{\text{Hz}}$). The phase calibration was generated by differencing a multiple linear regression with the smoothly varying phase data obtained during the narrow band transmission.

3.6.1. Method Description and Data Collection

Narrowband. The narrowband method depends on modeling the signal arriving at the array by correctly simulating the ocean environment at the test site. The transmission was conducted on Julian day 267 from 2246 GMT until 00 GMT, under benign environmental conditions; wind velocity was 6 to 7 kts at 250 °, swell was 0.5 m at 310 °. A deep conductivity, temperature and depth (CTD) cast (3885 m) was executed coincident with the commencement of the narrow band transmission and this CTD data was desampled for utilization in the sound speed profile calculation [Sotirin and Hildebrand, 1989] required by the models. The water depth obtained by echo sounding from *FLIP* was 4668 meters, therefore the data from the deep CTD was extended by using data from a 4906 meter CTD taken on Julian day 264 at 1605 GMT near 37° 04.10' N and 134° 46.75' S. The ship was allowed to drift during transmissions and source range from *FLIP* (Figure 3.19) was calculated from radar measurements taken every 5 minutes, ship heading and deployment geometry. The source was deployed at a depth of 27 meters, and source level was monitored by a calibrated hydrophone at a range of 1 meter (Table 3.1) as each of the specified frequencies was transmitted for a period of 6 minutes.

Frequency Hz	range meters	source level dB re μPa
98	1141.375	192.0
135	1141.375	193.1
22	1331.655	179.7
56	1550.335	191.3
81	1853.546	199.3
27	1943.869	181.5
41	2141.568	186.6
115	2216.663	198.2
159	2275.890	186.0
16	2295.145	176.3
11	2358.765	170.0

Table 3.1 Narrowband Transmission Parameters.

Array depth was estimated from navigation measurements taken at 1730 GMT. Several propagation models, encompassing normal mode, parabolic equation, fast field and eigenray approaches, were compared using the array test environment parameters to determine the inputs [D'Spain, 1988]. This comparison showed 0.5 to 1.5 dB deviations between the different model spectral level predictions away from transmission loss peaks (Figure 3.20). The models require estimates of ocean bottom parameters such as layer thickness, compressional wave speed and attenuation, shear wave speed and attenuation and density and surface reflection coefficient which were estimated from references in the literature. Small deviations in the predicted transmission loss levels could be due to errors in these estimates. Small variations also occurred in determining the exact location and loss levels associated with the signal null (transmission loss peak) which is sensitive to source range and array receiver depth, changing the phase of the signal arriving across the array. The estimated parameters also affects the phase prediction and was probably responsible for the differences observed in the results, therefore only magnitude predictions will be used. The Generic Sonar Model (eigenray) was chosen as the prediction vehicle due to its robust simplicity in this application where the amplitude is controlled by two dominant paths, consistent results at close range and reasonable execution times. The array data was obtained by extracting the raw data from tape at the same time as the radar fix to obtain as precise a range measurement as possible for the modeling effort. Spectral estimates were calculated and averaged for each channel at the frequencies transmitted during the calibration. The time series, which had to be long enough to generate reasonable confidence limits, was limited to 98 seconds to reduce the errors in range due to ships drift to less than 50 m assuming a drift rate of 1 kt. A single transform estimate was compared to the averaged results at each frequency with slight differences (<0.5 dB) except near the transmission loss peak and at a few isolated channels where the difference was as much as 2 dB for one particular frequency. The 40-50 dB signal to noise ratio was more than adequate to alleviate doubts regarding interfering signals and random noise levels. The comparison between the data and model outputs indicated the necessity of iterating range and source level to match the location of the transmission loss peak and the mean received signal level. The range estimation by ship radar is accurate to within approximately ± 50 m, the range increment in the iteration was 5 m and the final deviation was less than 30 m at 56 Hz and the source level was adjusted by +1.8 dB. The GSM predictions were subtracted from the array received signal at selected frequencies and the element deviations were compared. The data at 56 Hz is shown in Figure 3.21 and results are discussed below.

Broadband. Ambient noise levels are reported to vary only slightly (e.g. 1 dB) with depth [Morris] therefore incoherently averaging the ambient noise measured during the sea test should yield a virtually constant level across the array. If this is the case, then deviation from this level offers an independent amplitude calibration. Figure 3.22 a, b, d and e are spectral averages and the standard deviation of the spectral estimates for data received by each channel at a specified frequency for 4 different time periods. The averages are calculated from linear estimates (middle trace) and dB estimates (bottom trace), and the standard deviation is based on the dB estimates offset to 90 dB for display purposes (top flat trace). The magnitudes of spectral estimates are calculated as described in Section III. The linear estimates were averaged, calibrated and plotted in dB re $\mu\text{Pa}/\sqrt{\text{Hz}}$ reflecting the estimate for each array channel at a specific frequency. The lower trace was calculated by converting the linear estimates to dB, then averaging and plotting the calibrated results. The standard deviations were calculated from the

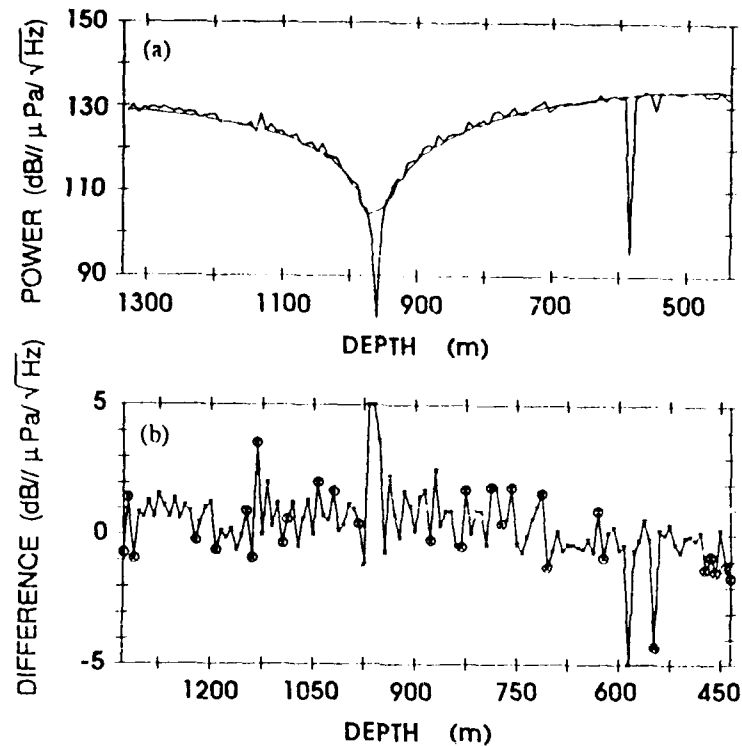


Figure 3.21 Narrowband magnitude results. (a) The model prediction vs. array data is plotted at 56 Hz. The GSM magnitude prediction is the smooth curve with a deep null at 960 m. (b) The difference between the model prediction and the array response is shown.

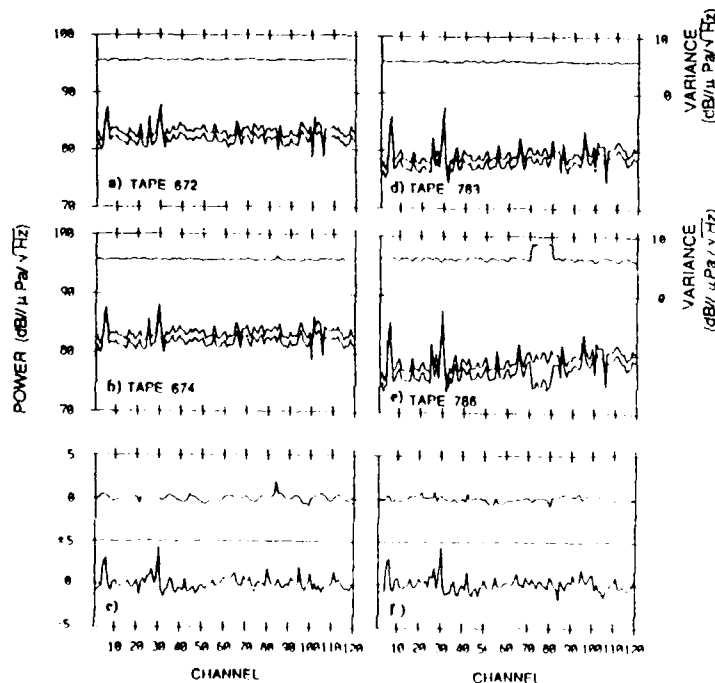


Figure 3.22 Ambient noise variability. The variation in ambient noise at 75 Hz is shown. The top four panels (a, b, c and d) represent the 75 Hz bin estimate across the array at different times. The smooth curve at the top of each panel is the variance of the dB estimates. The two similar curves in each panel are the linear (top) and dB (bottom) averages. The data was taken at four different times during the experiment to reflect 1 hour and 2 day variations: (a) Julian Day (Jday) 261 at 08:53 GMT, (b) Jday 266 at 09:41 GMT, (c) Jday 268 10:09 GMT, (d) Jday 268 11:19 GMT. Array telemetering errors are noticeable in the dB estimates of the data for channels 70-75 in (d); the data were corrected in the linear average which is more sensitive to error.

calibrated dB estimates. The standard deviation of the log values has been shown to be a constant value of 5.6 dB [Dyer, 1970] (displayed as 95.6 on the plot); the 95% confidence level for the averages is +0.166 dB, -0.162 dB for 2583*2 (real and imaginary estimates) degrees of freedom. The data were selected carefully avoiding any known nonstationary effects (e.g. seismic profiler, large strum amplitudes, nearby ships) with the expectation that the spectral level would vary smoothly across the array on the order of 1 dB, deviating only at the level of channel calibration.

Phase. The phase results presented below were the result of a single coherent FFT as described above. The raw phase data was processed by: (a) unwrapping the inherent 2π rollover, (b) accounting for the 0.2 ms/element/section sampling error in the array by subtracting $\omega n\tau$ where n is the channel position described in Section 1, (c) correcting for the 180° phase shift at the transmission loss peak as a result of the interference between the direct and surface reflected paths arriving at the array, and (d) subtracting a multiple linear regression curve to realize the plots in Figure 3.23.

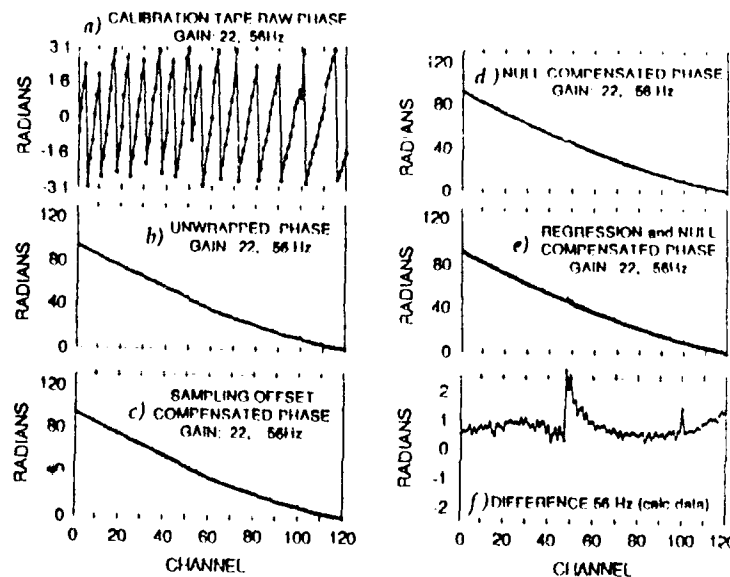


Figure 3.23 Narrowband phase results. The phase estimate across the array at 56 Hz is calculated from the narrowband calibration transmissions and processed; (a) The phase estimate from a coherent Fourier Transform has an inherent 2π phase shift. This is unwrapped (b) and deviation from the resulting smooth phase change across the array is due to the 0.2 ms sampling offset. Compensating for the deterministic sampling offset (c) reveals a phase shift of π radians at the transmission loss peak. The fully compensated phase curve (d) varies smoothly across the array except at the transmission loss peak where the SNR is too low to provide an accurate phase estimate. A multiple (order 3) linear regression (e) is subtracted and the difference (f) is an indication of the array phase error. The curvature of the difference is due to a mismatch in the regression and a more accurate estimate (order 4) is shown in Appendix C.

3.6.2. Results

Magnitude. Limitations in the calibration methods due to the incomplete knowledge of environmental parameters and the temporal variability of ambient noise were minimized. The modeling efforts of the narrowband transmissions resulted in 0.5 to 1.5 dB variations between various models and required iteration

in source level and range. The mismatch in Figure 3.21a especially apparent at either end of the array results in a spatially varying offset. Consequently, the absolute calibration levels (Figure 3.21b) were interpreted relative to the offset trend, and the modeling results were confined to an advisory position in terms of the smoothness of the array response. The response shown at 56 Hz reveals a smooth variation across the array. Relative deviation levels greater than 1 dB from the smooth response were empirically identified and recorded at specified frequencies. These results were reviewed for consistency and the average results tabulated (Table 3.2).

Channel:	1	2	3	4	5	6	7	8	9	10
P1	-1	+1	-2							
P2					-1				-1	
P3					+1	-1	+2			
P4		-2	+5							
P5		-5					+1			
P6										
P7	-1						-1	+1		
P8			+1		-1		+1			
P9			+5	-1						
P10				+1.5	-1					
Pi1					-5					
P12					-1	-1	-1		-1	-1

Table 3.2 Results of the Narrowband Calibration.

The ambient noise collected every 7.5 m for 18 days, varies smoothly with depth on a large scale. The small scale deviations however, are on the order of ± 1.5 dB. The variation across the array is illustrated in Figure 3.22 for 75 Hz at 4 different times (a, b, c and d) where the time difference between the averages is about 1 hour for the vertical panels (a-b and c-d), and 2 days for the horizontal panels (a-c and b-d). The degree of channel to channel variability increased during the 2 day period. This variation in time is seen by examining the bottom panels (e and f). A multiple linear regression was subtracted from the linear averages to estimate the relative channel variation. The top plot in panels e and f represent the difference in relative channel variation between the two panels directly above and the difference in relative channel variation between the 2 day estimates in the bottom plot. Short term (1 hour) time variation is small, only one channel has more than a ± 1 dB variation. The variance across the channels is 0.13 dB (e) and 0.095 dB (f); because the channel calibration should remain constant, these differences represent changes in the ambient noise field. Long term (2 days) time variation is larger, with more than 10% of the channels having deviations of greater than ± 1 dB. The variance across the channels is 0.68 dB (e) and 0.78 dB (f) increasing from the 2 hour variance due to the nonstationarity of the noise field. It is this variability in the ambient noise field which limits the broadband calibration. To minimize the effects, estimates of the ambient noise field were calculated at 15 different times during the experiment in hopes that the variations were random and would average

out, leaving a more accurate estimate of the channel calibration levels. The standard deviation of the 15 time estimates (Figure 3.24a for 56 Hz) for the 3 frequencies processed exhibit 3 channels with consistently high variance (21, 55 and 100). The broadband amplitude results for 56 Hz, illustrated in Figure 3.24b, were compared to the narrowband calibration results at 56 Hz shown in Figure 3.21b. Ignoring channels 40 to 60 in the narrowband calibration which are close to the interference peak at 56 Hz and the channels with high variance, the comparison shows that most channels deviations of more than 1 dB are noticeable in both results, however there are some obvious differences. These differences, notably channels 5, 6, 29, 30, 65 and perhaps 85 are a result of excessive system noise levels. The ambient noise measurements for these channels are distorted even at low frequencies. These channels do not exhibit a high variance at a specified frequency due to the consistency of the level; the level of channel 30 in Figure 3.13 is 88 dB re $\mu\text{Pa}/\sqrt{\text{Hz}}$ at frequencies other than line harmonics. This imposes a frequency dependent calibration as the ambient noise level changes with frequency. Another obvious difference is the channel 27 estimate which is consistently high in the narrowband results but is not identified as a deviant in the ambient noise results. The cause of the apparent transient nature in a few of the channel levels has not been resolved.

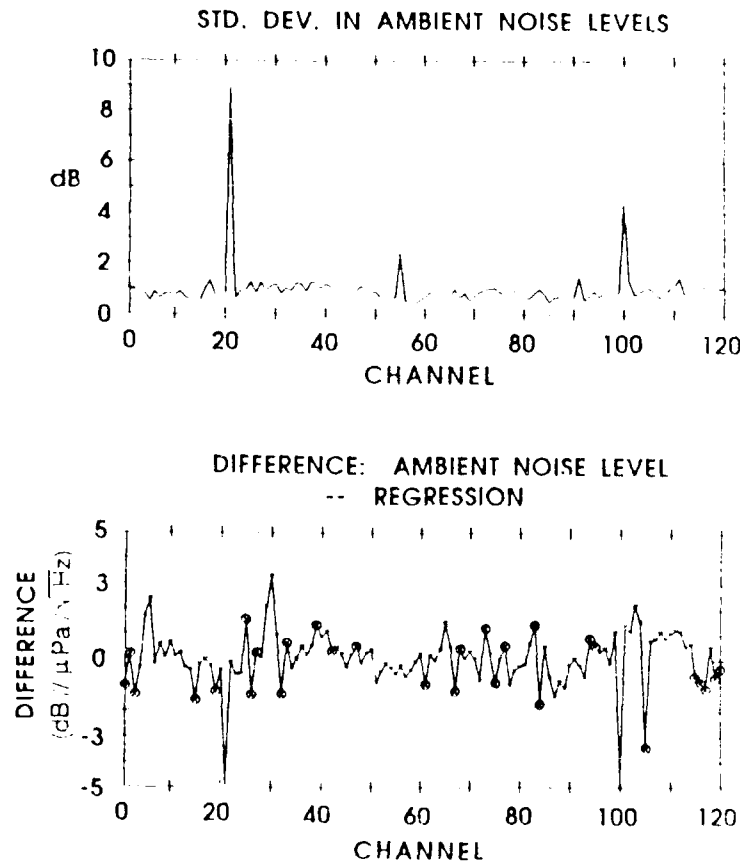


Figure 3.24 Broadband magnitude results. Ambient noise measurements were used to estimate the spectral levels at 56 Hz for each array channel. These estimates ($N=2583$) were calculated at 15 different times during the experiment and the results averaged to minimize the variability of the ambient noise. (a) The standard deviation of the 15 different time estimates was calculated. (b) A multiple linear regression was subtracted from the mean. The calibration results using ambient noise

Phase. The phase regression differences were examined for 5 different frequencies, the result for 56 Hz is shown in Figure 3.23f. Besides channel 100, the only other identifiable error mode were the channels which are filtered within the processor case (e.g. 5, 6, 15, 16). These channels are most likely affected by the switching noise identified in the previous section. The phase of the incoming signal should vary smoothly across the array; ignoring the mismatch in the regression curve and the transmission loss peak, the deviation in phase at 56 Hz is within 0.1π radians. The smooth phase variation assisted in identifying the channels with reversed polarity discussed previously. Phase deviations are also evident in the time series plots (e.g. Figure 3.8) during an impulsive arrival. The deviations for acoustic arrivals such as the seismic profiler are small as discussed above however for mechanical vibration (strum), every fifth channel per section (e.g. 5, 15, 25, etc) is delayed on the order of 50 ms due to propagation interference by the processor pressure case.

3.7. CONCLUSIONS

Large aperture low frequency arrays are inherently difficult to test because of the physical size and number of channels which impose time and facility constraints. Utilizing ambient noise in system tests allows the array performance to be monitored throughout the experiment, identifying low performance channels and their effect on experimental results. The tests discussed here, although not exhaustive and yet to some extent repetitive, illuminate problems associated with the array hardware and software. The repetitive aspect of the tests is necessary due to the random nature of the ambient noise and the specific manifestation of the problem being investigated. In addition to system noise testimony, *in-situ* data was successfully used to calibrate the individual channels. A combination of narrowband transmissions and ambient noise measurements provides magnitude deviations to within ± 1 dB.

Although the tests amplify the negative aspects of the array system, based on the results shown here, the array might well be used without adjustments to the nominal calibration. The -35 dB array side lobe level is more than adequate for many applications. However, spectral levels for individual channels are frequency limited due to system noise. Specific results for the array discussed show that four elements in each array section (the closest to and furthest from the processor) potentially have noise problems at high frequencies. The noise in the furthest elements is coherent and with the exception of channel 30 (consistently above 85 dB in the data processed to date) and channel 29 (slightly lower), the average level is about 78 dB// $\mu\text{Pa}/\sqrt{\text{Hz}}$ but affects few enough channels that the degradation in the directionality plots is minimal. The noise in the closest elements is incoherent but at about the same levels with the exception of channels 5 and 6 which exhibit a frequency dependence when compared to spectra from other channels. The distinct comb-like pattern fades as the amplitude of the ambient noise increases. The high frequency contamination was identified during the self noise laboratory test as a common mode problem in the channels furthest from the processor. The system noise in the channels filtered within the processor case was not identified because the electronic packages were removed from the case and separated physically to provide access to test points reducing the coupling effect. Precursory laboratory system tests are required to eliminate system noise sources prior to deployment. The coherence shown in channels 5 and 6 indicates substantially higher noise levels than most of the other channels, and although not shown, this is corroborated by

their spectral estimate distribution. Few channels show this level of noise contamination however, and it is not expected to affect coherent processing results. This is supported by the -35 dB side lobe levels in the array beampattern. Few of the tests would individually provide conclusive evidence of a system noise problem due to the stochastic nature of ambient noise and the particular manifestation of a specific system problem. However, as evidence is accumulated through the results of the series of tests, these problems may not only be identified but cause may be narrowed. The impact on experimental results is of course tied to the specific purpose of the experiment. For the results shown here, absolute spectral levels for ambient noise are obviously damaged for specific channels and specific frequency bands, however the array is capable of measuring signals above the system noise levels defined by the test results, and the directionality estimates would satisfy most application specifications.

An *in-situ* array calibration was demonstrated successfully at a ± 1 dB re $\mu\text{Pa}/\sqrt{\text{Hz}}$ level by comparing the results of the two independent methods for relative channel to channel information. Although the narrowband results have the potential of providing absolute calibration values, modeling the narrowband transmission requires precise knowledge of environmental parameters. Some of this information is not readily available for specific test sites and must be estimated, increasing the error of the modeled response. Consequently the model outputs were utilized as an indication of the smoothness of the array response at specified frequencies. The level of system noise and the temporal variation of the ambient noise levels posed problems during the broadband array calibration which examines channel variation after averaging large numbers of spectra. Deviation from a regression across the array removes the time-varying mean of the ambient noise and allows comparison of channel to channel variation. The variance of the estimates must also be considered as confidence in the mean deviation increases. Comparing broadband calibration results to the narrowband results yields good agreement however, with the exception of the channels with excessive system noise levels. Being aware of the potential for deviation between the two methods facilitates the analysis. Phase calibration results were based on the assumption of smooth phase variation across the array and were identified as deviations from a multiple linear regression. The deviation in phase was small (0.1π at 56 Hz) with the exception of those channels identified with system noise degradation.

Chapter 4

FINE-SCALE MEASUREMENTS OF THE VERTICAL AMBIENT NOISE FIELD

4.1. ABSTRACT

Use of a large aperture vertical array allows investigation into the fine scale structure of the directional ambient noise field. Frequency and directional spectral estimates are calculated during the passage of a local storm, providing a detailed study of ambient noise levels at low frequencies as wind speed increases from 2 m/s to 12 m/s over a 21 hour period. Spectral levels of horizontal beams reflect distant sources. Spectral levels of beams directed toward the surface and the bottom display a threshold type behavior, suggesting the abrupt onset of a source mechanism such as breaking waves. Subsequent thresholds may indicate a change in source mechanism such as the conversion from spilling breakers to plunging breakers.

4.2. INTRODUCTION

To measure low frequency (20 - 200 Hz) vertical directionality of the oceanic ambient noise field requires a long array of hydrophones. Initial vertical directionality investigations were at high frequencies (near 1 KHz) with shorter arrays [Anderson, 1958; Rudnick and Squier, 1967]. These measurements showed a non-uniform spatial distribution with more noise in vertical directions than in horizontal directions due to a dominance of local environmental noise sources at high frequencies. Initial low frequency measurements provided a general spatial distribution description of ambient noise and its variation with wind speed [Fox, 1964; Axelrod *et al.*, 1965]. Omnidirectional spectral measurements indicated that ship noise dominates the environmental noise in this frequency region, and the directional measurements showed that more noise arrives from the horizontal than from the vertical, a reversal of the patterns characteristic of high frequencies.

More recently, the spatial distribution of ambient noise at low frequencies has been described as a broad pedestal of energy arriving between $\pm 20^\circ$ of horizontal in the deep sound channel [Anderson, 1979] with levels up to 25 dB above the higher angle levels. Ray tracing showed that the surface interacting rays which would contain ship noise, arrive within a narrow band of angles around $\pm 12^\circ$ to $\pm 15^\circ$. This implied that the low frequency spatial distribution in a range independent environment should have a double-humped pattern with the width of the notch between the humps decreasing with depth [Cavanagh and Renner, 1980]. Yet measurements showed a pedestal with broad frequency and spatial characteristics, although the pedestal width did decrease with depth.

Two mechanisms were suggested by Anderson [1979] to account for the additional noise at near horizontal angles: (1) high latitude ducting, based on the shallower sound speed minimum at high latitudes and (2) down slope conversion (or the slope enhancement effect), based on on sloping bottom reflection. These

mechanisms would convert noise traveling at near vertical angles to horizontal angles so that it travels with low loss in the deep sound channel, filling in the predicted noise notch. Initially the idea of slope-converted ship dominated spectra directed the investigations. The downslope conversion of noise from ships driving over seamounts and the continental slope was discussed by Morris [1975] and later by Wagstaff [1981] who emphasized the importance of directional measurements since the omnidirectional measurements of a single hydrophone may be dominated by the horizontal component. More recently, ducted transmission and wind generated mechanisms have gained more prominence. Three models of ocean noise were considered by Dashen and Munk [1984]: scattering, downslope conversion and ducted transmission from high latitudes; the effect of scattering was shown to be too weak to be effective and although these authors preferred the ducting process on a physical basis, they concluded that the shipping density at high latitudes was insufficient to produce the absolute levels measured, and that continental slope conversion was the most probable mechanism by default. The significance of high latitude winds was discussed by Bannister [1986] who estimated the contributions arriving horizontally from ducting and downslope conversion of wind noise, and concluded that ducting of high latitude winds could produce horizontal levels comparable to those of downslope converted ship noise.

Experimental verification of these mechanisms is difficult due to the obstacles encountered in separating the sources and source mechanisms. Experimental evidence of ducted wind generated noise [Bannister, 1986] was based on interpretation of vertical noise distributions in the low shipping density areas near New Zealand, measured by Browning *et al* [1982] and Burgess and Kewley [1983] which were similar to those measured in the high density shipping regions of the North Pacific. Burgess and Kewley [1983] found significant wind dependencies at frequencies from 37 to 800 Hz, however it was not conclusively shown that the wind dependencies were a ducted or converted effect rather than a local effect. Experimental verification of slope-converted ship generated noise was reported by Wales and Diachok [1981] at a site bathymetrically shielded from contamination of high latitude ducting effects, by Carey [1986] using a towed narrowband source and by Hodgkiss and Fisher [1987] who present decreasing noise magnitude results as a function of range from the California coast. Downslope conversion has been accepted as a mechanism for translating surface generated noise to the deep sound channel, however the existence of the pedestal structure in the vertical directionality from low shipping density areas suggests a major energy source is that of distant storms.

Local storm energy has been shown to contribute to the ambient noise field as well. Storm induced noise has been observed at high frequencies as the spectral levels increase with wind speed. At low frequencies however, there is no consensus regarding the extent of the wind induced effects. Efforts to conform to the logarithmic dependencies seen at high frequencies has led to a variety of predicted low frequency spectral levels [Urlick, 1984]. Difficulties arise in estimating the "wind dependent portion" [Crouch and Burt, 1972] of an omnidirectional signal which may be affected by other sources. An obvious experimental approach is the use of the directional capabilities of an array, however, previous measurements [Burgess and Kewley, 1983; Hodgkiss and Fisher, 1987] introduced additional parameters in terms of variations in location and time which complicate interpretation of wind induced effects.

The advent of large aperture arrays with many elements provide measurements of ambient noise characteristics with high resolution. In this report,

use of a large aperture array equipped with an acoustic navigation system which allows array shape estimation, enables study of ambient noise fine-scale structure. The array, deployed from Research Platform *FLIP* which was moored in the NE Pacific, was positioned at three nominal depths covering the water column from 400 m to 3100 m with 7.5 m sampling increments. The 900 m array aperture produced a 1° beam at 100 Hz. A detailed estimate was obtained of the vertical spatial variability of ambient noise as wind speed increased from 2 m/s to 12 m/s over a 21 hour period.

Previous work indicated that the array shape may be estimated as straight and nearly vertical, moving for the most part like a simple pendulum [Sotirin and Hildebrand, 1989]. Array calibration showed that specific channels may be limited by system noise and should be avoided, however the accumulated effect of these channels does not contaminate the directional spectral levels [Sotirin and Hodgkiss, 1989].

The present work is presented in three sections. Preliminary statistical test results, reported in Section I, show that ambient noise data consist of independent samples of normally distributed processes which are stationary over limited time periods. Temporal variability of ambient noise is studied to assist in comparisons of data recorded at different times. Issues of spectrum restoration, beamformed sidelobe leakage and angular resolution are discussed in Section II. Ambient noise spectral levels, presented in the last section, are compared to previous measurements. The small noise level variation with depth, the shape of the spatial distribution and deviations with respect to frequency, time and wind speed are presented. A fine scale analysis of ambient noise during the passage of a local storm is shown.

4.3. TEMPORAL VARIABILITY

This section describes the temporal variability of ambient noise as a prerequisite to data processing and interpretation. The ambient noise field is analyzed for independence and time stationarity. Earlier investigations indicated that the time period of fluctuation depends upon the mechanism generating the noise; measurements above 150 Hz correspond to weather patterns whereas noise measurements between 20 and 150 Hz correspond to the proximity, density and speed of ship traffic [Jobst and Adams, 1977]. Our results show that complex narrowband samples at 75 Hz, a ship dominated frequency, are independent and Gaussian with stationarity lengths longer than previously reported (3 minutes at high wind speed [Arase and Arase, 1968] and 22 minutes at unreported wind speed [Jobst and Adams, 1977]). The underlying processes create an ambient noise field which varies with ship distribution, speed and density, and with environmental parameters such as wind speed and sound speed profile. The mean distribution is modulated by small scale variations which impose a limit on the significance of measurement deviations. The variance of ambient noise spectral measurements increases with the length of time between samples, even for constant array depth, wind speed and time of day.

4.3.1. Statistical Tests

Statistical tests were used to analyze ambient noise data for independence, stationarity and normality. The test data consisted of sequential complex spectral estimates at 75 Hz every second (1.024 s) over a 50 minute interval for each of the 120 array channels. The estimates were calculated with a 1 Hz bandwidth from 512 data samples windowed with a Kaiser-Bessel function ($\alpha = 2.5$). Two data segments were selected: (1) local wind speed of 4 kts (Julian day 268, GMT 1010 where GMT is Greenwich Mean Time) with the array deployed vertically between 2200 m and 3100 m and (2) local wind speed of 20 kts (Julian day 258, GMT 1437) with the array deployed between 400 m and 1300 m.

Sample independence was determined using the nonparametric runs test based on pair-wise deviations [Middleton, 1969]. Sequential sign consistent values, calculated as the difference between sequential sample pairs, constitute a run. If the narrowband process at a sensor is $A(t)\cos(\omega t + \phi(t))$ and the inphase and quadrature components are $I(t) = A(t)\cos\phi(t)$ and $Q(t) = A(t)\sin\phi(t)$ respectively, then the pairwise values employed in the runs test are $SGN[I(t) - I(t+1)]$, and $SGN[Q(t) - Q(t+1)]$, where t is incremented ($\delta t = 2$ s) over the data segment. The number of runs then is illustrated by example; i.e. ++++---+---+---++ has $r=7$ runs, $M_1=8$ positive values, $M_2=9$ negative values, and $M=17$ values. If the data are independent observations of the same random variable then, for large M ($M > 40$), r is a normally distributed random variable with a mean and variance of [Bendat and Piersol, 1971]:

$$\mu_r = \frac{2M_1M_2}{M} + 1; \quad \sigma_r^2 = \frac{2M_1M_2(2M_1M_2 - M)}{M^2(M-1)}; \quad Z_s = (r - \mu_r)/\sigma_r$$

where Z_s is the test statistic. The test statistic Z_s is a zero mean Gaussian random variable which is tested against an a priori determined threshold Z_α , where α is the significance level. The null hypothesis for this test is that the M observations are independent samples of the same random variable. If $Z_s \leq Z_\alpha$ then the null hypothesis is accepted at the α level of significance. The data segments for this test were each 50 minutes long ($M > 4000$) and results for the 0.05 and 0.1 significance levels were calculated. The significance level is the probability that the null hypothesis will be rejected when the segment is independent; at the 0.1 level of significance, 90% of the segments should pass. Inphase and quadrature components for each array channel result in 240 data segments, so at the 0.1 level of significance, 24 test results would be falsely rejected and at the 0.05 level of significance, 12 test results would be falsely rejected. At low and high wind speeds, 18 and 24 segments failed the test at the 0.1 level of significance level respectively, and 10 failed at the 0.05 level of significance, showing that the data are independent.

The stationarity time length was determined by the Kolmogorov-Smirnov two-sample test. This method used the cumulative distribution function (CDF) of the data (Figure 4.1) which is the fraction of samples whose amplitudes are less than a specified value. Procedurally, the data segment is divided in half and the CDF is calculated for each half. The Kolmogorov-Smirnov test statistic is the maximum value of the absolute difference between the two CDF's:

$$Z_{\text{sample}} = \max |F_{\nu_1}(x) - F_{\nu_2}(x)|.$$

The null hypothesis is that the two data sets belong to the same distribution. If

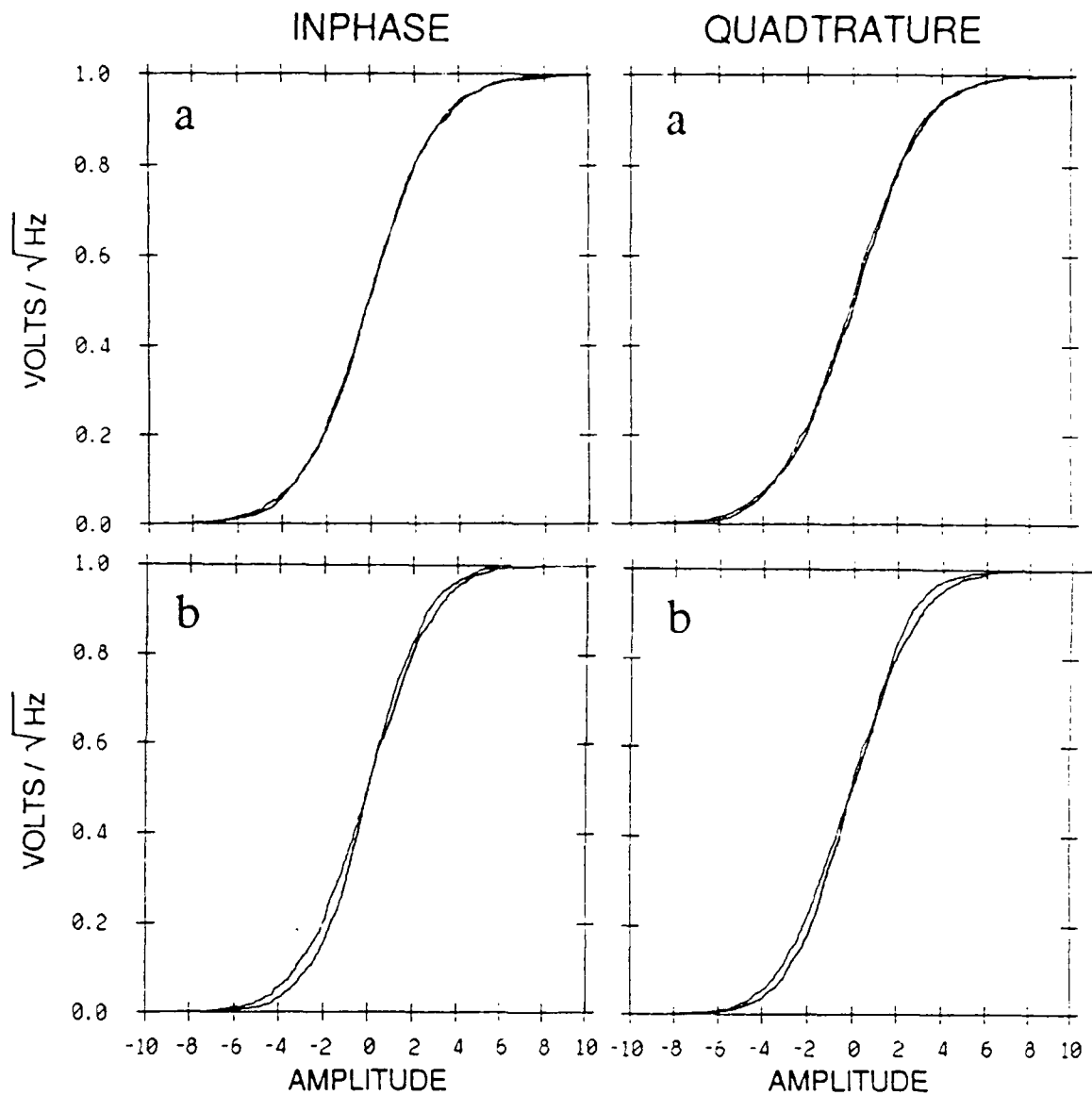


Figure 4.1 Cumulative distribution two-sample test. The results of the Kolmogorov-Smirnov two-sample test are shown for the inphase and quadrature components of array channel 23 for a 50 minute time segment at 75 Hz. The segment on top (a) is accepted as being stationary at the 0.05 level of significance. This segment was recorded during a low wind condition (2 m/s) and the array was deployed nominally to 2650 m. The segment on the bottom (b) fails at the 0.05 level of significance; 10 m/s winds prevailed and the array was deployed at a nominal depth of 850 m. The Julian day (Jday) and Greenwich mean time (GMT) are indicated.

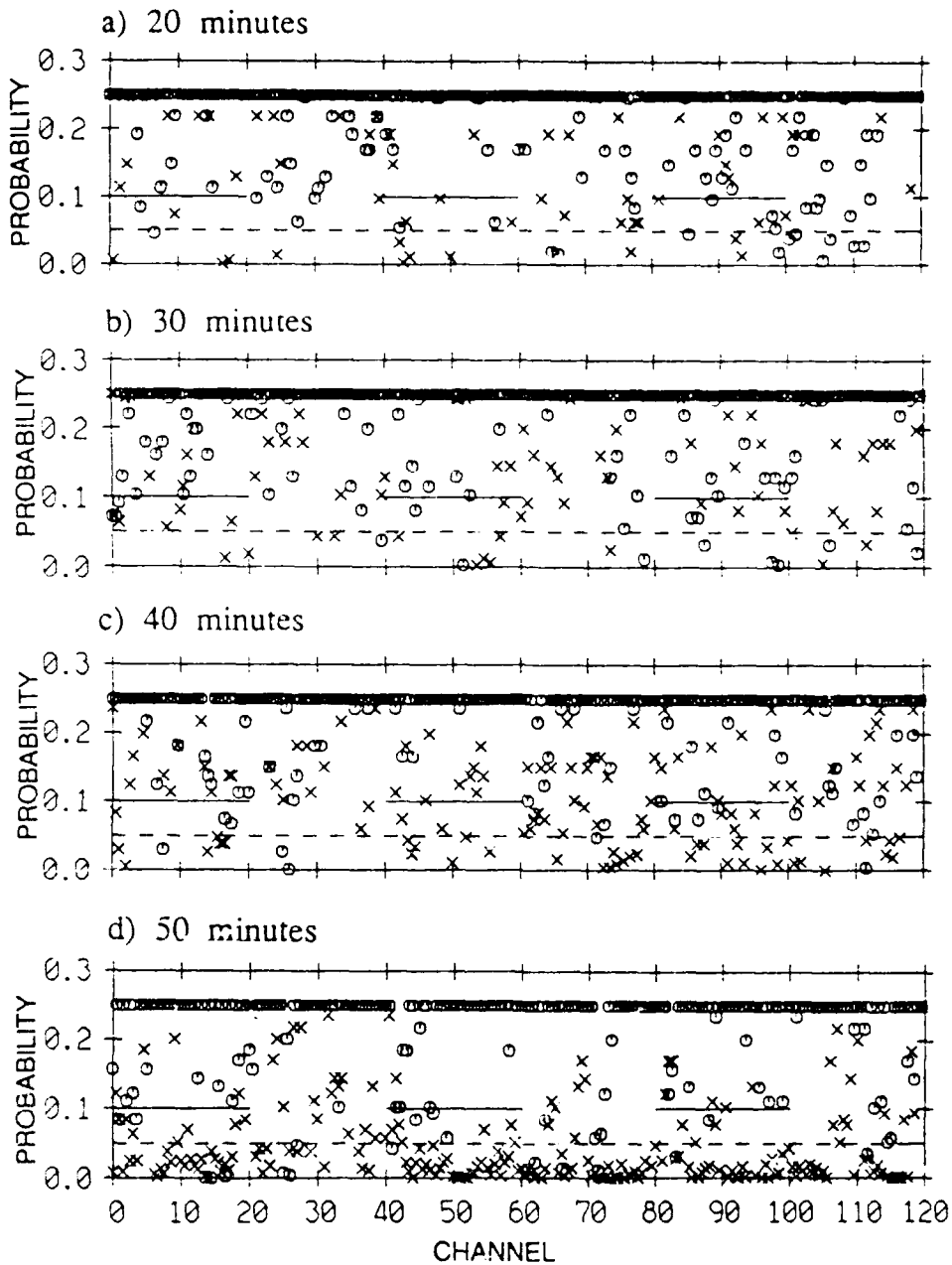


Figure 4.2 Data stationarity. The probability α of the observed test statistic is shown for the inphase and quadrature components of each array channel. The o's represent the low wind speed data segments; the x's represent the high wind speed data segments. The 0.05 level of significance is shown with small dashed lines; the 0.1 level of significance is shown with large dashed lines. Probabilities greater than 0.25 were clipped for illustrative purposes. Interpretation of this data is such that any test result represented as an x or o which is less than a specified probability fails at that level of significance; e.g. the null hypothesis that the two data segments have the same distribution is rejected at the 0.05 level of significance for any result which is less than 0.05.

$Z_{sample} \leq Z_{\alpha}$ then the hypothesis is accepted at the α level of significance. For a large number of data points ($N > 20$), the significance level of the test statistic Z_{sample} is [Press, *et al*, 1986]

$$Q_{KS}(Z_{\alpha} > Z_{sample}) = Q_{KS}(\lambda) = 2 \sum_{j=1}^{\infty} (-1)^{j-1} e^{-2j^2 \lambda^2},$$

$$\text{where } \lambda = \sqrt{\frac{N_1 N_2}{N_1 + N_2}} Z_{sample}$$

The significance level was calculated for the inphase and quadrature components of each array channel over time periods of 20, 30, 40 and 50 minutes (Figure 4.2).

The results are different for the two data segments. The low wind speed segment is stationary at the 5% level of significance for up to 50 minutes. At 60 and 70 minutes, the number of individual test which fail is still less than 9% at the 0.05 level of significance. For the high wind speed segment however, the stationarity hypothesis is accepted at the 0.05 level of significance for a segment length of 20 minutes, but fails by a narrow margin (5.42%) at 30 minutes with the number of failures increasing significantly above 30 minutes.

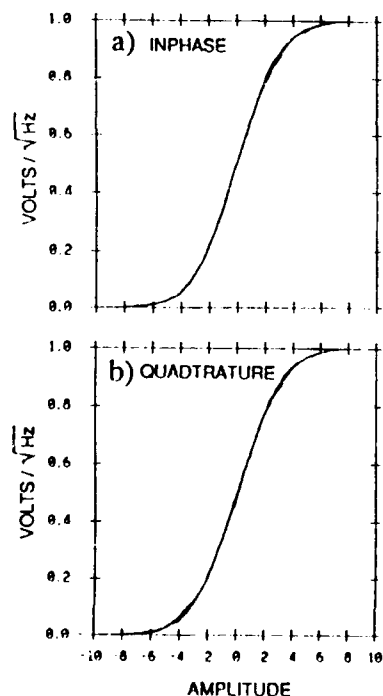


Figure 4.3 Cumulative distribution one-sample test. The Kolmogorov-Smirnov one-sample test results are shown for the 75 Hz inphase and quadrature components for array channel 23 for a 50 minute data segment with a Gaussian distribution of the same mean and variance as the data segment. The data was from the high wind speed segment. The sample mean and variance for the inphase segment was $6.99e-02$ and 7.67 , respectively. The sample mean and variance for the quadrature segment was 0.157 and 7.70 , respectively. Data segment lengths of 20, 30 and 40 minutes also passed.

The hypothesis that the data components are normally distributed is tested using the Kolmogorov-Smirnov one-sample test. The procedure is similar to the two-sample test with the test statistic Z_{sample} defined as the maximum difference between the experimental cumulative distribution and that of a normally

distributed function with the same mean and variance as the data segment. The null hypothesis that the inphase and quadrature components of the narrowband noise are normally distributed is accepted at the α level of significance if $z_{sample} \leq z_{\alpha}$. The probability that $z_{sample} \leq z_{\alpha}$ is calculated from the equation above with $\lambda = \sqrt{N}z_{sample}$, where N is the number of data samples in the segment. Although the probability is defined for an a priori determined theoretical distribution, use of the data sample mean and variance leads to a more conservative test by decreasing the observed test statistic [Middleton, 1969]. The cumulative distribution functions for array channel 23 and the Gaussian distribution with sample mean and variance are shown in Figure 4.3. The hypothesis was accepted for the inphase and quadrature components for both the high and low wind speed segments at the 0.05 level of significance.

There appears to be a local wind speed dependence in the stationarity results (Figure 4.2). However, additional data samples were not available to corroborate this hypothesis, and due to the difference in array depth during the recording of the samples, a wind dependence can not be substantiated without further analysis. Although these tests were conducted over only a few data segments, it is assumed that under similar conditions, the data segments used in the ambient noise analysis may be considered independent, stationary and normally distributed.

4.3.2. Spectral Estimate Variability

In many investigations, the variation in ambient noise due to specific processes requires that the noise field be sampled at different times. For instance, to investigate ambient noise versus wind speed, the data recorded at specific wind speeds but at different times are compared. The mean spectral level is a not solely a function of wind speed and an estimate of the small scale variability is required to ascertain the significance of changes in wind speed. This variability is a combination of spatial and temporal interference patterns across the array during the sampled interval. To estimate the variability of ambient noise spectral values with time, spectral estimates at 75 Hz were calculated from data recorded during similar environmental conditions and at approximately the same time of day. The data were analyzed in terms of the variance of spectral differences across the array versus time. Squared magnitude estimates over a 22 minute interval were averaged, calibrated [Sotirin and Hodgkiss, 1989] and plotted for each array channel at 75 Hz. The data were selected to be free of any known nonstationary effects (e.g. seismic profiler, large strum amplitudes, nearby ships) with the expectation that the spectral level would vary smoothly across the array. A regression fit to the data (whose mean level varies little with depth) was subtracted leaving channel deviations. The time difference between these channel deviations is illustrated in Figure 4.4 where increasing variability is seen with increasing time lengths. This increase is quantified by calculating the variance across the array for each of the data segment pairs, and is plotted as a function of the logarithm of the time difference in Figure 4.5, demonstrating time variability of the ambient noise field. Although a sparse sampling is presented, a definite increase of variance is observed with time. Differences in spectral measurements taken at different times or at different spatial locations which are about 1 dB, could be due to either temporal and/or spatial variability of the source mechanisms in force.

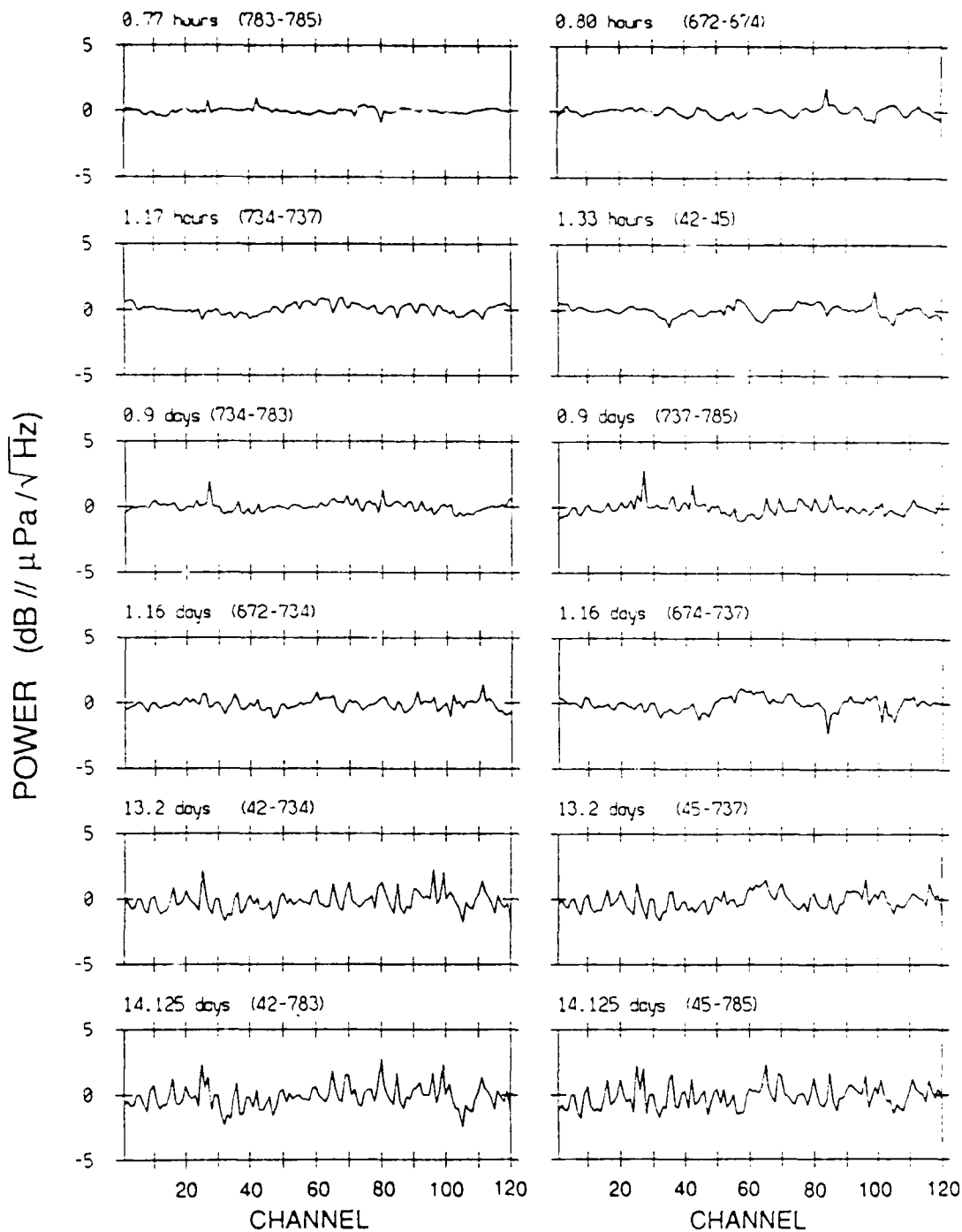


Figure 4.4 Variability of ambient noise spectral levels across the array. Spectral deviations as a function of time were differenced to investigate temporal variability across the array. The panels represent the channel to channel variation of spectral estimates separated in time by the amount shown above each panel. The spectral estimates were generated by incoherently averaging the squared magnitude FFT outputs for each array channel. The input segments were 50% overlapped, Kaiser-Bessel windowed ($\alpha=2.5$), 1 second time series resulting in 2583 estimates of 0.98 Hz bin width. Each data sequence was 22 minutes in length and the results were plotted in dB re $\mu\text{Pa}\sqrt{\text{Hz}}$. The 95% confidence interval of the estimates is +0.166 dB, -0.162 dB.

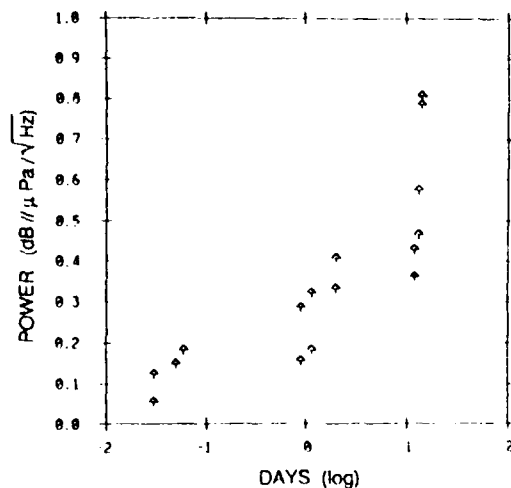


Figure 4.5 Variance as a function of time. The variance across the array of the spectral estimate differences is plotted as a function of the logarithm of the time difference.

4.4. INTERPRETING BEAMFORMED DATA

An acoustic array is a collection of hydrophones at discrete points in space whose outputs may be coherently combined in the beamforming process to estimate the directional spectrum of the ambient noise field. Use of such an array produces a distorted picture of the true directional spectrum, which may be discussed as two separate artifacts. The first is attributable to the discrete sampling of a continuous process, yielding limitations in wave number amplitude and spatial aliasing at frequencies above $f = c/2d$ where c is the propagation speed and d is the array element spacing. The second is attributable to the spatial response of the array (a function of the array aperture) which bounds the angular resolution in vertical angle of arrival. If the array response (beam pattern) were represented by an impulse function, then the beamformer output would accurately reflect the actual noise field input. This is not the case for the array considered here whose weighted spatial characteristics, due to finite length and limited number of elements, are described by a main beam of non-zero width which varies with frequency, and sidelobe levels between -30 and -40 dB.

The array beam pattern is a spatial filter which is convolved with the true noise field to produce the estimated spatial spectrum. The Fourier transform of the beam pattern illustrates the angular resolution of the array and is shown for 55 Hz in Figure 4.6. The estimated spectrum has a band limited angular response because the angular resolution is band limited. The zero crossing of the beam pattern, known as the critical angle ϕ_c [Bracewell and Roberts, 1954], is approximated by $\frac{\lambda}{l}$ where λ is the wavelength and l is the array aperture. The critical angle for the specific range of wave lengths considered here varies from 0.112 to 0.013 requiring a minimum sampling interval of 0.056 to 0.0065 radians (3.21 to 0.37 °) which is satisfied by the 512 point transforms discussed in the next section.

Recognizing the limitations of the array, various approaches have been suggested to estimate the true noise field, assuming that the array response function is independent of steering direction and is well known [Bracewell, 1958; McDonough, 1975]. These methods are constrained by the nonuniqueness of the solution, numerical difficulties, processing artifacts and uncertainty in the array beam pattern response. A technique known as successive substitution [Bracewell and Roberts, 1954] was applied to samples of the measured ambient noise field at various frequencies to ascertain the gross effects of the array as a measurement

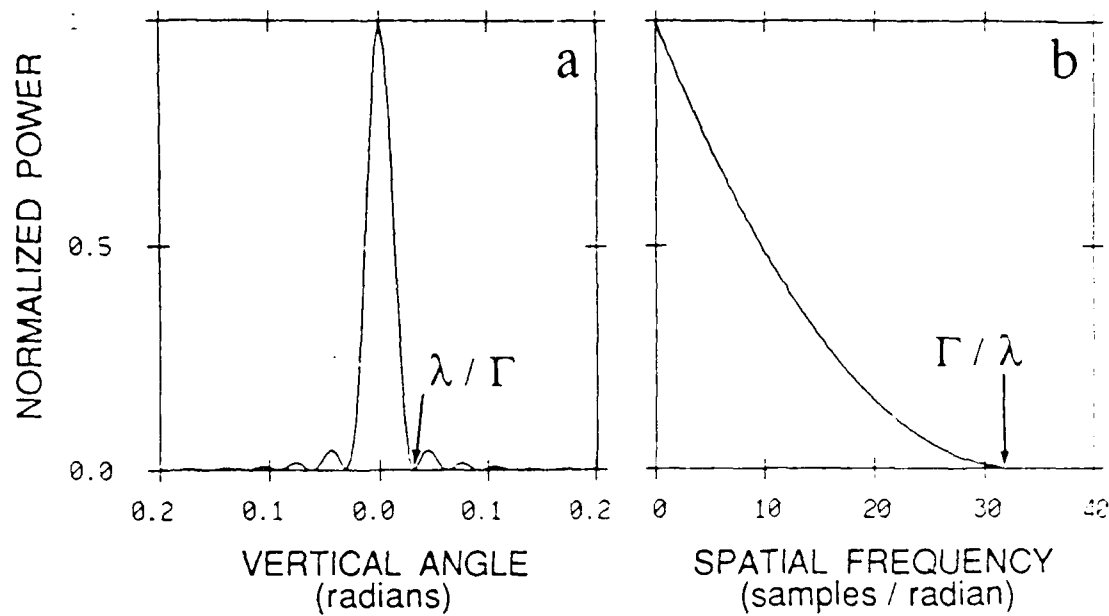


Figure 4.6 Angular resolution of the array. The theoretical array beampattern at 55 Hz is shown (a) for physical angles in normalized linear units on an expanded horizontal scale ($-\pi/16$ to $+\pi/16$). The Fourier transform of this beampattern shows the bandlimited angular frequency cutoff at $\chi = \Gamma/\lambda$.

system. An alternative to the restoration scheme in determining the limits of array distortion is that of a more controlled environment in which the "true" noise field, completely determined a priori, is convolved with the estimated array beampattern and compared to the measured data. Simulations indicate a sensitivity to array sidelobe structure under certain conditions, consequently absolute levels outside the ambient noise pedestal, must be viewed with regard to the parameters discussed below.

4.4.1. Spectrum Restoration

This technique is an iterative method of correcting the distortion produced by the array in estimating the true spectrum. Adjustment ΔM to an initial approximation of the true directional power spectrum M_{app} is accomplished by subtracting the convolved output of M_{app} and the known array beampattern A , from the measured directional power spectrum M_a :

$$\Delta M = M_a - (A * M_{app}).$$

The initial approximation M_{app} is adjusted producing a new approximation for the next iteration, proceeding until the adjustment is small; typically only a few iterations are required. Using the array beamformed output M_a as the initial

approximation, the procedure is shown below;

$$M_n = M_{n-1} + (M_d - A * M_{n-1}).$$

The resulting restored spectrum remains band limited because of the angular resolution of the array and is termed the principle solution, restoring the components within the array's measurement capability. If the true spectrum contains components outside the band of the array ($> \lambda$ in Figure 4.6), then the Fourier transform of the principle solution will contain a discontinuity at λ which may produce oscillatory characteristics in the restored spectrum. To illustrate the seriousness of this effect for the vertical array measurement of the ambient noise field, a simulated field was constructed (Figure 4.7). This field is defined in terms of normalized wave number

$$\frac{v}{2\pi} = k \left(\frac{d \sin \theta}{2\pi} \right),$$

where the limits of visible space correspond to $\sin \theta = \pm 1$, or $-kd \geq v \leq +kd$; k is the wave number, d is the array element spacing and θ is the look direction. It is possible to incorporate phase delays which correspond to space that is not physically realizable. This space is referred to as invisible space and the beams corresponding to delays $> |k|d$ are called virtual beams. The ambient noise field used for this simulation is typical of ambient noise at 55 Hz with high angular frequencies (Figure 4.7a). This field was convolved with a known array beampattern (Figure 4.7b) at 55 Hz to produce the measured spectrum (Figure 4.7c) which was introduced as the initial approximation in the iterative restoration scheme. Comparing the principle solution (Figure 4.7d) to the true spectrum (Figure 4.7a) illustrates their differences including: overshoot in regions of sharp angular change, oscillation particularly in the invisible region, a slight broadening of the pedestal width and a small amplitude deviation of less than 0.5 dB. An example of restoration of the ambient noise data discussed in the following sections is shown in Figure 4.8. The array beampattern (Figure 4.8a) used a Kaiser-Bessel ($\alpha=1.5$) amplitude weighting function and the estimated array amplitude and phase calibration errors [Sotirin and Hodgkiss, 1989]. The original angular distribution (recorded on Julian day 270 at 0400 GMT) is typical of ambient noise data at high wind speed for 55 Hz with a 15 dB pedestal approximately between $\pm 18^\circ$ of horizontal. Restoration sharpens the discrete source components, minimally increasing the peaks and decreasing the valleys, but preserves the absolute levels and overall shape. There are noticeable oscillations in this example, particularly at the higher angles. The gain in directional resolution, particularly in the pedestal region, is offset by the additional processing required, the relatively minor level corrections, the obscure distinction between processing artifacts and restored distribution, and possible errors in the estimated beampattern. Therefore, restoration was not applied to the bulk of the data but used as a tool to aid in data interpretation for select cases.

The small differences between the measured noise field and the restored noise field outside the pedestal region in Figure 4.8, indicate that this region is not contaminated by array sidelobe levels as illustrated by the 2-3 dB level change in Figure 4.7 for the same region. The susceptibility to array sidelobe contamination of different measured distributions is quantified by simulations below.

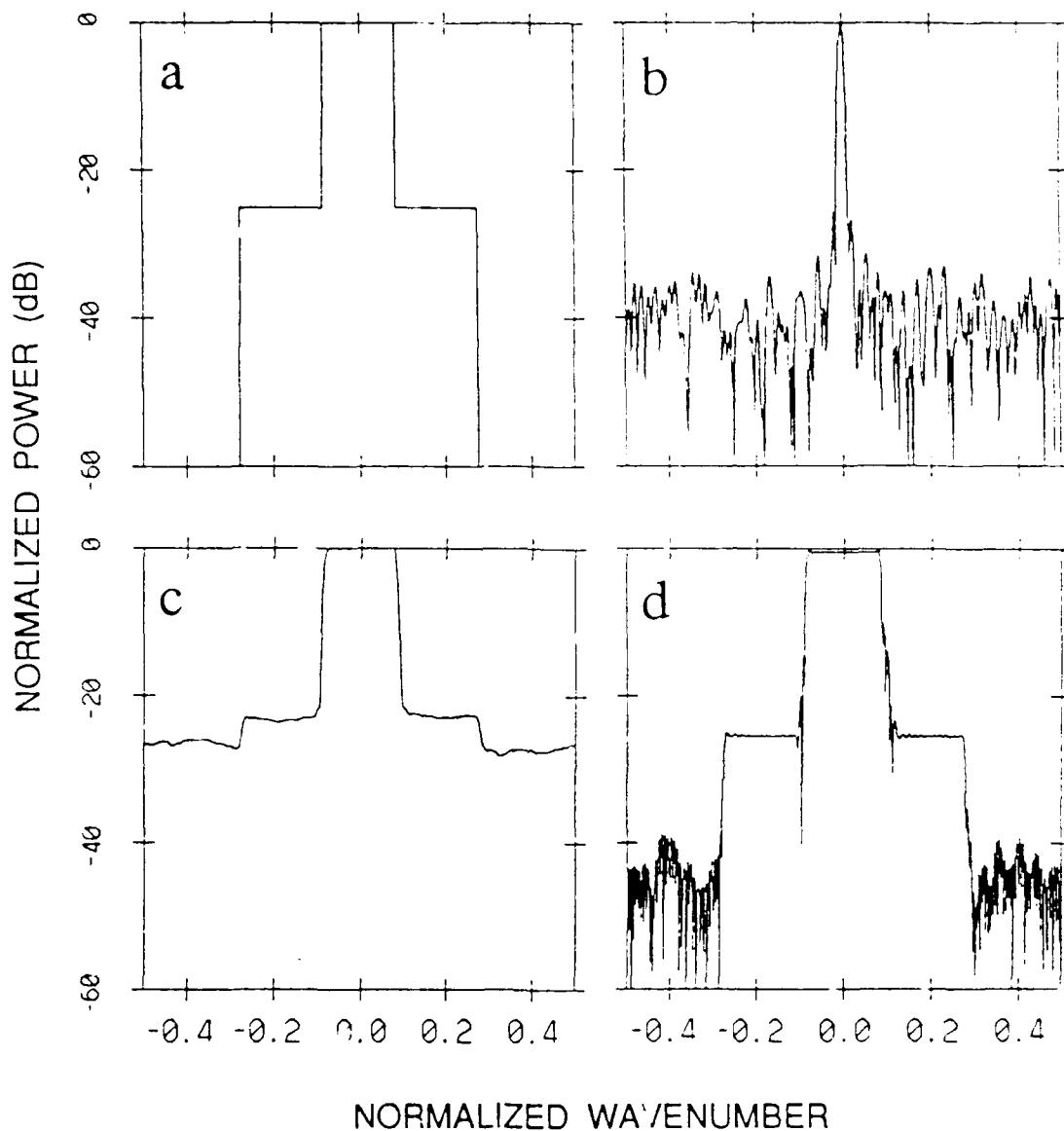


Figure 4.7 Spectrum restoration simulation. The spectrum restoration method is tested for simulated ambient noise data by defining the "true" vertical ambient noise field where the ambient noise pedestal is represented here with a 0 dB level between ± 0.085 . The level then drops to -25 dB until the limit of real space at ± 0.275 , beyond is invisible space at a -100 dB level. This "true" noise field (a) is convolved with a known array beam pattern at 55 Hz (b) to provide a measured spectrum (c) with which to test the method expecting to restore the original spectrum (a). The resulting solution is shown in (d) to exhibit some oscillatory characteristics and a slight level decrease.

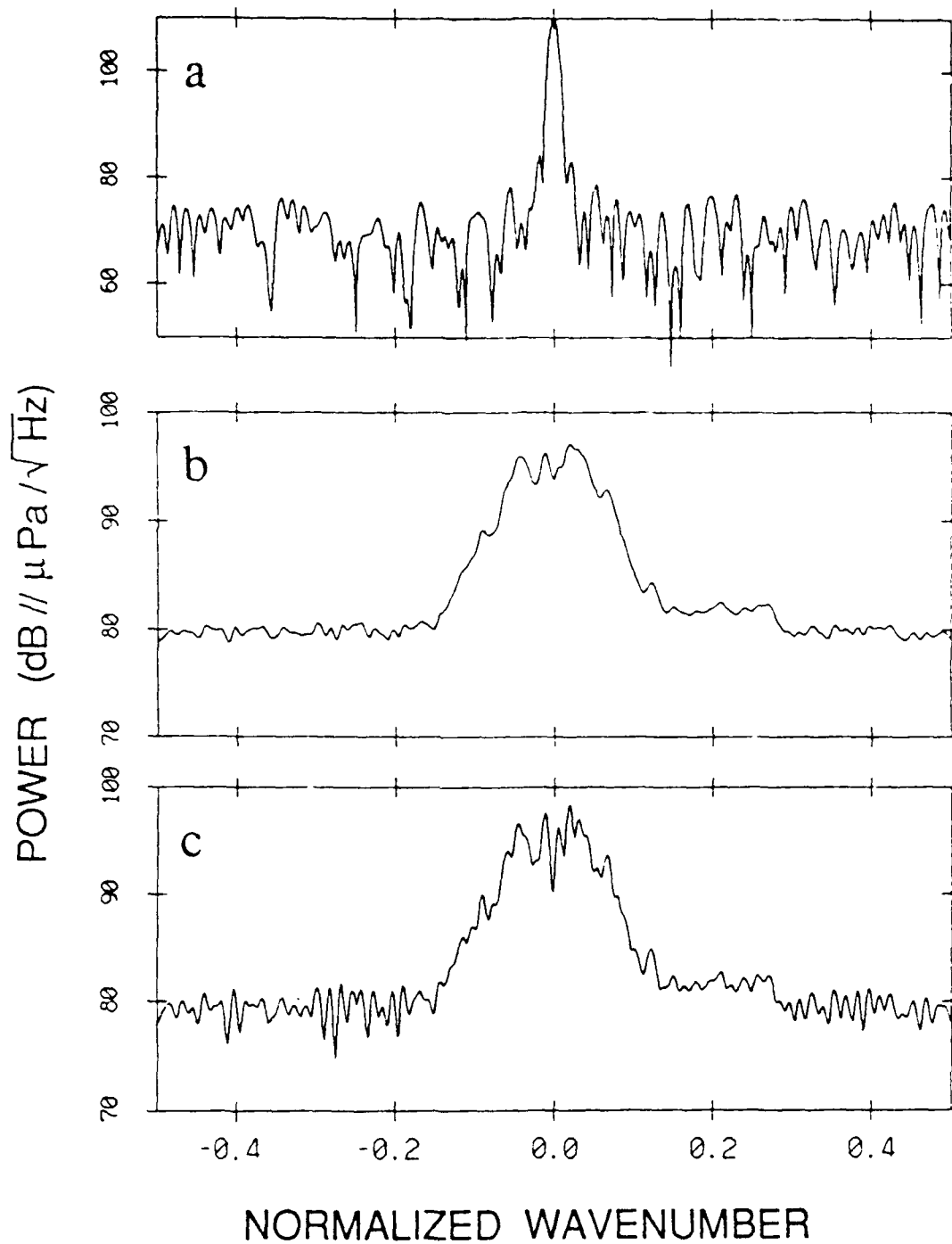


Figure 4.8 Ambient noise spectrum restoration. A representative example of the spectrum restoration using array beamformed data at 55 Hz from Julian day 270 at 0400 GMT with an 11 m/s wind speed. The positive angles represent upward looking angles. The array beam pattern used in the restoration is shown in (a), the original angular spectrum is shown in (b) and the restored spectrum is shown in (c). The restoration increases the peaks in the pedestal by as much as several dB and decreases the valleys similarly. The levels outside the pedestal exhibit oscillatory characteristics, but in general, the absolute levels and overall shape are preserved.

4.4.2. Simulations

Insight into the distortion imposed by the array may be gained by convolving a simulated spatial noise field with the array beampattern, and quantifying the result in terms of a main beam to sidelobe ratio. The spatial ambient noise field is approximately described by a $\pm 15^\circ$ to $\pm 20^\circ$ pedestal at a level of 5 to 30 dB above the high angle level where "high angles" are defined to be visible space outside the pedestal region. Although the pedestal height is defined relative to the high angle level, a change in pedestal height actually reflects a change in the high angle level as opposed to a change in the pedestal level. The array beampattern is approximately described by a narrow rectangular main beam with flat sidelobes at -30 to -35 dB. The width of the rectangular main beam is calculated to provide a power gain equivalent with that achieved with the calibrated main beam, shown in Table 4.1 as equivalent beam width (EBW) for a broadside and 45° looking beam. For the normalized beampattern in Figure 4.6, the EBW =

$\sum_{n=-\frac{\lambda}{\Gamma}}^{+\frac{\lambda}{\Gamma}} B(n\theta)$ where B is normalized power magnitude shown in the figure. The main beam to sidelobe ratio (MSR) is then defined as the integrated power seen by the main beam when it is steered to a specified direction over the integrated power seen by the array sidelobes, given the known spatial ambient noise field.

Frequency (Hz)	15	35	55	75	95	105	115	125
broadside EBW	8.4°	3.6°	2.3°	1.7°	1.3°	1.2°	1.1°	1.0°
45° look angle EBW	12.1°	5.1°	3.3°	2.4°	1.9°	1.7°	1.6°	3.7°

Table 4.1 Equivalent beamwidth.

Two sets of simulations were conducted. The parameters varied during the simulations were pedestal width, pedestal height, array sidelobe level, look direction and frequency. The first set was conducted at 55 Hz for various spatial noise fields and array sidelobe levels with results shown in Table 4.2. The noise fields considered were $\pm 15^\circ$ pedestal width at power levels of 10, 20 and 30 dB above the high angle levels, and $\pm 18^\circ$ and $\pm 20^\circ$ widths at 10 and 20 dB levels. Two array sidelobe levels were specified at -30 and -35 dB relative to the main beam, and two look directions were specified at broadside and $+45^\circ$. Interpretation of the MSR results are enhanced by examining the relative differences in angular component levels. That is, for a pedestal of $\pm 18^\circ$ width and 20 dB height, the convolved response accurately measures the pedestal width but distorts the height. Relative differences between the true height and the convolved height are shown in parenthesis in Table 4.2 preceding the corresponding MSR for selected cases. To achieve a measured response to within a 1 dB level of the true distribution requires an MSR of about 0.85 dB. The results show that the MSR is more than adequate to measure the pedestal distribution irrespective of the specific parameters, however the higher angle levels are sometimes distorted. As the pedestal width is increased, the MSR decreases as more energy is picked up by the array sidelobes. As the pedestal height is increased, the MSR at the $+45^\circ$ look angle decreases. The second

Noise field description	Array sidelobe level (dB)	Mainbeam to Sidelobe Ratio (dB)	Look direction
flat	-30	1.1 1.3	broadside +45°
	-35	1.6 1.8	broadside +45°
±15° pedestal at 10 dB	-30	1.7 0.90	broadside +45°
	-35	2.2 1.4	broadside +45°
±15° pedestal at 20 dB	-30	1.9 0.08	broadside +45°
	-35	2.4 0.57	broadside +45°
±15° pedestal at 30 dB	-30	1.9 -1.0	broadside +45°
	-35	2.4 -0.40	broadside +45°
±18° pedestal at 10 dB	-30	1.7 (0.75) 0.85	broadside +45°
	-35	2.2 1.3	broadside +45°
±18° pedestal at 20 dB	-30	1.8 (4.0) 0.0	broadside +45°
	-35	2.3 (1.75) 0.49	broadside +45°
±20° pedestal at 10 dB	-30	1.7 0.81	broadside +45°
	-35	2.2 1.3	broadside +45°
±20° pedestal at 20 dB	-30	1.8 -0.05	broadside +45°
	-35	2.3 0.43	broadside +45°

Table 4.2 Mainbeam to sidelobe ratio (dB) at 55 Hz.

set of simulations was conducted for various frequencies, pedestal heights of 10 and 20 dB and a constant pedestal width of ±18°, which approximates the ambient noise field observed during the experiment. The results, shown in Table 4.3, exhibit a decreasing MSR with increasing frequency, expected as the main beam width decreases.

Frequency (Hz)	Noise field description		Mainbeam to Sidelobe Ratio (dB)	Look direction
15	$\pm 18^\circ$ pedestal	10 dB	2.8 2.0	broadside +45°
		20 dB	3.0 1.2	broadside +45°
35	$\pm 18^\circ$ pedestal	10 dB	2.4 1.6	broadside +45°
		20 dB	2.5 0.69	broadside +45°
55	$\pm 18^\circ$ pedestal	10 dB	2.2 1.4	broadside +45°
		20 dB	2.3 0.49	broadside +45°
75	$\pm 18^\circ$ pedestal	10 dB	2.0 1.7	broadside +45°
		20 dB	2.2 0.34	broadside +45°
95	$\pm 18^\circ$ pedestal	10 dB	1.9 1.1	broadside +45°
		20 dB	2.1 0.2	broadside +45°
115	$\pm 18^\circ$ pedestal	10 dB	1.9 1.0	broadside +45°
		20 dB	2.0 0.15	broadside +45°

Table 4.3 Mainlobe to sidelobe ratio (dB) with -35 dB array sidelobes.

It has been suggested that virtual beam levels (beams outside visible space) may be used to indicate the sidelobe suppression levels of an array [Berrou, Bluy and Wagstaff, 1982; Wagstaff, 1988]. The virtual beam level is indeed a function of the array sidelobe level however other significant factors (array main beam width, directional spectrum input) affect this level such that its interpretation is not straight forward. For the directional spectrum provided by a typical ambient noise field, and the specific characteristics of the array considered here at 55 Hz, the drop in level between visible beams and virtual beams is shown in Figure 4.9 to be less than 5 dB for array sidelobe levels of -35 dB and about 2 dB for sidelobe levels of -30 dB. If the array calibration errors were to be included in the array beampattern, the drop would be even less conspicuous. For a wider main beam and a strong directional source [Wagstaff, Berrou and Cotaras, 1982], this technique may be more valuable as an array assessment tool. The directional spectrum in Figure 4.9 is plotted in terms of normalized wavenumber where ± 0.275 represent the limits of visible space. The 'real' data represents a $\pm 18^\circ$ pedestal width at a 20 dB level relative to the higher angles and 100 dB relative to the invisible space level.

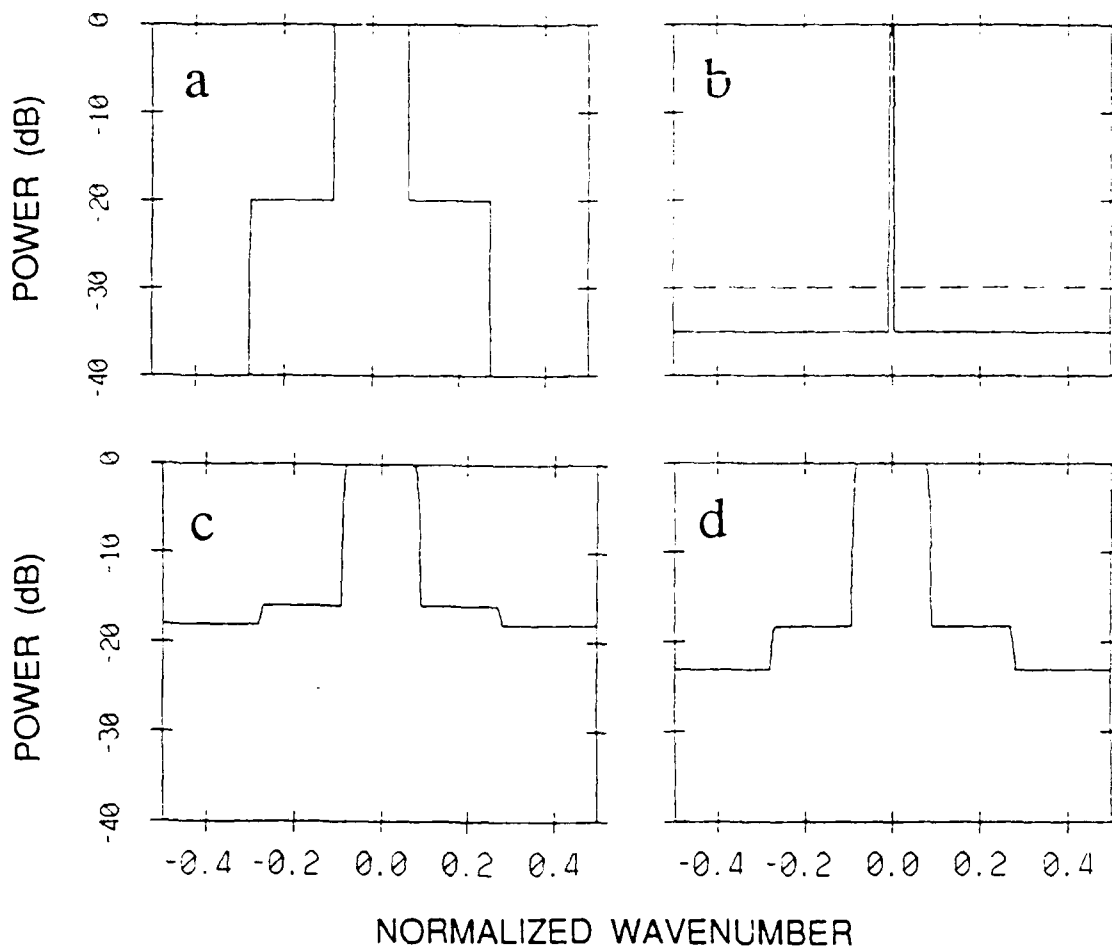


Figure 4.9 Virtual beam simulation. Virtual beams are those whose phase delay does not correspond to a part of the visible spectrum. At 55 Hz, these beams are those between +0.275 to +0.5 and -0.275 to -0.5. The drop in level between real space and invisible space is a function of the ambient noise field and the array characteristics. The original spectrum (a) is convolved with the array beampattern (b) shown for two sidelobe levels. The simulation results (c) and (d) represent sidelobe levels of -30 dB and -35 dB respectively.

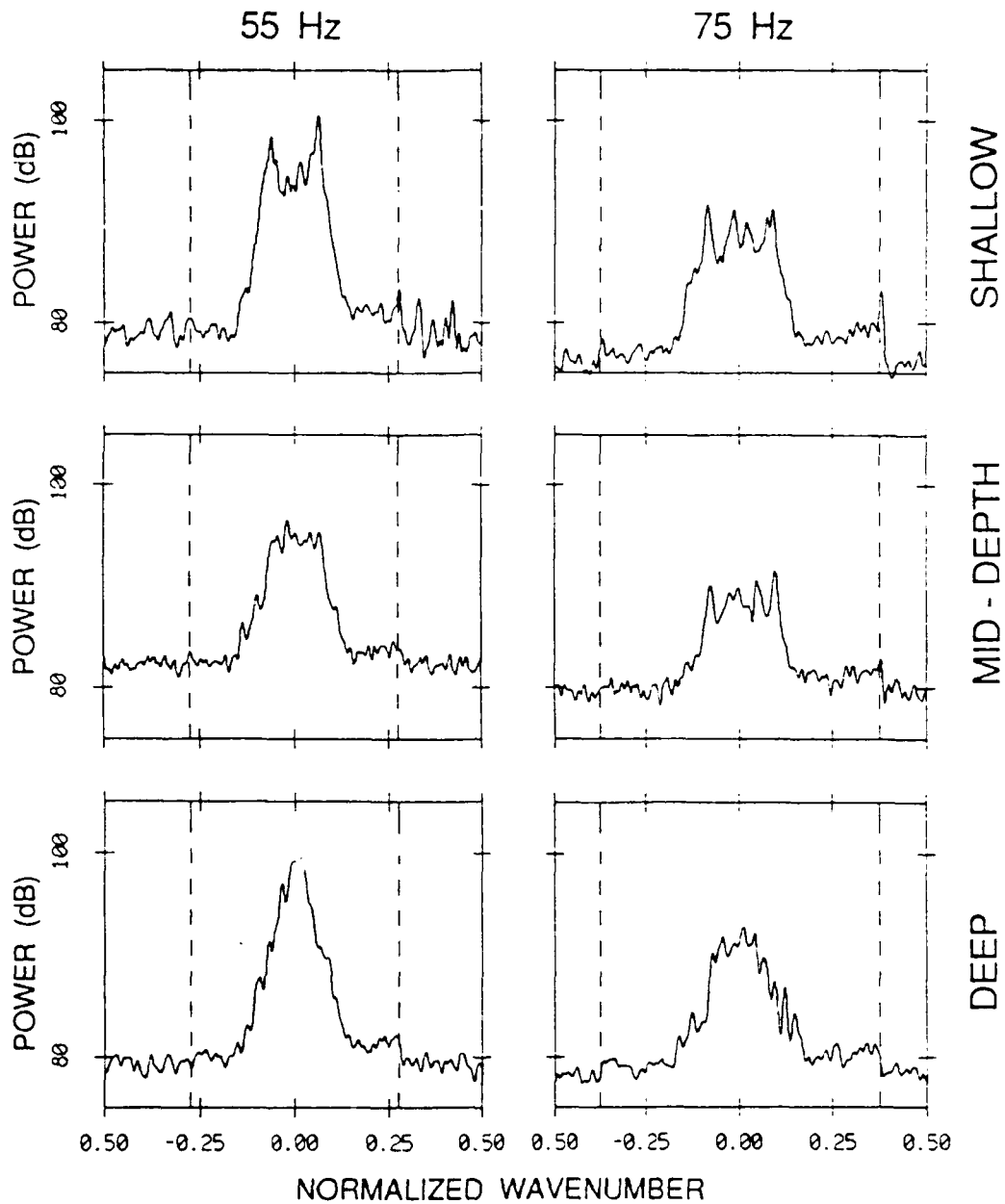


Figure 4.10 Measured virtual beam levels. The drop in level between real space and invisible space for vertical ambient noise is seen at 2 to 5 dB levels. The data were recorded during high wind conditions (11.3 m/s) at three array depths.

The -100 dB level of the virtual beams represents the array electronic noise floor, mechanical energy, and energy from incoherent sources. The array sidelobe levels were constant at -30 and -35 dB relative to the main beam. The virtual beam level is demonstrated for experimental measurements in Figure 4.10 where the expected drop is evident particularly for 75 Hz whose corresponding MSR is less than that at 55 Hz.

The beamformed array data reflects the true ambient noise directional spectrum with some constraints. The beamformer has been shown to have limitations in wave number and vertical arrival angle resolution due to discrete sampling and a nonzero main beamwidth. The large number of elements in this particular array minimizes the distortion caused by the beamwidth but increases concern regarding array sidelobe levels. By observing the main beam to sidelobe ratio under various noise field conditions, it is seen that the array correctly estimates the level and width of the ambient noise pedestal but distorts the high angle level. This amount of distortion increases with frequency, pedestal height and pedestal width. For a $\pm 18^\circ$ pedestal, the array is capable of measuring a 10 dB pedestal height to within 1 dB at all frequencies considered, however as pedestal height increases to 20 dB, the MSR decreases with frequency until at 115 Hz, there is approximately a 3 dB error in high angle level.

4.5. VERTICAL DIRECTIONALITY AS A FUNCTION OF WIND SPEED

The large array aperture (900 m) provides greater directional resolution than any previous work at low frequency. While increasing the resolution, the large aperture also raises concerns about the validity of conventional beamforming due to array shape and wavefront curvature. The array was equipped with an acoustic navigation system [Sotirin and Hildebrand, 1989] which, for the data set presented here, showed the array was straight and vertical to within 1° . Wavefront curvature, resulting from variations in sound speed across the array aperture, is not a major source of error in the ambient noise analysis [Tran and Hodgkiss, 1989], mainly affecting signals arriving within $\pm 5^\circ$ of horizontal with small losses in signal level and a slight distortion in arrival angle. Another concern is mechanical motion or array strum injecting signals which could interfere with ambient noise measurements. It is shown below that although the array does exhibit strum characteristics, the signals are narrow in frequency and in apparent direction.

Ambient noise directionality data were studied at various array depths and local wind speeds. During the passage of a storm, the array was deployed at three depths, provides an opportunity to examine the variation with depth at three nominal wind speeds. Nine 2-minute data segments were processed. The mid-array depth for the three deployments were 850, 1750 and 2650 m, and recorded wind speeds were within 0.5 m/s of 3.1, 7.2 and 11.3 m/s, for the low, medium and high designations. The passage of another storm increased local wind speed from 2 to 12 m/s over a 21 hour period. Two minute samples were selected every 20 minutes during this event to provide a detailed investigation of the directional variability with increasing wind speed.

4.5.1. Data Processing

Data integrity was verified by examining time series and spectra for representative elements. Two-second time series of the 120 channels were scanned at the beginning, middle and end of the 21 hour time series to note any channel variations during the storm. For each 2 minute segment analyzed, the time series for a representative element was plotted over the entire segment to identify any obvious contaminants, such as a seismic profiler operating off the California coast. The profiler signature was perceptible in the time series as shown in Figure 4.11, and was removed prior to subsequent processing. The removal involved piece-wise incoherent averaging in the frequency domain. Calculating the spectra of one channel per array section provided a mid-process verification of the data.

Further processing consisted of selecting desired frequency bins, compensating for an array sampling offset [Sotirin and Hodgkiss, 1989] and beamforming across the full array aperture as well as two 20 element subsections. The data segment (65536 samples for each of the 120 channels) was frequency transformed using a 1024-point Fast Fourier Transform (FFT) after application of a Kaiser-Bessel ($\alpha=2.5$) window. Spectral estimates (0.49 Hz/bin) were selected at 5 Hz increments from 15 to 130 Hz, avoiding narrow band contaminants at 60, 115 and 120 Hz by shifting to 61.0, 113.8 and 118.7 Hz. A frequency dependent phase correction was implemented to account for the sampling offset. The spatial conversion was accomplished using an FFT beamformer, analogous to the time to frequency domain FFT as discussed below. For a time sampled plane wave signal $s(t) = e^{j\omega t}$ arriving at the array at an angle θ from the horizontal, the output of the n th array element is $a_n(t) = s(t + \frac{nds\sin\theta}{c})$ where d is the array element spacing, and c is the propagation speed. A time delay beamformer is a delayed sum of the N weighted element outputs:

$$B_m = \sum_{n=0}^{N-1} w(n) a_n(t - n\tau) = \sum_{n=0}^{N-1} w(n) s(t + \frac{nds\sin\theta}{c} - n\tau)$$

$$= \sum_{n=0}^{N-1} w(n) e^{j\omega t} e^{j\omega \frac{nds\sin\theta}{c}} e^{-j\omega n\tau} = e^{j\omega t} \sum_{n=0}^{N-1} w(n) e^{jn(\frac{2\pi}{\lambda} ds\sin\theta - \eta)}$$

where η is the delay corresponding to the look direction θ_l of the main beam and is equal to $kds\sin\theta_l$ where $k = 2\pi/\lambda$. Defining ϕ as

$$\phi = kd(\sin\theta - \sin\theta_l)$$

the beamformer may be evaluated using FFT algorithms:

$$B_m = e^{j2\pi ft} \sum_{n=0}^{N-1} w(n) e^{jn\phi_m}$$

The parameters of the temporal transform are compared to the spatial transform in Table 4.4. The beamformer was implemented with $M=512$ points, a Kaiser-Bessel ($\alpha=1.5$) shading function $w(n)$ and a spatial sampling frequency of 0.131579 samples/meter. This sampling deviates slightly from the array design element spacing of 7.5 m due to strain in the kevlar strength member under tension. The

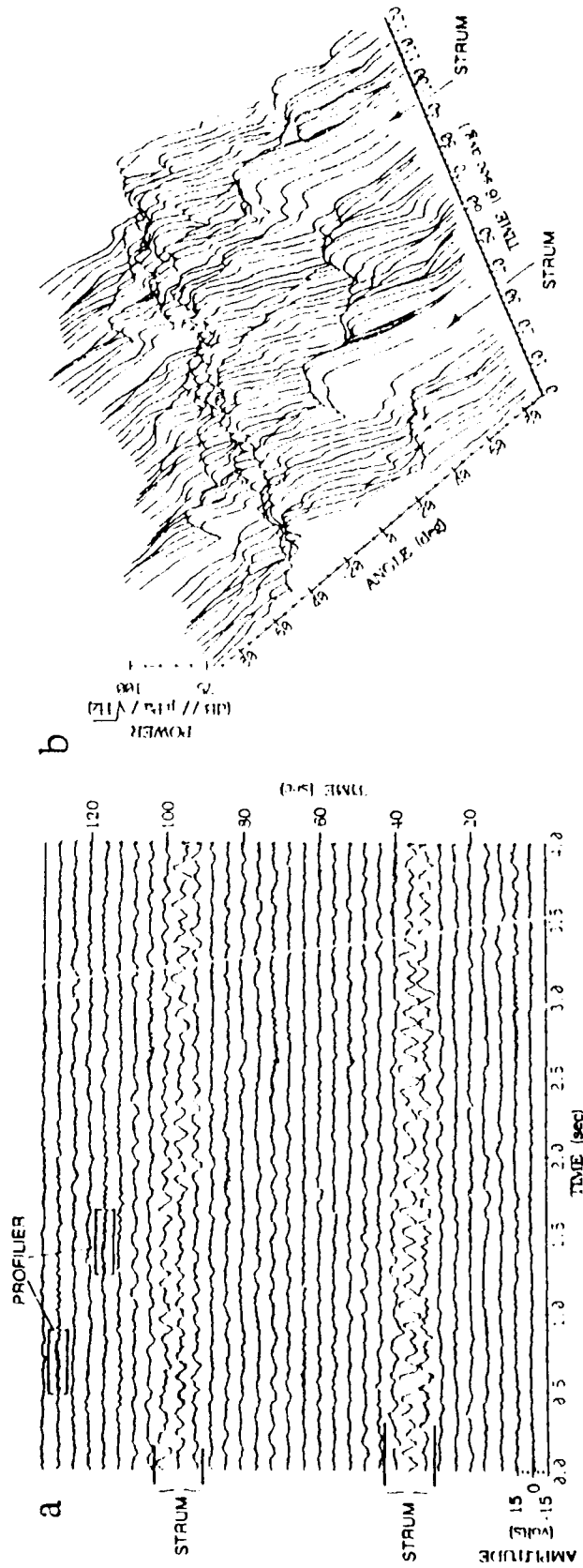


Figure 4.11 Array strum arrivals. The time series (a) of one element in the array over 2 minutes shows strong mechanical vibration events which travel down the array from the surface with an attenuated reflection at the bottom. A running directional spectrum (b) consisting of 6 second averages and 2 second shifts between estimates shows the apparent directional structure of the strum signal as a broad arrival centered at about 56°. The zero-crossing main beamwidth at 20 Hz and a 56° look angle is 35°.

spatial samples were incoherently averaged, and converted from electrical angle ϕ to physical angle $\theta = a \sin(\phi/kd)$. The average magnitude-squared results were calibrated to dB re $1 \mu\text{Pa}/\sqrt{\text{Hz}}$ Deg by normalizing by the number of points N , the power in the window function ($\frac{1}{N} \sum_{n=0}^N w^2(n)$) and the spatial sampling frequency, and by converting wavenumber to degrees with the factor

$$dk_v/d\theta = \frac{\pi f}{180c} \cos\left(-\frac{\pi}{180}\theta\right)$$

where k_v is the digital spatial frequency $\frac{1}{\lambda} \sin\theta$ analogous to the digital time frequency f . This normalization presents the data in terms of average narrowband intensity received by the array per vertical degree.

Temporal	Spatial	Mode
$\omega_c = \frac{2\pi}{T} = 2\pi f$ $f = \text{temporal frequency}$	$k_c = \frac{2\pi}{\lambda}$ $\frac{1}{\lambda} = \text{spatial frequency}$	continuous
$\omega_d = \omega_c T_s = \frac{2\pi f}{f_s}$ $f = \text{temporal frequency}$ $f_s = \text{temporal sampling frequency}$	$k_d = \frac{2\pi}{\lambda} d \sin\theta$ $\frac{\sin\theta}{\lambda} = \text{spatial frequency}$ $\frac{1}{d} = \text{spatial sampling frequency}$	discrete

Table 4.4 Temporal vs. spatial transform parameters.

4.5.2. Array Strum

The mechanical vibrations of the array, induced by water currents and surface platform motions, are limited to low frequencies (5-30 Hz). There are two modes of vibration identified in the array time series data which may potentially contaminate the ambient noise data. The transverse component, modeled as if the array were an infinitely flexible string, has a computed speed of $c = \sqrt{T/\mu}$ where T is the tension (Newtons), and μ is the array mass/unit length (kg/m), and assuming standing wave propagation, the frequency is $\nu_n = nc/2l$, where $n=1$ for the fundamental frequency, and l is the length of the string [Morse and Ingard, 1968]. The array system is composed of 4 component parts: uplink wire, array, kevlar strength member and weights. The system mechanical parameters were estimated as follows: mass of 1887 kg, center of mass at 954 m, weight in water of 5880 N and

density of 1.44 gm/cm³. Using these parameters for an infinitely flexible string with uniformly distributed mass and small displacements, the velocity of a transverse wave traveling down the array would be 54 m/s, and the fundamental frequency assuming standing waves would be about 0.03 Hz. Velocity measurements of this component are difficult because of the relatively low amplitudes and propagation interference due to the stiff section splices and processor pressure cases, however, from a typical time series plot [Sotirin and Hildebrand, 1988, Figure 8] the speed is estimated to be 43 - 53 m/s, comparing favorably to the calculated speed. The speed and frequencies characteristic of the longitudinal mode are more difficult to predict because of uncertainty in elastic moduli estimation. Observationally, the longitudinal mode is more apparent than the transverse mode, traveling down the array at a measured speed of 1800 m/s from the surface and a frequency of about 20 Hz. Since the speed of propagation for ambient noise beamforming is 1500 m/s, signals propagating at other phase velocities appear at non-endfire angles. Using Snell's law:

$$\frac{c_1}{\sin\theta_1} = \frac{c_2}{\sin\theta_2}$$

where $c_1 = 1800$ m/s, $c_2 = 1500$ m/s, and $\theta_1 = 90^\circ$, gives $\theta_2 = 56^\circ$. A series of directional spectra with prominent longitudinal strum are shown in Figure 4.11 demonstrating the arrival structure and time variability of the strum events.

The transverse component of strum is not apparent in the directional measurements due to its low amplitudes and relatively slow propagation speed. The longitudinal mode however, is evident in the ambient noise directional spectrum at arrival angles from 45° to 65° . The angular isolation of the strum signal allows the pedestal structure of the ambient noise field to be analyzed without contamination unless the strum signal is strong enough to compete with the power seen by the mainbeam through array sidelobe leakage.

4.5.3. Ambient noise as a function of wind speed

Ambient noise has been shown to be a function of frequency, location, depth, direction and source mechanism. The frequency dependence of ambient noise has been studied extensively and is summarized by Urick [1984]. We consider the frequency band between 15 and 130 Hz, referred to in the literature as the low frequency band or low sonic band (20-200 Hz). Within this band the predominant sources are man-made (shipping and seismic exploration) and environmental (wind and wave induced turbulence). The importance of location is related to the proximity of major shipping lanes and storm tracks. The difference in spectral levels with depth is small until critical depth (where the sound speed at depth is equal to that at the surface) is reached [Morris, 1978]. Directional characteristics, the major emphasis of the data analysis below, is far from isotropic, depending on source distribution and relative strength, and propagation parameters such as sound speed profile, mid-water reverberation and range dependent boundary coefficients. The purpose of this report is to investigate the influence of local storms on the directional spectra of low frequency ambient noise data collected in the NE Pacific above the critical depth.

Low frequency measurements show persistent directional characteristics, associated with distant shipping lanes and density patterns, which are smoothed by

environmental contributions. This dependence is manifested in vertical distributions as a broad, angular distribution of noise intensity near the horizontal referred to as the ambient noise pedestal. The range of angles spanned by the pedestal, or pedestal width, is a function of the ocean boundary and refractive effects on propagation. The pedestal height reflects the contributions from shipping and environmental sources arriving at near horizontal angles relative to those arriving at higher vertical angles. Coastal shipping, narrow in frequency and direction, and coastal storms, which fill in the spectrum, may be converted to horizontal angles by downslope conversion [Wagstaff, 1981]. Other distant shipping noise may be converted to horizontal angles by surface reflecting rays which refract at a depth above the ocean floor. High latitude storms may also contribute by means of the depth varying sound speed minimum [Anderson, 1979; Bannister, 1986]. Outside the pedestal, local effects may dominate. The patterns which reflect distant sources are confined to low frequencies and near horizontal angles due to the relatively low attenuation for non-bottom interacting paths.

The data discussed here were recorded during September 1987 in a high shipping density area about 400 nm west of Monterey, CA in deep (4667 m) water. Spectral levels are consistent with high shipping density [Urlick, 1984] when the effects of the seismic profiler operating off the California coast are removed: measurements at 100 Hz were about 79 dB re $\mu\text{Pa}/\sqrt{\text{Hz}}$ for low wind speeds. The broadside beam levels at 100 Hz were about 80 dB re $\mu\text{Pa}/\sqrt{\text{Hz}}$. These measurements are 10 dB re $\mu\text{Pa}/\sqrt{\text{Hz}}$ higher than those measured by Anderson [1979] and slightly lower (3 dB) than those measured by Wales and Diachok [1981]. These levels are about the same as those measured by Hodgkiss and Fisher [1987], however, we observed a pedestal height at low wind speeds about 10 to 15 dB lower. For a typical measurement of 12 dB pedestal height over $\pm 16^\circ$, the power integrated over the pedestal is 3.5 times that contained in the higher angles. Thus, omnidirectional spectral levels would only deviate on the order of 1 dB due to the power difference in the higher angles. Estimating levels from gray-level type plots, it would appear that the pedestal height for data at 100 Hz measured at 30° from broadside, shown by Carey, *et al* [1985] is 12-13 dB, whereas Wales and Diachok [1981] measured about 10 dB. Burgess and Kewley [1985] present data measured in the South Fiji basin, where ship traffic is light, having lower absolute levels and a 15 to 20 dB pedestal height. Since broadside levels are a function of the proximity of shipping lanes and storm tracks, a lower absolute level is expected.

The test site 400 nm off the coast of California was affected by major shipping lanes to the north, coastal shipping to the east and for the duration of the experiment, storm tracks to the south, an area riddled with complex bottom topography providing opportunities for downslope conversion [Morris, 1975]. Using only a vertical array, however, the azimuth of the pedestal source is not determinable.

Although ambient noise is normally considered to exclude identifiable ship sources, with increased directional resolution, the effect of ships (identified as angular point sources) at times dominates the pedestal structure. Arrays with less resolution smear these arrivals, producing a much smoother distribution. To allow comparison, the discrete sources should be integrated. To measure the true value of ambient noise an estimate of the level between the discrete ship sources should be recorded (thereby smoothing over signals which are not resolved by the present array). At 100 Hz, the inter-ship level in the pedestal is about 78 dB re $\mu\text{Pa}/\sqrt{\text{Hz}}$ or 58 dB re $\mu\text{Pa}/\sqrt{\text{HzDeg}}$ for wind speeds up to 10 m/s, this level increased by several dB at about 1500 GMT, possibly due to downslope conversion of energy from the

approaching storm.

Surface ships at propagation convergence zones also present strong directional lines which can vary rapidly with time (Figure 4.12), the magnitude changing as much as 2.5 dB/minute. A limited radar range was available during the experiment, so ships further away than 42 km (just short of the first convergence zone) were not logged. The strong narrow beam signals outside the pedestal are most probably generated by the same ship at fairly close range even though it was not observed by radar. A surface source at a range of 27 km would arrive at the array with one bottom bounce at $+24^\circ$ and two bottom bounces at -31° and $+38^\circ$ as seen in Figure 4.12.

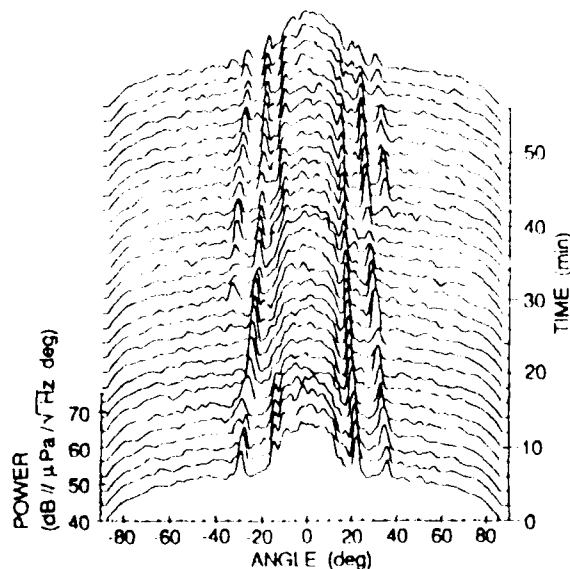


Figure 4.12 Continuous directional time series. Directional spectral levels were estimated from consecutive 2 minute time segments over 58 minutes at 75 Hz (0.5 Hz bin width). The time samples were recorded on Julian day 268 at 1000 GMT with a mid-array depth of 2650 m and 3 m/s wind speed. The narrow band estimates were shaded with a Kaiser-Bessel ($\alpha=1.5$) window prior to the spatial transform (2.8 samples/degree). The magnitude variation of the signal seen beginning at 38° was as much as 2.5 dB/minute.

Ray diagrams are helpful in visualizing pedestal dynamics. Ambient noise pedestal height reflects the energy trapped in the deep sound channel and pedestal angular width is defined by the bottom grazing rays (Figure 4.13a). The structure of the pedestal is modified by rays which reflect from the surface and whose turning depth is above the ocean floor such that the energy is not attenuated by bottom interaction. These rays transfer surface noise to the array increasing the pedestal height within a narrow band of angles, thereby producing the pedestal "ears" exhibited at certain times. The distribution varies slightly with array depth and with local environmental conditions which are discussed below.

During the passage of a storm where wind speed increased from 2 to 13 m/s, the array depth was varied such that elements spanned the water column from 400 to 3100 m, albeit at different times. The mid-array depths were 850 m, 1350 m and 2650 m. The differences, as a function of these depths, in the directional spectrum are expected to be small, with the pedestal width decreasing slightly [Anderson, 1979]. The range of angles which exhibit the pedestal characteristics and surface shipping "ears" vary with array depth as shown in Figure 4.13a, b and c.

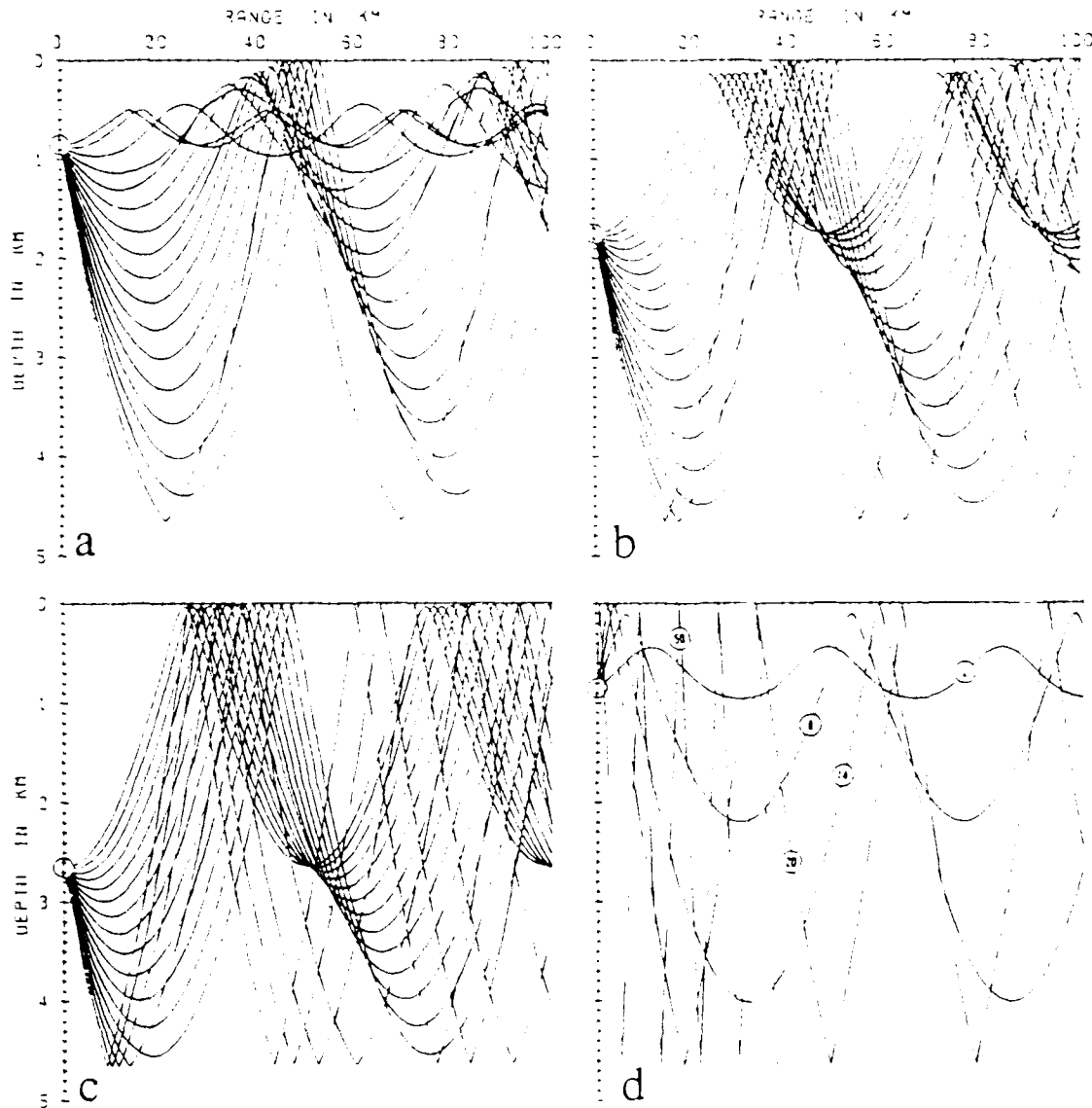


Figure 4.13 Pedestal rays. The rays producing the ambient noise pedestal vary slightly with array depth for the sound speed profile measured at the experiment site. For the shallow array depth (850 m) (a), the arrival angles contained within the pedestal are between $\pm 15^\circ$, and surface noise arrives between $\pm 12^\circ$ and $\pm 15^\circ$. The mid depth (1750 m) (b) pedestal is defined between $\pm 14^\circ$ with surface noise arriving between $\pm 10^\circ$ to $\pm 14^\circ$. The deep depth (2650 m) (c) pedestal is between $\pm 11^\circ$ with surface noise arriving between $\pm 6^\circ$ to $\pm 11^\circ$. The ray paths of specific arrival angles are shown (d) which correspond to data in Figure 4.19. The associated arrival angles are notated.

however the difference is limited to a few degrees for the range of depths considered here. The pedestal width should decrease slightly from $\pm 15^\circ$ at the shallow array depth to $\pm 11^\circ$ at the deep depth, and those arrival angles containing surface noise from reflecting rays should broaden from $\pm 12^\circ$ to $\pm 15^\circ$ at the shallow depth to $\pm 6^\circ$ to $\pm 11^\circ$ at the deep depth. The amount of surface noise is highly dependent on the amount of ship traffic and its distribution and produces large variations in the measured levels. The pedestal height, since it is relative to the high angle level, is also dependent on wind speed, decreasing as wind speed increases. In general, the measured directional spectrum followed the expected pattern but due to the temporal variability of ambient noise, strong discrete sources and small predicted changes, the observed difference is not significant for the range of depths considered. These predictions are based on the sound speed profile at the experiment site and do not account for the range dependency of the profile. The directional spectrum is shown in Figure 4.14 at 75 Hz for the three nominal array depths and three wind speeds detailed in Table 4.5.

Julian Day	GMT	Wind Speed	Array Depth	Tape
266	15:10	low	shallow	688
265	18:02	medium	shallow	634
270	20:25	high	shallow	914
267	13:16	low	mid	736
265	08:38	medium	mid	612
270	03:56	high	mid	878
267	03:28	low	deep	714
268	23:33	medium	deep	812
269	14:04	high	deep	849

Table 4.5 Vertical Directionality Data: Wind Speed vs. Depth.

The pedestal height tends to decrease with wind speed, and surface noise arrival angle ("ears") decrease with depth, however the predicted decrease in pedestal width is obscured. The array remained above critical depth, where other data have shown substantial decreases [Morris, 1978], so it is not surprising that no significant differences in omnidirectional spectral levels were observed for this range of depths.

The frequency dependent aspects observed in the measured directional spectra are a combination of effects such as frequency dependent attenuation and main beamwidth variability. The increasing beam width of the broadside beam from 2.0° at 95 Hz to 5.5° at 35 Hz (measured at the zero crossings) tends to smooth the spectra as the frequency decreases (Figure 4.15). The smoothing increases the apparent width and height of the pedestal as narrow beam signals are integrated over adjacent angles. The increase in pedestal height is also due to the decrease in attenuation with decreasing frequency. There is also a slight increase in the levels outside the pedestal at higher frequency about 2 dB between 35 Hz and 95 Hz as seen in Figure 4.15. The time axis in this figure also corresponds to increasing wind speed as described in detail below. There is a decrease in the pedestal height relative to the high angle level as wind speed increases, and the sharp drop off occurring at $14-15^\circ$ is obscured as the high angle levels increase. The effect is more apparent in the upward looking angles which at high wind

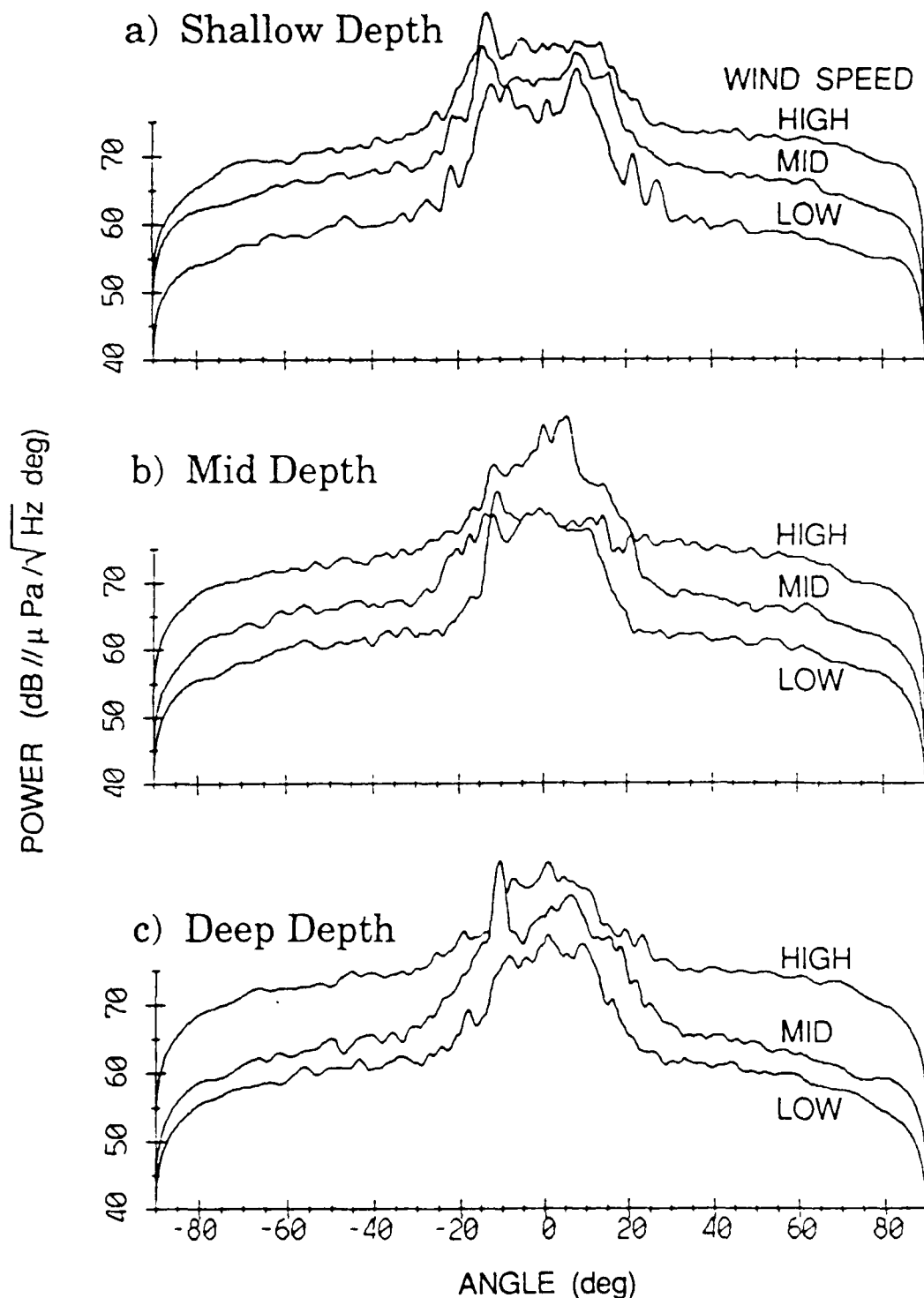


Figure 4.14 Spatial distribution of ambient noise as a function of depth. The factors impacting spatial distribution with depth are due to the small variation in arrival angles of the rays which define the pedestal shape. In general, the pedestal width should decrease with depth and the "ears" should arrive at angles which are slightly more horizontal. Due to the temporal variability in ambient noise and the strong discrete sources, these effects are not a significant factor for the range of depths considered here. Specific parameters for the 75 Hz data plotted are found in Table 4.5.

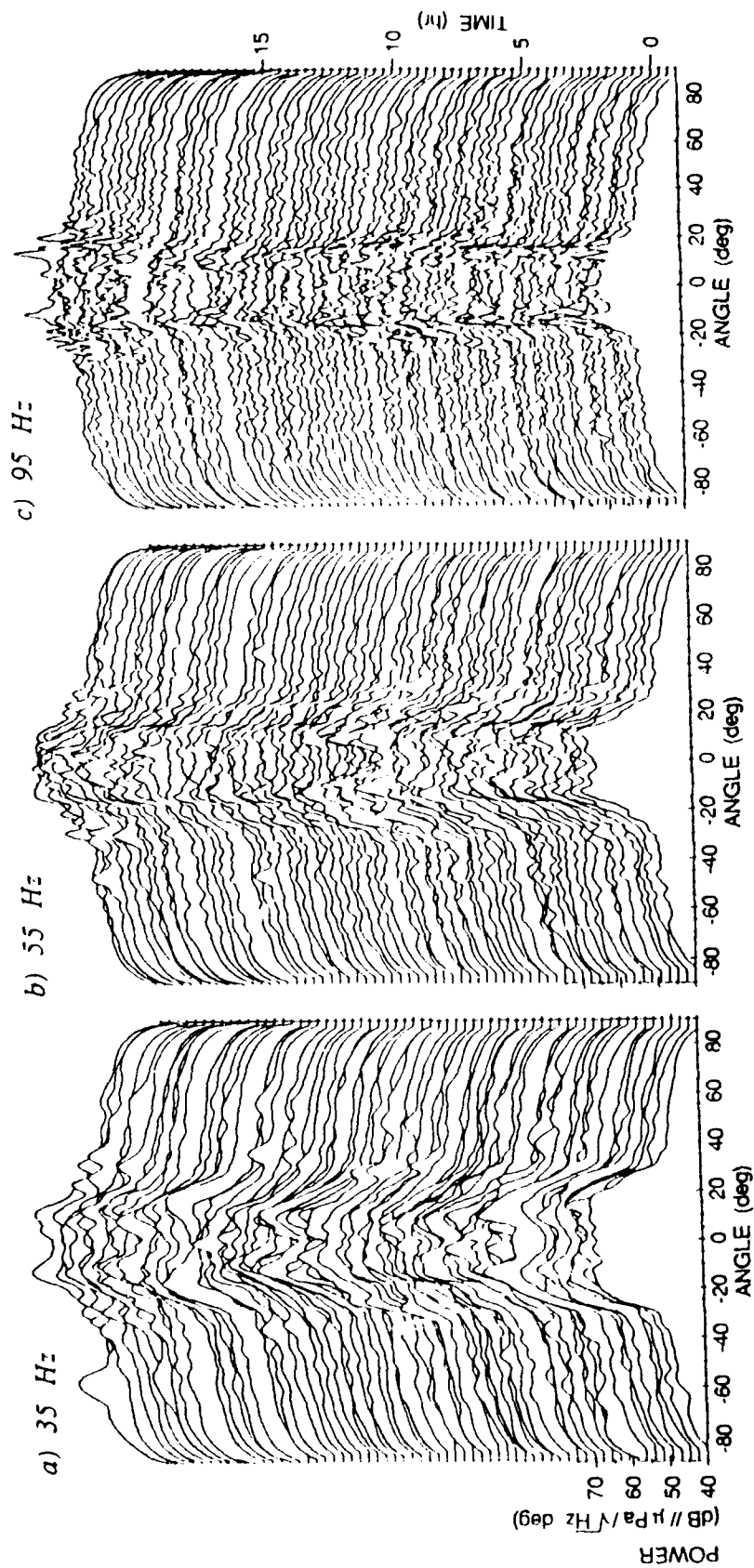


Figure 4.15 Spatial distribution of ambient noise as a function of frequency. The directionality of ambient noise spectra is shown at 3 frequencies as a function of direction, time and power. The narrowband components (0.5 Hz bin width) are at (a) 35 Hz, (b) 55 Hz and (c) 75 Hz. The time axis also corresponds to increasing wind speed from 2 m/s to 12 m/s. The mid-array depth was at 850 m.

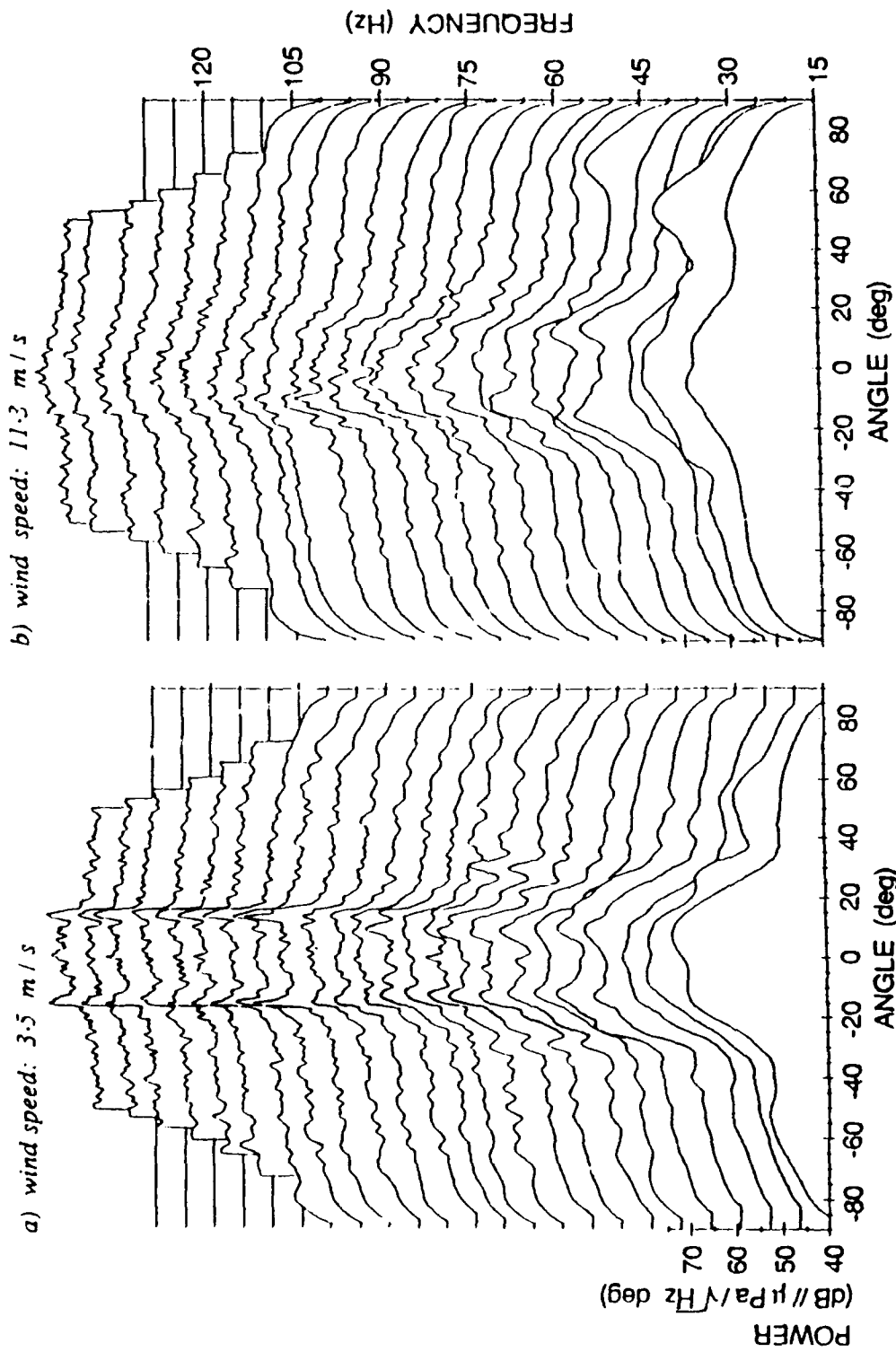


Figure 4.16 Spatial distribution of ambient noise as a function of wind speed. The spatial distribution for a (a) low wind speed (3.5 m/s) from data recorded on Julian day 258 at 0040 GMT and a (b) high wind speed (11.3 m/s) from data recorded on Julian day 258 at 1600 GMT, are displayed as a function of direction, frequency (every 5 Hz from 15 to 130 Hz) and power. The mid-array depth was at 850 m.

speeds, have slightly more power than the corresponding downward angles. This occurs because the downward looking angles receive the local surface noise via a bottom reflection. Although this difference is small, it occurs at all frequencies, and is measured from Figure 4.14 to be about 1 dB at 40° and about 2 dB at 70°. The clouding of the pedestal shape is more obvious in Figure 4.16 which presents data at a low (a) and high (b) wind speed as a function of frequency, angle and power. Absolute pedestal levels are approximately the same for all frequencies above 25 Hz however the increase in the angles outside those defined by the pedestal at high wind speed tends to obscure the pedestal shape. This increase is estimated at 3 to 4 dB and does not appear to be a function of frequency.

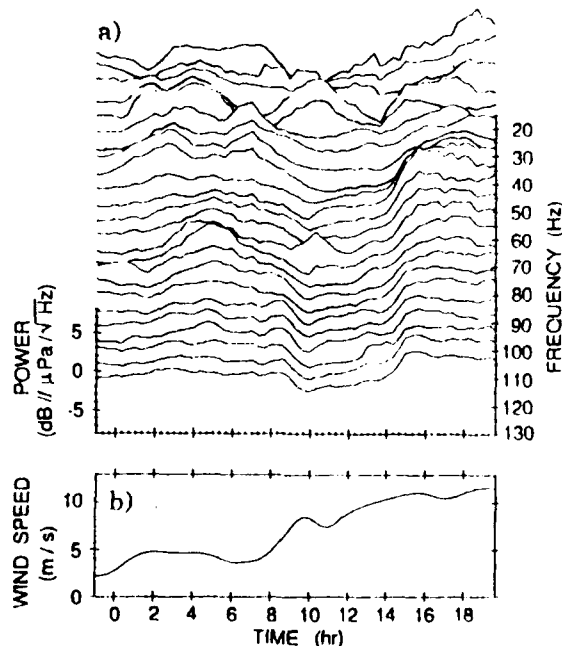


Figure 4.17 Spectral levels versus time. The magnitude squared values from the 2 minute samples were averaged across the 2 minutes and then across selected channels giving one value for each frequency every 20 minutes for 21 hours. The averaged values were calibrated to $\text{dB} // \mu\text{Pa} / \sqrt{\text{Hz}}$ and the 21 hour mean for each frequency was removed to observe relative deviation from the mean value. The data smoothed slightly by a time-corrected running mean filter ($n=4$). Hourly wind speed estimates were smoothed by the same filter (Figure 4.19 shows the original unsmoothed version). The time axis represents GMT on Julian day 257/258.

The small scale effects of wind speed dependence on ambient noise are more easily observed from deviations about the mean levels. For this particular data set, the wind velocity and swell height were recorded once an hour. The data set analyzed commenced at the onset of an increase in local winds due to the approach (>700 nm) of a hurricane shown on area weather maps. Comparing average array spectral deviations to wind speed estimates in Figure 4.17, two discrete level changes are observed, one occurring at approximately 1000 GMT and the other at 1420 GMT. The increase in wind speed at 1000 GMT was caused by a squall accompanied by gusting winds and heavy rain but lasting for only about an hour. The corresponding decrease in spectral levels however, is shown not to reflect local conditions but rather distant variations, by the directional spectrum estimates of the same data set discussed below. The individual frequency data (Figure 4.15) do show a slight increase in the high angle level at 0920 GMT with heavy rain recorded at the local experiment site at 0916 GMT. The second level change is caused by local events, most likely the commencement of breaking waves

as the storm intensity increased. Unfortunately estimates of sea state, wave action, or whitecap coverage are not available therefore it is not possible to ascertain absolute source identification and levels. Earlier investigations have interpreted the wind dependent portion of the low frequency spectrum in terms of the logarithm of the wind speed as proposed by Crouch and Burt [1972]; $NL_f = B_f + 20n_f \log v$ where NL_f is the noise spectrum level in dB re μPa at frequency f , B_f is the spectrum level at a wind speed of 1 knot, n_f is a coefficient determined empirically from the data, and v is the wind speed in knots. The unexplained discrepancy in spectrum level predicted by the coefficients estimated by different investigations was noted by Urick [1984] and tabulated for low frequency by Carey [1987]. The plot of spectral levels vs. linear wind speed (Figure 4.18) is shown in Figure 4.18 where the wind dependent portion of the data could be described as those levels above 8 m/s, with spectral levels below 8 m/s dominated by distant shipping or storm noise. Any quantitative relationship to wind speed must account for the relatively sparse and instantaneous estimates of wind speed. Although this data might be interpreted similarly (as a logarithmic dependence), the directional spectrum leads to a slightly different conclusion.

Analysis of the local wind effects is separable from distant changes by observing the directional spectrum deviations. The directional spectrum levels as a function of time are shown at 55 Hz in Figure 4.15b. Carefully scrutinized, this data shows a decrease in relative pedestal height as time and wind speed increase. By selecting specific directions, the small scale variability is evaluated. These directional data are displayed in Figure 4.19 for which 4 of the beams point more toward the horizontal and are influenced by distant sources, and 4 of the beams reflect local sources, pointing toward the higher vertical angles. The beams at 50° and 80° are plotted with the corresponding downward looking beams at -50° and -80° . The mean difference is seen to be only 1 dB indicated to the right of the beam plots, increasing slightly at higher wind speeds for the 80° beam. The ray diagram corresponding to the 4 pedestal beams and the 50° beam is shown in Figure 4.13d. The decrease in spectral level between 1000 and 1400 GMT (Figure 4.17) is seen to be confined to the horizontal beams indicating that it is a distant effect. The presence of complicated bottom topography in the area of the hurricane track may account for the increase in horizontal beams at 1400 GMT which would reflect long distance variations. However without supporting data, changes in the distant shipping profile or energy from a high latitude storm cannot be discounted. However the increase in level at 1420 GMT is a local effect with the higher vertical angle levels increasing suddenly by as much as 5 dB. This effect is apparent at all frequencies and the abruptness of the change would indicate the onset of an additional source mechanism. The broad band frequency and spatial qualities of this change indicates that the mechanism is not system induced noise (array strum, FLIP noise). A second, broad band increase of smaller amplitude is seen at 1620 GMT which is more distinct at lower frequencies. Is this indicative of a change in source mechanism, for instance from spilling breakers to plunging breakers? Although preliminary simulations in the spectra of noise generated by breaking waves implies that plunging breakers drops off below 90 Hz [Papanicolaou and Raichlen, 1987], investigations in the area of wind induced noise mechanisms is in its infancy and future work may support the implications of the data presented here, that these noise mechanisms produce discrete changes in spectral values as opposed to a continuous function.

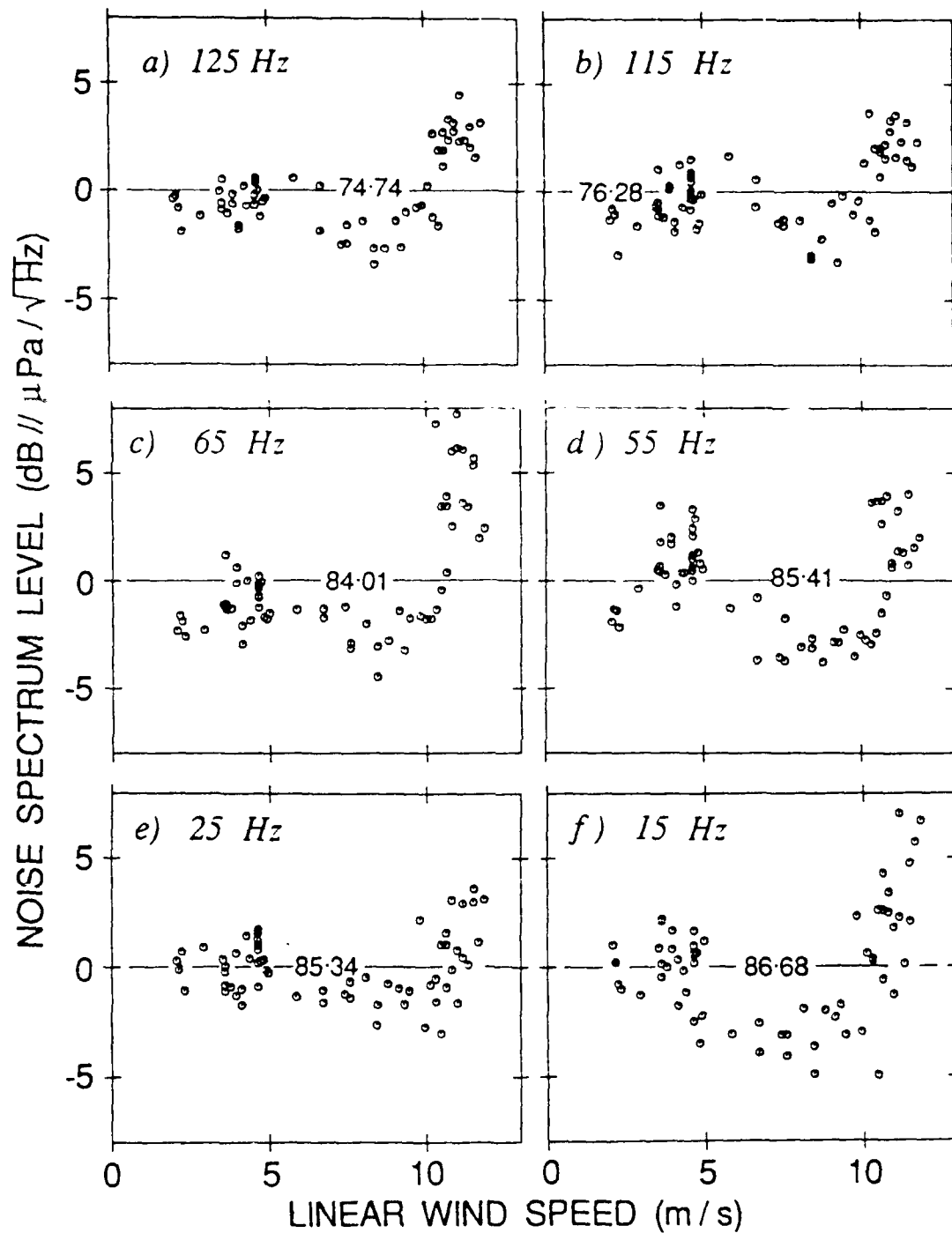


Figure 4.18 Spectral levels as a function of linear wind speed. Spectral levels at 6 different frequencies (2 low, 2 mid and 2 high) are plotted as a function of wind speed. Any quantitative relationship to wind speed must account for the relatively sparse and instantaneous estimates of wind speed. The specific frequency is notated in the corresponding panel. The number in each panel at the 0 dB mark is the normalization factor in dB// $\mu\text{Pa}/\sqrt{\text{Hz}}$.

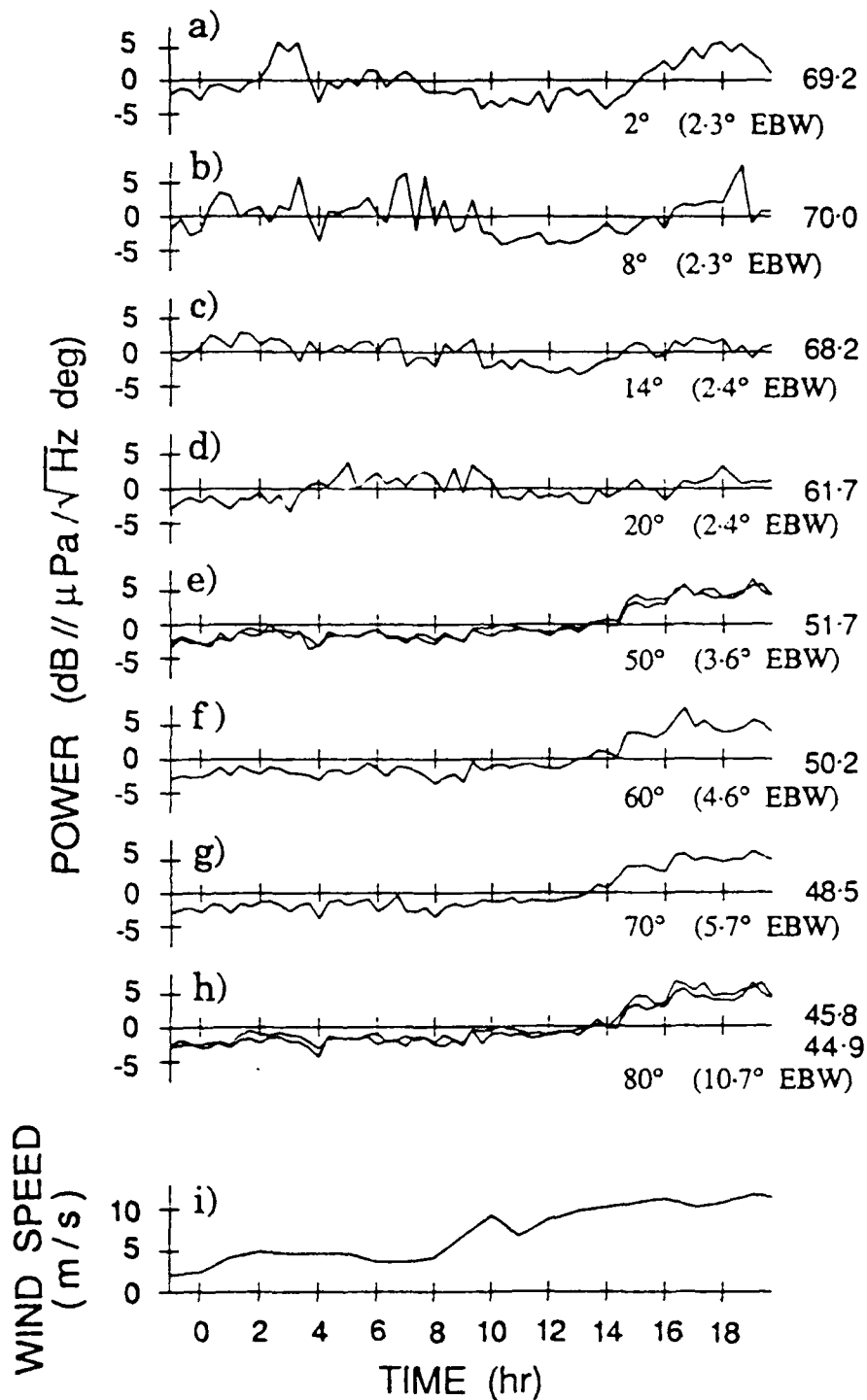


Figure 4.19 Directional time series. Specific beams are displayed with time at 55 Hz. The top 4 beams (2° , 8° , 14° and 20°) are influenced by the ambient noise pedestal which is caused by distant sources. The bottom 4 beams (50° , 60° , 70° and 80°) are affected by local sources. Two downward looking beams (-50° and -80°) are also shown. The number to the right of the beam is the normalization factor (downward looking beam normalization factor below). The number after the beam direction is the EBW.

4.6. CONCLUSIONS

Prior to interpreting the ambient noise data, several factors relating to the quality of the data set were considered. The data were shown to be independent samples of a stationary Gaussian process for the time intervals used in the analysis. The impact of array calibration errors, sidelobe leakage, mechanical vibration and array shape was shown to be either negligible or predictable, affecting a isolated portion of the data set. Simulations indicated that for the majority of the data, measured spectral levels were not contaminated by array sidelobe leakage.

Ambient noise levels presented were reasonable for an area of high shipping density. The angular resolution of the array emphasizes the fact that much of the energy in the ambient noise pedestal is due to discrete sources (ships) which are smoothed by wider beams. Directional spectral levels did not vary significantly as a function of depth, not an unexpected result for the range of depths considered. Omnidirectional levels at low frequency are a function of processes besides local environmental changes thus directional data should be utilized in estimating wind induced noise levels.

Low frequency spatial distributions of ambient noise as a function of wind speed suggest more than one mechanism and display threshold type behavior observed previously [Carey, 1987]. The high wind speed domain (>10 m/s) demonstrated abrupt level changes, for beams outside the pedestal, corresponding to possible source mechanism onset, such as the commencement of breaking waves, or a change in source mechanism such as the conversion from spilling breakers to plunging breakers. This hypothesis cannot be substantiated due to lack of supporting environmental measurements, however because the array data represent continuous samples of the noise field throughout the storm, the level changes are significant relative to the variability of the ambient noise field with time. These level changes, as much as 5 dB, were observed at all beam directions outside the ambient noise horizontal pedestal and at all frequencies processed between 15 and 130 Hz. The increase in absolute pedestal level and the increase observed in the near horizontal beams is a possible indication of downslope conversion of storm noise, but without azimuthal directivity, other possible mechanisms (coastal shipping variation, high latitude storm effects) cannot be ruled out.

REFERENCES

- Anderson, V. C., "Arrays for the investigation of ambient noise in the ocean," J. Acoust. Soc. Am., Vol. 30, pp. 470-477, 1958.
- Anderson, V. C., "Variation of the vertical directionality of noise with depth in the North Pacific," J. Acoust. Soc. Amer., Vol. 66, no. 5, pp. 1446-1452, Nov. 1979.
- Anderson, V. C., private communication, Jan. 1989.
- Arase, T. and E. M. Arase, "Deep-sea ambient noise statistics," J. Acoust. Soc. Am., Vol. 44, no. 6, pp. 1679-1684, 1968.
- Axelrod, R. H., B. A. Schoomer and W. A. Von Winkle, "Vertical directionality of ambient noise in the deep ocean at a site near Bermuda," J. Acoust. Soc. Amer., Vol. 37, no. 1, pp. 77-83, 1985.
- Bannister, R. W., R. N. Denham, K. M. Guthrie, D. G. Browning and A. J. Perron, "Variability of low frequency ambient sea noise," J. Acoust. Soc. Maer., Vol. 65, no. 5, pp. 1156-1163, 1979.
- Bannister, R. W. "Deep sound channel noise from high-latitude winds," J. Acoust. Soc. Am., Vol. 79, no. 1, pp. 41-48, Jan. 1986.
- Bendat, J. S. and A. G. Piersol, *Random Data: Analysis and Measurement Procedures*, New York: Wiley-Interscience, p. 113, 128 and 191, 1971.
- Berrou, J. L., O. Z. Bluy and R. A. Wagstaff, "A real-time system for towed-array calibration and performance analysis, or how to get 50 dB sidelobes from a towed array," CP-32, SACLANT ASW Research Centre, La Spezia, Italy, June 1982.
- Boegeman, D. E., private communication, May 1988.
- Browning, D. G., N. Yen, R. W. Bannister, R. N. Denham and K. M. Guthrie, "Vertical directionality of low frequency ambient noise in the south Fiji Basin," NUSC TD 6611, Naval Underwater Sys. Ctr., New London, CT, 1982.
- Buckingham, M. J. and S. A. S. Jones, "A new shallow-ocean technique for determining the critical angle of the seabed from the vertical directionality of the ambient noise in the water column," J. Acoust. Soc. Amer., Vol 81. No. 4, pp. 938-946, 1987.
- Burgess, A. S. and D. J. Kewley, "Wind-generated surface noise source levels in deep water east of Australia," J. Acoust. Soc. Amer., Vol. 73, no. 1, pp. 201-210, 1983.

- Carey, W. M. and D. Browning, "Low frequency ocean ambient noise: measurements and theory," NUSC Technical Document 8175, Naval Underwater Systems Center, New London, CT, December 1987.
- Carey, W. M., "Measurement of down-slope sound propagation from a shallow source to a deep ocean receiver," J. Acoust. Soc. Am., Vol. 79, no. 1, pp. 49-59, Jan. 1986.
- Carey, W. M., R. A. Wagstaff, B. A. Brunson and M. R. Bradley, "Low-frequency noise fields and signal characteristics," NUSC Technical Report 131, Naval Underwater Systems Center, New London, CT, 1985.
- Cavanagh, R. C. and W. W. Renner, "Vertical directionality and depth dependence of averaged acoustic signals and noise," J. Acoust. Soc. Am., Vol. 68, no. 5, pp. 1467-1474, Nov. 1980.
- Churgin, J., and S. J. Halminski, "Temperature, salinity, oxygen and phosphate in waters off the United States, Eastern North Pacific," vol. 3, National Oceanographic Data Center, Washington DC, 1974.
- Clay, C. S., and H. Medwin, *Acoustical Oceanography: Principles and Applications*, New York: Wiley Interscience, p. 3, 1977.
- Cron, B. F., B. C. Hassell and F. J. Keltonic, "Comparison of theoretical and experimental values of spatial correlation," J. Acoust. Soc. Am., Vol. 37, no. 3, pp. 523-529, March 1965.
- Crouch, W. W. and P. J. Burt, "The logarithmic dependence of surface-generated ambient-sea-noise spectrum level on wind speed," J. Acoust. Soc. Am., Vol. 51, no. 3, part 2, pp. 1066-1072, 1972.
- D'Spain, G. L., private communication, May 1988.
- Dashen, R. and W. Munk, "Three models of global ocean noise," J. Acoust. Soc. Am., Vol. 76, no. 2, pp. 540-554, Aug. 1984.
- Duckworth, G. L., "A robust algorithm for tracking of drifting acoustic arrays in the Arctic," Signals, Systems and Computers, 21st ASILOMAR Conference Proceedings, Pacific Grove, CA, Nov. 2-4, 1987.
- Dyer, I., "Statistics of sound propagation in the ocean," J. Acoust. Soc. Am., 48(1), pp. 337-345, 1970.
- Fofonoff, N. P., and R. C. Millard Jr., "Algorithms for computation of fundamental properties of seawater," Technical Paper 44, Unesco Division of Marine Sciences, Paris, France, 1983.
- Fox, G. R., "Ambient noise directivity measurements," J. Acoust. Soc. Am., Vol. 36, pp. 1541-1564, 1964.

- Garrett, C., and W. Munk, "Internal waves in the ocean," in *Ann. Rev. Fluid Mech.*, Annual Reviews Inc., pp. 339-369, 1979.
- Gill, P. E., W. Murray and M. H. Wright, *Practical Optimization*, Orlando, FL: Academic Press, p. 100, 1981.
- Hodgkiss, W. S. and F. H. Fisher, "Vertical directionality of ambient noise at 32° N as a function of longitude," Technical Memorandum 387, Marine Physical Laboratory, Scripps Institution of Oceanography, San Diego, CA, 1987.
- Hodgkiss, W. S., and G. L. D'Spain, private communication, July, 1988.
- Hu, J-H., and P. P. Niiler, "NEPAC current netter and XBT data for circulation in NE Pacific thermocline," SIO Reference No. 87-4, Scripps Institution of Oceanography, University of California, San Diego, February 1987.
- Jobst, W. J. and S. L. Adams, "Statistical analysis of ambient noise," *J. Acoust. Soc. Am.*, Vol. 62, no. 1, pp. 63-71, 1977.
- Lastinger, J. J., "Measurements on Norda/DTAG AQ-1 hydrophones," USRD TM 6891, Underwater Sound Reference Detachment, Orlando, FL, 1982.
- Lowenstein, C. D., "Computations for transponder navigation," in *Proc. Nat. Marine Nav. Meet.*, pp. 305-311, 1966.
- McDonough, R. N., "Spectrum restoration for uniformly spaced arrays," *J. Acoust. Soc. Am.*, Vol. 57, no. 4, pp. 913-922, 1975.
- McGehee, M. S. and D. E. Boegeman, "MPL acoustic transponder," *Rev. Sci. Instr.*, Vol. 37, pp. 1450-1455, 1966.
- Middleton, D., "Acoustic modeling, simulation, and analysis of complex targets. II. Statistical evaluation of experimental data," ARL-TR-69-22, Applied Research Laboratories, University of Texas at Austin, Austin, TX, 1969.
- Morse, P. M. and K. U. Ingard, *Theoretical Acoustics*, New York: McGraw-Hill Inc, p. 99, 120 and 178, 1968.
- Morris, G. B., "Preliminary results on sea mount and continental slope reflection enhancement of shipping noise," SIO Ref. 75-34, Scripps Institution of Oceanography, La Jolla, CA, Nov. 1975.
- Morris, G. B., "Depth dependence of ambient noise in the Northeastern Pacific ocean," *J. Acoust. Soc. Am.*, 64(2), pp. 581-590, Aug. 1978.
- Munk, W., "Internal waves and small-scale processes," in *Evolution of Physical Oceanography*, Cambridge, MA: The MIT Press, pp. 264-291, 1981.

- Nuttall, A. H., "Effects of random shading, phasing errors, and element failures on beampatterns of linear and planar arrays," NUSC TR 6191, Naval Underwater Systems Center, New London, CT, 1979.
- Papanicolaou P. and F. Raichlen, "Wave and bubble characteristics in the surf zone," NATO Advanced Research Workshop on Natural Mechanism of Surface-Generated Noise in the ocean, La Spezia, Italy, 15-19 June, 1987.
- Press, W. H., B. P. Flannery, S. A. Teukolsky and W. T. Vetterling, *Numerical Recipes: the art of scientific computing*, Cambridge, England: Cambridge University Press, 1986.
- Perrone, A. J., "Deep-ocean ambient-noise spectra in the Northwest Atlantic," *J. Acoust. Soc. Amer.*, Vol. 46, no. 3, pp. 762-770, 1969.
- Pinkel, R., private communication, February 1989.
- Quazi, A. H. and A. H. Nuttall, "Effects of random shading, phasing errors and element failures on the beampatterns of line and planar arrays," *IEEE ICASSP Proc.*, 79CH1379-7 ASSP, pp. 290-293, April, 1979.
- Quazi, A. H., "Array beam response in the presence of amplitude and phase fluctuations," *J. Acoust. Soc. Am.*, Vol. 72, no. 1, pp. 171-180, July, 1982.
- Ramsdale, D. J. and R. A. Howerton, "Effect of element failure and random errors in amplitude and phase on the sidelobe level attainable with a linear array," *J. Acoust. Soc. Am.* Vol. 68, no. 3, pp. 901-906, Sept. 1980.
- Rudnick, P. and E. D. Squier, "Fluctuations and directionality in ambient sea noise," *J. Acoust. Soc. Am.*, Vol. 41, no. 5, pp. 1347-1351, 1967.
- Sherrill, M. S. and R. L. Streit, "*In Situ* optimal reshading of arrays with failed elements," *IEEE Journal of Oceanic Engineering*, OE-12, No 1, pp. 155-162, Jan. 1987.
- Shooter, J. A., and M. L. Gentry, "Wind generated noise in the Parece Vela Basin," *J. Acoust. Soc. Amer.*, Vol. 70, no. 6, pp. 1757-1761, 1981.
- Smith, W., W. M. Marquet and M. M. Hunt, "Navigation transponder survey: design and analysis," in *Oceans 75 Record*, San Diego, CA: I.E.E.E. Press, pp. 563-567, 1975.
- Sorenson, H. W., *Parameter Estimation - Principles and Problems*, New York: Marcel Dekker, Inc., p. 45 and 225, 1980.
- Sotirin, B. J., and J. A. Hildebrand, "Large aperture digital acoustic array," *IEEE Journal of Oceanic Engineering*, OE-13, No. 4, pp. 271-281, October 1988.
- Sotirin, B. J., F. V. Pavlicek and J. A. Hildebrand, "Low frequency digital acoustic array," in *Current Practices and New Technology in Ocean Engineering - 1988*, G.

- K. Wolfe and P. Y. Chang, Eds., New York: ASME, pp. 19-27, 1988.
- Sotirin, B. J. and W. S. Hodgkiss, "Navigation software for the MPL vertical line array," Technical Memorandum 409, Marine Physical Laboratory, Scripps Institution of Oceanography, San Diego, CA, March, 1989.
- Sotirin, B. J. and J. A. Hildebrand, "Acoustic navigation of a large aperture array," J. Acoust. Soc. Am., submitted for publication March, 1989.
- Sotirin, B. J. and W. S. Hodgkiss, "Fine-scale measurements of the vertical ambient noise field," in progress, 1989.
- Spiess, F. N., M. S. Loughridge, M. S. McGehee and D. E. Boegeman, "Acoustic transponder system," J. Inst. Navigation, Vol. 13, no. 2, pp. 154-161, 1966.
- Spiess, F. N., Chairman of the Panel on Ocean Bottom Positioning, National Research Council Committee on Geodesy, *Seafloor Referenced Positioning: Needs and Opportunities*, Washington D.C.: Academy Press, 1983.
- Spiess, F. N., "Analysis of a possible sea floor strain measurement system," Marine Geodesy, Vol. 9, No. 4, pp. 385-398, 1985.
- Tran, J-M. and W. S. Hodgkiss, "High resolution beamforming on vertical arrays in a realistic oceanic environment," Technical Memorandum 408, Marine Physical Laboratory, Scripps Institution of Oceanography, San Diego, CA, Jan. 1989.
- Tyce, R. C., "Depth dependence of directionality of ambient noise in the North Pacific: Experimental data and equipment design," CP-32, SACLANTCEN, La Spezia, Italy, 1982.
- Urick, R. J., *Principles of Underwater Sound*, 3rd ed., New York: McGraw-Hill Book Co., pp. 6-11, 1983.
- Urick, R. J., *Ambient noise in the sea*, Washington, D.C.: Undersea Warfare Technology Office, Naval Sea Systems Command, Department of the Navy, 1984.
- Wagstaff, R. A., "Low frequency ambient noise in the deep sound channel- the missing component," J. Acoust. Soc. Am., Vol. 69, no. 4, pp. 1009-1014, April, 1981.
- Wagstaff, R. A., J. L. Berrou and F. D. Cotaras, "Use of the towship for assessing towed-array performance and analyzing data quality," J. Acoust. Soc. Am., Vol. 72, no. 3, pp. 983-992, Sept. 1982.
- Wagstaff, R. A., private communication, February 1988.
- Wales, S. C. and O. I. Diachok, "Ambient noise vertical directionality in the Northwest Atlantic," J. Acoust. Soc. Amer., Vol. 70, no. 2, pp. 577-582, August 1981.

Weinberg, H., "Generic sonar model," NUSC Technical Document 5971D, Naval Underwater Systems Center, New London, CT, 1985.

Wenz, G. M., "Acoustic ambient noise in the ocean: Spectra and sources," J. Acoust. Soc. Amer., Vol. 34, pp. 1936-1956, 1962.

Wilson, J. H., "Site and frequency dependence of ambient noise in the Northeastern Pacific Ocean," J. Acoust. Soc. Amer., Vol. 73, no. 2, pp. 539-545, 1983.

APPENDIX A: ELEMENT AND PROCESSOR IDENTIFICATION

Element Identification: Identification of the hydrophone elements varies with the associated stage of array fabrication. Tables A.1 and A.2 illustrate the ID cross-reference for the vertical deployment during the VLA1 experiment in September 1987. The first column results from the 'at sea' configuration recorded on magnetic tape, the second column refers to the laboratory array test setup, the third column is the identification scheme used during hose fabrication and testing, and the fourth column lists individual element numbers. *Channel* numbers represent the order in which the data was recorded on magnetic tape throughout the experiment. The channels are numbered from the bottom or physically deepest phone (# 1) to the top phone (# 120) which was closest to *FLIP*; the phase-reversed channels are indicated. The *ID* is referenced to a particular processor. P1 is the deepest processor which collects data from 5 phones below it (channels 1-5) and 5 phones above (channels 6-10). The H designation refers to the acquisition timing. The data from each 10 channel P-section are stored as equally spaced time multiplexed samples, starting with H0. The clocks are resynchronized every 2 ms with a pulse generated in the array telemetry module. This results in a phase shift of $\omega n\tau$ where ω is the frequency, n is the channel position H_n , and τ is the 0.2 ms sample frequency. The effect of this phase shift on the beampattern is significant as frequency increases (Figure 3.15c). The *hose* designation identifies which physical hydrophone hose section was being sampled. The hose sections are identical facilitating construction, testing and maintenance, and were tested individually in the laboratory prior to array installation. The lab test results are summarized in the last three columns; *100 Hz level* is the amplified output of the differentially received line driver in dB referenced to the signal injected electronically at the hydrophone, *low and high -3 dB* are the frequency cutoff points in Hz. The *phoneid* identifies the individual phones prior to installation within the hose section.

Processor Identification: The processors are identified with a software ID and a hardware ID (Table A.3). The software ID reflects the physical position the processor claims within the array and is programmed as such in the EPROM. Each processor transmits the data sampled during a 2 ms frame within a time window dictated by its software ID. This ID may be reprogrammed by the operator and will have the effect of changing the position of data transmission window for the specified processor. The hardware ID is hardwired for each individual processor, providing a fixed ID reference. The bit stream location refers to the processor data location within a 2 ms frame of data. The contents of the 8 locations assigned to each processor varies with the commands the processor receives [Sotirin and Hildebrand, 1988].

REFERENCES

- Sotirin, B. J., and J. A. Hildebrand, "Large aperture digital acoustic array," IEEE Journal of Oceanic Engineering, OE-13, No. 4, pp. 271-281, October 1988.

channel	ID	hosc	phone ID	100Hz level	low3db Hz	high3db Hz
1	P1H9	20B5	196	-1.2	6.4	214
2	P1H8	20B4	197	+0.7	4.0	220
3	P1H7	20B3	198	-1.2	5.8	216
4	P1H6	20B2	199	-0.7	5.1	221
5 (-)	P1H5	20B1	200	-0.1	4.6	15.0 k
6 (-)	P1H4	12A1	111	+0.3	3.9	14.6 k
7	P1H3	12A2	112	+0.2	4.7	226
8	P1H2	12A3	113	+0.1	5.2	217
9	P1H1	12A4	114	+0.2	4.5	225
10	P1H0	12A5	115	+0.4	4.6	232
11	P2H9	12B5	116	+0.1	4.4	217
12	P2H8	12B4	117	0	4.8	240
13	P2H7	12B3	118	+0.1	4.4	211
14	P2H6	12B2	119	-0.1	4.8	204
15	P2H5	12B1	120	-1.2	5.1	15.2 k
16 (-)	P2H4	19A1	181	-0.4	6.1	14.7 k
17	P2H3	19A2	182	+0.1	4.6	217
18	P2H2	19A3	183	+0.2	4.9	223
19	P2H1	19A4	184	-0.8	5.5	220
20	P2H0	19A5	185	-0.6	6.3	221
21 (-)	P3H9	19B5	186	-0.3	4.5	230
22 (-)	P3H8	19B4	187	-0.3	4.7	223
23	P3H7	19B3	188	-0.6	5.3	217
24	P3H6	19B2	189	-0.8	5.3	218
25 (-)	P3H5	19B1	190	-0.6	4.7	15.3 k
26	P3H4	16A1	151	-1.1	5.2	15.0 k
27	P3H3	16A2	152	-0.6	4.7	220
28	P3H2	16A3	153	-0.4	4.8	211
29	P3H1	16A4	154	+0.3	4.6	230
30	P3H0	16A5	155	+0.4	4.4	229
31	P4H9	16B5	156	0	5.0	225
32	P4H8	16B4	157	+0.1	4.7	224
33	P4H7	16B3	158	0	4.9	223
34	P4H6	16B2	159	-0.7	5.5	218
35 (-)	P4H5	16B1	160	-0.7	6.0	14.1 k
36 (-)	P4H4	11A1	101	-0.5	5.0	14.3 k
37	P4H3	11A2	102	-0.5	5.0	220
38	P4H2	11A3	103	-0.7	4.6	217
39	P4H1	11A4	104	0	4.3	227
40	P4H0	11A5	105	0	4.9	225
41	P5H9	11B5	106	+0.3	4.5	231
42	P5H8	11B4	107	+0.1	4.5	220
43	P5H7	11B3	108	-0.4	4.6	220
44 (-)	P5H6	11B2	109	+0.1	4.8	223
45 (-)	P5H5	11B1	110	-0.2	4.3	14.6 k
46 (-)	P5H4	7A1	61	-0.3	4.2	15.3 k
47	P5H3	7A2	62	-0.3	4.7	216
48	P5H2	7A3	63	-0.3	4.2	218
49	P5H1	7A4	64	+0.3	4.6	222
50	P5H0	7A5	65	-0.3	4.0	214
51 (-)	P6H9	7B5	66	-0.4	5.0	211
52	P6H8	7B4	67	+0.2	4.7	214
53	P6H7	7B3	68	-0.3	5.8	217
54	P6H6	7B2	69	0	4.1	216
55 (-)	P6H5	7B1	70	-0.3	4.7	15.2 k
56 (-)	P6H4	5A1	41	-0.3	4.4	14.2 k
57	P6H3	5A2	42	+0.5	4.0	220
58	P6H2	5A3	43	-0.1	4.8	220
59	P6H1	5A4	44	0	3.8	210
60	P6H0	5A5	45	0	4.5	225

Table A.1. Element identification for channels 1-60 1987.

channel	ID	hose	phone ID	100Hz level	low3db Hz	high3db Hz
61	P7H9	5B5	46	0	4.8	222
62	P7H8	5B4	47	+0.3	4.4	223
63	P7H7	5B3	48	-0.2	5.0	226
64 (-)	P7H6	5B2	49	+0.1	4.0	226
65	P7H5	5B1	50	-0.4	4.2	15.2 k
66 (-)	P7H4	2A1	0	-0.6	4.7	14.5 k
67 (-)	P7H3	2A2	0	-0.6	5.9	228
68	P7H2	2A3	13	0	3.7	230
69 (-)	P7H1	2A4	0	-0.6	3.7	201
70 (-)	P7H0	2A5	0	-0.1	4.9	217
71 (-)	P8H9	2B5	0	-0.4	6.0	219
72 (-)	P8H8	2B4	17	-0.5	4.6	205
73 (-)	P8H7	2B3	0	+0.4	4.3	235
74	P8H6	2B2	212	-0.2	4.6	228
75 (-)	P8H5	2B1	0	0	5.8	14.8 k
76 (-)	P8H4	13A1	121	-0.3	5.1	14.9 k
77 (-)	P8H3	13A2	122	-0.7	5.1	210
78	P8H2	13A3	123	-0.8	5.3	218
79	P8H1	13A4	124	-0.8	5.6	219
80	P8H0	13A5	125	-0.7	5.7	212
81	P9H9	13B5	126	-0.4	4.8	225
82	P9H8	13B4	127	+0.5	4.8	219
83	P9H7	13B3	128	+0.5	4.6	230
84	P9H6	13B2	129	-0.8	5.4	212
85 (-)	P9H5	13B1	130	-0.5	5.1	14.8 k
86 (-)	P9H4	17A1	161	-0.6	5.6	13.9 k
87	P9H3	17A2	162	-0.6	5.0	215
88	P9H2	17A3	163	-0.4	5.0	211
89	P9H1	17A4	164	-0.5	4.9	214
90	P9H0	17A5	165	-0.5	4.9	217
91	P10H9	17B5	166	-0.7	5.2	217
92	P10H8	17B4	167	-0.6	5.0	224
93	P10H7	17B3	168	-0.7	5.1	223
94	P10H6	17B2	169	+0.7	4.1	226
95 (-)	P10H5	17B1	170	-0.6	4.6	14.26 k
96 (-)	P10H4	14A1	131	-0.4	4.3	14.8 k
97	P10H3	14A2	132	+0.7	4.4	232
98	P10H2	14A3	133	-0.7	5.3	216
99	P10H1	14A4	134	+0.2	4.6	226
100	P10H0	14A5	135	-0.1	4.9	220
101	P11H9	14B5	136	-0.5	4.9	227
102	P11H8	14B4	137	-0.3	5.1	220
103	P11H7	14B3	138	-0.1	4.6	218
104	P11H6	14B2	139	+0.4	4.4	240
105 (-)	P11H5	14B1	140	0	4.5	15.5 k
106 (-)	P11H4	4A1	31	-0.3	5.0	15.8 k
107	P11H3	4A2	32	+0.4	4.5	230
108	P11H2	4A3	33	0	4.4	234
109	P11H1	4A4	34	-0.1	4.9	223
110	P11H0	4A5	35	-0.1	4.8	231
111	P12H9	4B5	36	+0.2	4.6	225
112	P12H8	4B4	37	+0.3	4.0	231
113	P12H7	4B3	38	-0.3	4.2	219
114	P12H6	4B2	39	0	4.7	223
115 (-)	P12H5	4B1	40	-0.5	5.0	15.6 k
116 (-)	P12H4	21A1	201	-0.6	8.2	15.6 k
117	P12H3	21A2	202	-0.5	5.1	222
118 (-)	P12H2	21A3	203	+0.2	4.5	226
119	P12H1	21A4	204	-0.6	6.5	211
120	P12H0	21A5	205	-1.1	6.2	215

Table A.2. Element identification for channels 61-120.

Hose #	Processor		Bit Stream Location
	SWID	HWID	
	*** FLIP ***		
	Adaptor		-----
21B			
21A			
4B	12	6	91-98
4A			
14B	11	14	83-90
14A			
17B	10	13	75-82
17A			
13B	9	11	67-74
13A			
2B	8	15	59-66
2A			
5B	7	7	51-58
5A			
7B	6	10	43-50
7A			
11B	5	16	35-42
11A			
16B	4	12	27-34
16A			
19B	3	3	19-26
19A			
12B	2	C	11-18
12A			
20B	1	8	3 - 10
20A			
	Terminator		

Table A.3. Processor Identification - September 1987.

APPENDIX B: ARRAY BEAMPATTERN

The directional characteristics of the array may be used as an indicator of the robustness of coherent processing schemes when confronted with random errors in amplitude shading and phase response. The expressions are also useful in evaluating the effect of modifying array design parameters eg. number of elements and element separation. Generation of the array beampattern follows a similar development to that described by Stutzman and Thiele [1981]. The array is an equally spaced linear array with 10 elements per section and 12 sections per array.

The hydrophone response is omnidirectional and is designated as $A_0 = A_1 = \dots A_N$ where N is the number of elements. A beampattern in terms of angle of arrival θ is calculated by summing the phase corrected response for each element to an incoming plane wave; this pattern is referred to as the array factor when it is expressed in terms of phase angle ϕ described below. The phase of the incoming wave arriving at the middle of the array is arbitrarily set to zero. The phase of the incoming wave arriving at the element just below the middle is delayed by a factor which is proportional to the distance traveled by the wave $\frac{(1/2)d\cos\theta}{\lambda} = \frac{\phi}{2\pi}$ such that for this element $\phi = \frac{2\pi(d/2)\cos\theta}{\lambda}$, where d is the distance between elements in meters, λ is the wavelength of the incoming wave, and θ is the angle of arrival of the incoming wave where a wave arriving normal to the array has an angle of arrival of $\frac{\pi}{2}$ radians. The phase of the incoming wave arriving at subsequent array elements is calculated similarly thus:

$$AF = \sum_{n=0}^{N-1} A_n e^{jk(n - \frac{N-1}{2})d\cos\theta}$$

where $k = \text{wavenumber} = \frac{2\pi}{\lambda}$ and the index n is initialized to 0 at the top element of the array. By assuming that the amplitude response is identical for each element, the array factor may be written in closed form which permits evaluation of specific beampattern parameters by inspection. With ϕ defined as $\phi = kd\cos\theta$ and by assuming that the element amplitude response is equal to A , the array factor becomes,

$$AF = Ae^{j\frac{N-1}{2}\phi} \sum_{n=0}^{N-1} e^{jn\phi}$$

Although the above equation could be evaluated using Fourier series in terms of ϕ , the beampattern is normally plotted in terms of θ , the angle of arrival. Manipulating the summation:

$$\begin{aligned} AF &= Ae^{j\frac{N-1}{2}\phi} \frac{1 - e^{jN\phi}}{1 - e^{j\phi}} = Ae^{j\frac{N-1}{2}\phi} \left[\frac{e^{jN\phi/2}}{e^{j\phi/2}} \frac{e^{jN\phi/2} - e^{-jN\phi/2}}{e^{j\phi/2} - e^{-j\phi/2}} \right] \\ &= Ae^{j\frac{N-1}{2}\phi} \left[e^{j\frac{(N-1)\phi}{2}} \frac{\sin(\frac{N\phi}{2})}{\sin(\frac{\phi}{2})} \right] = A \frac{\sin(\frac{N\phi}{2})}{\sin(\frac{\phi}{2})} \end{aligned}$$

The array factor may be normalized by the maximum response $A \sum_{n=0}^{N-1} 1 = AN$ at $\phi=0$

resulting in an expression which is symmetric about π :

$$AF_{normalized} = f(\phi) = \frac{\sin(N\phi/2)}{N\sin(\phi/2)} = \frac{\sin((Nkd\cos\theta)/2)}{N\sin((kd\cos\theta)/2)}$$

The main beam width and number and location of the sidelobes are easily evaluated from the closed form notation. The width of the main lobe may be measured by the position of the first zero crossing which occurs when $\sin(N\phi/2) = 0$, or $\phi = 2\pi/N$. This occurs at $\theta = \arccos(\frac{\lambda}{Nd})$. A rule-of-thumb, using a small angle approximation, is that the mainlobe width $\approx 2 * (\pi/4 - \theta) = 2 * \arcsin(\lambda/r) = 2\lambda/r$, where r is the array aperture Nd , and to half power is $0.886\lambda/r$. For the array at 100 Hz, $\lambda = 15$ meters, $d = 7.5$ meters, $N = 120$ and the first zero crossing occurs at $\phi = \pm \pi/60$ or $\theta = \pi/2 \pm 0.0053\pi$ yielding a main beam width measured at the zero crossings of 1.9° which corresponds to a half-power beamwidth of less than 1° . Subsequent zero crossings define the widths of the sidelobes and occur at $\phi_i = \frac{i2\pi}{N}$. This indicates that for one period of $f(\phi)$ there are $N-2$ sidelobes plus one mainlobe, that the width of each sidelobe is $2\pi/N$, and that the width of the mainlobe is twice that or π/N . The array factor response pattern of an equally spaced linear array is independent of the incoming wave frequency and of the element spacing. It is dependent only on the number of elements in the array N . The beam pattern is not however, and in terms of θ , further inspection indicates that as the aperture Nd increases (this parameter may increase with the inter-element spacing or with the number of elements) or the frequency increases the number of sidelobes increases, the width of the sidelobes decreases, and the width of the mainlobe decreases. The mainlobe can be thought of as a spatial sampling instrument whose bandwidth is $2\lambda/r$. The finest angular resolution of the noise field that can be achieved then is related to the array aperture size in terms of the mainlobe width. This angular resolution, termed the critical angle is half the mainlobe width or $\theta_c = \lambda/r$.

The beam pattern of a vertical linear array is a function of elevation angle θ but not of the azimuthal angle. Thus the beam pattern exhibits cylindrical symmetry about the line of the array, and it is completely determined for $0 < \theta < \pi$ or $-1 < \cos\theta < 1$. This region, known as the visible region, is described in terms of ϕ as $-kd < \phi < kd$. Interpretation of directional data is facilitated with an intuitive understanding of the mapping between electrical phase ϕ and physical phase θ . If the element response is linearly phase-shifted electronically to redirect the pattern in space, the phase-shift factor α is additive redefining the visible region as $\alpha - kd < \phi < \alpha + kd$. The array described was cut for a $\lambda/2$ spacing at 100 Hz of 7.5 meters between elements. Therefore at 100 Hz, exactly one period of the array factor appears within the visible region. At 50 Hz, only half a period is visible; in terms of steering the main beam as shown in Figure 3.14, as ϕ is increased beyond the visible region, the main beam disappears and only the side lobes of the array remain directed toward real space. Increasing the frequency to 200 Hz, two periods are visible giving rise to the grating lobes, which are at the same magnitude as the main beam, at 0 and 180 degrees for a broadside beam. These grating lobes restrict the ability of the array to discriminate between signals arriving at different angles.

REFERENCES

- Bracewell, R. N. and J. A. Roberts, "Aerial smoothing in radio astronomy," *Aust. J. Phys.*, Vol. 7, pp. 615-640, December 1954.
- Stutzman, W. L., and G. A. Thiele, *Antenna Theory and Design*, New York: John Wiley and Sons, Inc., pp. 108-167, 1981.

Appendix C

NAVIGATION SOFTWARE FOR THE MPL VERTICAL LINE ARRAY

C.1. ABSTRACT

This report describes the navigation software and demonstrates its operation using data obtained during an experiment in which a large aperture low frequency acoustic array, designed and built at the Marine Physical Laboratory (MPL), was deployed vertically from the Research Platform *FLIP* in the NE Pacific. The array was equipped with a 12 KHz acoustic navigation subsystem. Travel time measurements from near bottom acoustic transponders of known position were received by specific array elements throughout the deployment. These measurements were converted to spatial positions of the array elements by a nonlinear least squares technique. The data collection methods and navigation software programs which locate the transponders, calculate the travel time from detected returns and convert travel times to spatial positions are documented.

C.2. INTRODUCTION

A high frequency acoustic navigation system is an integral part of the large aperture vertical array deployed in 4700 m of water in the NE Pacific during September 1987. Navigation is defined in this context as the process of locating individual elements of the array in 3-dimension space at any particular time. The method implemented in the array involves a transceiver near the ocean surface which sends unique interrogation signals that are detected by bottom moored transponders who reply with a pulse at 12 KHz. This reply is monitored by the array and the time delay between the initiation and reception of each of the pulses is calculated. Knowing the sound speed in the water column, and the location of the transceiver and the transponders, this travel time defines a slant range between each array receiver and each bottom transponder. A slant range from a known point (a transponder) describes a sphere of possible receiver locations. Intersecting spheres described by the slant ranges from three known points identify a single location if there are no errors. Because there are always sources of error in real data, a least squares filter is implemented to approximate the location by minimizing the squared difference between the calculated and measured values, which defines the error in the assumed position. This report documents the data collection methods and the navigation software used to locate 12 array receivers during the September experiment. The array itself is documented in [Sotirin *et al.*, 1988] and [Sotirin and Hildebrand, 1988]. The array navigation system, least squares filter and navigation data analysis are documented in [Sotirin and Hildebrand, 1989].

The navigation processing is separated into three programs. The first program locates the bottom transponders. The second program calculates travel times from a continuous recording of the 12 KHz detected returns for each

navigation receiver. The third program uses the travel times and transponder locations output from the first two programs to estimate the spatial positions of the receivers using a non-linear least squares filter. The logic flow and input/output files are detailed for each program in [Sotirin and Hodgkiss, 1989].

C.3. TRANSPONDER LOCALIZATION

The transponder positions must be surveyed to acquire the location parameters defining the transponder net which are ultimately used to navigate the array. Due to errors in the measured data, an estimation technique (least squares) must be implemented. Due to the nonlinear conversion from travel time space to xyz positional space, the least squares method proceeds iteratively. A data set is obtained containing spatial positions and travel time measurements. If all parameters were known exactly, the travel times calculated using the spatial positions and the measured value would be identical. This is obviously not the case, and the difference between the calculated and measured values defines the error in the assumed position which is minimized during the iteration. Transponder positions with accuracies of less than a meter are achieved by this method. The description below details the data collection, the program inputs, the least squares implementation, and the resulting transponder positions.

C.3.1. Data Collection

The input data set for the least squares iteration requires initial spatial positions of the transponders and transceiver in meters from an arbitrary origin, and slant ranges between the transponders and transceiver. The data collected in the form of travel times and Global Positioning Satellite (GPS) fixes are transformed into the input parameters required by the least squares filter. GPS fixes are converted into initial xy positions in meters from an arbitrary origin. Travel times are converted to slant ranges with knowledge of the local sound speed profile. The travel times required are normally recorded during an intensive surface ship survey during which the ship criss-crosses the area in which the transponders were deployed recording the travel time data and GPS fixes for its own position. [Spiess, 1985], [Smith *et al*, 1975] A transceiver is either hull mounted or towed on a short line such that its position relative to the ship is known. The transceiver sends a continuous stream of unique transponder interrogation pulses, and the transponder replies are recorded while the ship criss-crosses the area. Using this method, a series of travel times are obtained from a wide variety of ship positions. As the ship crosses over the top of a transponder, an estimate of transponder depth is acquired, and as the transponder baselines are crossed, intertransponder distances are defined.

During the September experiment, although travel times were recorded as described, the 12 KHz receiver was deployed on a 200 m line due to the noise level of the ship. This introduces the interrogator/receiver depth as an unknown defining an underdetermined set of equations which cannot be solved for a unique solution. Since the measurements described above were not sufficient for the transponder survey, the travel time data collected by the navigation equipment installed on *FLIP* were utilized instead. This is unfortunately not an optimum choice of observation configurations [Spiess, 1985] so the results of several

simulations devised to assess the effect on the estimated positions are also presented. The horizontal motion of *FLIP* was constrained by a three point moor. The *FLIP* data set provides sufficient range information but the azimuthal component was not well constrained. The vertical component was estimated from the echo sounding depth at *FLIP* and apriori information that the sea floor in the experiment area was relatively flat. The inputs used to locate the transponders are the vertical sound speed profile in the test area, the initial xy positions of *FLIP* from the arbitrary origin, the depth of the interrogation transponder hardwired to the *FLIP*, the slant ranges from each transponder to *FLIP* as determined by chart recorder traces and associated errors, the initial transponder xy positions from the arbitrary origin using the satellite fixes and the transponder depths.

The initial GPS positions in latitude and longitude are converted to xy distances in meters from an arbitrary origin. For the September experiment, the origin was chosen as 34° 47' N, 126° 00' W, with x increasing positively toward the east and y increasing positively toward the north. A GPS position of the ship is recorded during each transponder deployment. The transponders have 45 kg negative buoyancy when they are deployed from the fantail of the surface ship to insure that the GPS position of the ship is an accurate initial position of the actual transponder position on the sea floor. Latitude and longitude for each set of travel time measurements (one measurement from each transponder) are also converted to m to provide the initial estimate of the transceiver position during the survey. The 'survey' from *FLIP* had such a limited range that the same initial position was used for all measurement sets. During a normal ship survey, travel time data is collected from a large variety of horizontal positions and individual initial positions are important. If GPS positions are not available, a technique detailed in [Sotirin and Hodgkiss, 1989] may be used to estimate the initial position from the measured travel time data. Positions in latitude and longitude were converted to meters by calculating the radius of the earth at the position using the following equations [Stacey]:

$$x = r_p \delta(lat) , \quad y = r_p \cos(lat) \delta(long)$$

$$r_p = a (1 - f \sin^2(lat)) , \quad f = \frac{a - c}{a}$$

where x is the E-W distance in meters of the position from the origin, y is the N-S distance in meters of the position from the origin, r_p is the radius of the earth at the position latitude, $\delta(lat)$ is the difference in latitude in radians between the position and the origin, $\delta(long)$ is similarly the difference in longitude, lat is the latitude of the position, a is the equatorial radius of the earth in meters and c is similarly the polar radius.

The conversion between travel time and xyz positions requires knowledge of the sound speed profile at the experiment site. The local sound speed profile was calculated from measurements of conductivity, temperature and depth. Travel time deviations due to the variations within the thermocline and to refraction of acoustical energy were shown to be negligible for this experiment therefore a constant sound speed (harmonic mean) was used for the conversion [Sotirin and Hildebrand, 1989].

The travel time measurements used for transponder localization were collected by transmitting the transponder interrogation signals from *FLIP* once an hour for 18 days and recording the returns on a chart recorder. The transceiver is mounted on the bottom (90 m in depth) of *FLIP* and the pulse level is adjusted

manually above the ambient noise for consistent transponder replies. Round trip travel times for navigating *FLIP* are measured carefully by hand on the chart recorder output with an estimated random gaussian error of 2-3 ms. The chart recorder trace, set on a one second sweep rate, records the filtered 12 kHz (500 Hz bandwidth) replies received from the transponder being interrogated (Figure C.1) delayed 6-7 seconds from the interrogation pulse. Each transponder is interrogated individually by transmitting its unique signal, triggered by the chart recorder, once per second for 45 seconds, and notating its reply on the chart by sweep number with color-coded pens (red, green or blue). The figure shows the direct and multipath (surface/bottom bounce) returns for each transponder. Differentiation between the surface and bottom bounces is difficult because the *FLIP* transceiver is the same distance below the surface as the transponder is above the sea floor. The direct return from the red and blue transponders is strong and consistent. Several error modes are evident in the returns from the green transponder however. The sporadic direct return of the green transponder (G_d) is caused by the transponder detecting either the surface or bottom bounce of the transmitted signal. The error was attributed to the transponder because the same transceiver system detects the returns from all transponders and this type of error was not evident on all transponders. Detection of the multipath arrival of the interrogation pulse delays the arrival of the transponder direct return such that it arrives at the same time as the multipath return of a direct interrogation pulse (G_{m1}). The multipath return of the multipath interrogation arrives 120 ms later (G_{m2}) clearly identifying the first error mode. The second error mode of the green transponder is displayed as the smaller perturbations in the time of arrival of the G_d return. It is more difficult to identify because the deviation from the true return is smaller (although still significant) and not as consistent as the first type of error. These error modes were identified during about 20% of the experiment at random intervals, causing concern during array detection post-processing discussed in the next section.

C.3.2. Software Implementation

Once the ingredients for the least squares method have been accumulated, all xyz positions are adjusted until the root mean squared (rms) error satisfies the convergence criteria. This is accomplished in several parts by first maintaining constant transponder positions and perturbing the *FLIP* positions, then holding the current *FLIP* positions constant while perturbing the transponder positions, and finally examining the mean squared error of each *FLIP* position to determine whether it should be preserved as a viable contributor. A general outline of the method is presented in Figure C.2 and discussed below. This is followed by a detailed description of the conversion from travel times to slant ranges and spatial positions.

The program consists of three concentric stages, the first stage adjusts the xy positions in two inner loops each testing the rms error against specific convergence criteria for the least squares filter, the second stage tests the total transponder rms error against a second set of convergence criteria, and the third stage tests yet again. The three stages are referred to within the software as stage 1: *xpfil*, stage 2: *xploop* and stage 3: *xpmain*. The two first stage loops shown in Figure C.2 have similar internal operations. The measured travel times, sound speed profile, *FLIP* depth and transponder depths are considered known, while the xy positions of *FLIP* and the transponders are considered unknown. The measured

travel times are converted to slant ranges by multiplying by the harmonic mean of the sound speed profile. This slant range is projected as a horizontal range and compared to the range calculated from the xy positions. For the first loop, the squared difference between these two ranges are summed over the number of transponders for a particular *FLIP* position and the square root is taken to yield the rms error. If the rms error does not satisfy the convergence criteria, then the *FLIP* position is adjusted and the loop repeats with the adjusted position. The adjustment is calculated with the search direction as the negative gradient and the step size as a constant (1.5 m) unless the rms error is less than 1 m at which time the step size begins to decrease; as the minimum is approached, the step size is calculated as a function of the percent change in iterated rms error. The convergence criteria for the first stage loops are defined such that an absolute rms error less than 0.15 m, a 0.015 percent change in the iterated rms error, or a maximum number of iterations (30) will terminate the loop and save the current position. These criteria test each adjusted position individually. The first loop is repeated for each *FLIP* position. The second loop of the first stage performs the same cadence maintaining the current *FLIP* positions constant while adjusting the transponder positions. The rms error is calculated over the number of *FLIP* positions, and evaluated using the same criteria. The second loop is repeated for each transponder position. In the second stage, these two loops are initiated again based on the percent reduction (< 0.35%) in the transponder rms error summed over all transponders and total number of iterations (> 30). Upon completion of the first two stages, the rms error for all the transponders is calculated and evaluated according to the following criteria:

- 1) The rms error * $\sqrt{\text{number of } FLIP \text{ positions}}$ is < 1.0.
- 2) The percent reduction in rms error is less than a specified value (0.1%).
- 3) The absolute rms error is less than a specified number (0.75).

If the rms error satisfies any of the above criteria, the current positions are written out and the program is terminated. If the rms error does not satisfy any of the above criteria, then the rms errors associated with each *FLIP* position are examined and any position with an error greater than the transponder rms error times a user specified value (default=2) is deleted from the array and the entire process begins again. The rms error is initialized to 10000 prior to each loop/stage so that unless the absolute error is small, the loop/stage will always be executed more than once.

The conversion from travel time to slant range and the spatial position adjustment is straight forward and executed within the subroutines *xxcor* and *xpfil*. The program originates with the Marine Physical Laboratory's DEEPTOW group and has been in existence since the late 1960's. The version documented here is the most recent in a long series and, unfortunately, every programmer has left a mark. Consequently, the subroutines each have unique variable names for the parameters, increasing the confusion in documentation. The text below attempts to maintain the variable names within the subroutines specified. The travel time to slant range conversion is computed in *xxcor*. The measured information is input to the program as a slant range assuming a homogeneous medium with a sound speed of 1500 m/s. This is not normally the case, and for the September test the sound speed profile was measured and input as a data statement in *xxcor* into the array *vdp* as a horizontally stratified medium. If sound speed corrections are requested by the user, the input slant ranges are converted back to the original time measurement (*t*) and the slant range contribution for each sound speed layer is summed, returning the corrected slant range (*xnew*). If the slant range is a depth,

for example, the summation starts at the surface and sums the contribution in each layer until the accumulated time (t_a) is equal to the measured travel time. This is an implementation of the following equation in which x is the corrected slant range:

$$x = c * t - \frac{(z_T - z_0) * t}{\int_{z_0}^{z_T} \frac{dz}{C(z)}}$$

where in terms of the subroutine, $z_0 = \text{xdepth} = 0$, $z_T = z$ is the unknown depth, $C(z) = v$ is the sound speed in the layer, and $dz = \text{deltad}$ is the layer depth. When the unknown is a slant range, the implementation is an approximation to the above equation (where dz is the slant range component in the layer assuming the launch angle is constant) which is accurate for the configuration of the data set considered for the September experiment. Errors increase as the horizontal range or projection (defined below) of the slant range increases however, so for larger scale experiments a more accurate implementation is advised.

Once the slant range has been calculated, the conversion to spatial coordinates is visualized as the geometric relationship between the transmitter (t subscript) and receiver (r subscript).

$$\text{slant range} = [(x_t - x_r)^2 + (y_t - y_r)^2 + (z_t - z_r)^2]^{\frac{1}{2}}$$

Because the error in the depth parameters are small compared to the horizontal parameters, the slant range is projected onto the xy plane prior to the adjustment (Figure C.3):

$$\text{horizontal projection} = [(\text{slant range})^2 - (z_t - z_r)^2]^{\frac{1}{2}} = [(x_t - x_r)^2 + (y_t - y_r)^2]^{\frac{1}{2}}$$

The left half of the equation is calculated in *xpread*, $CRANS(NTR, NPOS) = (S^2 - D^2)^{\frac{1}{2}}$ where NTR = the number of transponders, $NPOS$ = the number of *FLIP* positions, S = slant range between a position and a transponder, D = transponder depth - *FLIP* depth, and passed into *xpfil* as an array *HRAN* which is redefined within a loop as a variable *HH*. The right half of the equation is calculated in *xpfil*, $RNGEC = \sqrt{(XDIFF)^2 + (YDIFF)^2}$, where $XDIFF = XG - XF(NDAT)$, $YDIFF = YG - YF(NDAT)$, (XG, YG) are the xy positions being interated, (XF, YF) are the fixed positions indexed over *NDATA* data points, and the error *ERR*, summed over the number of fixed positions, is $(RNGEC - HH)^2$.

The adjustment is calculated using the steepest descent method to minimize the error by following the mean squared error gradient to a minimum. For known transponder positions and the x-direction, the perturbed position is:

$$XG = \sum_{NDAT=1}^{NDATA} XG + h LRR(NDAT)$$

where h is the step size, and *LRR* is the negative derivative of the error function with respect to *XG*. The y-direction adjustment is calculated similarly. The error derivative expands to

$$\begin{aligned}
 ERR &= \frac{d(RNGEC-HH)^2}{dXG} = 2(HH - RNGEC) \frac{d(XDIFF^2 + YDIFF^2)^{\frac{1}{2}}}{dXG} \\
 &= \frac{(HH - RNGEC)}{RNGEC} \frac{d(XG-XF)^2}{dXG} = \text{RATIO} * XDIFF
 \end{aligned}$$

where $RATIO = (HH - RNGEC)/RNGEC$, and the constants are absorbed by the step size h .

C.3.3. Simulations

Several simulations of the array navigation system were conducted to examine the sensitivity of the estimated transponder positions to errors in travel time measurements and initial positions. The spatial configuration used closely resembles the experimental set up of the September sea test as shown in Figure C.4. The transponders and *FLIP* were initially assigned to known positions with determined slant ranges as shown. Two simulations were conducted to illustrate the transponder position response to errors; two other simulations were conducted to show the effect of transponder and *FLIP* positional errors on the estimated array positions and are presented in [Sotirin and Hildebrand, 1989]. The result of the first simulation was the 3D error surface for various parameters. The second was a Monte Carlo simulation of the initial transponder positions. The simulations provide an understanding of the effect of the unconventional survey data.

To examine the error surface for the least squares configuration used in the previous section, specific model parameters were perturbed systematically. The error is the rms value of the differences between the slant ranges based on the travel time measurements corrected for sound speed deviations (Eq 1.1 dividing through by c) and those calculated from the spatial positions of the transponders and *FLIP* which were output from the least squares filter. Ideally this produces a single well-defined minimum for which the optimization method searches. This is not the case in many real applications however, and the possibility of local minima and/or a broad global minimum should be investigated. The inverted error surface for perturbations in the horizontal positions of the blue transponder is shown in Figure C.5. It exhibits a narrow channel of local minima which appear as a ridge plotted as the negative logarithm of the error against the perturbation amplitude in x and y position. The ridge is orientated perpendicularly to the *FLIP*/transponder range direction indicating that the azimuthal component is not well constrained. Perturbing the horizontal positions of the other transponders produced similar results.

The system displays a sensitivity to initial positions which is shown to be an artifact of the limitations in the *FLIP* 'survey' discussed previously and of the structure of the error surface. The direction in which the transponders are moved is constrained to nearly parallel to the *FLIP*-transponder baseline (Figure C.6). This occurs because the distribution of *FLIP* positions shown in Figure C.4, provide adequate range information but minimal azimuthal information regarding the transponder positions as was indicated by the error surface. There are no sure techniques for locating a global minimum in the company of local minima. Without independent positional data corroborating the results, either Monte Carlo techniques would have to be incorporated in the initial position of each

transponder, or knowledge of the error surface would have to be employed as a constraint (search range/azimuth space rather than xy space). Fortunately, the initial estimate of the transponder positions were acquired from accurate GPS fixes and the resulting error in GPS positions compared to the estimated *FLIP* positions at corresponding times had an rms value of only 10 m. Thus the estimated transponder positions were declared adequate.

C.4. ARRAY TRAVEL TIME ACQUISITION

Travel time measurements were acquired by interrogating three bottom mounted transponders from *FLIP* and detecting their replies at the navigation receivers distributed across the 900 m aperture array. There are 24 navigation receivers located at ± 3.75 m from each processor which are separated by 75 m (Figure C.7). Due to bandwidth constraints, data from 12 of the navigation receivers (one/section) were decimated and recorded during the September 1987 sea test. The data bit stream from transmit time of the interrogation pulse to receive time of the reply at the array was reconstructed during post-processing for each navigation receiver and the travel times calculated.

The navigation timing was based on a 16 bit clock driven at a 1 KHz rate which initiated the navigation sequence. This clock is referred to as the hardware clock to differentiate it from the real-time clock (local time) and the Greenwich Mean Time (GMT) clock. The timing is illustrated in Figure C.8 and described below. A transceiver located at the bottom of *FLIP* transmitted a series of 65536 ms transponder sequences (Figure C.8a). A transponder sequence consisted of 4 interrogation pulses 10 ms long at 10 s intervals beginning at a 16 bit clock rollover followed by a 35.536 s silent interval (Figure C.8b). The first three pulses were at the unique transponder interrogate frequencies of the bottom transponders (10, 10.5 and 11 KHz). Upon receiving an interrogation pulse the bottom transponders replied with a 3 ms pulse at 12 KHz. The turn around time of the transponders is signal to noise dependent, however due to the strength of the transmitted signal, the delay was assumed to be less than 1 ms. The fourth interrogation pulse transmitted by the *FLIP* interrogate transceiver was at 12 KHz which simulates a bottom transponder reply. The array therefore received four consecutive 12 KHz reply pulses about once a minute (Figure C.8c). The navigation receivers were capable of detecting a 12 KHz signal 6 dB below the noise level in a 200 Hz band. The binary output of the detector was sampled at 5 KHz and decimated by 2 to provide a continuous time series consistent with the 5 bits per processor every 2 ms allowed for navigation data within the specified data format. Thus the data from 12 navigation receivers located 3.75 m below each processor (H5 in Figure C.7) in the array were multiplexed in with the low frequency acoustic data, transmitted to the surface and recorded. The interrogation sequence was synchronized with the timebase in the array and the initiation time of the sequence (as indicated by the rollover of the hardware clock) was sampled every 128 ms and recorded on the tape. The tape format showing the placement of the navigation data is illustrated in Figure C.9. The navigation data time series are reconstructed from this recorded data by the method described below.

The structure of the data on tape was not optimized to facilitate extraction of the navigation bit stream. The header containing the timing information appears in the first 8 words of each tape buffer which contains 128 ms of data. Most of the 6280 16-bit words within a buffer are assigned to low frequency acoustics rather

than navigation as seen in Figure C.9. To reconstruct the sampled time series output from each navigation receiver, the 5 bits/processor must be extracted and stored. The major programming effort was in initializing and incrementing pointers and in error checking. The extraction of the data begins with the data buffer containing the hardware clock rollover. The rollover may occur anywhere within the data buffer. The program examines each buffer header for the hardware clock rollover. This is determined by testing between consecutive clock times for a negative difference, and linearly interpolating within the buffer for the correct frame. For example, if the hardware clock in buffer 1 is $hwc_1 = 65430$ and the hardware clock in the next consecutive buffer is $hwc_2 = 22$, then the difference ($hwc_2 - hwc_1 = -65408$) is negative and the clock rollover occurs within buffer 1 at frame 53; the data stored would begin at frame 0, buffer 1. The time difference from the beginning of the buffer to the rollover is stored in a parameter called *start* and passed to the subroutine *navloc* which calculates the travel time. Once the rollover is identified, the navigation data associated with each processor is masked off and stored as the 10 most significant bits in a 16-bit word (*fillnav*).

The travel time calculation is a simple difference once the time of the transponder reply is determined. To locate the reply, the data is treated as a time series of 0.4 ms bits, and a correlation between the time series data and a replica transponder pulse is initiated as a matched filter detector. Due to inconsistencies in receiver detection threshold and noise level, each receiver is assigned an individual replica pulse length. Temperature sensitivity of the capacitors and high failure rate of the inductors in a phase matching tuned filter caused the mismatch in the detection threshold of the individual receivers. This variation in receiver error is apparent in the positional error distribution shown in Figure C.10, in which the only hardware or processing difference is in the navigation receiver itself. Additional variation in receiver signal to noise level of the incoming reply could have been caused by the 12 KHz beam pattern of the individual elements. Each element consisted of two hydrophones wired in series with a spacing between 8 and 9 cm such that at 12 KHz, a notch in the beam pattern appears between 46° and 52° from broadside. From Figure C.4, the arrival angle of the transponder replies when the array was nominally at 400 m was between 58° and 65° from broadside and signal to noise was high enough to be detected; at deeper depths, however, this is potentially a problem. The rms error used in the distribution calculations accompanies each receiver position estimation described in Section III. The transponder reply is a CW pulse, so the correlator is implemented as a moving adder, with a detection defined as the first occurrence of a normalized correlation amplitude greater than or equal to 1.0 within a valid data window.

The window was installed due to excessive noise levels and the interference seen in the return of a single navigation receiver from the hardware clock rollover as shown in Figure C.11. The window must be determined prior to program execution. An option in the program *harrynav* (-p) will print out all bits set by the navigation receiver, packed into the least significant 10 bits of a 16-bit word (for a maximum of 3FF) to allow the user to determine the window parameter. An example is seen in Figure C.12: the return for processor 2 is clean and the transponder reply is quite clear. The last 4 bits of word 1503 are set followed by 8 bits in word 606, for a total of 12 sequential bits set. The words have a maximum of 10 bits or 4 ms. The valid data window length is a minimum of 100 ms and varies with the transponder. Only the leading edge of the window is specified in the window parameter input file *window.dat*. An estimate of the leading edge of the window for a particular receiver p may be obtained by multiplying the first word of the

transponder reply W_p by 4 and subtracting 184 ms. A window parameter for each processor and each transponder must be specified, 48 total. The algorithm for computing the time of arrival of the leading edge of the reply is

$$T_a = W_p * 4 + (10 - B_p) * 0.4 - start - c$$

where W_p is the first word, and B_p is the number of bits set in the first word, start is the time difference between the beginning of the data buffer and the hardware clock rollover as described earlier (printed in line 1 of Figure C.12 as Start: 14), and c is a constant = 134.68 ms; e.g. $W_p = 1503$, $B_p = 4$, $T_a = 5865.72$ ms which is the result shown in Figure C.12 for Roll: 1, Xponder: 1 Start: 14, Proc# 2 in the Figure. The constant c is a sum of the delays through the array system in ms determined by laboratory tests to be $7 + (128 - 0.016 * (32 - NPROC))$ where NPROC is the number of processors in the array. The 7 ms is due to data buffering in the array hardware and the remainder is due to buffering within the driver for the magnetic tape. This buffering delay was discovered later to be in error by 112 μ s and should have been calculated as $(128 \text{ ms/frame} - [125 \text{ (words/frame)} - 2 \text{ (header words)} - NPROC * 8 \text{ words/processor}] * 0.016 \text{ ms/word})$.

The result of the correlation is seen as a series of returns across the array for each of the transponders as shown in Figure C.13. One second of data for each processor is plotted during each transponder reply with the deepest processor P1 plotted on the bottom. The reply from the bottom transponders (Figure C.13a, b and c) appear at the deepest processor first and arrive sequentially at the shallower receivers as the pulse travels up through the water column. The pulse from the last transponder (Figure C.13d) travels down from FLIP. The squared amplitudes are normalized to 1.0 and plotted such that a value of 1 will be slightly above the zero level of the next processor. The noise and interference mentioned earlier is also evident; processor 6 represents a particularly noisy time series and interfering signals are seen travelling up and down the array, e.g. between 0.6 and 0.7 s on the plot of transponder 3. Each valid data window is marked with "x's"; the window length for the first and last transponders is 100 ms, but was increased for transponders 2 and 3 to 250 ms to enable detection of the transponder error modes illustrated by the green transponder (transponder 2) in Figure C.1. The time of arrival of the detected reply may be estimated from the plot by adding the time indicated by the plot to the number of ms notated at the top of the plot and subtracting a constant $c = 134$ ms defined previously. The travel times are converted into slant ranges by assuming a constant sound speed of 1500 m/s and written into ascii files for use in the spatial position calculation computed in the next program.

C.5. ARRAY SPATIAL LOCALIZATION

The navigation algorithm for the array elements is virtually identical to that described for the transponders once the initial array X-Y position is determined, except that the transponders are considered stationary. The element to transponder slant ranges corrected for sound speed, the depth of the transponder installed on FLIP and the adjusted transponder locations constitute the data required to navigate the array. The array positions are iterated to achieve the best fit to the data in a least squares sense. Array element relative location accuracies of a few meters are achieved by this method.

The array is not moored but hangs vertically from *FLIP* under 320 kg of tension; its horizontal range of motion is significant during a one minute time interval. Consequently, receiver locations are iterated using a single time slice of slant range data. The receiver slant range is the path from *FLIP* to the transponder to the receiver; *FLIP* slant range is simply the path to the transponder. The slant ranges are corrected for deviations due to a sound speed profile which differs from the assumed 1500 m/s, as are the receiver depths (which are obtained from the travel time measurement of the *FLIP* transceiver to each receiver), using the harmonic mean described earlier. The noise in the receiver slant range measurements (Figure C.14) is contributed to not only by the receiver noise as shown in the previous section but by the transponder malfunction described in the first section and by high frequency *FLIP* motion (recall that *FLIP* slant ranges are available only once per hour). Constraints on the difference in receiver depths and slant range measurements from one minute to the next are implemented as user parameters *thresd* and *thres*. If these thresholds are exceeded, the noisy data is ignored and another user parameter *alter* determines which interpolation scheme will be implemented, if any.

Localization of the array receivers now proceeds to the least squares filter. A constant initial xy position is assigned to *FLIP* based on a GPS position as was done during the transponder iteration for the *FLIP* initial position; the initial positions for the first receiver iterated is the estimated *FLIP* position; the initial positions for subsequent receivers is the estimated position of the previous receiver. The *FLIP* slant range is subtracted from the receiver slant ranges leaving the transponder to receiver portion. The horizontal slant ranges are calculated and the xy positions are iterated minimizing the squared error in calculated and 'measured' positions. With the transponder positions fixed, the iteration is confined to *FLIP* and the array receiver positions whose x, y and z positions are output with an associated rms error. The resulting analysis of data processed in this manner is presented in [Sotirin and Hildebrand, 1989].

C.6. ACKNOWLEDGEMENTS

This work was supported by the Office of Naval Research under Contract nos. N00014-87-K-0225 and N00014-87-C-0127. The authors are indebted to the undaunting work of the MPL staff. We wish to thank Vince Pavlicek for engineering expertise, Eric Wolin, Paul Henkart, Dick Currier and the MPL Deeptow Group for software support, Tony Aja, Dave Ensberg and Pam Scott for their assistance in the data processing effort and Jo Griffith for her illustrative talents. The captain and crew of the research platform *FLIP* contributed to the sea-going operation. Special thanks goes to Chris deMoustier for his critical reviews and valuable suggestions.

REFERENCES

- Smith, W., W. M. Marquet and M. M. Hunt, "Navigation Transponder Survey: Design and Analysis", in I.E.E.E. Ocean 75 Record, San Diego, CA, 563-567, Sept., 1975.
- Sotirin, B. J., F. V. Pavlicek and J. A. Hildebrand, "Low Frequency Digital Acoustic Array", in Current Practices and New Technology in Ocean Engineering-1988, ed. G. K. Wolfe and P. Y. Chang, American Society of Mechanical Engineers, NY, OED-Vol. 13, 1988
- Sotirin, B. J. and W. S. Hodgkiss, "Navigation software for the MPL vertical line array," MPL TM-409, Marine Physical Laboratory, Scripps Institution of Oceanography, La Jolla, CA, March, 1989.
- Sotirin, B. J. and J. A. Hildebrand, "Acoustic Navigation of a Large Aperture Array", J. Acoust. Soc. Am., submitted for publication, March 1989.
- Spiess, F. N., "Analysis of a Possible Sea Floor Strain Measurement System", Marine Geodesy, Vol. 9, No. 4, 385-398, 1985.

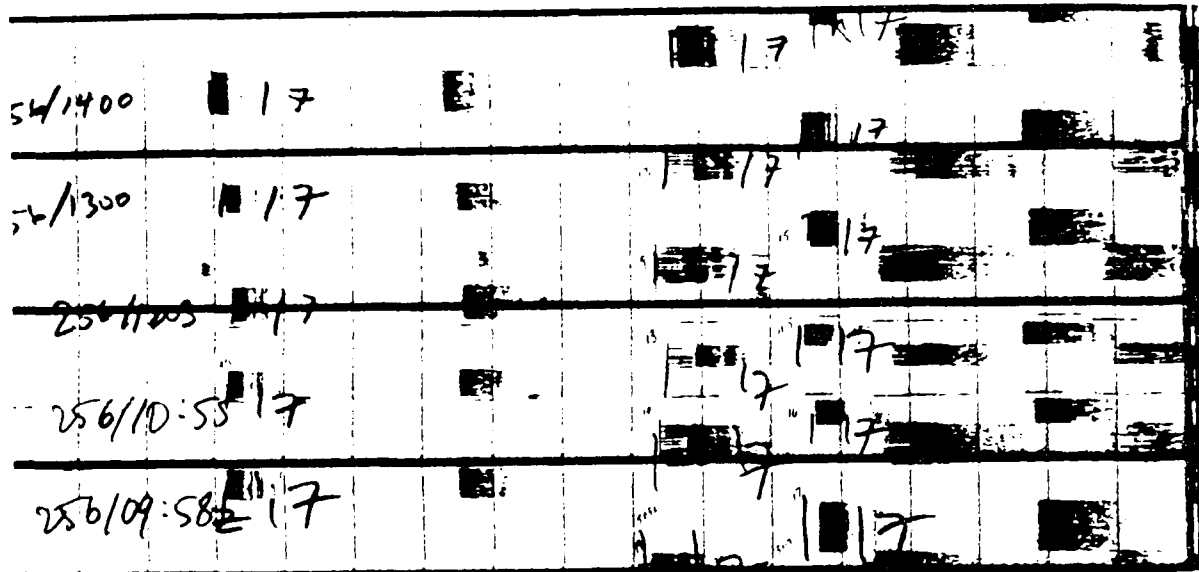


Figure C.1 FLIP Navigation System Detection of Transponder Replies. The signals represent the transponder replies plotted by a chart recorder. Each sweep represents one second of round trip travel time, each tic mark is 33.33 ms. Each transponder direct return is marked by Julian day/GMT and by the sweep number with colored pens for easy identification. A normal detection is clear and concise and may be measured by hand to within 2-3 ms. Two types of errors are evident in the returns of the green transponder. The first illustrates a weak direct return G_d , and the spacing between returns G_d , G_{m1} and G_{m2} indicates that the transponder is replying to a bounce of the interrogation signal. The second type of error illustrates smaller scale random returns, inconsistent in occurrence and amplitude.

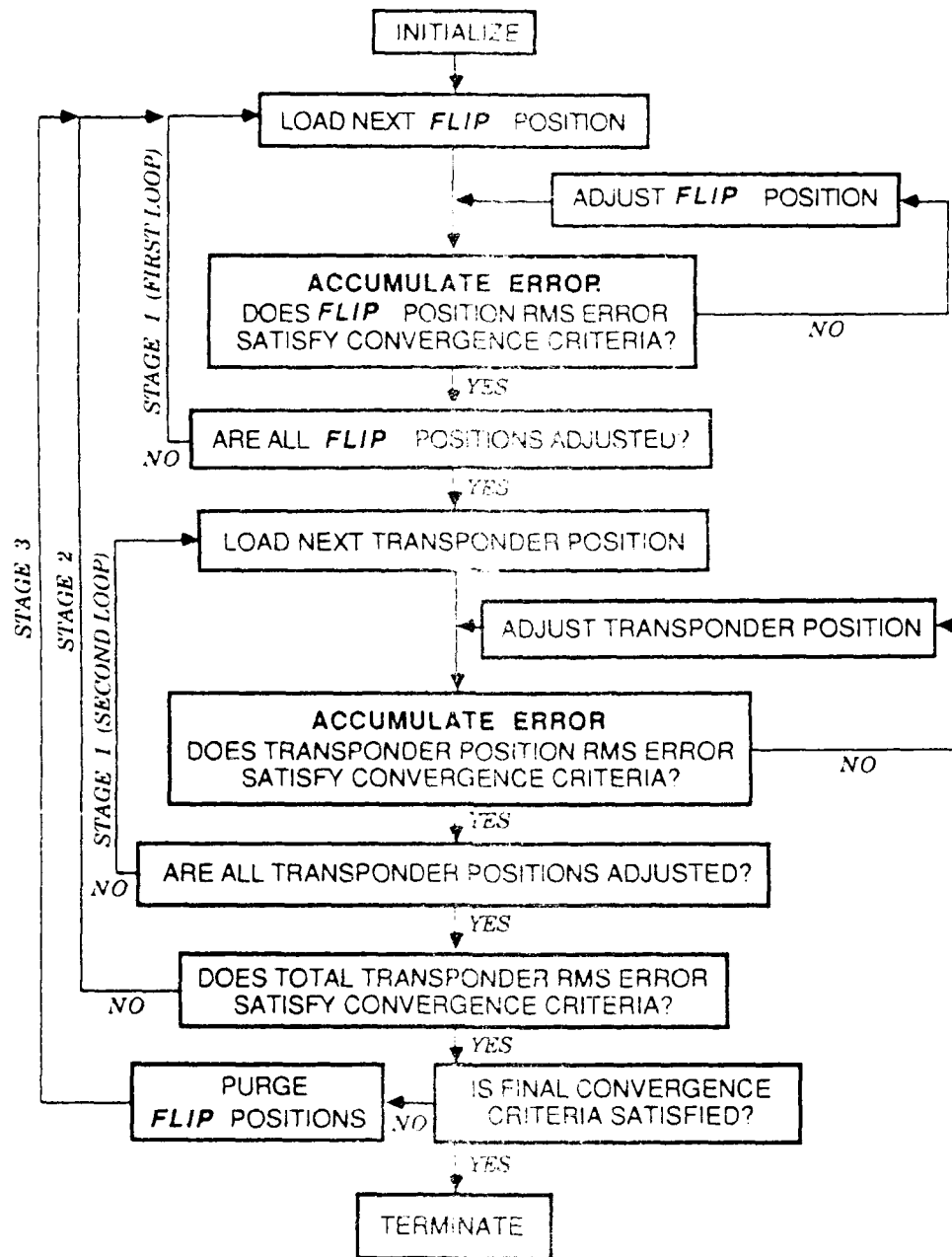


Figure C.2 Transponder Localization Program flow. A general outline of 3 stages in the least squares program logic is presented. During stage 1, the *FLIP* positions are iterated first, followed by the transponder positions and the rms errors are calculated for the positions iterated and compared to a set of convergence criteria; stage 2 compares transponder rms errors to a second set of convergence criteria; stage 3 compares transponder rms errors against a third set of convergence criteria and determines whether to delete *FLIP* positions with excessive errors.

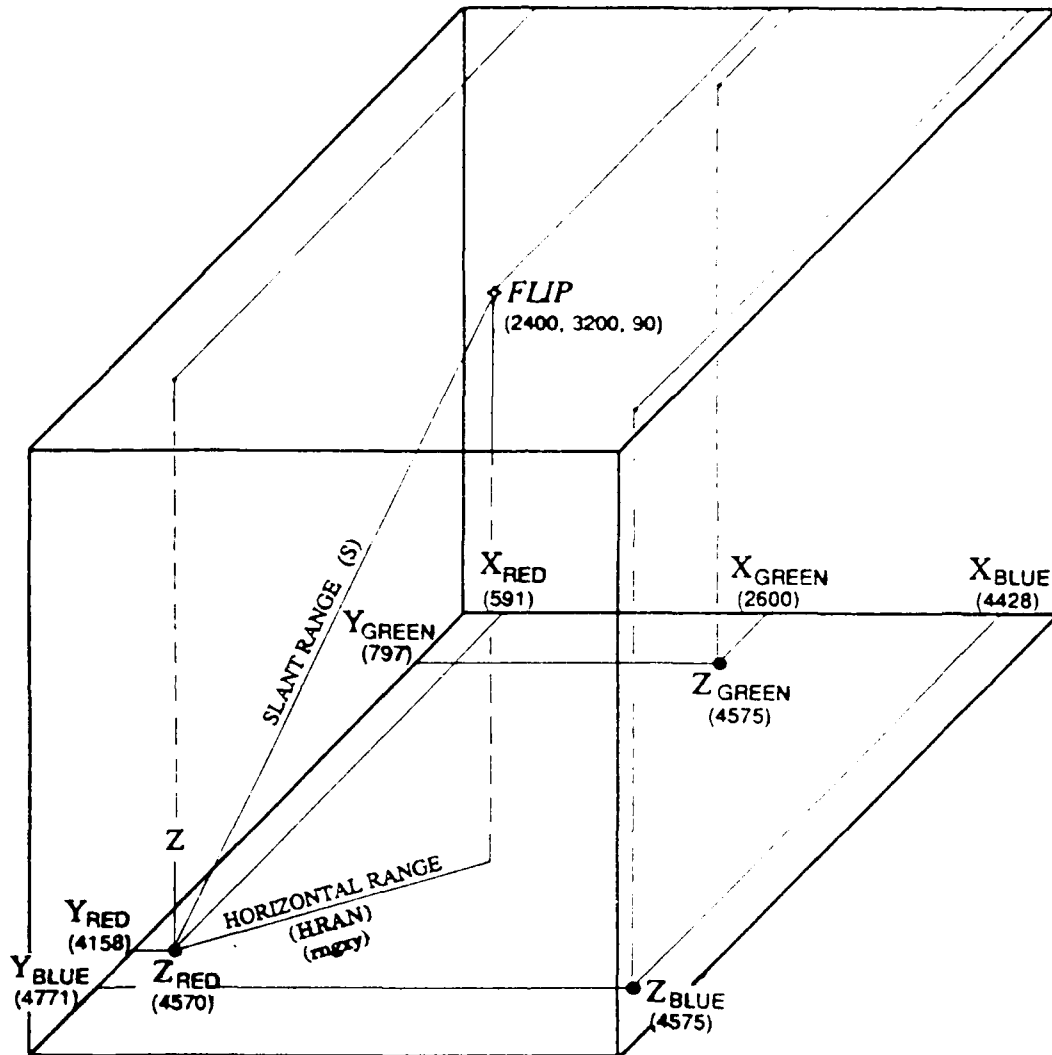


Figure C.3 Navigation Overview. The horizontal projection is estimated first by using the measured slant range and depths (*HRAN*) and then by using the initial xy positions (*rngxy*). The initial xy positions of the transponders (T1=red, T2=green, T3=blue) and *FLIP* as measured by a GPS fix are notated in meters on the axis, and beneath the transponder for depth.

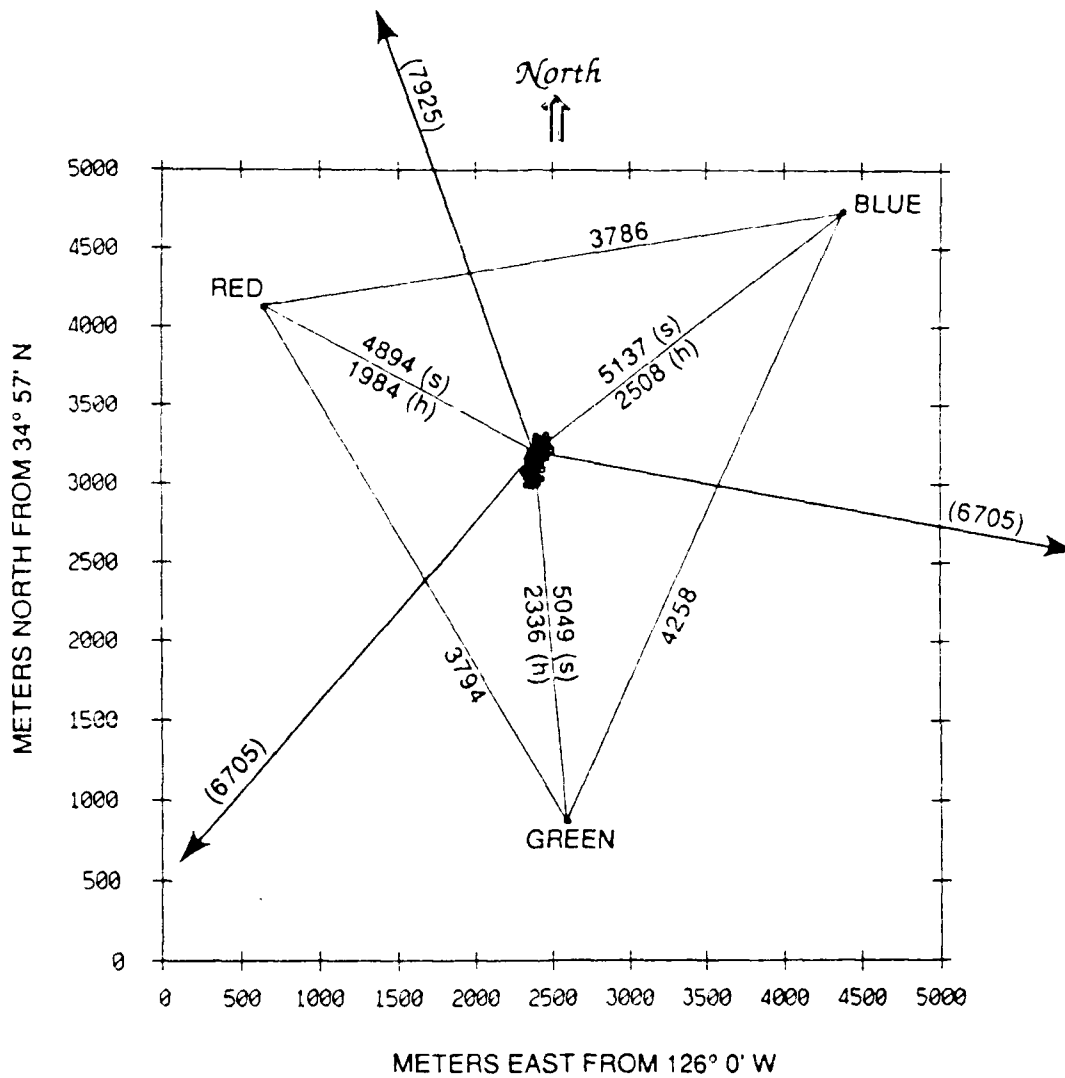


Figure C.4 Spatial Configuration for Navigation During the September 1987 Sea Test. The estimated xy positions of the 3 fixed bottom transponders and of *FLIP* measured hourly over 18 days are shown in plan view. The mooring lines are represented by arrows, and the slant range (s) and horizontal projection of the slant range (h) are indicated in meters from an arbitrary *FLIP* xy position of (2400,3200) m. Transponders baseline distances are also indicated in meters.

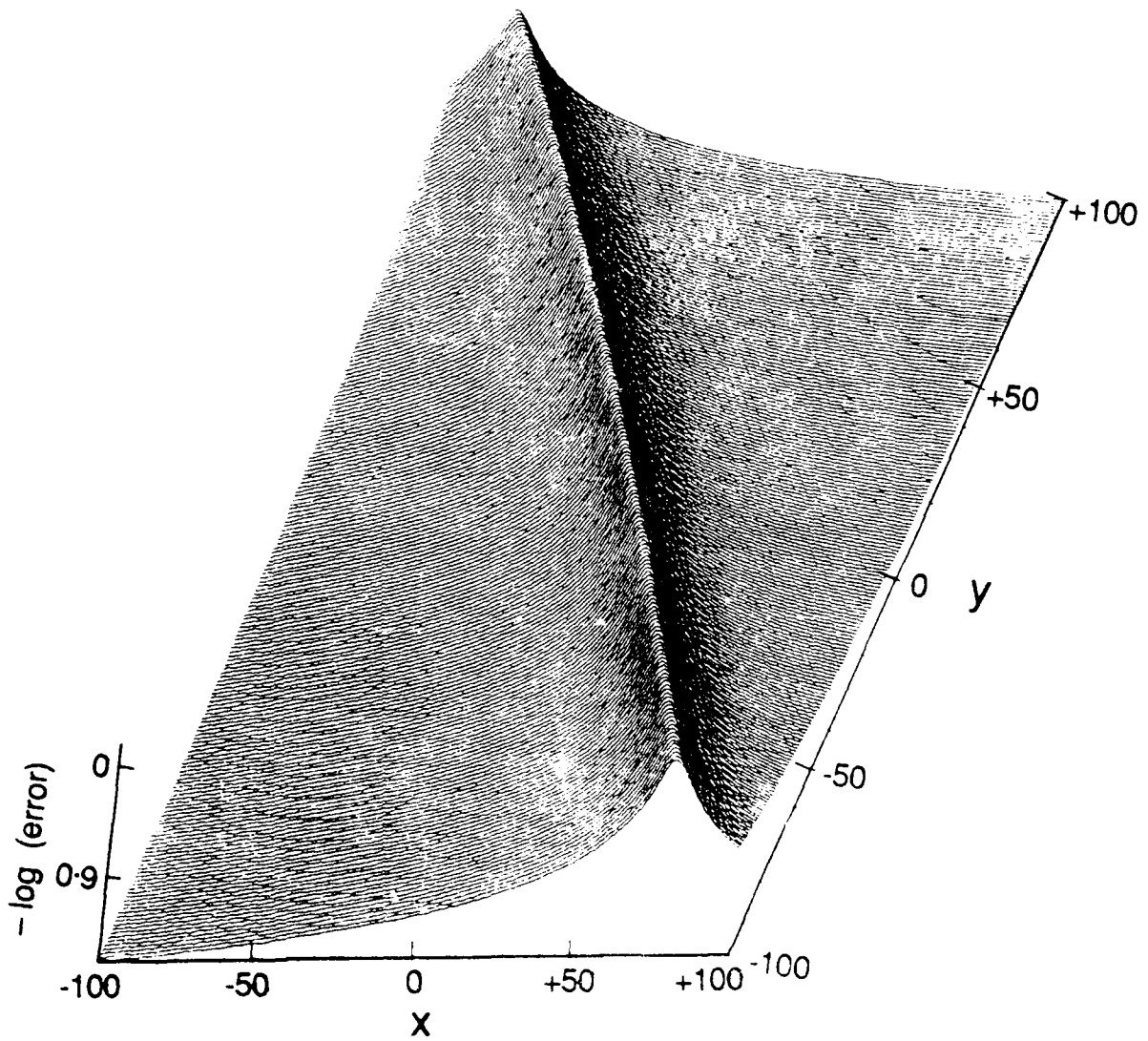


Figure C.5 3D Error Surface. The estimated positions of *HIP* and the transponders were considered known, selected parameters were perturbed and the resulting error calculated. In this example, the blue transponder *x* and *y* positions were perturbed in 1 meter increments to ± 100 m from the original known position which is plotted at the center. The *z* axis is plotted as the negative logarithm of the error to allow visualization of the minima.

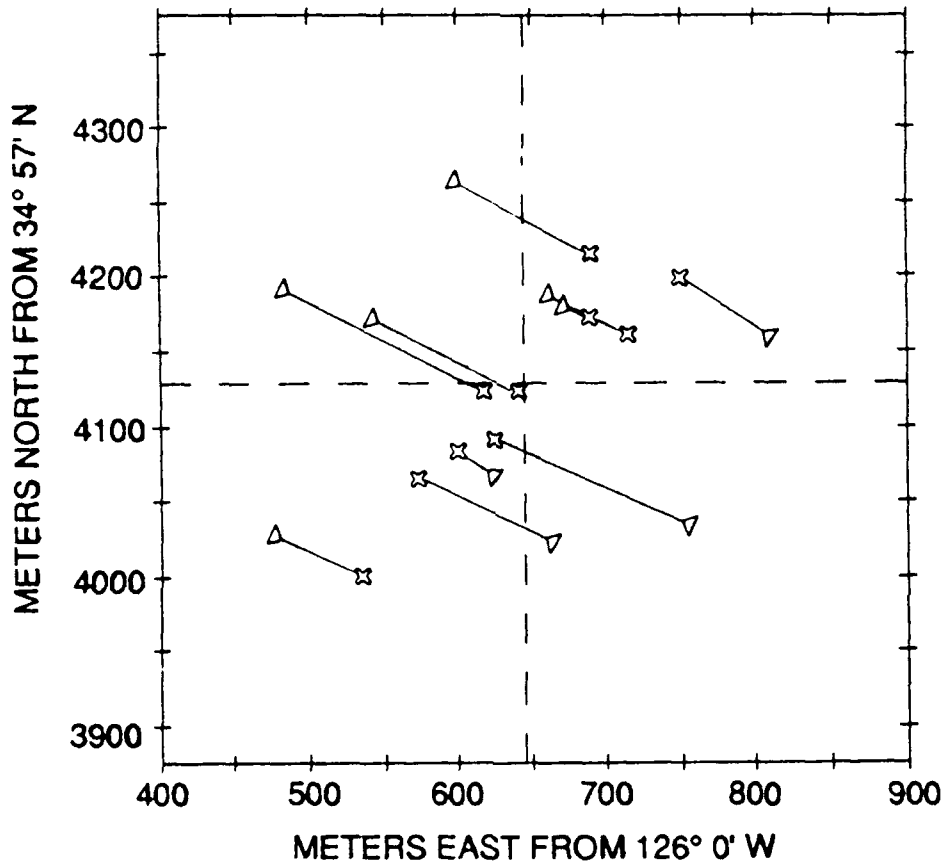


Figure C.6 Monte Carlo simulation of initial transponder positions. This simulation illustrates the constraints in search direction placed on the least squares iteration by the spatial configuration of the survey points. The azimuthal position of the transponders is not accurately determined by the *FLIP* data set used. The transponders tend to move along the transponder to *FLIP* direction. The initial transponder position is notated by a triangle, the final position by a cross.

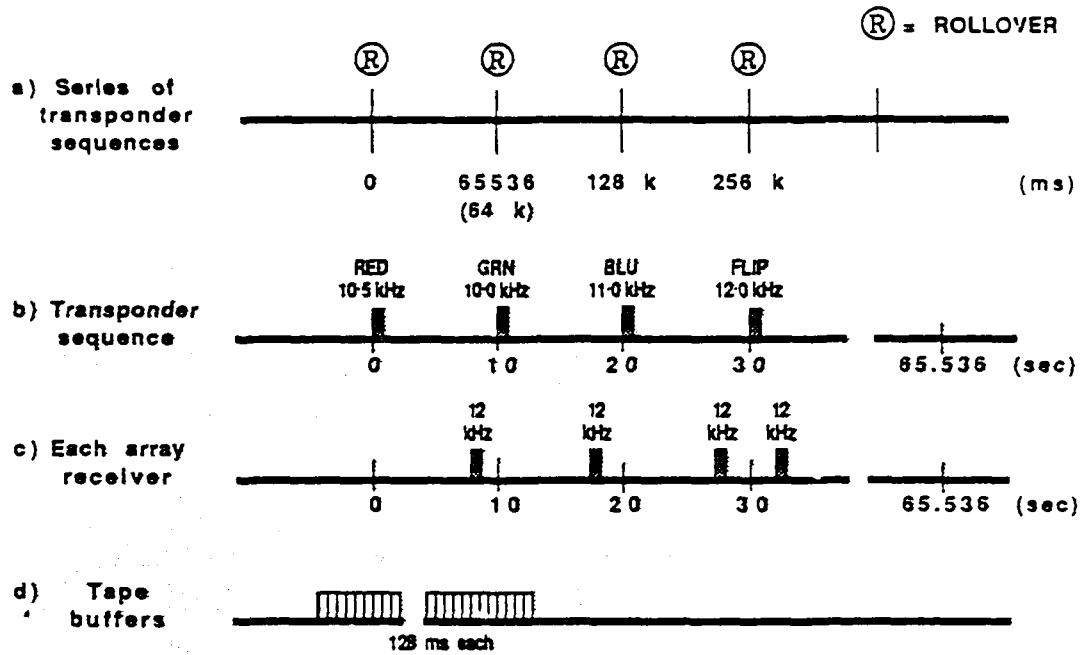
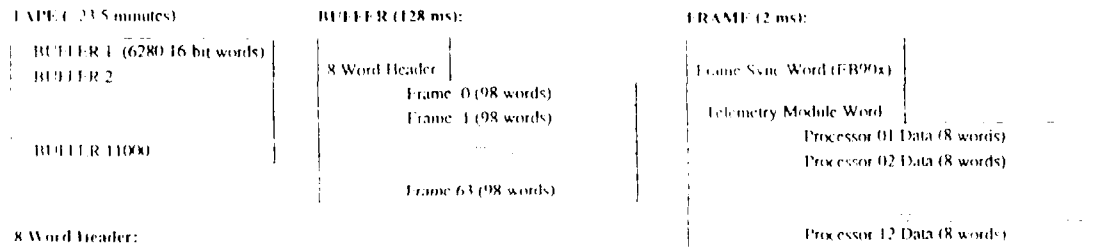
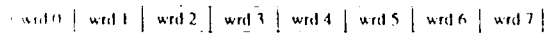


Figure C.8 Navigation Timing Diagram. The timing associated with the array navigation system is illustrated. (a) The transponder interrogation sequence is initiated every 65536 (64 K) ms by a 16-bit hardware clock rollover (R). (b) Each transponder sequence consists of 4 transmissions at unique frequencies issued from a transceiver mounted on the bottom of *FLIP* (90 m depth) spaced 10 s apart. (c) The array receives the 12 KHz transponder replies and the 12 KHz pulse from *FLIP*. The time of arrival of a transponder reply reflects the time it took the acoustic pulse to travel from *FLIP* to the transponder to the array receiver. The time of arrival of the *FLIP* 12 KHz pulse corresponds to the distance from the array receiver to *FLIP*. (d) The hardware clock rollover and 12 KHz arrivals may occur anywhere within a 128 ms tape buffer which complicates the data extraction procedure.



8 Word Header:



Word 0: **Hardware clock** - a 16 bit binary clock which is synchronized with the array and the transponders. It is used as a second order time approximation with a millisecond resolution, turning over every 65536 milliseconds. Since it is read on interrupt from the DMA controller AFTER the data is read into the tape buffer, the value must be corrected to reflect the time at the beginning of the buffer ($128 \cdot 0.016^* (12 \text{ NPRXC}) \text{ ms}$).

Word 1: **Sequence number** - a 16 bit counter associated with each buffer. It is set to zero when the tape driver is initialized and indicates whether any buffers are missing from the tape.

Words 2 and 7: **GOES Satellite Receiver Clock** - this is the clock which allows synchronization of the array data timebase with the real world. The clock is read in as 8 BCD digits: hours (1), minutes (2), seconds (2), and milliseconds (3) on interrupt from the DMA controller AFTER the data buffer is read in. Word 2 contains the first 4 digits (hours, minutes and 10's of seconds); Word 7 contains the second 4 digits.

Word 3: **Unread buffers (MSB) and buffer number (LSB)** - housekeeping words used to monitor the tape driver.

Words 4, 5 and 6: **Real-time clock** - free running time of day clock which is not synchronized with any of the other clocks. It is used for a first order time and date approximation with a one second resolution.

PROCESSOR DATA

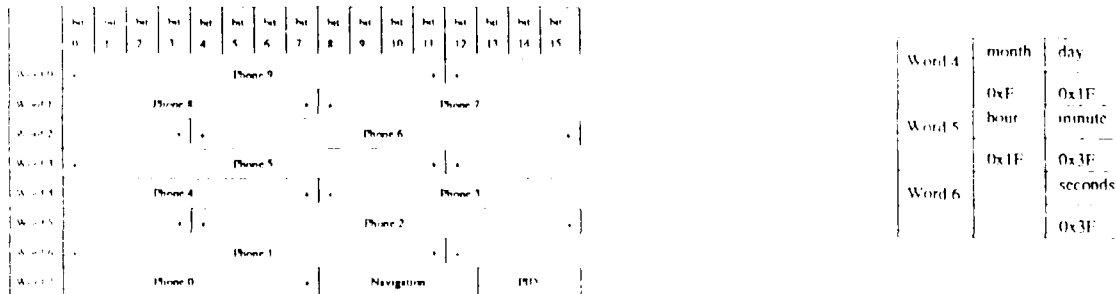


Figure C.9 Data Tape Format. The tape consists of 11000-12000 buffers, a buffer includes an 8 word header and 64 98-word frames, the header stores relevant timing and error information, a frame contains a frame sync word, a frame counter, and twelve 8 word processor data groups, a processor data group has ten samples of the low frequency acoustic field, 5 navigation bits and a 3 bit processor ID. The information relevant to the navigation includes the 8 word header, frame sync word, telemetry module word, 5 (0.4 ms sample rate) navigation bits (bit 8 occurring first in real time) and a 3 bit processor ID (PID).

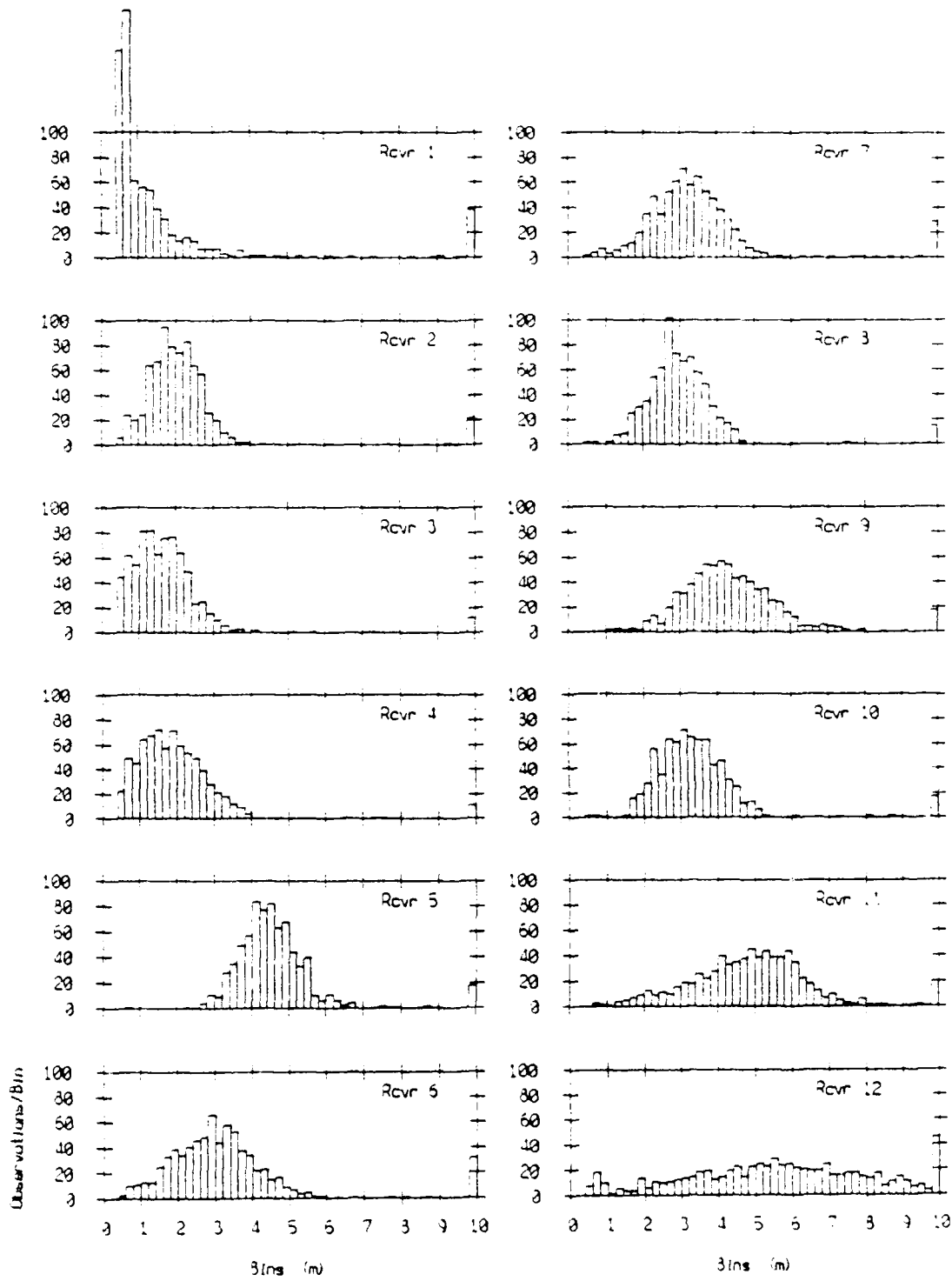


Figure C.10 Receiver Error Distribution. The detection threshold mismatch in the array receivers causes a variation in receiver positional error distribution. This rms error is an output of the program *flpnav* described in Appendix C.

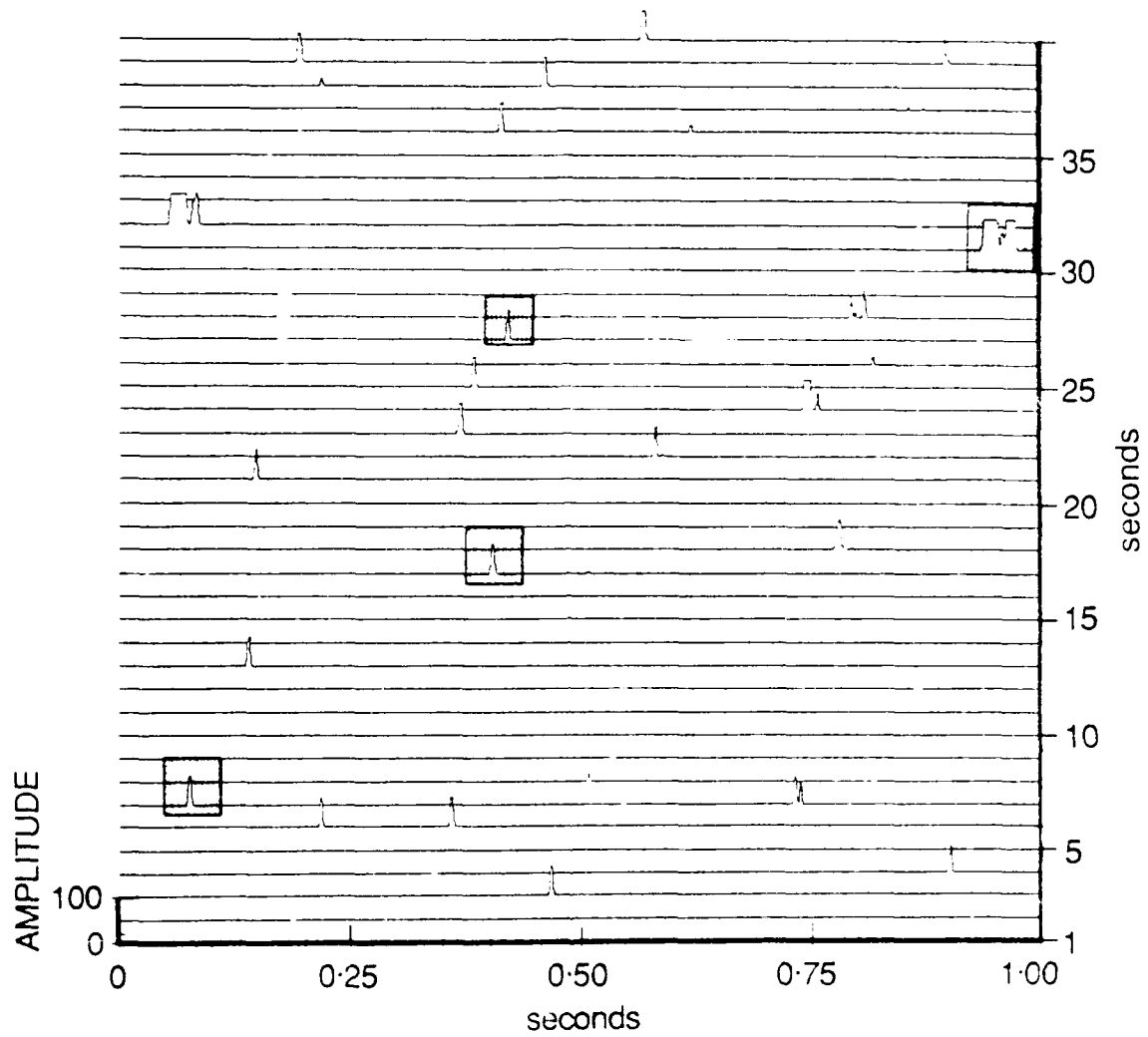


Figure C.11 Correlated Output from a Single Receiver. A single receiver should ideally display only 4 detections during a transponder interrogation sequence. Shown is a 40 s time series of the correlated output of processor 3. Each line represents one second of data, a signal is detected as a transponder return if the amplitude is above the zero level of the line above it. The noise and interfering signals warranted that only data within a valid data window be considered. The desired detections are indicated by the stipled boxes.

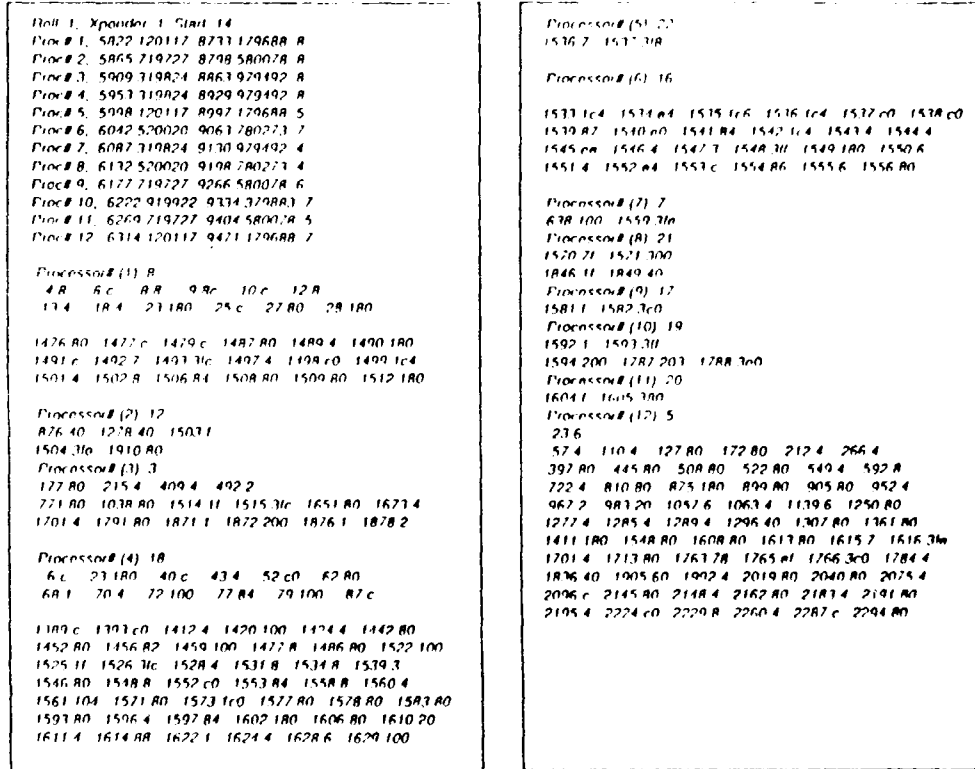


Figure C.12 Raw Navigation Data. Raw data output for one transponder return. Some of the receivers are very noisy and the dashes indicate that data have been deleted for clarity. The processed output is listed first indicating that this is the first rollover, the first transponder and that the difference between the hardware clock rollover and beginning of the buffer is 14. The processors are numbered 1 to 12 with 1 located at the deep end of the vertical array. The first number is travel time in ms, the second is slant range in m assuming a constant sound speed of 1500 m/s, and the third is an indication of the strength of the return. The raw data is printed below, listing the processor number and ID, followed by the data word number and bits set of the hardware receiver output. Each word represents 4 ms or 10 bits for a maximum of 3FF if all 10 bits are set.

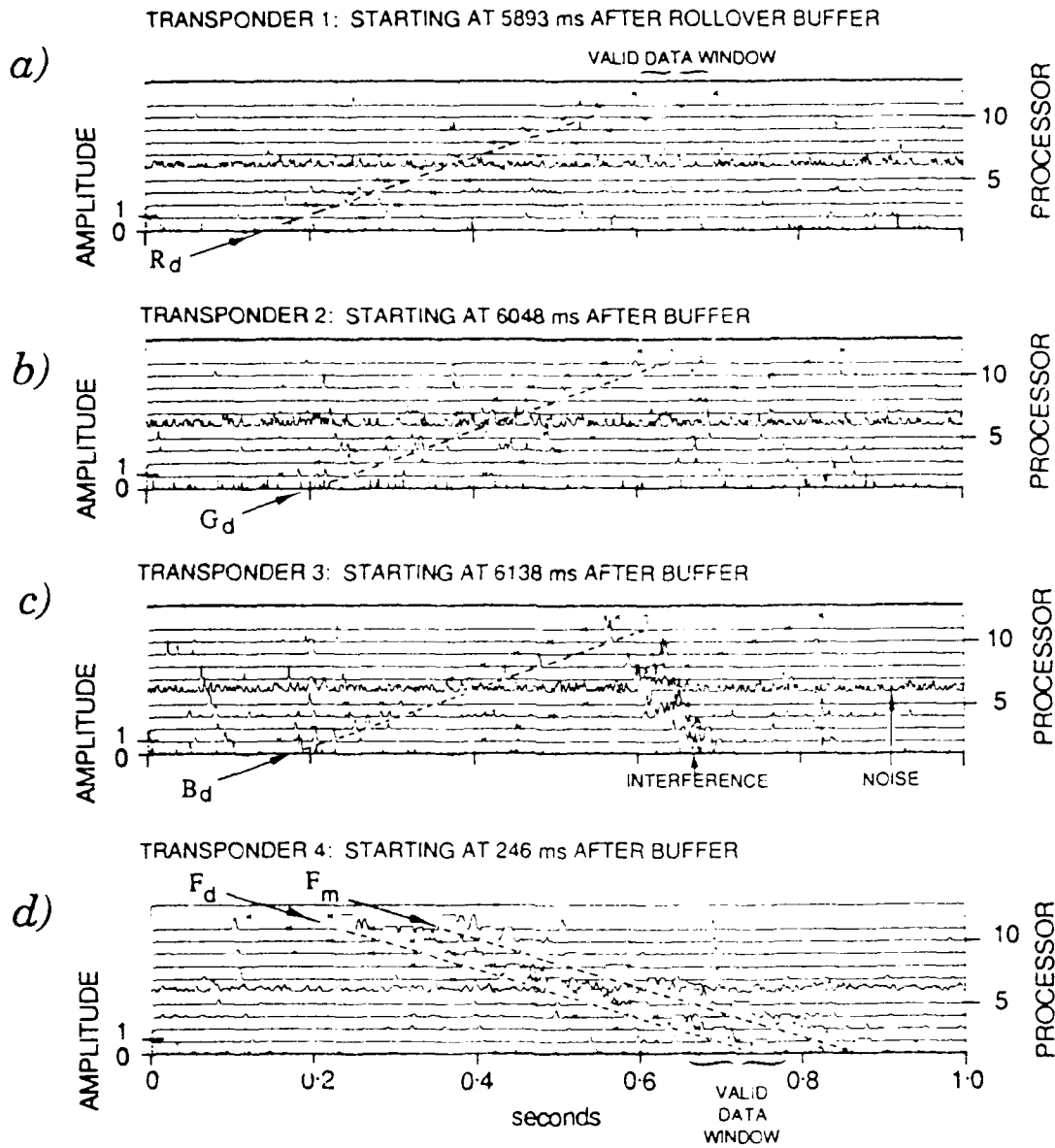


Figure C.13 Transponder Reply Detection. The correlator output for each processor is plotted for 1 second around the time of each of the transponder replies. The top processor plotted is the top processor in the array. The valid data window is indicated by the small x's. The bottom mounted transponder replies are evident as upward traveling pulses, arriving at the bottom of the array first. (a) T1 (red) transponder reply arriving between 0.15 and 0.55 for processors 1 and 11 respectively; (b) T2 (green) transponder reply; (c) T3 (blue) transponder reply; (d) the 12 KHz pulse transmitted from *F11P* arrives as a downward traveling pulse with the surface bounce 120 ms behind.

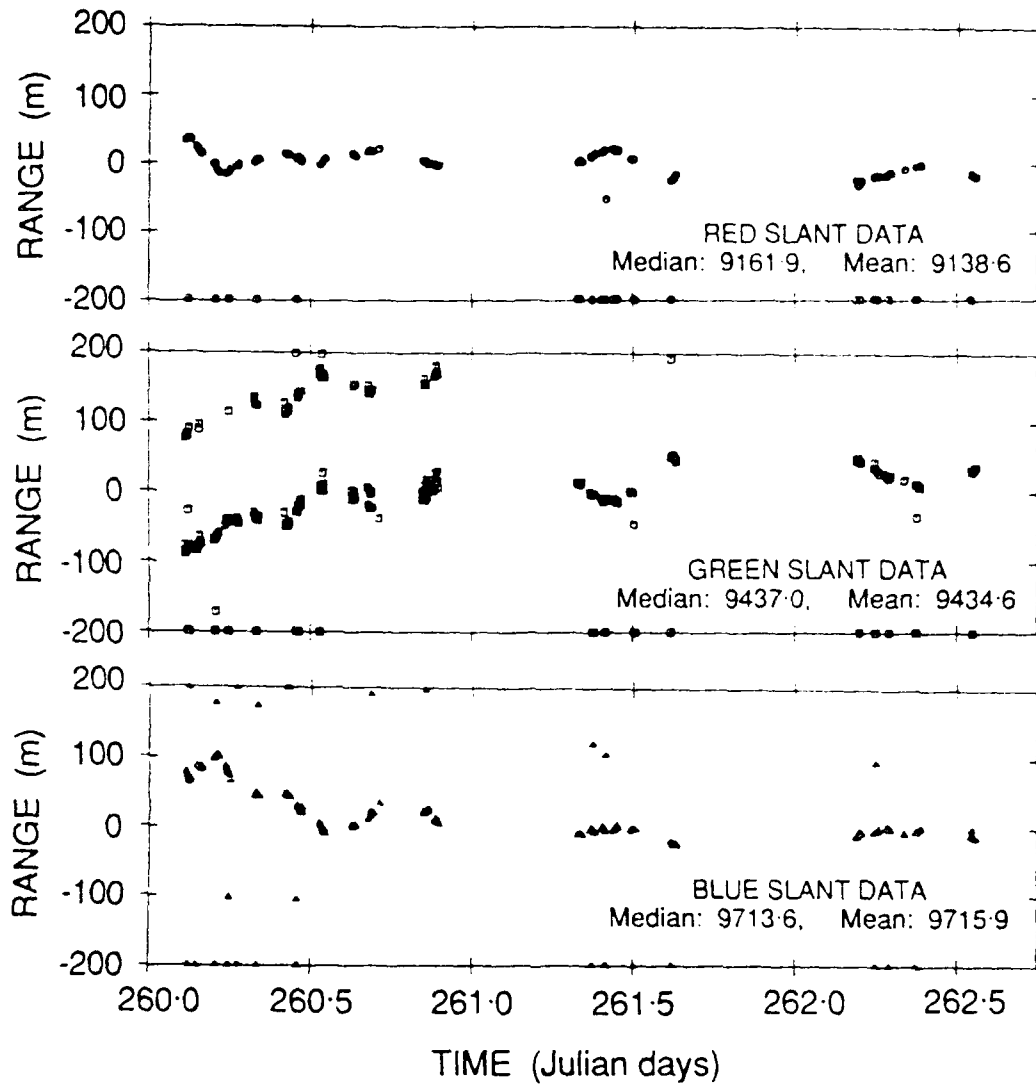


Figure C.14 Slant Range Data. The slant range data for each of the bottom transponders (as detected by the navigation receiver sampled by processor 8) are plotted relative to the median value for a series of nonconsecutive tapes. The data were clipped at ± 200 m from the median value. The errors shown in Figure A.1a for the green transponder are evident as a shadow return 160 m from the direct return. Most of the data appearing at -200 m illustrates a lack of detection due to the navigation of *FLIP* once an hour for several minutes. *FLIP* navigation continues to interrogate the transponders consequently the 12 KHz returns are there, but because the *FLIP* navigation system is not synchronous with the array, the valid data windows filter out most of the unwanted returns.